NORTHWESTERN UNIVERSITY

Barium Titanate Photonic Crystal Electro-Optic Modulators for Telecommunication and Data Network Applications

A DISSERTATION

SUBMITTED TO THE GRADUATE SCHOOL
IN PARTIAL FULFILLMENT OF THE REQUIREMENTS

for the degree

DOCTOR OF PHILOSOPHY

Field of Materials Science and Engineering

By

Peter D. Girouard

EVANSTON, ILLINOIS

December 2016

Abstract

Barium Titanate Photonic Crystal Electro-Optic Modulators for Telecommunication and Data Network Applications

Peter D. Girouard

The microwave, optical, and electro-optic properties of epitaxial barium titanate thin films grown on (100) MgO substrates and photonic crystal electro-optic modulators fabricated on these films were investigated to demonstrate the applicability of these devices for telecommunication and data networks. The electrical and electro-optical properties were characterized up to modulation frequencies of 50 GHz, and the optical properties of photonic crystal waveguides were determined for wavelengths spanning the optical C band between 1500 and 1580 nm.

Microwave scattering parameters were measured on coplanar stripline devices with electrode gap spacings between 5 and 12 µm on barium titanate films with thicknesses between 230 and 680 nm. The microwave index and device characteristic impedance were obtained from the measurements. Larger (lower) microwave indices (impedances) were obtained for devices with narrower electrode gap spacings and on thicker films. Thinner film devices have both lower index mismatch between the co-propagating microwave and

optical signals and lower impedance mismatch to a 50 Ω system, resulting in a larger predicted electro-optical 3 dB bandwidth. This was experimentally verified with electro-optical frequency response measurements. These observations were applied to demonstrate a record high 28 GHz electro-optic bandwidth measured for a $BaTiO_3$ conventional ridge waveguide modulator having 1 mm long electrodes and 12 µm gap spacing on a 260 nm thick film.

The half-wave voltage and electro-optic coefficients of barium titanate modulators were measured for films having thicknesses between 260 and 500 nm. The half-wave voltage was directly measured at low frequencies using a polarizer-sample-compensator-analyzer setup by over-driving waveguide integrated modulators beyond their linear response regime. Effective in-device electro-optic coefficients were obtained from the measured half-wave voltages. The effective electro-optic coefficients were found to increase with both applied electrical dc bias and with film thickness. A record low $0.39\,\mathrm{V}\cdot\mathrm{cm}$ ($0.45\,\mathrm{V}\cdot\mathrm{cm}$) voltage-length product was measured for barium titanate modulators operating at telecommunication wavelengths on a device with 5 µm electrode gap spacing on a 500 nm thick film modulated at a frequency of 100 Hz (1 MHz). This measured voltage-length product is more than a factor of 5 lower than that reported for state-of-the-art silicon conventional waveguide modulators.

The electro-optical characterization of $BaTiO_3$ films revealed a trade-off that exists for traveling wave $BaTiO_3$ modulators: lower voltages are obtained in thicker film devices with narrow electrode gap spacing while larger bandwidths are obtained in thinner film devices with wider electrode gap spacing. These findings were supported by calculations of the film thickness dependent half-wave voltage and electro-optic bandwidth. In order to

demonstrate modulators having simultaneously low voltage operation and high electro-optic bandwidth, photonic crystal waveguide modulators with large group index were investigated through theory and experiment. The theory for slow light phase delay in linear optical materials was extended for second order nonlinear optical materials. This theory was incorporated into a detailed model for predicting photonic crystal modulator performance in terms of voltage-length product and electro-optic bandwidth. Modeling shows that barium titanate photonic crystal modulators with sub-millimeter length, sub-volt operation, and greater than 40 GHz electro-optic bandwidth are achievable in a single device.

Two types of photonic crystal waveguides (PC) on $BaTiO_3$ films were designed, fabricated, and characterized: waveguides with hexagonal lattice symmetry and waveguides with hexagonal symmetry having a line defect oriented in the direction of light propagation. Excellent agreement was obtained between the simulated and measured transmission for hexagonal lattice PC waveguides. An extinction of 20 dB was measured across a 9.9 nm stop band edge, yielding a record large band edge sharpness of 2 dB/nm for all photonic crystal waveguides on ferroelectric films. A 12-fold enhancement of the electro-optic coefficient was measured via optical spectral analysis in a line defect $BaTiO_3$ modulator, yielding an effective electro-optic coefficient of 900 pm/V in the photonic crystal region at a modulation frequency of 10 GHz. This enhancement was demonstrated over a 48 nm range, demonstrating the wideband operation of these devices.

Acknowledgements

I first extend my gratitude to my advisor, Prof. Bruce Wessels, for his guidance and for giving me the opportunity to perform the work presented in this dissertation. Under his guidance, I learned how to critically evaluate and defend my work and how to approach complex scientific problems of societal import. I am grateful to have had many discussions with him spanning from the gritty details of my measurements to higher level aspects of my work and career goals. In doing this work, I have had the opportunity to gain experiences in a unique combination of technical areas. I know that I will benefit from this and his tutelage over the course of my scientific career.

I also thank my committee members, Prof. Lincoln Lauhon, Prof. Vinayak Dravid, Prof. Hooman Mohseni, and Prof. Koray Aydin for taking the time to critically evaluate my work. I acknowledge support from the National Science Foundation under grants ECCS-1201853 and IIP-1500222 and support from the Hierarchical Materials Cluster Program sponsored by The Graduate School at Northwestern University allowing me to complete this work.

At Northwestern University, I was fortunate to work with a number of cordial and inspiring colleagues. I am thankful for Dr. Zhifu Liu's mentorship covering all technical aspects of this work and for Dr. Archibald Peter's generous support and advice. Dr. Young Kyu Jeong provided the majority of thin films for this work, and Dr. Pice Chen contributed to thin film growth, basic characterization of films, and technical expertise for

data acquisition in a number of measurements. I am thankful for both their contributions, which allowed for me to focus on the novel aspects of my work presented in this dissertation. I am also grateful to have had the company and support of a number of other post-docs — Svetlana Kostina, Sanjib Das, and Micah Hanson — and graduate students — Maria Sebastian and Kyle McCall — in our group. I was fortunate to have had the opportunity to advise two visiting students during the course of this work, Guillaume Stanguenec and Yutong Dai.

This work was made possible by a number of collaborations both within and outside Northwestern University. The high-speed measurements were done using equipment shared with Prof. Chandrasekhar of the Physics Department. Sam Davis was my point of contact for coordinating the sharing of equipment and also an inspiring colleague and friend. The wavelength-dependent measurements were done using a tunable laser source borrowed from Prof. Ho in the EECS Department. I am grateful to have had access to this equipment and to have had Yongming Tu's assistance with the wavelength-dependent measurements and for his friendship and support. Dr. Il Woong Jung and Dr. Leonidas Ocola provided invaluable technical assistance in ion beam milling at the Center for Nanoscale Materials (CNM) at the Argonne National Laboratory.

Outside of formal collaborations, I was fortunate to have cultivated a mentorship with Dr. Chad Husko of the CNM. Chad provided valuable feedback on my work from an outside perspective and welcomed me into his professional network. Chad introduced me to a number of other colleagues in the field, including Leif Oxenløwe and Lars Frandsen, my new supervisors whom I currently work with at DTU Fotonik.

I would finally like to acknowledge the support of my closest friends and family. While at Northwestern University, I was extraordinarily lucky to have cultivated friendships with Andrew Mannix, Tasha Sharp, Justin Railsback, Dina Kats, Kelvin Chang, and Sarah Howell. As the first PhD in my family, it has not been easy to explain to my siblings and parents the nature of my work and the potential benefits it has for my career; nevertheless, I am thankful to have had their continued support, regardless of which continent my work takes me to.

List of Abbreviations and Symbols

λ_c ..... Center wavelength of the photonic crystal stop band edge.

λ_w ..... Width of the photonic crystal stop-band edge.

a ..... Lattice parameter, in reference to that of a photonic crystal.

h_{BTO} .... Depth of the holes of a photonic crystal array into the $BaTiO_3$ film.

L_P ..... Photonic crystal length.

r ..... The nominal hole radius for a photonic crystal array.

CW ..... Continuous wave

G ..... Group, in reference to a group of waveguides on a wafer.

IL ..... Insertion loss

PC ..... Photonic crystal

PSCA ... Polarizer-sample-compensator-analyzer

U.C. ..... Unit cell, in reference to the total number of unit cells in a photonic crystal array along the propagation direction.

WG ..... Waveguide, in reference to a specific waveguide on a wafer.

Contents

List of Figures

List of Tables

CHAPTER 1

Introduction

Most modern, high-bandwidth communication systems employ optical links to transfer data. Long-haul fiber optic networks were first implemented in the 1980s, and optical interconnects started to appear in shorter distance local area networks in the 1990s and data networks (datacom) in the 2000s. With time, shorter and shorter electrical links are being replaced with optical ones[14]. In addition to their inherently larger bandwidth, optical links can be integrated into denser arrays than their electrical counterparts as they do not suffer from cross-talk interference between adjacent devices[106]. Optical links also promise lower operating power than their electrical counterparts since they do not require capacitive line charging. Perhaps the most appealing characteristics of optical links are the added degrees of freedom for increasing data bandwidth through spatial[163], time[152], wavelength[16], and mode division multiplexing[15] and the exciting opportunities for ultra-high speed ($>$ 1 Tbit/s single channel operation) all-optical signal processing obtained by harnessing optical nonlinearities[125]. The limiting factors in replacing electrical interconnects with optical ones are cost and complexity. Optical links must also exhibit a significant power reduction over electrical links in order to be favored commercially. A major sub-component of optical interconnects which presents the greatest challenge to their successful implementation in inter- and intra-chip data links is high bandwidth, low power devices controlling electrical to optical signal conversion.

In current datacom applications, backplane optical interconnects consist of internally modulated semiconductor vertical cavity surface emitting lasers (VCSELs) operating at 850 nm for the electrical to optical conversion. VCSEL transceivers currently operate at clock speeds up to 12.5 Gb/s; however, reliable commercially available VCSEL transceivers operating beyond 20 Gb/s will likely require several years of further development[64]. Other material platforms which are being actively researched for optical interconnects include $LiNbO_3$, Si, various electro-optic polymers, III-Vs, Ge/SiGe multiple quantum wells, transparent conducting oxides (TCOs) and two-dimensional materials such as graphene and transition metal dichalchogenides. Of these, $LiNbO_3$ and polymeric materials exhibit the electro-optic effect, Si platforms employ electro-refractive effects, III-Vs and TCOs employ electro-absorption effects, and graphene uses an electrically induced fermi-level shift for modulation. Each material platform, however, has its own challenges. $LiNbO_3$ is a mature platform for long-distance telecom networks but requires long electro-optic interaction lengths and cannot be integrated directly on silicon. Electro-refraction modulation effects in Si enabled by p-n junction waveguides have gathered much interest but suffer from either high insertion loss or low modulation depth. Electro-optic polymers have larger electro-optic coefficients than $LiNbO_3$ but require constant poling. III-V multiple quantum well structures have shown greater than 10 dB extinction ratio[145] and over 67 GHz bandwidth[146] but require complicated processing techniques and cannot be directly integrated onto silicon without wafer bonding. Graphene modulators and plasmonic modulators based on free carrier absorption in transparent conducting oxides are emerging material platforms and show promise for low energy-per-bit devices with device footprint less than 100 µm[137]. These devices have only recently been demonstrated to operate with high electro-optic

bandwidths but still suffer from high insertion losses due to coupling between a purely photonic and purely plasmonic mode[55,105].

An alternative material platform for electro-optic modulators which was investigated in this work is epitaxial thin-film $BaTiO_3$. As a bulk material, ferroelectric $BaTiO_3$ has one of the highest known electro-optic coefficients, 800 pm/V at a wavelength of 1500 nm, and pico-second response time[173]. $BaTiO_3$ is also optically transparent at telecom wavelengths and has a Curie temperature of 120 °C that enables its use in commercial applications. As a ferroelectric, however, $BaTiO_3$ has a high bulk dielectric constant of almost 3000 at dc which remains high into millimeter-wave frequencies[147]. For a traveling wave modulator, these features were thought to severely limit the achievable electro-optic bandwidth through high absorption loss and phase velocity mismatch between the co-propagating electrical modulating signal and optical wave. However, as a thin epitaxial film grown on MgO, the composite dielectric constant is significantly reduced at microwave frequencies to approximately 20[161], enabling near phase-velocity matching. $BaTiO_3$ thin films have been shown to have electro-optic coefficients as high as 360 pm/V and electro-optic response out to 50 GHz in a compact 1.5 mm long device[81]. Recently, there has been great interest in achieving epitaxial integration of $BaTiO_3$ onto silicon-on-insulator (SOI) as a way to add $\chi^{(2)}$ properties to the already present $\chi^{(3)}$ properties of the silicon platform[2–4,24,25,60,116,168].

The central goal of this work is to demonstrate that photonic crystal electro-optic modulators with wide electro-optic bandwidth, low voltage operation, compact size, and wide optical bandwidth are simultaneously attainable by combining the high electro-optic coefficients of $BaTiO_3$ thin films with slow light enhancement. Achievement of this goal required further understanding of the high frequency microwave properties, development

of $BaTiO_3$ photonic crystal waveguides with moderate group indices and low group index dispersion, and demonstration of electro-optic coefficient enhancement at technologically relevant modulation frequencies above 10 GHz. These goals were achieved through an interdependent and synergistic combination of modeling, fabrication and characterization of devices.

The microwave properties of coplanar stripline devices on $BaTiO_3$ thin films were obtained through measurements of the microwave scattering parameters. Obtaining the microwave properties for devices with different electrode gap spacings on different film thicknesses provided insight into the dependence of microwave properties on these parameters. The measurement of the microwave properties was also essential for extracting the frequency-dependent effective electro-optic coefficient from high frequency phase modulation measurements and for making accurate predictions of the ultimate electro-optic bandwidth performance of $BaTiO_3$ modulators.

A major result from the microwave property measurements and modeling is that the total microwave losses can be decreased and electro-optic bandwidth significantly increased by simply decreasing the modulator length. While the high electro-optic coefficients of $BaTiO_3$ already enable low voltage modulators in a compact length that is an order of magnitude smaller than that of $LiNbO_3$, the total microwave losses are sufficiently large to limit the bandwidth to approximately 30 GHz in mm long devices. Further reductions in size and increases in bandwidth are potentially achievable, however, by employing slow light enhancement of the electro-optic coefficient to decrease the voltage-length product and hence also decrease the required modulator length for a π phase shift. In this work, a definitive enhancement of the electro-optic coefficient was demonstrated in a 1 millimeter

long modulator with a 37 micron long photonic crystal segment. An 12-fold increase in the effective electro-optic coefficient to 900 pm/V was obtained in the photonic crystal region.

The electro-optic coefficient enhancement measured in $BaTiO_3$ photonic crystal modulators provided strong evidence upon which to model the performance of shorter modulators with higher group index. The modeling was done with input from microwave property measurements of $BaTiO_3$ coplanar stripline devices. By shortening the electrodes to sub-millimeter lengths and including photonic crystal waveguides with lengths on the order of 100 µm and group indices between 5 and 10, electro-optic modulators with less than 0.2 V·cm and greater than 40 GHz 3dB electro-optic bandwidth are predicted in the same device.

CHAPTER 2

Background and Literature Review

2.1. The Linear Electro-Optic Effect

Electro-optic effects arise from the change in permittivity of a crystalline material due to a redistribution of (bound) charge caused by an applied electric field. The linear electro-optic effect only occurs in non-centrosymmetric crystals and dominates over the quadratic electro-optic effect, which occurs in all crystalline materials. The linear electro-optic effect is generally expressed in terms of the index ellipsoid[123,173]

$$\sum_{i=1}^{i=3}\sum_{j=1}^{j=3}\eta_{ij}(\mathbf{E})x_i x_j = \sum_{i=1}^{i=3}\sum_{j=1}^{j=3}\left[\eta_{ij}(0) + r_{ik}E_k\right]x_i x_j = 1 \tag{2.1}$$

where $\eta_{ij} = \epsilon_0(\epsilon^{-1})_{ij}$ is the impermeability tensor element, r_{ik} is the linear electro-optic tensor element expressed with contracted notation, and E_k is the electric field component with $k = 1, 2, 3$ denoting the principle axis directions. From Eqn. 2.1, it can be shown that the refractive index in a principle direction in the crystal in the presence of an electric field is of the general form

$$n_i' = n_i \pm \frac{1}{2}n_i^3 r_{jk}E_k a, \tag{2.2}$$

where n_i' is the refractive index in the direction of a principle optical axis of the rotated coordinate system, n_i is the refractive index in the original coordinate system, and a is a term arising from the coordinate transformation. In the presence of an electric field, any

cross terms in Eqn. 2.1 will change the orientation of the principle axes. In general, if cross terms are present the term a is linear in E_k, which gives a quadratic dependence to n_i'[173], as is the case for $BaTiO_3$ when the field is applied in the x or y directions[103].

The electro-optic properties of $\chi^{(2)}$ materials are intrinsically related to the dielectric constants and hence have a similar frequency dependence. For crystals with $P4mm$ symmetry such as $BaTiO_3$, the non-zero electro-optic tensor elements are[37]

$$\begin{aligned} r_{13} &= 2g_{12}P_s\epsilon_0(\epsilon_3 - 1) \\ r_{33} &= 2g_{11}P_s\epsilon_0(\epsilon_3 - 1) \\ r_{51} &= g_{44}P_s\epsilon_0(\epsilon_1 - 1) \end{aligned} \tag{2.3}$$

where g_{ik} are the quadratic electro-optic tensor elements, P_s is the spontaneous polarization, ϵ_0 is the permittivity of free space, and ϵ_k is the relative permittivity along the k^{th} principal direction. As shown in Eqn. 2.3, the electro-optic tensor elements are directly proportional to the principal dielectric constants. The dielectric constant and electro-optic coefficient of ferroelectric materials includes dipolar, ionic, and electronic contributions. The frequency dependence of these contributions is illustrated in Fig. 2.1. At low frequencies below 10 GHz, dipolar contributions from domain switching and the oscillation of domain walls between pinning sites are dominant[80,147]. At intermediate frequencies up to 100 GHz, ionic contributions arising from the displacement of atoms dominate the frequency response[147]. Above 100 GHz, only the polarization of electronic orbitals contribute to the electro-optic coefficient.

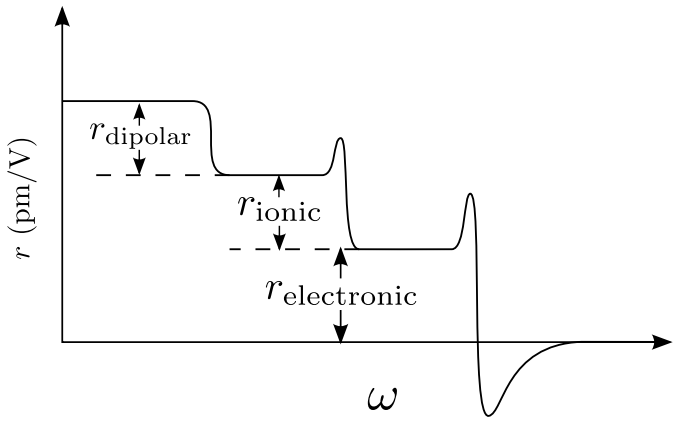

Figure 2.1. Frequency depence of the electro-optic coefficient, showing dipolar, ionic, and electronic contributions[134].

2.2. Properties of Coplanar Stripline Electrodes

Coplanar stripline (CPS) electrodes were first introduced along with coplanar waveguide (CPW) electrodes as a method of integrating microwave transmission lines onto wafers in the 1970s[71] and 1980s[119]. These complementary structures have since been used in numerous applications, including balanced mixers[6], printed dipole antennas[93], directional couplers[160], filters, amplifiers[120], integrated waveguide detectors[166], and high speed optical modulators[112]. The development of millimeter wave integrated circuits required rapid characterization of CPW and CPS electrodes, resulting in analytical and semi-empirical relations for important properties such as the effective index, characteristic impedance, and attenuation losses[44,52,154,159]. Models have also been developed for devices on multilayer dielectric substrates[28,51]. The modeling equations applicable to the analysis of the microwave properties of CPS devices on multilayer dielectrics are discussed in the following sections.

2.2.1. Microwave Index and Characteristic Impedance

The effective microwave index is analogous to an effective optical mode index and describes the factor by which microwave propagation is slowed in a medium. The effective index is defined as[28,50]

$$n_{mw} \equiv \sqrt{\epsilon_{re}} \tag{2.4}$$

where ϵ_{re} is the real part of the effective microwave dielectric constant. The effective dielectric constant ϵ_{re} is the dielectric constant which would be experienced by the propagating wave in an equivalent homogeneous medium. The concept of an effective dielectric constant and effective index are especially important for CPS and CPW devices on integrated ferroelectric thin films. For these devices, the dielectric constant of the film is typically two orders of magnitude larger than that of the substrate; the thickness of the film, however, is on the order of 100 nm to 1 µm, which means that the effective index is dominated by that of the substrate and the medium above the device[161]. The order of magnitude difference in the dielectric constant and the disparity in length scales for integrated ferroelectric devices usually precludes the use of analytical models such as those of Chen et al[28] and Gevorgian[51] for accurately calculating the microwave index. Hence, either full-wave calculations or measurements are preferred.

The characteristic impedance is related to the microwave index by[28]

$$Z = \frac{120\pi}{n_{mw}} \frac{K(k')}{K(k)} \tag{2.5}$$

where K is the complete elliptic integral of the first kind and the elliptic moduli are

$$\begin{aligned} k &= \sqrt{1-\left(\frac{g}{2w+g}\right)^2} \\ k' &= \sqrt{1-k^2} \end{aligned}$$

where g and w are the electrode gap spacing and width, as defined in Fig. 2.2.

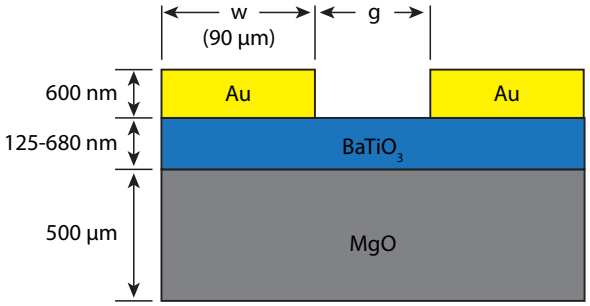

Figure 2.2. Schematic of the coplanar stripline device cross-section.

The complete elliptic integral of the first kind is given by

$$K(k) = \frac{\pi}{2}\sum_{n=0}^{\infty}\left[\frac{(2n-1)!!}{(2n)!!}\right]^2 k^{2n}$$

As shown in Fig. 2.3, the ratio $K(k')/K(k)$ is single-valued and well behaved over a reasonable range of gap spacings spanning that used in this work. The impedance calculated from Eqn. 2.5 is hence a robust method of calculating the characteristic impedance of CPS electrodes on ferroelectric thin films as long as an accurate value for the effective index is known.

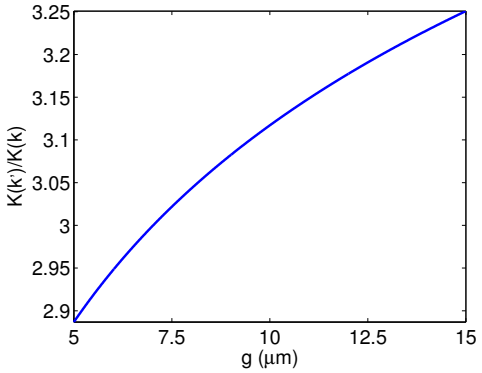

Figure 2.3. Calculated ratio $K(k')/K(k)$ used in Eqn. 2.5 over a relevant range of electrode gap spacings.

2.2.2. Conductor Loss Coefficient

The total microwave attenuation losses are modeled as a summation of contributions from conductor and dielectric portions as[58]

$$\alpha = \alpha_c\sqrt{f} + \alpha_d f \quad [\text{dB/cm}]$$

where α_c is the conductor loss coefficient in units of $\text{dB/cm}/\sqrt{\text{GHz}}$ and α_d is the dielectric loss coefficient in units of dB/cm/GHz. A numerical calculation of the conductor loss was proposed by Yamashita et al[172] based on the Wheeler inductance formula[162] in which α_c is given by

$$\alpha_c = \alpha_{c,0} n_{eff} = 8.686\frac{\pi}{\lambda_0} n_{eff}\left(\frac{C^a - C^a_\delta}{C^a_\delta}\right)$$

where λ_0 is the free space microwave wavelength, n_{eff} is the microwave index, C^a is the capacitance of the transmission line in vacuum, and C^a_δ is the capacitance of the line when the walls of the conductor are receded by half of the skin depth, δ. This approach requires either a numerical calculation of the capacitances C^a and C^a_δ. Analytical models have

been proposed separately by Garg et al[50] and Ghione[52]. In the model by Ghione, α_c is calculated as

$$\alpha_c = \frac{8.68 R_s \sqrt{\epsilon_{re}}}{480\pi K(k)K(k')(1-k^2)} \left\{ \frac{1}{a}\left[\pi + \ln\left(\frac{8\pi a}{t}\frac{1-k}{1+k}\right)\right] + \frac{1}{b}\left[\pi + \ln\left(\frac{8\pi b}{t}\frac{1-k}{1+k}\right)\right]\right\}$$

where R_s is the surface resistance, ϵ_{re} is the effective dielectric constant, K is the complete elliptic integral with arguments $k = (b-a)/(b+3a)$ and $k' = \sqrt{1-k^2}$, $2a$ is the gap spacing g, $b = g + a$, and t is the electrode thickness. The calculations are valid for $t > 3\delta$ where δ is the skin depth and $t << a$ and $t << (b-a)$. The skin depth is calculated as

$$R_s = \sqrt{\frac{\pi f \mu}{\sigma}}$$

where σ is the electrode conductivity. In the model by Garg et al, α_c is calculated as

$$\alpha_c = 4.88 \times 10^{-4} R_s \epsilon_{re} Z_0 \frac{P'}{\pi w}\left(1 + \frac{w}{g}\right) \cdot \left\{ \frac{1 + 1.25t/\pi w + (1.25/\pi)\ln(4\pi w/t)}{\left[2 + w/g - (1.25t/\pi g)(1 + \ln(4\pi w/t))\right]^2}\right\}$$

with

$$P' = \left(\frac{K(k)}{K(k')}\right)^2 P$$

and

$$P = \begin{cases} \frac{k}{(1-\sqrt{1-k^2})(1-k^2)^{3/4}} & \text{for } 0 \le k \le 0.707 \\ \frac{1}{(1-k)\sqrt{k}}\left(\frac{K(k')}{K(k)}\right)^2 & \text{for } 0.707 \le k \le 1.0 \end{cases}$$

Ghione has shown that Gupta's method is an over-estimate of the conductor loss for the case of narrow electrode widths and wide gaps. Both methods, however, are valid only for frequencies where the conductor thickness is more than three times the skin depth. For

conditions where $t < 3\delta$, numerical calculations of the conductor loss using the approach of Yamashita et al[172]are recommended[126].

2.2.3. Dielectric Loss Coefficient

The dielectric loss coefficient for coplanar lines on a multilayer substrate is given by[113]

$$\alpha_d = \frac{\pi f}{n_{\mu w} c} \left(\Gamma_f \epsilon_f \tan\delta_f + \Gamma_s \epsilon_s \tan\delta_s\right) \tag{2.6}$$

where f is the microwave frequency, c is the speed of light in free space, ϵ is the dielectric constant, Γ is the microwave power confinement factor, and $\tan\delta$ is the dielectric loss tangent. The subscripts f and s indicate properties of the film and substrate, respectively. The microwave power confinement factor is calculated numerically from the simulated microwave fields as

$$\Gamma_a = \frac{\iint_a |E_m|^2 dx\, dy}{\iint_A |E_m|^2 dx\, dy}$$

where a represents the area of interest, for example the film, A represents the entire cross sectional area of the device, and $|E_m|$ is the magnitude of the electric field.

2.3. Electro-Optic Modulators

The electro-optic change in refractive index can be employed as a means for modulating both the phase and intensity of laser light. A schematic of an integrated electro-optic phase modulator is given in Fig. 2.4. This device architecture was used to study the electro-optic properties of $BaTiO_3$ thin films in this work. The advantage of this device architecture for studying electro-optic material properties is that it is a versatile configuration for measuring both phase and intensity modulation properties. By operating a phase modulator in a

polarizer-sample-compensator-analyzer setup, the electro-optic intensity modulation can be measured. This approach was used to directly measure the half-wave voltage, as discussed in Section 3.7.1. In this configuration, the input light is linearly polarized such that it is equally decomposed into the two normal modes of propagation, TE and TM, with refractive indices n_o and n_e and effective electro-optic coefficients r_o and r_e, respectively. The phase retardation accumulated between the two co-propagating modes is expressed using Eqn. 2.2 as

$$\phi = k_0 \left[n_o(E) - n_e(E) \right] L = k_0 (n_o - n_e) - \frac{1}{2} k_0 (n_o^3 r_o - n_e^3 r_e) \frac{V}{g} L \quad \text{(radians)} \tag{2.7}$$

where k_0 is the wavevector in free space, V is the applied voltage, g is the gap spacing between the electrodes, and L is the electrode (electro-optic interaction) length. In Eqn. 2.7, the delay due to the natural birefringence is given by $k_0(n_o - n_e)$ and the electro-optic phase delay is $-\frac{1}{2} k_0 (n_o^3 r_o - n_e^3 r_e) \frac{V}{g} L$. A mathematical model describing the intensity modulation obtained by operating a phase modulator with phase delay given by Eqn. 2.7 in a PSCA setup is given in 3.7.1.

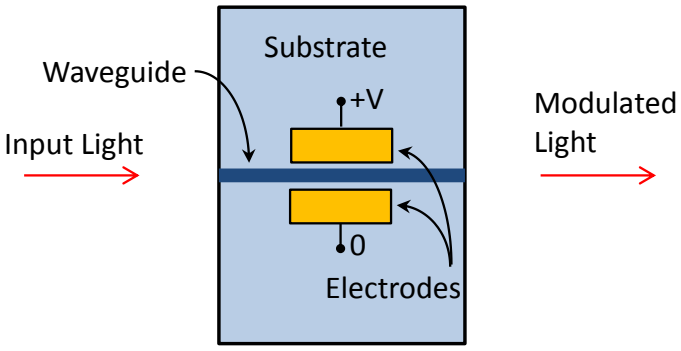

Figure 2.4. Top-view schematic of an electro-optic phase modulator.

Electro-optic intensity modulators typically consist of an integrated Mach Zehnder interferometer with one of the arms containing a phase modulator. The phase modulator is typically used to impart a phase delay to one of the arms; when the phase delay between the two arms is π radians, complete destructive interference at the output occurs. By applying a potential V between the electrodes shown in Fig. 2.5, the transmitted intensity I is modulated as

$$I(V) = \cos^2\left(\frac{\phi_0}{2} - \frac{\pi}{2}\frac{V}{V_\pi}\right)$$

where V_π is the voltage required to cause a π phase retardation in one of the arms. V_π is given by

$$V_\pi = \frac{\lambda_0 g}{n^3 r_{eff} \Gamma L}$$

where λ_0 is the free space wavelength and Γ is the electro-optic overlap factor which accounts for the overlap of the modulating and optical electric fields.

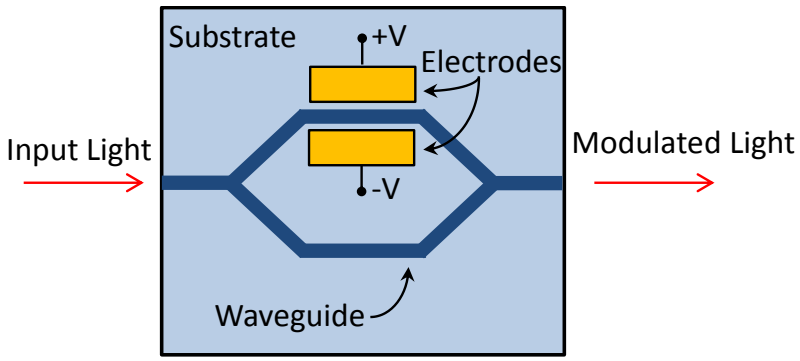

Figure 2.5. Top-view schematic of a Mach-Zehnder intensity modulator.

2.4. Performance Metrics for Electro-Optic Modulators

In this section, the performance metrics for all intensity electro-optic modulators regardless of the modulation mechanism are be introduced. These performance metrics represent

the most important descriptors for optical modulators for optical interconnects according to the latest report from the International Technology Roadmap for Semiconductors (ITRS) for optical interconnects[1]. While this report applies to datacom interconnects, in most cases, with a few exceptions as noted below, these metrics are more aggressive than those currently applied to telecommunication light modulators and are hence comprehensive. The specific values of the metrics discussed here are the projected values for the year 2022 according to the ITRS report.

2.4.1. Drive Signal Voltage

The drive signal voltage refers to the amplitude of the modulating electric field required for intensity modulation. Drive voltages of 1 V or smaller are required in order to be compatible with the voltage levels of CMOS chips. The push for smaller modulating voltages for both optical interconnects and transistors is to reduce the power consumption and deleterious local heating.

2.4.2. Electro-Optic Bandwidth

The latest ITRS report specifies that future optical interconnects should have bandwidths in excess of 20 GB/s. However, in order for optical interconnects to surpass the performance of current copper electrical interconnects in terms of energy per bit, the required bandwidth is likely much greater[106]. Before specifying target values, the distinction between clock rate and bandwidth is made: clock rate refers to the data rate of a single device whereas bandwidth refers to the clock rate multiplied by the total number of devices on a chip;

bandwidth therefore refers to the chip performance while clock rate refers to the performance of a single device. An additional distinction is made between on- and off-chip data rates; on-chip interconnects refer to those supplying data to electrical components on a chip, while off-chip interconnects refer to those supplying data between major components such as a central processing unit and off-chip memory. The clock rate for off-chip devices is predicted to be 67 GHz while the on-chip clock rate is expected to be 14.3 GHz[106]. While the required future on-chip data rate will be determined by the direction taken for computer architectures, it is expected to be approximately 5 times greater than that of the total off-chip bandwidth[106]. The predicted off-chip bandwidth is an astronomical 230 Tb/s, which will require at least 16 channel wavelength division multiplexing if the off-chip clock rate of 67 GHz is met. According to these numbers, there is a clear need for compact devices operating at clock rates in excess of 67 GHz. Furthermore, it is clear that optical interconnects have a better chance of superseding electrical interconnects for off-chip applications as long as high clock rates are achievable.

2.4.3. Optical Bandwidth

The optical bandwidth is the range of wavelengths over which a device can operate. Wide optical bandwidths over tens of nanometers are desired for flexible wideband operation that is not affected by thermal fluctuations[45]. For devices designed to operate at an optical resonance, the optical bandwidth decreases with increasing quality factor; a trade-off hence exists between enhancing light-matter interactions at an optical resonance via a high quality factor and operation over a wide optical bandwidth[9]. For these reasons, highly resonance devices such as ring resonators are less favorable than wideband devices

employing integrated waveguides slot or rib waveguides and dispersion-engineered photonic crystal waveguides. Wideband devices with moderate group indices also offer lower total losses[61] and less pulse broadening and signal degradation[41].

2.4.4. Modulation Depth

Modulation depth refers to the total attenuation of light, expressed in dB, achieved in the "off"-state. In long-distance telecommunication applications, modulation depths of 15 dB are typically achieved. Large modulation depths are required in long-haul telecommunication applications as longer propagation distances expose the modulated intensity signal to more sources of signal distortion. The required modulation depth according to the ITRS report is only 5 dB[1]. In datacom applications, propagation distances on the order of millimeters or centimeters reduces the probability of signal distortion, hence the lower required modulation depth.

2.5. Materials and Physical Mechanisms for Light Intensity Modulation

2.5.1. Electro-Absorption Modulators

An alternative mechanism to the electro-optic effect that is used for light intensity modulation is electro-absorption. Electro-absorption effects are those for which an applied electric field changes the absorption properties of a semiconductor material. Two physical mechanisms for electro-absorption include the Franz-Keldysh effect (FKE) and the quantum confined stark effect (QCSE). Material platforms currently under study for employing these electro-absorption effects include Ge/SiGe and III-V multiple quantum well (MQW)

heterostructures. Recent progress in III-V technology has shown hybrid silicon electroabsorption modulators consisting of a III-V MQW stack wafer bonded to silicon[146]. Tang et al have demonstrated up to 67 GHz bandwidth[146] in a traveling wave configuration and 30 GHz bandwidth with 112.5 fJ/bit in a lumped electrode configuration[145]. In the traveling wave configuration, a drive voltage of 2.2 V and extinction ratio of 9.6 dB were achieved; in the lumped electrode configuration, a lower driving voltage of 1 V was shown but the extinction depth was only 5 dB. While these devices show great potential for implementation as datacom interconnects, a combination of lower voltage and higher bandwidth is still needed.

Ge/SiGe MQWs directly grown onto silicon substrates have gathered great interest recently since they can be potentially integrated directly onto silicon platforms. These electroabsorption devices have demonstrated up to 9 dB modulation depth[27], bandwidths as high as 40 GHz[43] and energies per bit on the order of 10 fJ/bit, although these metrics have not been reported simultaneously in one device. A major issue with this platform, however, is that thick buffer layers are required to prevent dislocations from forming in the quantum wells due to lattice mismatch with the silicon substrate. These thick buffer layers prevent efficient side-coupling into the device as the thick buffer layers raise the devices off the surface of the chip by a considerable amount. If insufficiently thick buffer layers are used, threading dislocations propagating into the MQWs can become the source of power loss and decreased modulation depth[40]. While devices with thin buffer layers have been demonstrated[40], the most convenient geometry for Ge/SiGe MQW devices that minimizes optical insertion loss is vertical incidence of light[26]. This configuration is not suitable in applications where waveguide devices are needed.

2.5.2. Free Carrier Modulators

Devices reported on silicon platforms have generated great interest since they show potential for monolithic chips with both integrated electronic and photonic components. Since silicon has a diamond cubic crystal structure that has inversion symmetry, silicon only displays the quadratic electro-optic effect, which produces an order of magnitude weaker change in index with applied field than that of electro-refraction[133]. Progress in silicon modulators have therefore exploited other phenomena, such as electro-refraction via carrier injection in a p-i-n diode, for modulating light intensity. Xu, et al. reported in 2005 a compact, 12 µm diameter ring resonator light intensity modulator on silicon operating at a data rate of 1.5 Gb/s[169]. Other geometries employed since this seminal work include a lower-tolerace racetrack resonator[38] and photonic crystal Mach Zehnder interferometers[30,54,135]. A factor limiting the performance of silicon electro-refraction modulators is the slow recombination dynamics in the intrinsic region, which results in a design trade-off between modulation depth, bandwidth, modulating voltage, and insertion loss[135]. Additionally, while microring resonators are a clever approach to reduce the modulator size and enable wavelength division multiplexing, this approach is inherently temperature sensitive and requires local heaters to tune the ring resonance.

2.5.3. $\chi^{(2)}$ Modulators: Electro-optic Polymers, $LiNbO_3$, and $BaTiO_3$

$LiNbO_3$ is a standard material platform used in commercial, long-haul telecommunication networks. Several decades of work on $LiNbO_3$ have yielded devices with low insertion loss, large modulation depth, and low operating voltage[164]. Commercial devices using a Mach-Zehnder configuration are available with bandwidths of 40 Gb/s. These devices, however,

have large interaction lengths of several centimeters between the applied electrical signal and propagating optical signal. In order to reduce the interaction length, tunability of the photonic band edge of $LiNbO_3$ photonic crystal waveguides has been demonstrated[100,121,122]. A major challenge for these devices is weak overlap between the photonic crystal structure and the optical waveguide mode. This limitation has since been addressed by others using smart cut $LiNbO_3$ films[99,136]; however, electro-optic bandwidths of $LiNbO_3$ photonic crystal modulators larger than 1 GHz have not yet been demonstrated.

In order to further decrease the modulator size and reduce the driving voltage, alternative materials with higher electro-optic coefficients are sought. Various electro-optic polymers, including 4-dimethylamino-4'-nitrostilbene (DANS)[114], disperse red (DR) dyes[11], FTC[177], and CLD1[176] and their derivatives have been used in electro-optic modulators. For electro-optic polymers, a trade-off exists between high electro-optic coefficient and high thermal stability[94]. To overcome this compromise, various hybrid devices consisting of silicon photonic crystal slot waveguide infiltrated with a thermally stable electro-optic polymer have been demonstrated[63,87,178,179]. The high optical confinement obtained in the slot region combined with slow light effects of the photonic crystal enable a large electro-optic overlap for efficient modulation and an enhancement of the electro-optic coefficient, respectively. While effective electro-optic coefficients as high as 1230 pm/V have been demonstrated, the long-term temporal stability of these polymers have not yet been proven.

An alternative electro-optic material that has been previously developed by our research group and has seen renewed interest in recent years is barium titanate. In bulk crystal form, $BaTiO_3$ has electro-optic coefficient tensor elements $r_{42} = 800$ pm/V at GHz frequencies[173],

more than 25 times larger than that of $LiNbO_3$. In our group, we have previously developed a two-stage metal-organic chemical vapor deposition technique[66,150] for depositing epitaxial films onto (100) MgO substrates. Electro-optic coefficients as high as 360 pm/V have been measured on these films[141]. As-grown surface roughness less than 1 nm rms has been achieved[150], enabling low optical waveguide losses of $< 1.1\,\mathrm{dB/cm}$[142]. These films have been incoroprated into traveling-wave coplanar stripline devices having half-wave voltages as low as 1 V[139] and electro-optic 3 dB bandwidth as high as 15 GHz[140]; these were demonstrated, however, using different devices. The 1 V half-wave voltage was measured using a 5.2 mm long device, and the 16 GHz electro-optic bandwidth was measured using a device with a thick 850 nm SiO_2 buffer layer between the electrodes and $BaTiO_3$ film, which increases the half-wave voltage.

To further decrease the half-wave voltage and increase the electro-optic bandwidth through phase velocity matching, photonic crystal modulators with 1D and 2D symmetries were investigated. Liu et al proposed the first photonic crystal $BaTiO_3$ modulator in 2007[97]. In this device, a Si_3N_4 ridge waveguide on $BaTiO_3$ was patterned as a one-dimensional grating with periodicity in the direction of light propagation. The photonic crystal was patterned into the Si_3N_4 ridge using e-beam lithography and reactive ion etching. The $BaTiO_3$ film was not etched through due to its chemical inertness against the chosen etching chemistry consisting of CF_4 and O_2. A 27 nm wide stop band centered at 1550 nm was demonstrated. The measured extinction, however, was less than 2% across a 20 nm wide band edge. The low extinction was due to low overlap between the mode propagating in the $BaTiO_3$ film and the photonic crystal structure patterned into the top Si_3N_4 ridge.

To further increase the overlap between the photonic crystal structure and the optical field, photonic crystal patterned with direct-write focused ion beam lithography (IBL) were next investigated. IBL is a technique used to directly etch sub-micron patterns into materials. It is a physical sputtering technique and hence circumvents the challenge of chemically etching the $BaTiO_3$ film. Lin et al demonstrated the first $BaTiO_3$ photonic crystal waveguides with two-dimensional square lattice symmetry[89–91]. Compared with one dimensional structures, two dimensional photonic crystals have greater electro-optic tunability and require a shorter length for demonstrating a photonic bandgap[91]. An electro-optic photonic band edge tunability of -0.18 THz/V was predicted for a super-lattice photonic crystal with square lattice symmetry[91], potentially enabling compact sub-millimeter electro-optic switches. Using this device, Lin et al report that a 14 dB extinction is attainable with a 45 V applied dc voltage. Photonic crystal waveguides with a conventional square lattice were fabricated and characterized[90]. Similar to that reported for the one dimensional structure, a shallow extinction of less than 2% was measured for TE polarized light across the band edge within the optical C band.

$BaTiO_3$ photonic crystal waveguides with hexagonal symmetry were next investigated in order to obtain a bandgap for both TE and TM polarizations. In addition to the potential electro-optic tunability also investigated for square lattice structures, hexagonal lattice photonic crystal waveguides were proposed for matching the propagation speeds of the electrical and optical waves for high speed modulation[82]. An enhancement of the electro-optic coefficient was measured across the photonic band edge, and a significant improvement in the extinction (40%) was demonstrated[81]. Photonic crystal waveguides with hexagonal lattice symmetry and 35 µm length were incorporated into traveling-wave

$BaTiO_3$ modulators with total electrode lengths of 1.5 and 3 mm[81]. An electro-optic 3 dB bandwidth of 17 GHz and 5.3 V V_π were measured for the 3 mm long device. The authors claim a 50 GHz electro-optic bandwidth for the 1.5 mm long device and a half-wave voltage of 14 V.

The high frequency electro-optic response of the 1.5 mm long device reported by Li et al[81] was dominated by unusual resonant-like behavior reportedly due to microwave resonances. According to the simulations presented in Chapter 7, electro-optic 3 dB bandwidths greater than 40 GHz are only predicted for shorter devices with sub-mm lengths wherein the microwave losses that scale exponentially with the length are greatly reduced. These simulations are supported by microwave property measurements reported in Chapter 4 and electro-optic coefficient measurements of $BaTiO_3$ films in the 10-40 GHz region reported in Chapter 6. In this work, a low intermediate frequency (IF) bandwidth of 10 Hz was found to be critical to suppress noise from the vector network analyzer when measuring the electro-optic frequency response above 15 GHz. No mention of the impact of the IF bandwidth on the measured electro-optic response was reported by Li et al[81]. The 50 GHz bandwidth reported by Li et al could not be reproduced using the same device or other shorter $BaTiO_3$ devices fabricated in the same facilities using the same film growth and device fabrication techniques. It is therefore believed that the claimed 50 GHz bandwidth is an over-estimate of the true device performance.

There has been increasing interest in the integration of $BaTiO_3$ thin films onto silicon platforms in the last several years as a way to add $\chi^{(2)}$ nonlinear optical properties to chips fabricated using complementary metal oxide semiconductor (CMOS) technology. The heteroepitaxy of oxide perovskite films on silicon was first achieved in the late

1990s using molecular beam epitaxy[102]. McKee et al[102] and Lettieri et al[78] described the critical initial steps for achieving heteroepitaxy of perovskite oxides with silicon, which include starting with 2×1 surface reconstructed (100) silicon, formation of a submonolayer silicide with the alkaline metal of the perovskite, and overgrowth of the silicide with submonolayer alkaline metal. The epitaxial growth of $BaTiO_3$ on silicon was subsequently demonstrated using buffer layers of $SrTiO_3$ and $SrTiO_3$/MgO[111] and fully relaxed $Ba_xSr_{1-x}TiO_3$[153]. Demonstration of optical devices using these thin films is complicated by the fact that the refractive index of $BaTiO_3$ (2.31) is significantly smaller than that of crystalline silicon (3.47) at the telecommunication wavelength of 1550 nm. This challenge has been overcome by using vertical slot waveguides consisting of an amorphous silicon ridge patterned on top of the $BaTiO_3$ film, the latter of which is heteroepitaxially integrated onto a silicon on insulator (SOI) platform via a buffer layer of $SrTiO_3$[3,4,116,168]. Using this approach, waveguide devices on silicon-integrated $BaTiO_3$ films including ring resonators and traveling-wave electro-optic modulators have been reported. These devices have lower in-device effective electro-optic coefficients than the maximum reported for thicker films epitaxially grown on (100) MgO of 148 pm/V[4] versus 360 pm/V[139] at 1550 nm wavelength. The successful demonstration of $BaTiO_3$ electro-optic devices integrated onto silicon has spurred modeling of such devices. Hu et al[60]have predicted effective electro-optic coefficients as high as 277 pm/V in c-axis oriented $BaTiO_3$ films for propagation in $BaTiO_3$ along <100>, and Castera et al[24] have predicted a maximum effective electro-optic coefficient of 578 pm/V for propagation along <110> in purely a-axis oriented $BaTiO_3$ films.

2.6. Photonic Crystal Waveguides

Photonic crystals are periodic media in which the dielectric constant is periodic in one, two, or three spatial dimensions with periodicity on the order of the wavelength of light. Photonic crystals may be considered as an analog to atomic crystals. Many of the properties of matter which result from the interaction of electrons with a periodic potential are applicable in understanding the interaction of electromagnetic waves with a medium consisting of a periodic dielectric constant, including Brillouin zones, Bloch modes, effective mass, and band gaps[69 49].

In this work, the important characteristics of photonic crystal waveguides include the photonic bandgap, dispersion of the optical group index, and application of these waveguides for enhancing light-matter interactions, namely the electro-optic coefficient of $\chi^{(2)}$ materials. These characteristics are described along with recent progress in the following sections.

2.6.1. The Photonic Bandgap

Photonic crystals were first proposed separately by Yablonovitch[170] and John[68] in 1987 as engineered materials with prohibited light propagation for certain wavelengths in certain directions, referred to as a photonic band gap (PBG), as dictated by the dielectric properties. The properties of the PBG were incorporated into the growing literature on integrated optics in the 1990s by focusing on applications involving PCs with periodicity in one and two dimensions[21,130]. Waveguides with PBG have since been designed using the plane wave expansion (PWE) method for calculating the photonic band structure

of two and three dimensional photonic crystals[85] and the finite-difference time-domain (FDTD) method for calculating the transmission spectrum[138 67].

The application of the PBG for controlling light propagation within a line defect, as illustrated in Fig. 2.6, was first proposed by Mekis et al in 1996[104] and demonstrated by Lin et al in 1998[92]. This type of waveguide has since become an important template enhancing both linear and nonlinear optical phenomena. The large optical group index of line defect waveguide has been proposed for use in optical delay lines to serve as a buffer for optical information processing[157 77]. The strong localization of light in line defect waveguides due to PBG guiding has been proposed for enhancing nonlinear optical properties[131,132]. The localization is especially important for enhancing nonlinear optical properties that depend on the light intensity such as third harmonic generation[34] and pulse compression of solitons on-chip[31].

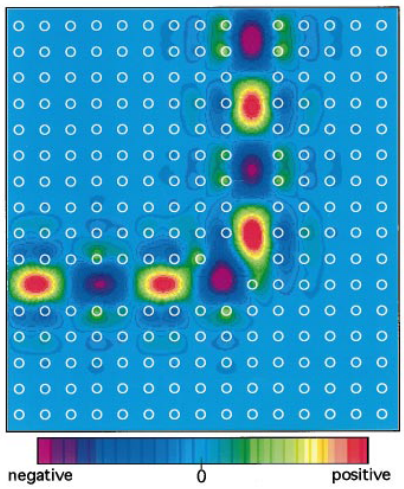

Figure 2.6. Simulated electric field in a line defect photonic crystal waveguide at a sharp bend.[104]

2.6.2. Optical Group Index

An important property of photonic crystal waveguides that has found numerous applications is its controllable optical group index and its dispersion. The optical group index is defined as[5]

$$n_g = c/(d\omega/dk)$$

and its dispersion (β_2) as[5]

$$\frac{dn_g}{d\omega} = c\frac{d^2k}{d\omega^2}$$

where c is the speed of light in free space, ω is the optical frequency, and k is the wavevector. The derivative $d\omega/dk$ is calculated from the band structure, enabling a theoretical calculation of the group index. An example of a photonic band structure for a two dimensional PC slab with hexagonal symmetry is shown in Fig. 2.7. As shown in the figure, $d\omega/dk$ approaches zero for allowed modes that approach the photonic band gap, which indicates that a a large dispersion and large group index should be expected near the photonic band edge. This has been confirmed experimentally[115], with group indices as high as 300 reported[155].

The control of the group index and its dispersion has been sought for devices with wideband optical operation. The line defect structure has emerged as a versatile template, with control of its group index and dispersion achieved through displacement of holes adjacent to the line defect[45,56,84,86] and changing the hole size[73].The same approaches have been applied to slot photonic crystal waveguides in which an electro-optic polymer

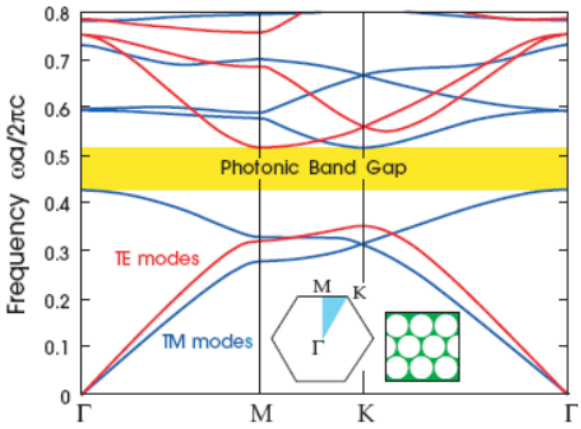

Figure 2.7. Band structure calculated for TE and TM modes in a hexagonal lattice photonic crystal slab. The hole geometry is shown in the lower right inset, and the high symmetry points in reciprocal space are shown in the inset at the center. A complete photonic band gap is indicated by the yellow horizontal bar.[67]

infiltrated slow resides in the line defect region[30,87,174,178,179]. The application of these waveguides for modulators is discussed in the next section.

The major difference between photonic crystals with hexagonal lattice symmetry versus square lattice symmetry is that a complete photonic band gap in the plane of the slab can be achieved for both TE and TM polarizations for the former but not for the latter. This is due to the connectivity of the high dielectric region and its impact on the location of the TE and TM stop bands[67]. As a result of the variational theorem, the electric field will preferentially be confined in the high dielectric region to reduce its frequency and hence energy. This is permitted for TE polarization in a square lattice of air holes, where there are k vectors for which there is a continuous straight path within the high dielectric region between unit cells. The orthogonal mode with the same k vector must necessarily be primarily concentrated in the low dielectric region with a higher frequency. Since orthogonal modes are highly concentrated in different materials, there is a large difference

in the allowed frequencies for the TE modes, which opens a band gap. This is not the case for the TM polarization however, since the electric field is only in the out-of-plane direction does not cross material interfaces. The orthogonal modes for TM polarization can then both be highly confined in the high dielectric constant region and have similar frequency. For this reason, bandgaps generally do not exist for TM polarization for square lattice photonic crystals consisting of air holes milled into a high dielectric constant material. The converse is true for photonic crystals consisting of dielectric columns surrounded by air; for these structures, TE bandgaps generally do not exist.

The differences between the TE and TM modes present in square lattice structures can be broken in a hexagonal lattice structure[67]. The hexagonal lattice represents a compromise of the complementary dielectric rod and air hole square lattice structures. In the hexagonal lattice of air holes, the interstices between air holes represent the regions favorable for creating TM bandgaps and the regions of high dielectric constant material connecting the interstices represent the continuous high dielectric constant material that is favorable for creating TE bandgaps. Hexagonal lattice structures are hence favorable when polarization insensitivity is required and can potentially be designed for imparting slow light on both TE and TM polarizations. In practice, however, fabrication imperfections such as sidewall roughness and non-vertical sidewalls favor wider TE bandgaps for hexagonal photonic crystals of air holes.

2.6.3. Photonic Crystal Waveguide Modulators

Enhancement of optoelectronic device performance for both the $LiNbO_3$ and silicon platforms has been demonstrated utilizing photonic crystal (PC) slow light structures.

In $LiNbO_3$, the tunability of the PC band edge has been investigated as a modulation mechanism[100,121,122]. A major challenge for the devices presented in[100,121,122] was weak overlap between the PC structure and the optical mode of the $LiNbO_3$ waveguides. This limitation has since been addressed by others using smart cut $LiNbO_3$ films[99,136]; high-speed PC modulators using $LiNbO_3$, however, have not yet been demonstrated. Silicon free-carrier modulators with dispersion-engineered line defect PC waveguides have been demonstrated with a reduced driving voltage and device length[17,18,54,110] resulting from an enhancement in the phase delay proportional to the optical group index[132]. Silicon PC modulators have been reported with 40 Gbps operation comparable to that achieved in the highest performing rib waveguide silicon modulators with an order of magnitude smaller footprint, demonstrating the effect of slow light in reducing the required modulator size[110]. Compared with the approaches taken thus far on $LiNbO_3$, the dispersion-engineered line defect waveguides on silicon offer the advantage of wideband optical operation for wavelength division multiplexing applications. Dispersion-engineered slot photonic crystal waveguides have been further used to enhance the EO coefficient of EO polymers, showing promise to reduce the voltage of $\chi^{(2)}$ modulators[63,165,178,179].

CHAPTER 3

Experimental Techniques

3.1. Metal Organic Chemical Vapor Deposition of $BaTiO_3$ Thin Films

The $BaTiO_3$ films used in this work were epitaxially grown on (100) oriented MgO substrates using a two-stage low-pressure metal-organic chemical vapor deposition (MOCVD) technique. The two-stage MOCVD technique for the deposition of $BaTiO_3$ films first reported by Towner et al[150] was modified in this study for using a new barium metal-organic precursor (Ba(*hfa*)$_2$·triglyme, where *hfa* is hexafluoroacetylacetonate)[66]. The modified reactor setup is shown in Fig. 3.1. The bubbler used previously by Towner[148], Lin[88], and Li[79] was replaced with a quartz boat containing the solid-state barium precursor inside the reactor. Use of a quartz boat for the new precursor required modifying the reactor from a cold-walled to hot-walled design. A quartz baffle was added between the region containing the barium precursor and the inlet stream of the titanium precursor to promote mixing and to prevent back-flow of the titanium precursor and contamination of the barium source.

Barium titanate films with thicknesses between 250 and 680 nm were grown using the horizontal hot-walled reactor shown in Fig. 3.1 using the optimized parameters given in Table 3.1. Prior to the growth stage, a nucleation layer was deposited at a lower temperature of 750 °C for 5 minutes, after which the temperature was ramped up to the growth conditions.

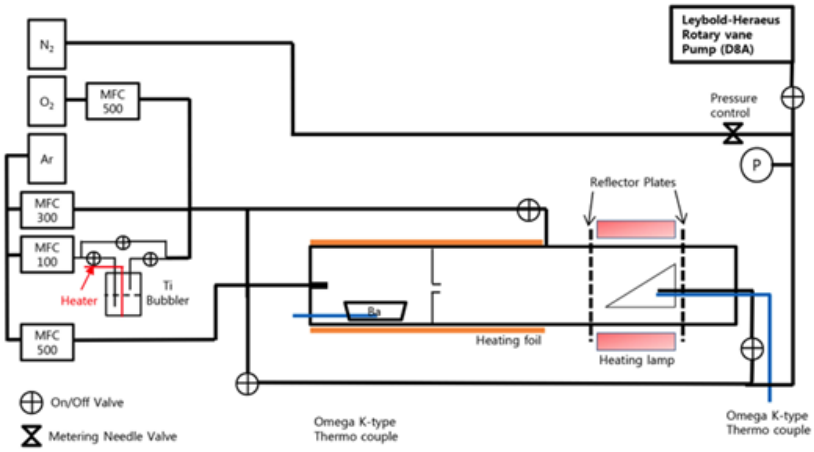

Figure 3.1. Schematic of the horizontal hot-walled MOCVD reactor used for epitaxial deposition of $BaTiO_3$ films.

Table 3.1. Optimized parameters for the growth of $BaTiO_3$ films using the horizontal hot-walled reactor shown schematically in Fig. 3.1

Parameter	Value	Unit
Boat Temperature	110	°C
Flow rate of Ba-carrier gas	125	sccm
Flow rate of Ti-carrier gas	35	sccm
Flow rate of Ti-dilute gas	60	sccm
Flow rate of O_2-push gas	225	sccm
Substrate temperature	850	°C
Base pressure	< 0.3	Torr
Working pressure	< 5	Torr
Growth rate	150	nm/h

3.2. Barium Precursor Synthesis and Properties

The barium metal-organic precursor Ba(hfa)$_2$·triglyme was synthesized and used for the first time to deposit epitaxial $BaTiO_3$ films on (100) MgO. The synthesis and characterization of the precursor was done by Dr. Young Kyu Jeong. Compared with the precursor Ba(hfa)$_2$·pentaethylene glycolethylbutylether (Ba(hfa)$_2$·PEB) used by Towner

et al, the synthesis of Ba(hfa)$_2$·triglyme is air-insensitive and is relatively simple and safe. The new precursor was chosen for its lower melting point, high voltatility, and long-term stability.

The new barium precursor was synthesized according to the procedure outlined by Belot et al[13]. The process was scaled to yield approximately 5 grams per synthesis (38 molar percent yield). The stability of the precursor was quantified by Dr. Jeong using thermogravimetric analysis. A plot of the temperature-dependent weight loss and isothermal weight loss at the operating temperature of 110 °C is shown in Fig. 3.2. The temperature-dependent weight loss (Fig. 3.2 (a)) shows that the precursor is stable at ambient temperatures below the operating temperature of 110 °C. At 110 °C and under 5 Torr of total pressure, the weight loss is linear with time at 1.4% per hour.

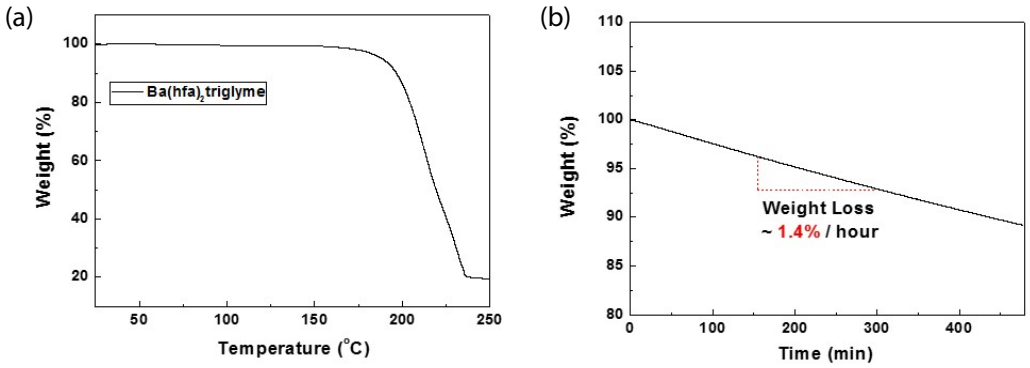

Figure 3.2. (a) Weight loss versus temperature and (b) isothermal weight loss versus time for the Ba(hfa)$_2$·triglyme precursor at 5 Torr. The iosothermal measurement is for a temperature of 110 °C.

3.3. Thin Film Characterization

$BaTiO_3$ thin films grown by MOCVD were characterized by optical reflectometry, atomic force microscopy, and X-ray diffraction to determine that the films were of sufficiently

high quality for further device processing. These characterization techniques were used as a screening step where the measured properties were compared to the best values obtained previously for $BaTiO_3$ films grown in our group.

3.3.1. Optical Reflectometry

The refractive index and thickness of the $BaTiO_3$ films were assessed using optical reflectometry (Filmetrics F20). Prior to measurements, the system was calibrated using a silicon standard. The refractive index and thickness of the $BaTiO_3$ film were the only degrees of freedom allowed in the fit to the measured reflection spectrum.

3.3.2. Atomic Force Microscopy

The surface morphology was measured using the MultiMode Nanoscope IIIa Scanning Probe Microscope in the NUANCE Center at Northwestern University. The measurements were done in contact mode over 1x1 and 5x5 μm^2 areas at randomly selected areas of the films to assess the local root mean square (RMS) roughness.

The film roughness should in general be minimized to reduce the scattering of light into radiating modes from the film surface and its interface with the Si_3N_4 ridge. It was found empirically that films with roughness larger than 5 nm RMS were unsuitable for waveguiding, with no optical modes visible for devices made on these films. All wafers used to make waveguide devices in this work had a film roughness less than 2 nm RMS. An example of the measured film topography is shown in Fig. 3.3.

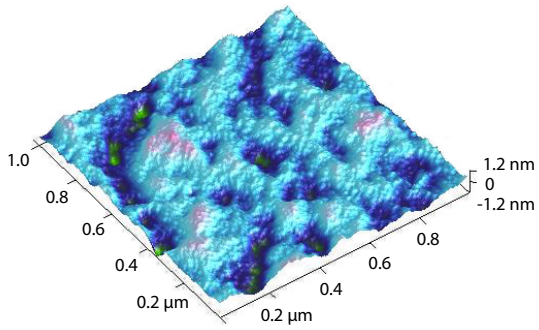

Figure 3.3. Example of the surface topology measured using AFM. The surface roughness in the 1x1 µm^2 area is less than 1 nm.

3.3.3. X-Ray Diffraction

3.3.3.1. $\theta - 2\theta$ and in-plane ϕ-Scan Measurements

The film purity and crystallinity were assessed using high resolution $\theta - 2\theta$ X-ray diffraction scans performed with the four-circle Rigaku ATXG diffractometer in the J. B. Cohen X-ray Facility at Northwestern University. The measurements and analysis were performed by Dr. Young Kyu Jeong and Dr. Pice Chen. The source (Cu $K\alpha_1$ with 1.5405 åwavelength) was collimated and filtered with Ge (111) crystals. The (100) and (200) peaks of $BaTiO_3$ and the (200) peak of MgO were measured with $\theta - 2\theta$ scans. Highly crystalline samples had a peak intensity on the order of 10^4 counts per second (CPS) for the $BaTiO_3$ peaks and 10^6 CPS for the MgO peak. Epitaxial deposition was confirmed using in-plane ϕ-scans to reveal the four-fold tetragonal symmetry expected for heteroepitaxy of $BaTiO_3$ on (100) MgO. The ϕ-scan measurements were done at the (111) Bragg condition. Examples of $\theta - 2\theta$ and in-plane ϕ-scans are given in Fig. 3.4.

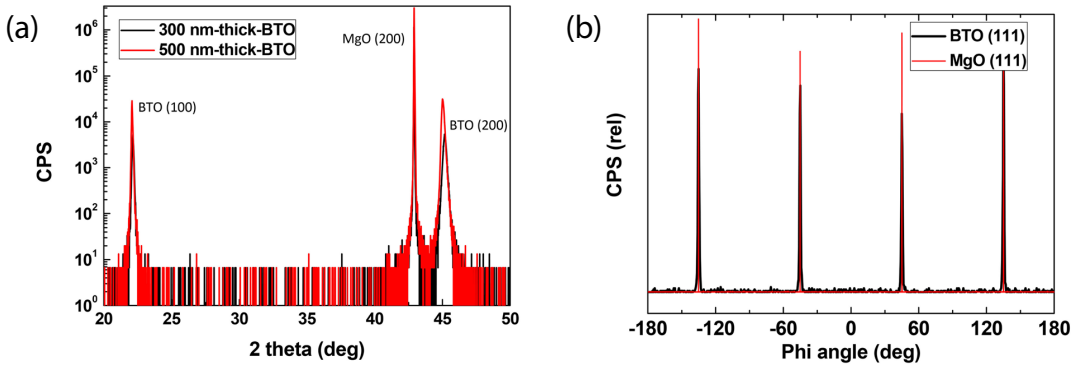

Figure 3.4. (a) High resolution $\theta - 2\theta$ XRD patterns of $BaTiO_3$ films with 300 and 500 nm thickness. (b) In-plane ϕ-scans showing four-fold symmetry. After Jeong et al.[66]

3.3.3.2. Rocking Curve Width

High resolution scans of the $BaTiO_3$ (200) peak were obtained by performing rocking curve measurements about this peak. As described by Towner et al[148,150], the fraction of ferroelectric domains with in-plane and out-of-plane orientation can be estimated by fitting Gaussian peaks to the measured (200) peak and accounting for the scatting factors of the (200) and (002) reflections. This technique was used to determine the fraction of ferroelectric domains with in-plane and out-of-plane orientation as a function of film thickness. An example of the rocking curve measurement with fitted Gaussian peaks is shown in Fig. 3.5.

3.4. Device Fabrication

3.4.1. CMOS Processing of Integrated Waveguide Modulators

Standard complementary metal oxide semiconductor (CMOS) clean room processing techniques were used to fabricate waveguide devices on the $BaTiO_3$/MgO platform. A

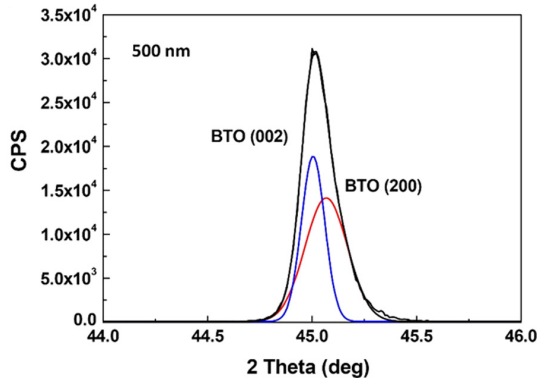

Figure 3.5. Example rocking curve measurement of the $BaTiO_3$ (200)/(002) reflection for a 500 nm thick film.

schematic illustrating the process flow is given in Fig. 3.6. CMOS processing of waveguide devices was done only on $BaTiO_3$ films meeting the requirements discussed in Section 3.3. The typical yield for good quality films is 15%. In this section, an overview of the CMOS processing steps is discussed; detailed process parameters and steps are provided in Appendix A.

After growing the $BaTiO_3$ film and ensuring that it is of satisfactory quality for waveguide devices, a layer of Si_3N_4 is deposited by plasma enhanced chemical vapor deposition using ammonia and silane gas precursors. The thickness of the Si_3N_4 layer (100-250 nm) and its refractive index (1.98-2.01) are measured by thin film reflectometry (Filmetrics F20) to ensure that the film is of sufficient quality for guiding light in the $BaTiO_3$ film. A positive resist photolithography step is then used to define ridge waveguides having widths between 2 and 7 µm. The waveguides are oriented along either the [100] or [110] direction on the $BaTiO_3$ film. A CF_4 and O_2 chemistry reactive ion etching (RIE) step is used to etch the waveguides. After etching the waveguides, the samples are annealed

in an O_2 environment at 300 °C for 30 minutes to restore the oxygen stoichiometry of the films after processing in the reducing environment for Si_3N_4 deposition.

Coplanar stripline electrodes are next patterned onto the $BaTiO_3$ film in the same orientation as the waveguides. A negative photoresist step is used to define the electrodes. A 600 nm thick gold film is deposited by electron beam evaporation after first depositing a thin ($\sim$ 15 nm) titanium adhesion layer. The excess metal is then lifted off by sonicating the sample in acetone for several minutes and gently brushing with a cotton swab.

Following waveguide and electrode fabrication, the end facets of the sample are polished to an optical-grade finish for coupling light into and out of the waveguides with tapered fibers. MgO is a cubic substrate material and cleaves along (100) planes. The MgO wafers are received from the manufacturer cut along <100>, and, due to the cleavage planes along (100), it is fairly easy to polish facets of wafers with waveguides oriented along <100>. Most devices in this work, however, were oriented along <110>. This was done so that all orientations of in-plane domains could be poled with an applied dc field and so that the large off-diagonal tensor elements of the electro-optic indicatrix could be accessed, resulting in higher effective in-device electro-optic coefficients. Fabricating waveguides along <110>, however, presents the issue of polishing the corners of the wafer into flat facets along a direction that is not a natural cleavage plane. These facets were prepared by using a multi-step polishing procedure, starting with 600 grit silicon carbide paper and ending with 1 µm diamond lapping film. This procedure was sufficient for producing wafers with 53-67% of waveguides having total insertion losses less than 25 dB on each wafer.

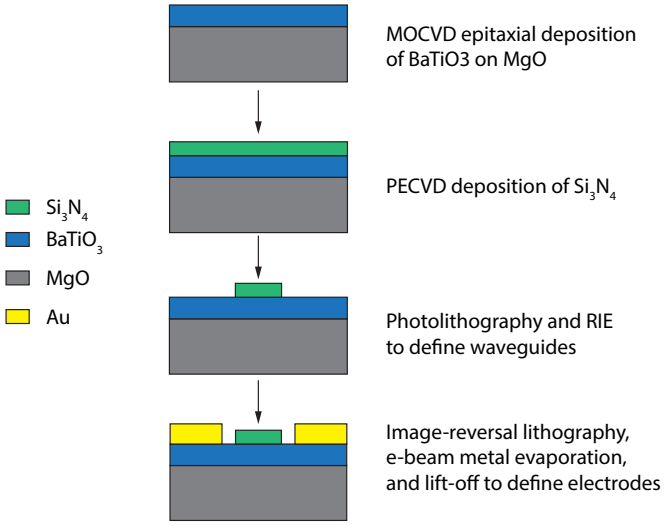

Figure 3.6. Schematic showing the processing steps for fabricating waveguide modulators.

3.4.2. Direct Write Focused Ion Beam Lithography

The direct write focused ion beam lithography (IBL) technique was used to pattern photonic crystal arrays onto $Si_3N_4/BaTiO_3/MgO$ waveguides. All ion beam lithography was done at the Center for Nanoscale Materials at Argonne National Laboratory using the FEI Nova 600 NanoLab Dual Beam FIB/SEM and Raith Elphy Multibeam lithography system. IBL is a physical sputtering technique used to directly etch vertical anisotropic patterns into materials. Ga^+ ions from a liquid metal ion source were used to etch the $BaTiO_3$ films. The minimum resolution of this technique is on the order of 5 nm, well below the minimum feature size of 190 nm.

IBL was chosen as the etching technique in this study over other nano-patterning techniques, namely e-beam lithography (EBL) and nano-imprint lithography (NIL) for several reasons. Compared with EBL, IBL is a one-step procedure in which material is directly removed by the rastering beam; no photoresist devlopment and post-etching steps

are required. The major hurdle in applying EBL to nano-patterning $BaTiO_3$ films is the chemical resistivity of $BaTiO_3$. Reactive ion etching with SF_6 has been demonstrated on other ferroelectric oxides such as $LiNbO_3$[74]; however, $LiNbO_3$ is typically nano-sructured using IBL and no successful anisotropic, vertical etching techniques for $BaTiO_3$ have yet been demonstrated. Compared with nano-imprint lithography, IBL offers much greater flexibility since the patterning is determined by digital GDSII files while nano-imprint lithography relies on the use of a hard mask.

The major drawback associated with IBL is the low throughput; however, for the purpose of developing prototype devices, this is not an issue, especially since IBL offers the ability to create different designs in the same processing step. Another potential issue with IBL is the implantation of Ga^+ ions into the material being etched. Implantation becomes the dominant mechanism for bombardment energies above 100 keV[29]. In this work, a bombardment energy of 30 keV was used in order to primarily sputter with rather than implant gallium ions. Furthermore, as discussed in Chapter 6, no adverse effects of Ga^+ implantation were detected in measurements of the electro-optic properties of photonic crystal devices fabricated with IBL.

The nominal milling parameters are given in Table 3.2. These parameters are based on those reported by J. Li for the FIB milling of $BaTiO_3$ films[79]. In order to sputter material in a uniform manner over a large area, the ion beam rastering was split over 50 patterning loops. The total ion beam dose imparted on the sample is determined by the relation

$$\text{Area Dose} = \frac{\text{Beam Current} \cdot \text{Area Dwell Time}}{\text{Step Size} \cdot \text{Line Spacing}} \tag{3.1}$$

where the "Area Dwell Time" is the time that the ion beam writes in the area A defined as A = (Step Size) $\times$(Line Spacing). The total area dwell time is divided equally over the number of patterning loops. The beam current was chosen to be 0.46 nA based on previously reported successful milling parameters on silicon[171]. Based on the prior work of Li[79], area doses of 3-10 $\mathrm{mC/cm^2}$ were used. The feature depth was found to scale linearly with the ion beam dose. A dose of 10 $\mathrm{mC/cm^2}$ was sufficient to fully penetrate a 500 nm thick $BaTiO_3$ film with a 120 nm thick Si_3N_4 ridge and 30 nm Cr/50 nm PMMA conducting layer, the thickest multi-layer stack thickness investigated in this work. Each pixel of ion beam writing had an area of 20×20 $\mathrm{nm^2}$with a digitized GDSII resolution of 1 nm, sufficient for accurately patterning photonic crystals which had a minimum feature size of a few hundred nanometers. With all other patterning parameters hence fixed, the resulting total area dwell time according to Eqn.3.1 was in the range 10-100 µs.

Photonic crystal arrays with lengths between 33 and 308 µm were patterned via IBL. In order to align the patterns precisely with the ridge waveguides, custom writefields and writefield alignment steps were developed. The writefield is the area in which a pattern is written and is characterized by the side length and ion beam magnification. A list of these parameter combinations is given in Table 3.3. For each writefield, a three point alignment technique was used to correct for the magnification, astigmatism, and position of the ion beam within the writefield. Detailed steps for this procedure are given in AppendixA. Excellent alignment was achieved between photonic crystals with lengths up to 308 µm and the ridge waveguides onto which they were patterned with less than 0.002° angular tolerance.

Two different conductive coatings were investigated for the photonic crystal patterning: the conductive polymer PEDOT:PSS, and Cr/PMMA multi-layer. PEDOT:PSS films were deposited onto wafers via spin coating following the steps in Appendix A. The PEDOT:PSS coating is highly conductive and yielded repeatable charging-free milling performance. The film, however, could not be fully lifted off after patterning in the areas of high ion beam dose. The penetration of the ion beam through the PEDOT:PSS film also led to a rounded instead of flat profile between the tops of adjacent holes, resulting in higher optical scattering losses. The Cr/PMMA coating was used in order to reduce the rounding between holes. A 30 nm layer of Cr was deposited on top of a 50 nm layer of PMMA using the steps detailed in Appendix A. A thin layer of PMMA was chosen to reduce the time milling through the sacrificial layer. Layer thicknesses greater than 30 nm of Cr on top of the 50 nm of PMMA resulted in a buckling topology unsuitable for FIB milling. While the Cr/PMMA multi-layer resulted in a flat profile between the tops of adjacent holes, the Cr film was susceptible to rupturing when imaged with the ion beam, resulting in charging of the sample. The Cr/PMMA films also posed issues during lift-off, resulting in higher optical insertion losses through the photonic crystal waveguides resulting presumably from scattering and absorption by the residual Cr and PMMA layers. Since the PEDOT:PSS coating posed fewer issues and more repeatable performance during IBL, it was used to fabricate the majority of photonic crystals in this study.

Table 3.2. Parameters used for focused ion beam lithography.

Parameter	Value	Unit
Accelerating Voltage	30	kV
Beam Current	0.46	nA
Patterning Loops	50	-
Area Dose	3-10	mC/cm^2
Area Step Size	20.0	nm
Area Line Spacing	20.0	nm
Dwell Time	1.4-88	µs

Table 3.3. Writefield parameters used for focused ion beam lithography.

Writefield Size (µm)	Magnification
100	1000
200	500
400	250
500	200

3.5. Electrical Characterization

3.5.1. S-Parameter Measurements

The microwave electrical properties of coplanar stripline devices on $BaTiO_3$ films were investigated via measurements of the microwave scattering parameters (S-parameters). S-parameters relate the voltages reflected at the ports of a device to the voltages incident on the ports, where a port is a point at which energy enters or leaves the device. The coplanar stripline electrodes studied in this work are two port devices, hence 2 port S-parameters were measured. For a 2 port network, the scattering matrix relates the voltage incident

and reflected at the ports by the equation

$$\begin{bmatrix} V_1^- \\ V_2^- \end{bmatrix} = \begin{bmatrix} S_{11} & S_{12} \\ S_{21} & S_{22} \end{bmatrix} \begin{bmatrix} V_1^+ \\ V_2^+ \end{bmatrix}$$

where V_i^- is the voltage amplitude reflected at port i and V_i^+ is the voltage amplitude incident on port i. These voltages are defined for a two port network in Fig.3.7 The two port scattering matrix elements are defined as

$$S_{ij} = \frac{V_i^-}{V_j^+}$$

The scattering parameter S_{ij} is measured by applying a voltage signal to port j and measuring the voltage amplitude of the signal exiting port i. A two-port vector network analyzer (Agilent N5230C PNA-L) was used for all measurements. The vector network analyzer (VNA) measures the full vectorial nature, i.e. the magnitude and phase, of 2 port scattering parameters in the frequency range 10 MHz to 50 GHz. For accurate measurements above 1 GHz, precision components are required. Coaxial cables rated for mode free operation up to 50 GHz (Bracke Manufacturing part number BM91529.24 semi-rigid cables and Gore 103-202 flexible cables) were used having 2.4 mm connectors. Since a repeatable connection between components is essential for minimizing random measurement errors due to higher order mode propagation, all connections were tightened to the recommended manufacturer's torque using a $9\,\mathrm{N}\cdot\mathrm{m}$ torque wrench. The transition between the coaxial connections of the network analyzer and the coplanar stripline geometry of the devices under test was achieved using source-ground and ground-source microwave probes (Cascade Microtech ACP50 SG and GS).

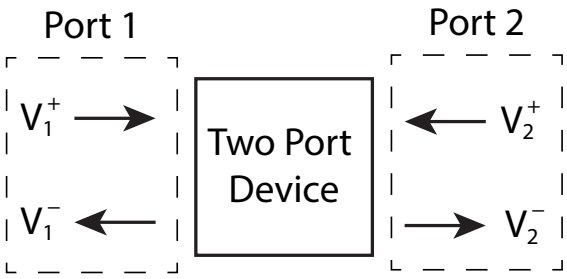

Figure 3.7. Schematic of a two port network showing the incident and reflected voltage signals at each port.

S-parameters were measured using the settings in Table 3.4. Measurements were taken over the range 10 MHz - 50 GHz. A total of 50 measurements were averaged with 19 smoothing points. Since the measurements are purely electrical, a low port power (-15 dBm) and moderate IF bandwidth (35 kHz) could be used without sacrificing measurement accuracy.

Table 3.4. Vector network analyzer settings used for S-parameter measurements.

Parameter	Value	Unit
Minimum Frequency	10	MHz
Maximum Frequency	50	GHz
Averaging Factor	50	-
Smoothing Points	19	-
Port Power	-15	dBm
IF Bandwidth	35	kHz

3.5.2. Network Analyzer Calibration

Network analyzers are not inherently precise instruments due to the prohibitive cost of manufacture. Errors introduced in the measurements include both random and systematic

errors. Systematic errors are those due to the precision of the instrument. Systematic errors include (1) signal directivity, or isolation between the incident and reflected signals at a given port; (2) signal cross-talk, or isolation between the ports; (3) source impedance mismatch; (4) load impedance mismatch; (5) frequency response errors caused by reflection tracking in the test receivers; and (6) frequency response errors caused by transmission tracking in the test receivers. These six systematic error terms apply for both the forward direction (voltage incident on port 1) and the reverse direction (voltage incident on port 2), resulting in 12 total systematic error terms. These systematic errors were minimized by performing a full two port calibration. Since the devices under test had a coplanar electrode geometry and coplanar stripline probes were used to contact the devices, an on-wafer calibration was required instead of a coaxial calibration to fully account for errors due to the VNA and probes. The system was calibrated using an on-wafer short-open-load-through (SOLT) sequence. The impedance standard substrate (part number ISS-103-726B) provided by the probe manufacturer was used for the calibration. The probe characteristics provided by the manufacturer for characteristic impedance, inductance, and capacitance were verified using the procedure detailed in Ref.[20] and were entered as fixed parameters (Table 3.5) during the calibration. Note that the capacitance is a negative value, which reflects the capacitance of the probe when it is in contact with a $50\,\Omega$ terminated transmission line.

Table 3.5. Parameters of the SG and GS microwave probes used for the SOLT on-wafer calibration.

Probe Parameter	Value	Unit
Capacitance	-11	pF
Inductance	33.5	pH
Characteristic Impedance	50	Ω

3.6. Optical Characterization

3.6.1. Optical Insertion Losses

Optical insertion losses of both ridge and photonic crystal waveguides were measured for wavelengths in the optical C-band. The measurements were done to characterize both the optical losses in conventional ridge waveguide $BaTiO_3$ modulators and the losses due to scattering from fabrication imperfections in the photonic crystal waveguides. The insertion losses are those due to propagation losses and mode mismatch between the tapered lensed fiber and ridge waveguide. Propagation losses occur along the length of the waveguide while mode mismatch losses occur at both the input and output facets of the waveguide where light is coupled between the tapered lensed fiber and the ridge waveguide. The minimum expected insertion loss is due solely to the coupling losses. An estimate of the minimum losses was obtained using the approach of Albert et al[7] in which the ridge waveguide mode is approximated as the summation of two ovals and the fiber mode profile is approximated as a circle. Using this approach, a minimum insertion loss of approximately 14 dB was calculated. Details of this calculation are given in Section 5.5.1.

The insertion loss was measured using the measurement setup shown schematically in Fig. 3.8 at 1562 nm using a 20 mW diode laser (Anritsu GB5A016) as the source. A photograph of the setup is shown in Fig. 3.9. TE-polarized laser light with 1562 nm

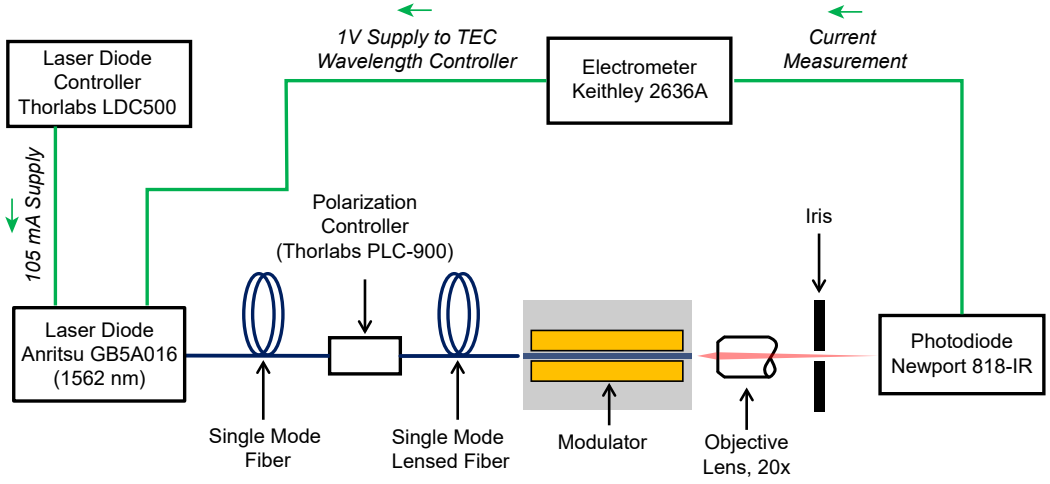

Figure 3.8. Experimental setup used to measure the optical insertion loss..

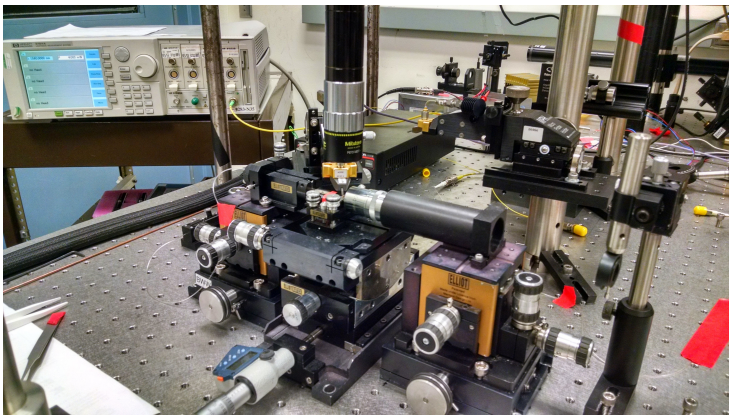

Figure 3.9. Photograph of the setup used to measure the insertion loss.

wavelength supplied by a diode laser (Anritsu GB5A016) was coupled into the waveguide via a tapered single-mode lensed fiber (Nanonics TLF SM-28) and coupled out using a 20x objective lens. The procedure for coupling the fiber to the waveguide is detailed in Appendix B. The light was polarized by adjusting an inline polarization controller to maximize the polarization extinction ratio as measured at the detector measurment plane. A constant voltage of 1 V was supplied by a Keithley 2636A sourcemeter to the

thermoelectric cooler wavelength controller of the laser diode to stabilize the wavelength at 1562 nm. An injection current of 105 mA was supplied to the laser, producing a lasing output power of 16.5 mW. The coupling of light into the waveguide was first optimized using an infrared camera (Electrophysics MicronViewer 7290), which was positioned in place of the photodiode shown in Fig. 3.8. An iris was used between the objective lens and the camera to block out light scattered in the substrate. A qualitative image of a typical waveguide mode profile captured with the infrared camera is shown in Fig. 3.10. The optical intensity in the waveguide mode was measured using a large area germanium detector (Newport 818-IR) operating in the photovoltaic mode. The photocurrent was measured using the second channel of the Keithley sourcemeter using BNC shielded cabling. The detector gain of 0.8 A/W at 1562 nm was used to calculate the total power from the measured photocurrent. All measurements of insertion loss were referenced to the measured transmission through the system in absence of the waveguide, i.e. with the tapered lensed fiber coupled directly to the objective lens.

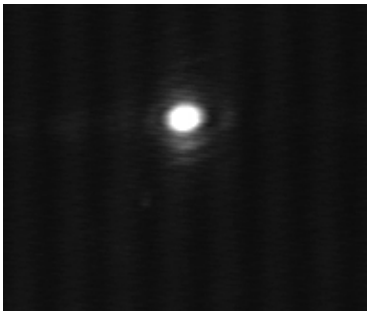

Figure 3.10. Typical image of an optical mode profile at the output facet of a $Si_3N_4/BaTiO_3/MgO$ ridge waveguide captured with an IR camera. Sample: YKJ-82B.

3.6.2. Wideband Transmission

The experimental setup used to measure the optical insertion loss was modified to the configuration shown in Fig. 3.11 to measure the wavelength-dependent transmission in the range of 1500-1580 nm. Light from the APC fiber-coupled tunable laser source (HP 8164A) was polarized in the plane of the film using an in-line fiber polarizer (Thorlabs PLC-900). Light was coupled into and out of the waveguides using tapered single mode lensed fibers (Nanonics TLF SM-28) with a spot size of 1.7 µm and working distance of 4 µm. Maximum coupling to the waveguide was obtained using the same approach as described for the insertion loss measurements (Section 3.6.1 and Appendix B). After maximizing the coupling at the input, the objective lens was replaced with another tapered lensed fiber mounted via a fiber mount (Elliot Martock MDE750) onto the precision stage (Elliot Martock MDE122, see Appendix B for further details). The output fiber was positioned in the same plane as the top surface of the device and positioned roughly at the waveguide output using the overhead camera. The position of the output fiber was adjusted first in the y, then x, then z directions until the transmission through the system was maximized. The coupling was performed with the room lights turned off to block stray light from infrared sources and assist with the coupling.

After coupling to and from the waveguide, the transmission was measured versus wavelength using a LabVIEW program written by Dr. Pice Chen to coordinate the tuning of the laser and acquisition of the photodiode current. The measurement system has a minimum wavelength resolution of 0.01 nm. The experimental noise floor for the measurements was 1.5 nW, the dark current of the photodiode. The maximum nominal laser power of 4.0 mW was used for all measurements. A dwell time of 0.1 s was sufficient

for repeatable and accurate measurements. The intensity measured at each wavelength was an average of ten measurements obtained within the dwell time.

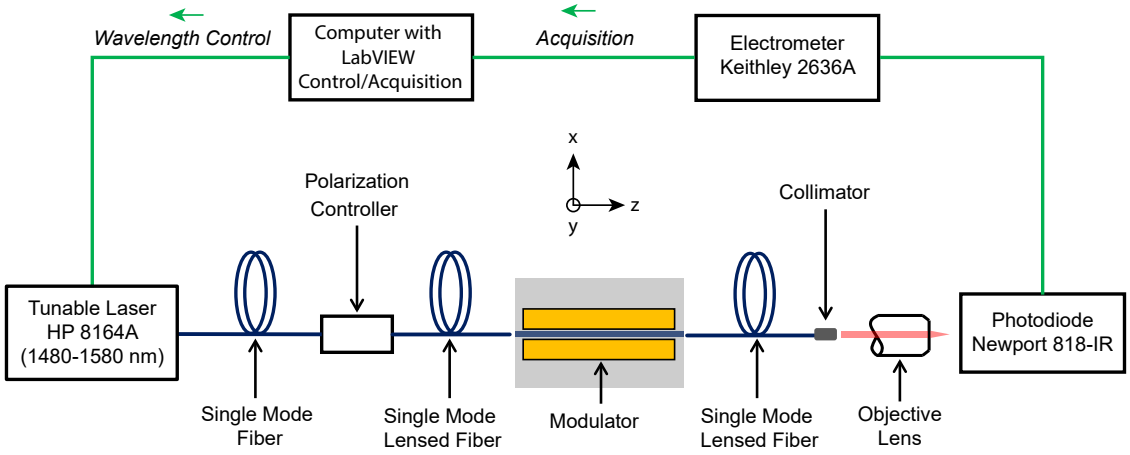

Figure 3.11. Experimental setup used to measure the wavelength-dependent transmission of $BaTiO_3$ ridge and photonic crystal waveguides.

3.7. Electro-Optic Characterization

The electro-optic properties of $BaTiO_3$ modulators were characterized using time, frequency, and spectral domain approaches. Time-domain measurements were done by operating $BaTiO_3$ phase modulators in a polarizer-sample-compensator-analyzer setup. Frequency-domain measurements over the range 10 MHz to 30 GHz were done using a calibrated vector network analyzer setup. The high frequency electro-optic properties in the range 10-50 GHz were investigated using an optical spectral analysis technique. Altogether, these approaches cover the frequency modulation range of 100 Hz to 50 GHz. The latter technique can be further applied to study EO properties into the THz region[75,128]. All of these techniques are wavelength agnostic and can be used to investigate material and

device properties at relevant optical windows other than the optical C band (1530-1565 nm) focused on here, including the visible and near infrared.

3.7.1. Half-Wave Voltage Measurement

The half-wave voltage at low frequency (1 MHz) was measured using a polarizer-sample-compensator-analyzer (PSCA) setup. A schematic of the experimental setup is shown in Fig. 3.12. The measurement of the half-wave voltage using the PSCA setup is a time domain approach. A sinusoidal voltage signal with a maximum 20 V_{pp} swing is applied to an unterminated, capacitively loaded modulator. A dc bias was applied to the ac signal using a bias tee (PulseLabs 5541A) with 80 kHz lower frequency cutoff. The electro-optic signal was detected using an InGaAs photodiode (Newport 818-BB-30A) that was ac-coupled to a 100 MHz bandwidth oscilloscope (Tektronix MSO2012B) with a high input impedance (100 MΩ). The detected signal was triggered by splitting the output of the signal generator (Stanford Research Systems DS335) to supply a voltage signal to both the device and trigger input of the oscilloscope.

The measured electro-optic waveform is a function of many variables related to the optical setup and is best explained by a Jones matrix formalism, as is typically used to describe the polarization state of light through a linear optical system[123]. The components of the PSCA setup and the angle correpsonding to their orientation with respect to the axis normal to the film surface are shown in Fig. 3.13. Each of the components labeled with a number in the figure has a corresponding transfer matrix, $\mathbf{T}_i$. The polarization state of the output light is described by the following general matrix representation,

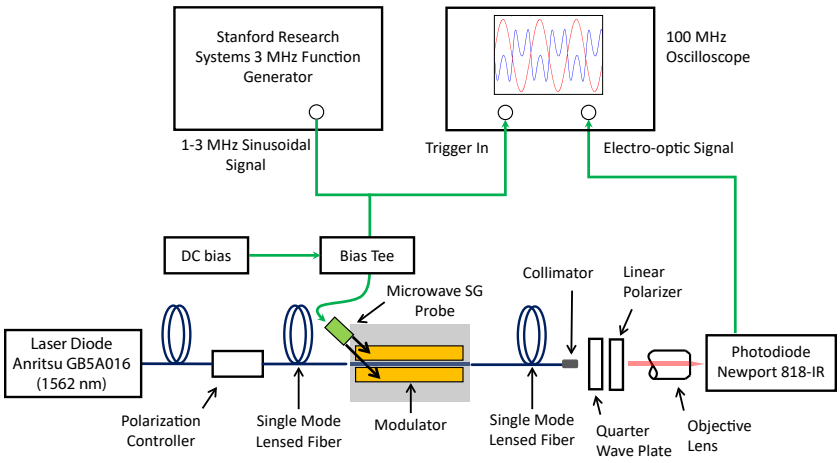

Figure 3.12. Schematic of the polarization-sample-compensator-analyzer (PSCA) setup used for measuring the large signal time-domain electro-optic response of $BaTiO_3$ phase modulators.

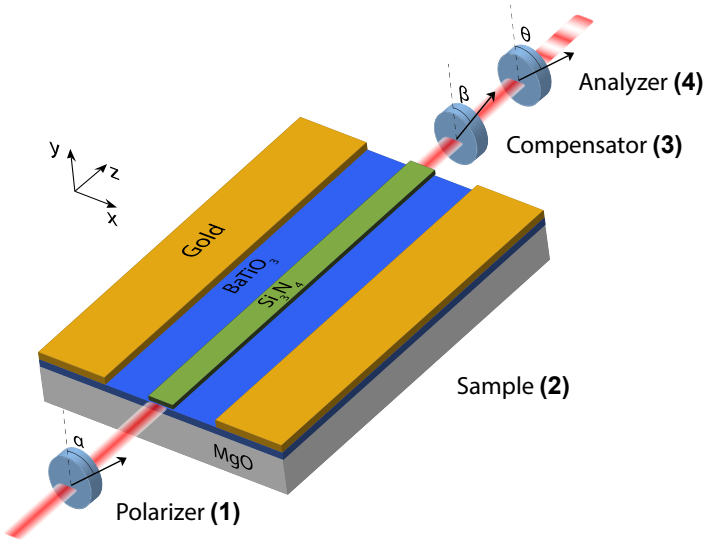

Figure 3.13. Schematic showing a $BaTiO_3$ ridge waveguide phase modulator being operated in a PSCA setup to measure the time-domain electro-optic response.

$$\begin{bmatrix} E_x \\ E_y \end{bmatrix}_{out} = \mathbf{T}_n \mathbf{T}_{n-1} \mathbf{T}_1 \begin{bmatrix} E_x \\ E_y \end{bmatrix}_{in} \tag{3.2}$$

where the column vectors labeled with the subscripts "out" and "in" describe the vectorial nature of the input and output polarization, i.e., the electric field components along the x and y directions defined in Fig.3.13. The input electric field has the general components

$$\begin{aligned} E_{x,in}(t) &= E_{0,x} e^{j(\omega_0 t - kz)} \\ E_{y,in}(t) &= E_{0,y} e^{j(\omega_0 t - kz)} \end{aligned} \tag{3.3}$$

where $E_{0,x}$ and $E_{0,y}$ are the complex amplitudes of the electric field components along the x and y directions, and ω_0 is the optical frequency. The light propagates in the z direction with propagation constant k. The transfer matrices for each of the polarization

components are the following:

$$
\begin{aligned}
\mathbf{T}_1 &= \begin{bmatrix} \cos^2\alpha & \sin\alpha\cos\alpha \\ \sin\alpha\cos\alpha & \sin^2\alpha \end{bmatrix} \\
\mathbf{T}_2 &= \begin{bmatrix} 1 & 0 \\ 0 & e^{-j\delta_{tot}} \end{bmatrix} \\
\mathbf{T}_3 &= \mathbf{R}(\beta)\begin{bmatrix} 1 & 0 \\ 0 & e^{-j\pi/2} \end{bmatrix}\mathbf{R}(-\beta) \\
\mathbf{T}_4 &= \begin{bmatrix} \cos^2\theta & \sin\theta\cos\theta \\ \sin\theta\cos\theta & \sin^2\theta \end{bmatrix}
\end{aligned}
\tag{3.4}
$$

where the rotation matrix $\mathbf{R}(\beta)$ is

$$
\mathbf{R}(\beta) = \begin{bmatrix} \cos\beta & \sin\beta \\ -\sin\beta & \cos\beta \end{bmatrix}
$$

In the transfer matrix for the sample ($\mathbf{T}_2$), the variable δ_{tot} is the total phase delay given by

$$
\delta_{tot} = \delta(V) + \delta_0
$$

where δ_0 is the phase delay due to birefringence and $\delta(V)$ is the electro-optically induced phase delay given by

$$
\delta(V) = \frac{\pi L}{\lambda_0} n^3 r_{eff} \Gamma_{eo} \frac{V(t)}{g} \tag{3.5}
$$

where L is the electro-optic interaction length, λ_0 is the free-sapce wavelength of light, n is the mode refractive index of the waveguide, r_{eff} is the effective electro-optic coefficient, Γ_{eo} is the electro-optic overlap factor, $V(t) = V \sin \omega_{mw} t$ is the applied modulation voltage at frequency ω_{mw}, and g is the electrode gap spacing. In terms of the half-wave voltage V_π,

$$\delta(V) = \pi \frac{V(t)}{V_\pi}.$$

Using Eqn. 3.2, the output electric field can be calculated as a function of the angles α, β, and θ and the phase delay δ_{tot}. The measured intensity is obtained as

$$I_{out} = \frac{1}{T} \int_0^T \left(E_{x,out}^2 + E_{y,out}^2 \right) dt$$

where $T = 2\pi/\omega_0$ is the period of one optical oscillation.

The half-wave voltage was measured by operating the device between crossed linear polarizers with the angles $\alpha = 45°$ and $\theta = -45°$. The quarter wave plate (compensator) was rotated to maximize the peak-to-peak voltage of the measured electro-optic signal. Under these conditions, the measured intensity has the simplified form given by

$$I_{out} \propto 1 + \sin \delta(V) \tag{3.6}$$

The intensity I_{out} is plotted for different voltages in Fig. 3.14.

The voltage is normalized by the half-wave voltage, which is obtained by setting Eqn. 3.5 equal to π and solving for $V = V_\pi$:

$$V_\pi = \frac{\lambda_0 g}{n^3 r_{eff} \Gamma_{eo} L} \tag{3.7}$$

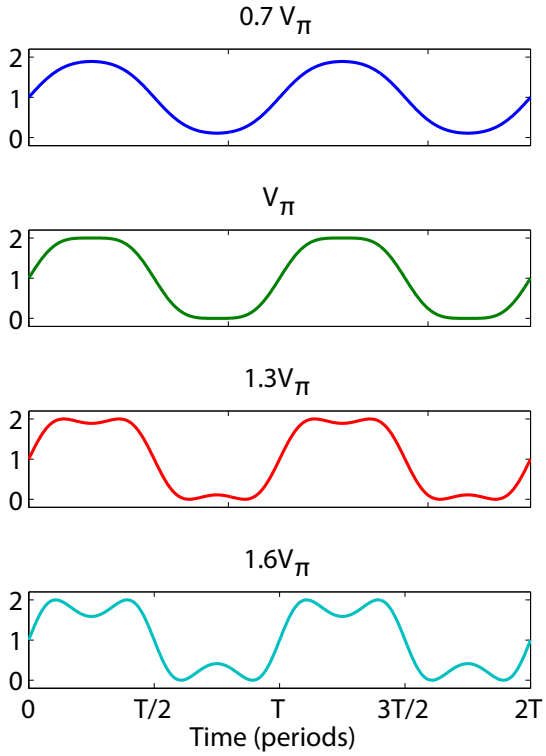

Figure 3.14. Electro-optic response modeled after Eqn. 3.6 for different applied voltages.

For a sinusoidal input voltage, it is observed that the peak-to-peak voltage for a π phase shift is that required to induce a doubling-over of the measured EO waveform at the peaks and troughs. The determination of the half-wave voltage is illustrated in Fig. 3.15 for an arbitrary wavelength. An important practical result of the modeling described by Eqns. 3.2-3.4 is that the determination of the half-wave voltage is not dependent on the variables α, β, θ, or δ_0. Optimization of the angles α, β, and θ, however, assist in clearly resolving the electro-optic waveform for accurately measuring V_π. After measuring V_π, the effective electro-optic coefficient was calculated from Eqn. 3.7, rearranged as

$$r_{eff} = \frac{\lambda_0 g}{n^3 V_\pi \Gamma_{eo} L} \tag{3.8}$$

In this equation, the mode index and electro-optic overlap factor were calculated while the remaining variables were either known from the measurement setup or device geometry. Calculations of the mode index and Γ_{eo} are given in Section 7.4.

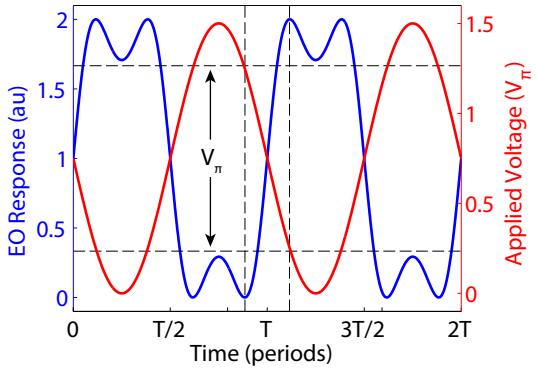

Figure 3.15. Modeled EO response after Eqn. 3.6 showing the direct measurement of the half-wave voltage. A π phase shift is added between the applied and measured signals for clarity.

3.7.2. Small Signal Frequency Domain Measurements

The frequency dependent electro-optic magnitude response was measured using a vector network analyzer in the measurement schematic shown in Fig. 3.16. Electrical lines are colored green and optical paths are colored blue in the schematic. In order to maximize the signal to noise ratio, the intermediate frequency bandwidth of the vector network analyzer (VNA) was set to 10 Hz. The output power of the VNA was set to -15 dBm and was amplified to a nominal output power of 12 dBm. The measurement was done while biasing the device at 5 V and terminating the electrodes in a 50 Ω load. Light was coupled into and out of the modulator with tapered fibers (Nanonics). The input light was polarized at 45° with respect to the out-of-plane direction in order to couple into both TE and TM fundamental modes. An inline polarizer was used to convert the phase

modulated light to an intensity modulated signal after coupling light out of the device. The intensity modulated light was collected and converted back to the electrical domain using an indium gallium arsenide photodiode (U2T XPRV2021A-VF-FP) with 39 GHz 3 dB electrical bandwidth. The output of the photodiode was connected to port 2 of the VNA. The measurements were done after calibrating the measurement system at points corresponding to the input of the amplifier at port 1 and the output of the photodiode at port 2. The effects of the amplifier, bias tee (PulseLabs 5541A with greater than 26 GHz bandwidth), and photodiode on the measurement were removed post-measurement by subtracting the measured frequency response of these components from the measured electro-optic response. The nominal laser power was typically set between 4 and 15 mW.

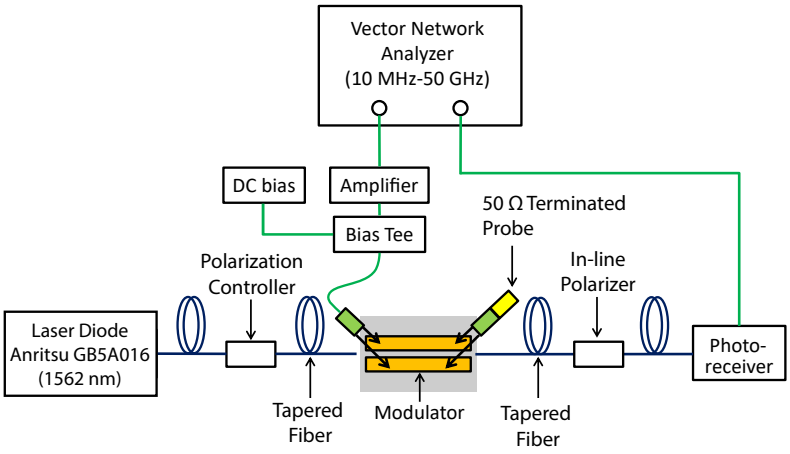

Figure 3.16. Schematic of the setup used for measuring the frequency-dependent electro-optic response.

The measured electro-optic small-signal frequency response was compared to that predicted by the model of Rahman and Haxha[58], which includes the effects of index mismatch between the co-propagating signals, microwave attenuation losses, and impedance

mismatch. The modeled electro-optic small signal magnitude response is

$$m(f) = \left| \frac{1 - S_1 S_2}{(1 + S_2)[\exp(i2u_+) - S_1 S_2 \exp(-i2u_-)]} \times \left[\exp(iu_+) \frac{\sin u_+}{u_+} + S_2 \exp(-iu_-) \frac{\sin u_-}{u_-} \right] \right| \tag{3.9}$$

with

$$u_\pm = \frac{1}{c} \pi f L (n_{mw} \mp n_o) - i \frac{1}{2} \alpha L$$

$$S_1 = \frac{50 - Z}{50 + Z} \qquad S_2 = \frac{50 - Z}{50 + Z}$$

where n_{mw} is the effective microwave index, n_o is the optical mode index, α is the total microwave attenuation in dB/cm, L is the electrode length in cm, and Z is the characteristic electrode impedance in Ohms. The electro-optic response was modeled using frequency-dependence measurements of n_{mw}, α, and Z obtained from microwave S-parameter measurements.

3.7.3. Optical Spectral Analysis

A third approach for investigating electro-optic material properties is through a spectral analysis of electro-optically phase modulated laser light. This approach involves measurement of the sideband peaks that are generated in the output spectrum of laser light that is phase modulated. The phase modulation can be achieved with any optoelectronic device in which the modulation mechanism involves a refractive index shift. This includes, for example, silicon plasma dispersion devices, graphene modulators, and Kerr and Pockels

effect electro-optic modulators. Here, the case for Pockels effect or $\chi^{(2)}$ materials such as $BaTiO_3$ is considered.

3.7.3.1. Theoretical Sideband Response

For $\chi^{(2)}$ materials, the electro-optic phase delay for linearly polarized light is

$$\Delta\phi_x = \frac{\omega_o n_x^3 r_{eff}}{2c}\Gamma E_m L \quad \text{(radians)} \tag{3.10}$$

where ω_o is the optical frequency, n_x is the mode refractive index for light polarized in the x direction, r_{eff} is the effective electro-optic coefficient of the polydomain film, E_m is the applied microwave electric field magnitude, and L is the interaction length or the length of the electrodes. The applied electric field is assumed to be sinusoidal such that

$$E_m(t) = A_m m(f) \sin \omega_m t \tag{3.11}$$

where A_{mw} is the driving amplitude and $m(f)$ is the electro-optic frequency response measured independently. The phase-modulated optical field is given by

$$E_o(t) = A_o \exp\left[-j(\omega_o t + \Delta\phi(t)\right]$$

Substituting in $\Delta\phi_x$ from Eqn. 3.10 and $E_m(t)$ from 3.11,

$$E_o(t) = A_o \exp(-j\omega_o t) \exp\left[-j\frac{\omega_o n^3 r_{eff}}{2c}\Gamma L A_{mw} m(f) \cos \omega_m t\right] \tag{3.12}$$

The modulation index z is defined as

$$z \equiv \frac{\omega_0 n_x^3 r_{eff}}{2c} \Gamma A_{mw} m(f) L. \tag{3.13}$$

Using the Bessel-function identity

$$e^{jz\cos\theta} = \sum_{n=-\infty}^{\infty} j^n J_n(z) e^{jn\theta}$$

the optical field is expressed as

$$E_o(t) = A_o \exp(-j\omega_o t) \sum_{n=-\infty}^{\infty} j^n J_n(z) e^{jn\omega_m t} \tag{3.14}$$

The spectral content of the electric field is obtained by taking the Fourier transform of Eqn. 3.14, the final result of which is

$$E_o(\omega) = \frac{1}{\sqrt{2\pi}} A_o \sum_{n=-\infty}^{\infty} j^n J_n(z) \delta(\omega_o - \omega - n\omega_m)$$

The intensity $I(\omega)$ is then

$$I(\omega) = E_o^* E_o = \frac{A_o^2}{2\pi} \sum_{n=-\infty}^{\infty} J_n^2(z) \delta(\omega_o - \omega - n\omega_m)$$

The intensity $I(\omega)$ is the signal measured by the optical spectrum analyzer. It is noted that this result is specific to the case of a phase modulator. The theoretical response is a series of peaks distributed equidistantly on either side of the center laser frequency ω_o with separation distance equal to an n^{th} order of modulation frequency. The intensity of the n^{th} order peak is given by $J_n(z)^2$, which is a function of the effective in-device electro-optic

coefficient, r_{eff}. Hence from a given measured spectrum the electro-optic coefficient can be calculated from the difference (in dB) of the measured peak heights.

The electro-optic phase modulated sideband response was measured using the experimental setup in Fig. 3.17. Light with 4 mW nomimal power from the tunable laser source (HP 8164A) was TE polarized in the plane of the $BaTiO_3$ film and coupled into and out of the PC waveguide using tapered lensed fibers (Nanonics SMF-28). An analog signal generator (Agilent E8257D) was used to produce a sinusoidal modulation signal, which was amplified to a saturated output of +23 dBm (Centellax OA4MVM broadband amplifier with greater than 45 GHz bandwidth). The voltage supplied by the amplified output was measured versus frequency for different input powers used in this study using a calibrated vector network analyzer (VNA) with a 30 dB attenuator placed between the amplifier output and VNA port. The power dependent frequency response of the amplifier is shown in Fig. 3.18. The measured power dependent response was used to accurately determine the applied voltage for calculating the electro-optic coefficient. A dc bias voltage up to 10 V was added to the microwave signal using a high frequency bias tee (PulseLabs 5541A), and the signal was applied to the 50 Ω terminated modulator using high-speed wafer probes (Cascade Microtech ACP50 SG and GS 100). The modulated light collected at the device output was coupled via fiber into an optical spectral analyzer (Yenista OSA20) with 6 GHz resolution bandwidth and greater than 55 dB optical rejection ratio for measuring the electro-optically phase modulated sideband response.

A sample calculation is considered here to demonstrate the procedure for obtaining the effective in-device electro-optic coefficient from the measured sideband response. For a 5 µm electrode gap spacing, the calculated electro-optic overlap factor is approximately

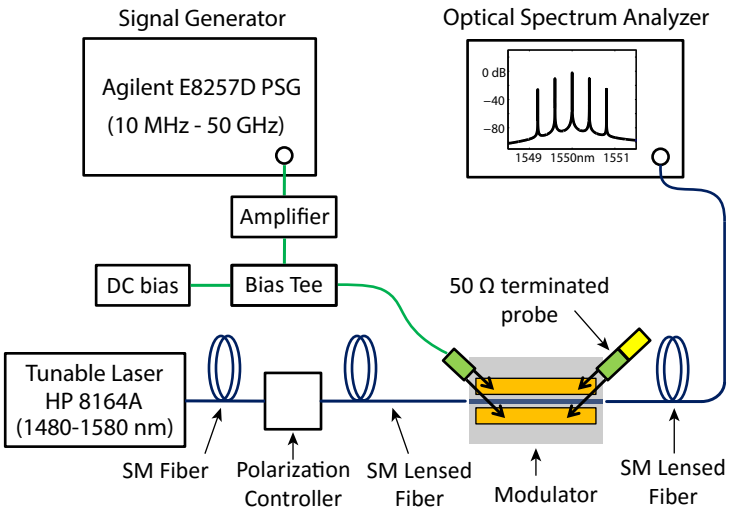

Figure 3.17. Optical spectral analysis setup used for measurements of the electro-optic properties at frequencies between 10 and 50 GHz and wavelengths between 1500 and 1580 nm.

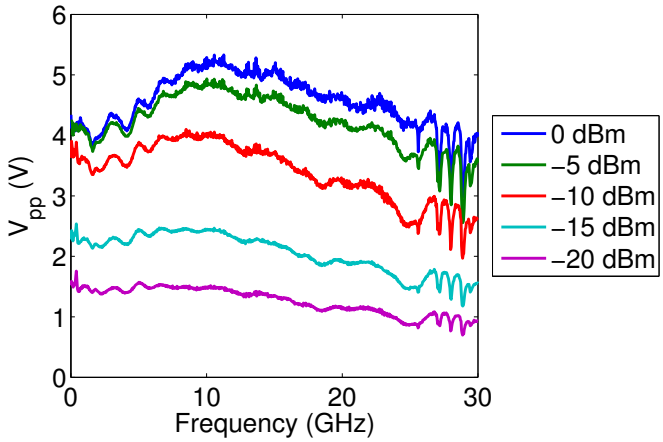

Figure 3.18. Measured output voltage from the amplifier that is supplied to the device for different input powers.

0.71 (see Section 7.5) and the optical mode index is approximately 2.13 (see section 7.4). The measured optical sideband response at 10 GHz modulation and an optical wavelength of 1530 nm is shown in Fig. 3.19. A second order sideband is visible at a

frequency displacement of -20 GHz. The assymetry of the second order side lobes is presumably due to a combination of a mixture of phase and intensity modulation (im-pure phase modulation) and the applied bias field, which provides an optical bias through the electro-optically induced birefringence. For 0 dBm input power and 10 GHz modulation frequency, the driving voltage obtained from Fig. 3.18 is 5.3 V_{pp}. The measured (unitless) electro-optic magnitude response of the device at 10 GHz is 0.433 (obtained from Fig. 2b in the main text). The difference in intensity between the zeroth and first order peaks for the measurement conditions is plotted versus electro-optic coefficient in Fig. 3.19 (b). Shown as a horizontal line is the measured difference in peak height, equal to 11.55 dB. The line and curve intersect at an electro-optic coefficient of 161 pm/V.

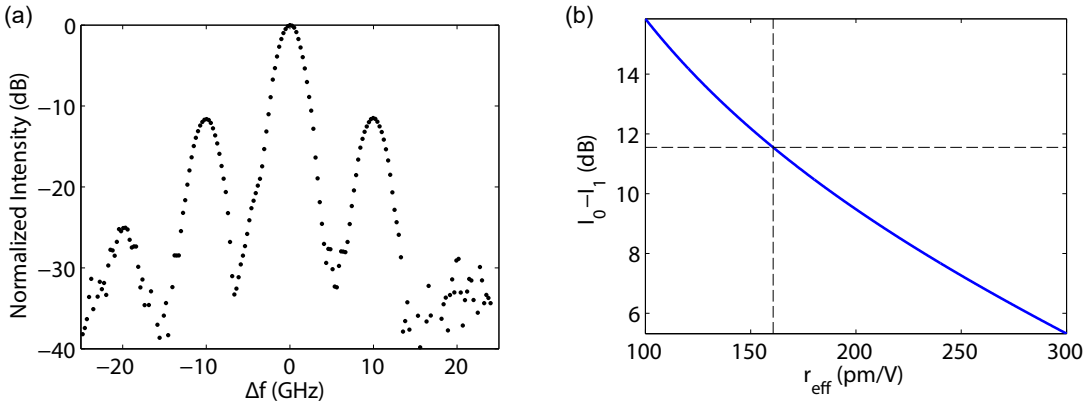

Figure 3.19. (a) Measured optical sideband response for 10 GHz modulation at 1530 nm. (b) Graphical calculation of the electro-optic coefficient from the measured difference in height between the first and zeroth order peaks and the theoretical dependence on the electro-optic coefficient.

3.7.3.2. Effect of Microwave Induced Optical Mode Coupling

For high frequencies at which the device length is comparable to the wavelength of the applied microwave signal, the propagation of the microwave signal must be considered.

In particular, coupling between the optical normal propagation modes, phase velocity matching between the microwave and optical wave, and microwave substrate mode coupling must be considered.

Coupling between the TE and TM optical modes is described by the equation of motion for the displacement field vector $\mathbf{D}$ in the presence of a perturbation — in this case, a microwave field — in an anisotropic material:

$$\left[\frac{\partial}{\partial\zeta} + \frac{1}{c}N\frac{\partial}{\partial t}\right]\mathbf{D} = 0$$

where ζ is the propagation direction and c is the speed of light in free space. The refractive index matrix N is given by

$$N = \begin{pmatrix} n_1 - \frac{1}{2}n_1^3\Delta\eta_{11} & -\frac{n_1^2 n_2^2}{n_1+n_2}\Delta\eta_{12} \\ \\ -\frac{n_1^2 n_2^2}{n_1+n_2}\Delta\eta_{21} & n_2 - \frac{1}{2}n_2^3\Delta\eta_{22} \end{pmatrix}$$

where n_1 and n_2 are the refractive indices of the normal modes in the absence of the microwave perturbation. The changes in the dielectric impermeability tensor $\Delta\eta_{\alpha\beta}$ are, for electro-optic modulation,

$$\Delta\eta_{\alpha\beta} = r_{\alpha\beta\gamma}E_\gamma$$

The subscripts α, β, and γ refer to the principal directions of the propagation axes. These axes are, in general, rotated with respect to the dielectric axes of the crystal. The electro-optic coefficient tensor elements in the rotated coordinate system are given by

$$r_{\alpha\beta\gamma} = a_{\alpha i}a_{\beta j}a_{\gamma k}r_{ijk}$$

where $a_{\alpha i}$, $a_{\beta j}$ and $a_{\gamma j}$ are directional cosines of the coordinate transformation. The requirement for pure phase modulation is $\Delta\eta_{12} = \Delta\eta_{21} = 0$, or $r_{12\gamma}E_\gamma = r_{6\gamma}E_\gamma = 0$. For the case of polydomain $BaTiO_3$, the four in-plane domain variants contribute to r_{61} and r_{62}. The incident light will therefore couple between the TE and TM modes as it propagates through the thin film, and the phase-modulated light measured with the optical spectrum analyzer will experience contributions from both a- and c-oriented domains. The measured electro-optic coefficient will therefore be an effective coefficient that is not associated with a particular domain variant or electro-optic tensor element.

CHAPTER 4

Measured Microwave Properties of $BaTiO_3$ Thin Films

4.1. Introduction

The microwave properties of coplanar stripline devices on $BaTiO_3$ thin films were investigated through measurements of two-port microwave scattering parameters (S-parameters). Measurements were done over the frequency range of 10 MHz to 50 GHz using the calibrated vector network analyzer setup discussed in Section 3.5.1. Films used in this study had thicknesses between 230 and 500 nm, and the coplanar stripline devices had electrode gap spacings of 5, 7.5, and 12 µm. The electron-beam evaporated electrodes consisted of 600 nm of gold on top of 10 nm of titanium. The measurements were done to elucidate the following: 1) the effect of the electrode geometry, namely the gap spacing, on the device performance at technologically relevant microwave frequencies; and 2) the dependence of device and film properties on film thickness. The device properties investigated were the effective microwave index, characteristic impedance, and conductor and dielectric loss coefficients. The following trends were elucidated for the first time for $BaTiO_3$ thin films and coplanar stripline devices on $BaTiO_3$ thin films:

(1) The effective microwave index and total attenuation losses increase with $BaTiO_3$ film thickness while the characteristic impedance decreases with film thickness.

(2) The effective microwave index and total attenuation losses decrease with electrode gap spacing while the characteristic impedance increases with gap spacing.

(3) The effective microwave index (characteristic impedance) decreases (increases) rapidly with frequency up to approximately 15 GHz, beyond which it is flat out to, and possibly beyond, 50 GHz.

(4) The microwave attenuation losses are dominated by conductor losses in thicker $BaTiO_3$ films with narrow electrode gap spacings and by dielectric losses in thinner films with wide gap spacings.

The observed trends 1-3 are in agreement with electromagnetic field calculations that show increasing microwave power confinement in the high dielectric constant $BaTiO_3$ thin film for devices with narrower electrode gap spacings and greater film thickness. The last trend is not intuitive and is solely an empirical finding.

The microwave properties of the coplanar stripline devices and $BaTiO_3$ thin films in the frequency range studied are important for determining the expected electro-optic frequency response and for predicting the ultimate achievable electro-optic bandwidth of photonic crystal devices through device modeling. In Chapter 6, the measured electro-optic frequency response is compared to the modeled response calculated using the measured microwave properties reported here. Good agreement is obtained between the measured and predicted responses, validating the device and film properties presented here. The measured microwave properties discussed here were used as a guideline for device modeling presented in Chapter 7.

The trends elucidated by this study and subsequent modeling in Chapters 6 and 7 indicate that there is a trade-off between the electro-optic bandwidth and voltage-length product that are achievable in a conventional modulator. The microwave losses — which include impedance mismatch, index mismatch, and attenuation — increase with narrower

gap spacing and greater film thickness. The voltage-length product, however scales directly with the gap spacing and is inversely proportional to the electro-optic overlap factor, which, according to calculations discussed in Chapter 7, increases with film thickness. The implications of this trade-off on device performance are discussed in Chapter 7. As discussed in the introduction and in Chapter 5, a reduction in the voltage-length product and an increase in electro-optic bandwidth is achievable with photonic crystal waveguide devices in which the electro-optic coefficient is enhanced by the high optical group index that slows the light.

The figures in this chapter include a selected set of data chosen to illustrate trends in the microwave properties. The full sets of data for all microwave measurements are included in Appendix C, organized by electrode gap spacing and in order of increasing film thickness. The selected data are indicated in the tables.

4.2. Measured S-Parameters

Full two-port S-parameters of the coplanar stripline devices were measured, from which the microwave index, characteristic impedance, and total attenuation loss were calculated. Since the coplanar stripline devices symmetric about the propagation direction, the measured S-parameter matrix is nominally symmetric, i.e., $S_{11} = S_{22}$ and $S_{12} = S_{21}$. For a two-port network, the matrix elements S_{11} and S_{22} represent reflection coefficients, while the matrix elements S_{12} and S_{21} represent transmission coefficients. In practice, there are slight differences due to the uncertainty of the probe parameter values used in the calibration that is done prior to taking measurements. The S-parameter measurements include both magnitude and phase information. As discussed in the following sections, the

phase of S_{21} is used to calculate the microwave effective index, and the magnitudes of S_{11} and S_{21} are used to calculate the total microwave loss.

The magnitudes of the S-parameters are plotted for three different film thicknesses and three different electrode gap spacings in Fig. 4.1. For reference, horizontal lines are drawn at $-3\,\mathrm{dB}$ and $-10\,\mathrm{dB}$ on the S_{21} and S_{11} plots, respectively. The 3 dB electrical bandwidth is defined as the frequency at which the measured $|S_{21}|$ falls to half of the value measured at dc. The 10 dB electrical bandwidth is similarly defined for the reflection coefficient S_{11}; it defines the frequency at which the reflected power surpasses a value that is 1% of the incident power. For a given electrode gap spacing, it is apparent from the S-parameter plots that the 3 dB and 10 dB bandwidths increase with decreasing film thickness. Similarly, for a given film thickness, the 3 dB and 10 dB bandwidths increase for larger gap spacings. These trends are further illustrated in Fig. 4.2, where the 3 and 10 dB bandwidths are plotted versus electrode gap spacing and $BaTiO_3$ film thickness. Apart from these general trends, it is also noted that the reflection coefficient reaches a maximum near 20 GHz, beyond which there is a dip and either a subsequent level or decreasing response out to 50 GHz. This trend is attributed to a decreasing permittivity of the $BaTiO_3$ film in across the entire frequency range, as reported previously by Hamano et al on $BaTiO_3$ films epitaxially grown on MgO[57]. This result is further discussed in the following sections in conjunction with the measured microwave index, impedance, and total microwave loss.

In addition to the measured magnitudes of S_{11} and S_{21}, the measured phase delay of S_{21} ($\arg\{S_{21}\}$) was used to calculate the effective microwave index. The measured $\arg\{S_{21}\}$ is plotted versus frequency for different gap spacings and $BaTiO_3$ film thickness

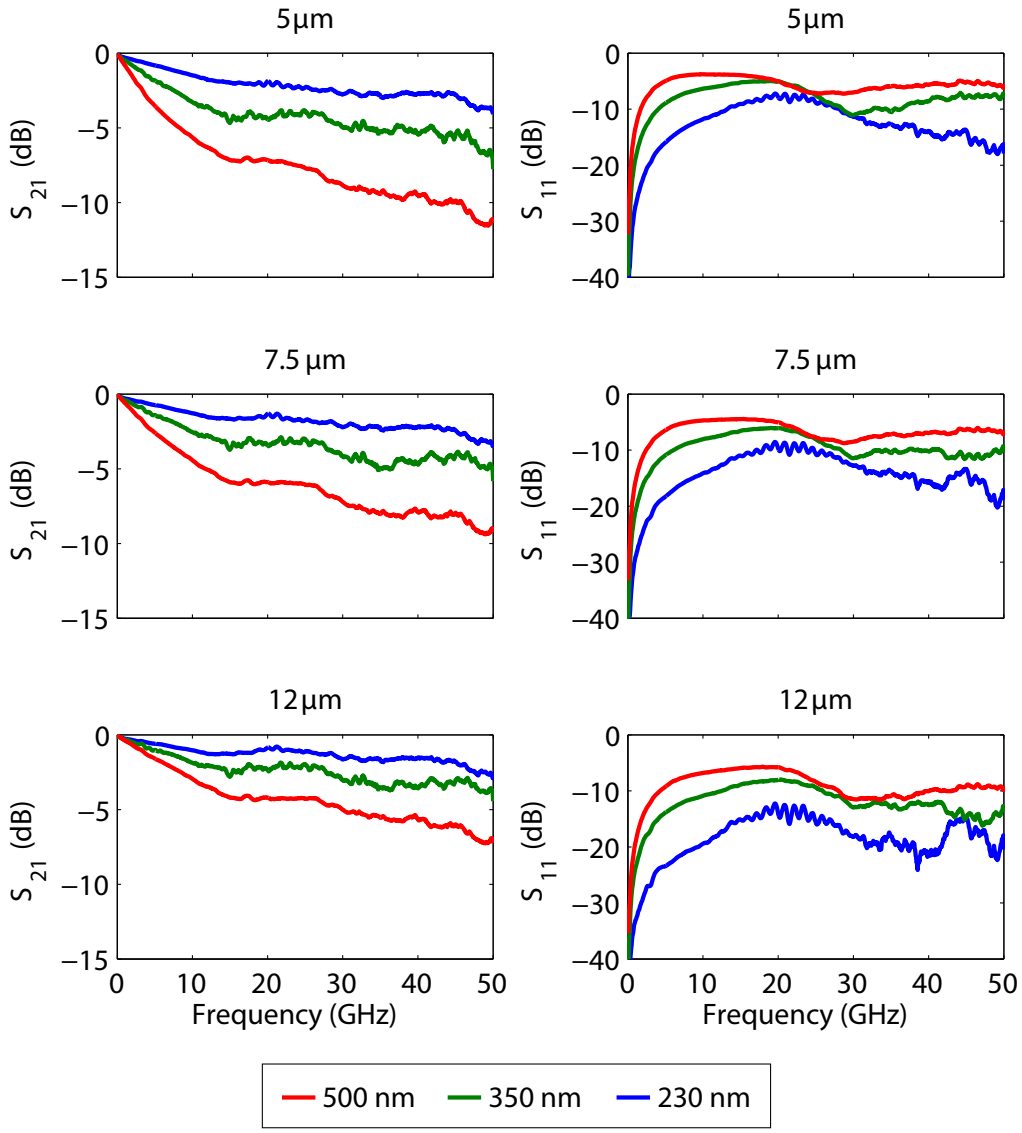

Figure 4.1. Measured S-parameters for electrode gap spacings of 5, 7.5, and 12 µm and $BaTiO_3$ thicknesses of 230, 350, and 500 nm. The films and devices are indicated in Tables C.1-C.3 in Appendix C.

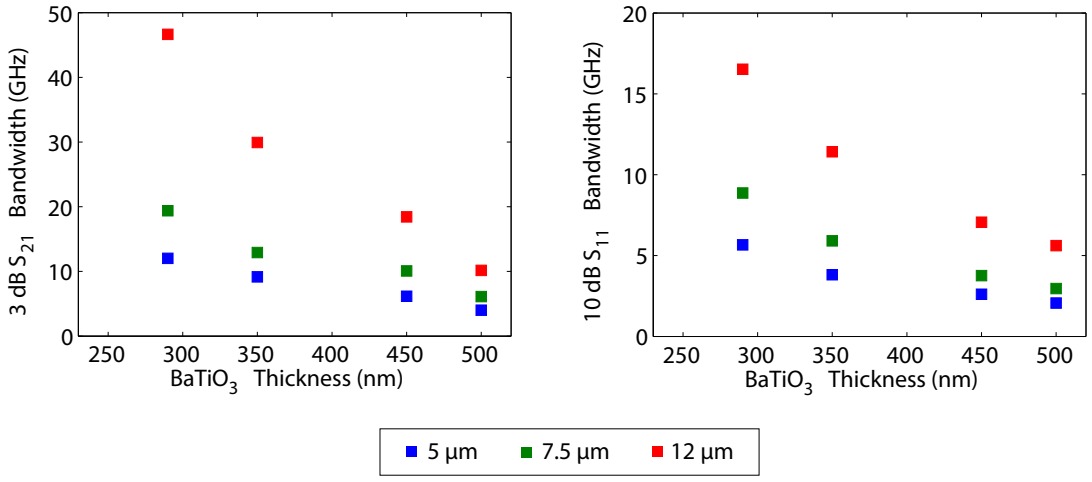

Figure 4.2. Measured 3 dB S_{21} bandwidth and 10 dB S_{11} bandwidth versus film thickness for electrode gap spacings of 5, 7.5, and 12 µm. The films and devices are indicated in Tables C.1-C.3 in Appendix C.

in Fig. 4.3. The phase measured by the VNA is recorded as a value between 0 and $-\pi$; the physical interpretation of the phase for calculating the microwave effective index, however, requires a monotonic increase in phase with frequency. The measured data is thus plotted as monotonically increasing phase with frequency, where the jumps in phase between $-\pi$ and π have been reconciled. The S_{21} phase increases nearly linearly for frequencies between 10 and 50 GHz. Below 10 GHz, there is an initial nonlinear increase in phase. For a given electrode gap spacing, the phase delay is larger at any frequency for thicker $BaTiO_3$ films. Similarly, for a given film thickness, there is a larger phase delay for narrower electrode gap spacing. The implications of these trends on the effective microwave index are explained in the following section.

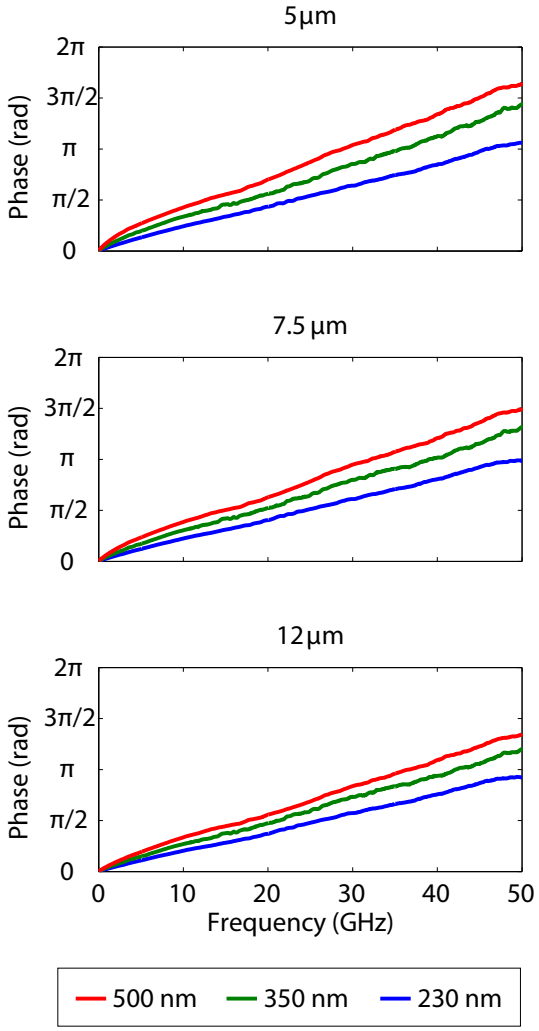

Figure 4.3. Measured S_{21} phase delay versus frequency for gap spacings of 5, 7.5, and 12 µm and film thicknesses of 230, 350, and 500 nm. The films and devices are indicated in Tables C.1-C.3 in Appendix C.

4.3. Microwave Index and Characteristic Impedance

The frequency-dependent microwave index and impedance were calculated from the measured phase delay of S_{21}. The microwave index was obtained as

$$n_{\mu w} = \arg\{S_{21}\}\frac{c}{2\pi f L} \tag{4.1}$$

where c is the speed of light in free space, f is the microwave frequency, and L is the electrode length. This relation is derived by equating the measured phase delay with the phase accrued over a path length $(2\pi f/c)n_{\mu w}L$. Using the calculated microwave index and the known geometry of the device, the impedance (Z) was calculated using Eqn. 2.5[28]:

$$Z = \frac{120\pi}{n_{mw}}\frac{K(k')}{K(k)}$$

The variables in this equation are described and defined in Section 2.2.1. The calculation of the characteristic impedance is semi-empirical; it includes both the measured value of the effective microwave index and a parameter calculated from purely the electrode geometry. Unlike other purely analytical methods proposed in the literature for calculating the index and characteristic impedance of multilayer dielectric structures[28,51], this calculation is not limited by any restrictions on the electrode thickness, film permittivity, or film thickness. In general, restrictions on these parameters prevent the accurate calculation of microwave device properties for $BaTiO_3$ thin films with sub-micron thickness. Additionally, the calculation of the characteristic impedance through Eqn. 2.5 involves a direct measurement of the dielectric properties of the multilayer, which includes the effects of both microstructure, such as ferroelectric domain size distribution, and processing-induced point defects such as

oxygen vacancies. The semi-empirical method used here is therefore the preferred method for investigating the microwave properties of thin film ferroelectric materials, especially those with high permittivity.

The measured frequency dependent effective microwave index and characteristic impedance are plotted for different electrode gap spacings and $BaTiO_3$ film thicknesses in Fig. 4.4. The microwave index decreases rapidly up to about 15 GHz, beyond which it is nearly flat out to 50 GHz. The initial decrease in microwave index with frequency is due to both the finite conductivity of the gold electrodes[113] and a reduction in the $BaTiO_3$ dielectric constant in this range[57]. For a given electrode gap spacing, the effective microwave index in the range 20-50 GHz is larger for films with greater thickness. Similarly, for a given film thickness, the index is larger for smaller gap spacings. These trends follow the same trends for confinement of microwave power, discussed in Section 7.3.3; the percent of microwave power confined within the $BaTiO_3$ thin film is larger for both thicker films and narrower electrode gap spacings. In addition to the confinement of microwave power, a larger effective microwave index is expected for thicker films due to the larger in-plane dielectric constant in the polydomain $BaTiO_3$ thin films, as described by a simple model for the in-plane dielectric constant with respect to the distribution of in- and out-of-plane domain variants in Chapter 7. Since the electric field due to the coplanar stripline electrodes is mostly in the plane of the film, the increase in in-plane dielectric constant with increasing film thickness also accounts for the increase in effective microwave index. Using the experimental results for the effective microwave index versus frequency, it is possible to estimate the increase in effective in-plane dielectric constant with film thickness; the results of this analysis are presented in Chapter 7.

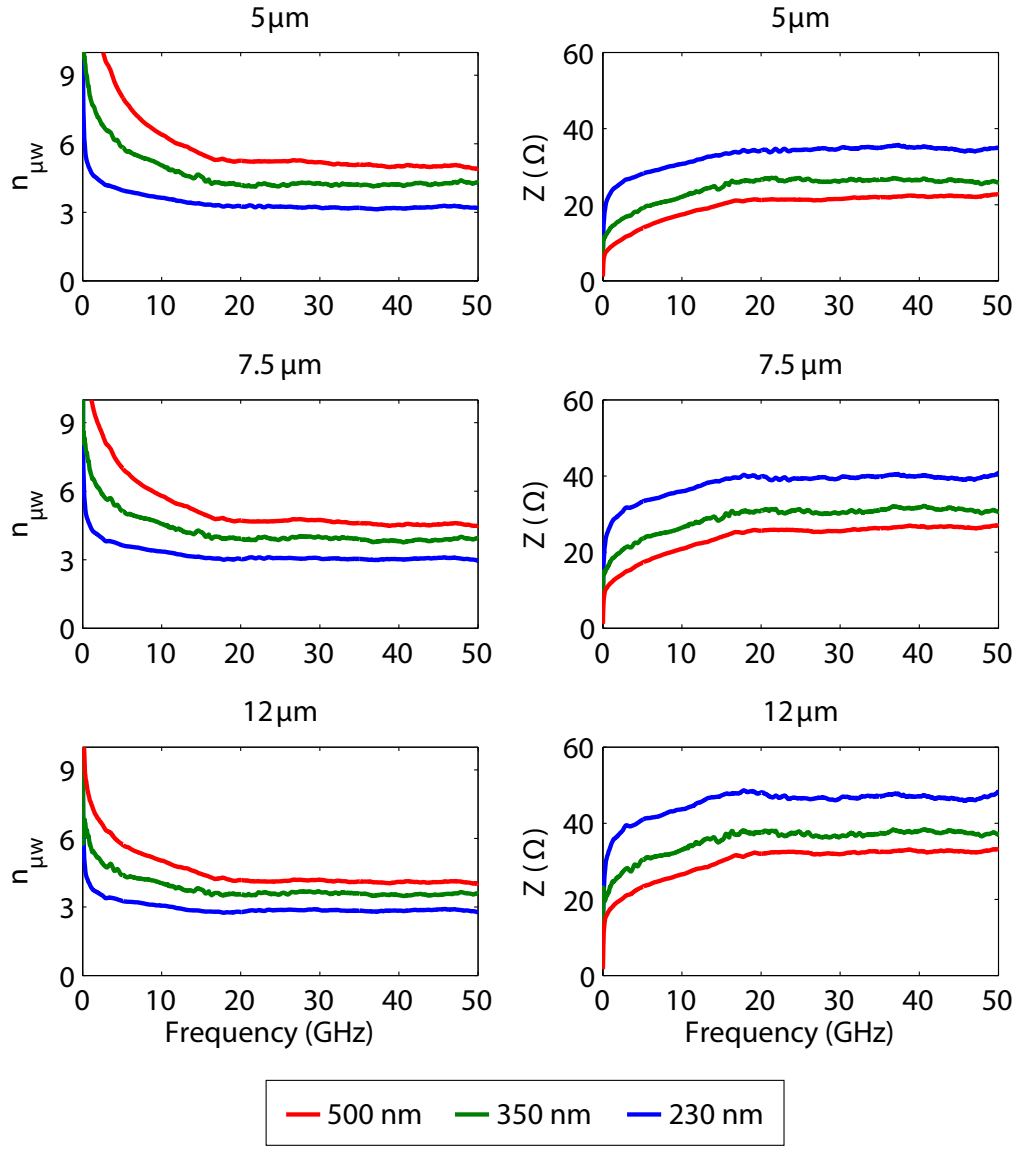

Figure 4.4. Measured effective microwave index and electrode characteristic impedance for electrode gap spacings of 5, 7.5, and 12 μm and film thicknesses of 230, 350, and 500 nm. The films and devices are indicated in Tables C.1-C.3 in Appendix C.

Compared with the microwave index, the characteristic impedance increases rapidly up to 15 GHz, after which it is flat out to 50 GHz. Due to the inverse relationship of index

with impedance in Eqn.2.5, the trends of impedance with respect to gap spacing and film thickness are reversed. For a given electrode gap spacing, the characteristic impedance decreases with increasing film thickness. For a given film thickness, the characteristic impedance increases with larger gap spacing. These trends are clearly visible in Fig. 4.5, where the average microwave index and characteristic impedance in the 20-50 GHz range are plotted versus film thickness for different electrode gap spacings.

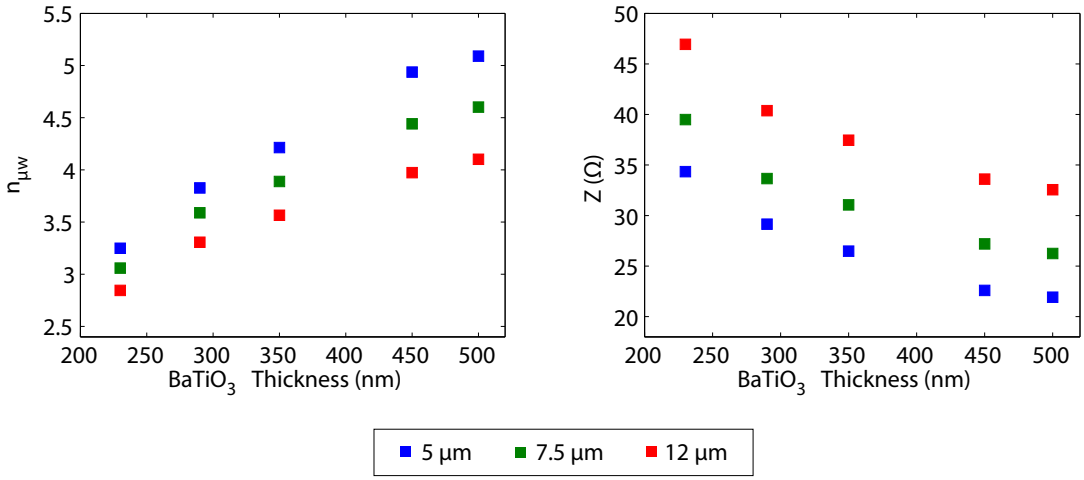

Figure 4.5. Measured index and characteristic impedance in the 20-50 GHz range versus film thickness for gap spacings of 5, 7.5, and 12 µm. The films and devices are indicated in Tables C.1-C.3 in Appendix C.

It is noted that the value of the microwave index in the 20-50 GHz range is much smaller than that expected if the measurements were done on a bulk $BaTiO_3$ crystal. For devices on a bulk substrate, the microwave power is confined approximately equally in the substrate and superstrate, and the effective index is approximately equal to $\sqrt{(1+\epsilon_{sub})/2}$, where ϵ_{sub} is the real part of the dielectric constant of the (MgO) substrate[50]. For bulk $BaTiO_3$ with an in-plane dielectric constant of 2200 under strain-free conditions[175], the expected microwave index would be approximately 33. In the other extreme case where

the coplanar lines are supported only on the MgO substrate, the expected microwave index is approximately 2.3. The dielectric constant is much reduced in thin film samples due to the sharing of microwave power in the low dielectric constant substrate. In this work, (100) oriented MgO with a dielectric constant of 9.8 at 1 GHz was used as the substrate for epitaxial growth of the $BaTiO_3$ films. The microwave indices reported here are therefore not unexpectedly small. They are, in fact, similar in magnitude to those reported previously for thin film $BaTiO_3$ [81,142] and for bulk $LiNbO_3$ [113].

The value of both the microwave index and characteristic impedance affect the electro-optic bandwidth of a traveling-wave modulator where the microwave field is transmitted by the coplanar stripline electrodes. The microwave index should be ideally matched to the optical index to minimize index mismatch loss, and the characteristic impedance should be matched to the system impedance ($50\,\Omega$) to minimize reflection losses. The mode index of the optical ridge waveguide is between 1.9 and 2.13 depending on the film thickness according to calculations presented in 7.4. For all devices reported here, the microwave index is above this value, with larger microwave indices measured for thicker films and devices with narrower gap spacings. The index mismatch losses therefore increase with increasing film thickness and with decreasing gap spacing.

A similar trend is observed for the impedance mismatch. For all film thicknesses and electrode gap spacings studied, no device is matched to $50\,\Omega$ in the range 20-50 GHz, and the characteristic impedance is below $50\,\Omega$. The effect of this on the microwave performance is quantified with the microwave reflection coefficient, defined as

$$R = \frac{Z - Z_S}{Z + Z_S}$$

where Z_S is the source impedance. The reflection coefficient in the 20-50 GHz range for a $50\,\Omega$ source impedance is plotted versus film thickness for the three gap spacings in Fig. 4.6. The reflection coefficient is larger for thicker $BaTiO_3$ films and for narrower electrode gap spacings. The trends in the calculated reflection coefficient can be used to explain trends in the measured S-parameters (Fig. 4.1). In section 4.2, both the 3 dB S_{21} and 10 dB S_{11} bandwidths were found to decrease with increasing film thickness and smaller gap spacing. Since S_{11} is essentially a measure of the reflected power, it is not surprising that the same trends observed for the 10 dB S_{11} bandwidth with respect to gap spacing and film thickness are observed for the reflection coefficient. It is noted, however, that the reflection coefficient at frequencies between 10 MHz and 20 GHz follows an opposite trend to that of the measured S_{11} due to the rapid change in index as the transition is made between the dc and microwave responses. The reflection coefficient in the 20-50 GHz range also follows the same trends observed for the 3 dB S_{21} bandwidth. This can be explained by a loss of transmitted power due partially to reflection losses. The additional S_{21} loss is due to microwave attenuation losses, which are considered in the following section.

4.4. Dielectric and Conductor Losses

The total microwave losses due to length-dependent signal attenuation were calculated as a function of frequency from the measured magnitudes of S_{11} and S_{21}. The total loss is given by

$$\alpha(f) = \frac{4.343}{L} \ln\left(\frac{1-|S_{11}|^2}{|S_{21}|^2}\right) \quad [\text{dB/cm}] \tag{4.2}$$

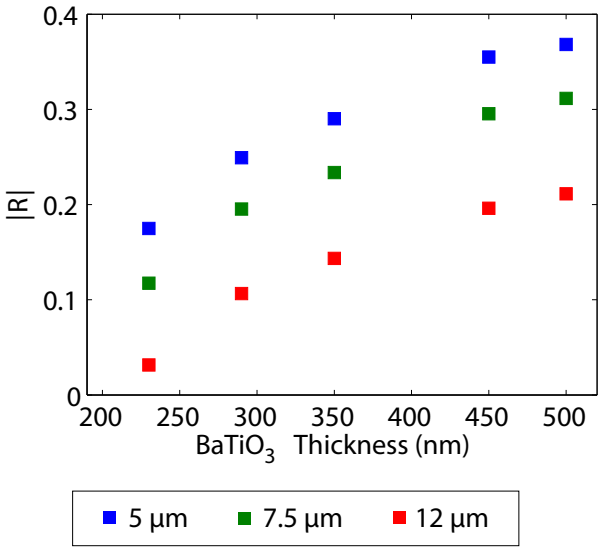

Figure 4.6. Reflection coefficient in the 20-50 GHz range calculated from the measured impedance. The films and devices are indicated in Tables C.1-C.3 in Appendix C.

where L is the electrode length in centimeters. It is important to note that the natural units for S-parameter measurements are Nepers (Np) since the S-parameters are measurements of field quantity ratios. The unit of decibels is a power ratio and is the correct unit for power-related quantities; as such a conversion to dB/cm is required when the loss coefficients are used in electro-optic magnitude response calculations. Another expression for the microwave loss is obtained from the complex-valued propagation constant (γ) given by Noguchi et al[113] as

$$\alpha = \mathrm{Re}\{\gamma\} = \mathrm{Re}\left\{\frac{1}{L}\cosh^{-1}\left(\frac{1 - S_{11}^2 + S_{21}^2}{2S_{21}}\right)\right\} \tag{4.3}$$

where the complex-valued S_{11} and S_{21} are used. Both Eqn. 4.2 and 4.3 give nearly the same value for the magnitude of total loss; however, the latter unnecessarily includes phase

information, which adds to the uncertainty and adversely affects fitting to the data. The total microwave loss was therefore calculated using Eqn. 4.2.

The total microwave loss is typically modeled as a summation of contributions from both conductor and dielectric portions as

$$\alpha = \alpha_c\sqrt{f} + \alpha_d f \quad [\text{dB/cm}] \tag{4.4}$$

where α_c is the conductor loss coefficient in units of $\text{dB/cm}/\sqrt{\text{GHz}}$ and α_d is the dielectric loss coefficient in units of dB/cm/GHz. Before fitting Eqn. 4.4 to the microwave loss data, it is important to understand the frequency dependence of terms included in α_c and α_d. The conductor loss coefficient is given by[50]

$$\alpha_c \propto \sqrt{\frac{\pi f \mu_{re}}{\sigma}}\epsilon_{re} Z \cdot \phi(g, w, t) \tag{4.5}$$

where μ_{re} is the effective permeability, σ is the electrode conductivity, ϵ_{re} is the effective dielectric constant, Z is the characteristic impedance which is a function of the dielectric constant (see Eqns. 2.52.4), and $\phi(g, w, t)$ is a geometry factor that is a function of the electrode width (w), gap spacing (g), and thickness (t). The full equation is given in Section 7.3.2. The dielectric loss coefficient is given by

$$\alpha_d = \frac{\pi f}{n_{\mu w} c}\left(\Gamma_f \epsilon_f \tan\delta_f + \Gamma_s \epsilon_s \tan\delta_s\right) \tag{4.6}$$

where f is the microwave frequency, c is the speed of light in free space, ϵ is the dielectric constant, Γ is the microwave power confinement factor, and $\tan\delta$ is the dielectric loss tangent. The subscripts f and s indicate properties of the film and substrate, respectively.

From equations 4.5 and 4.6, it is clearly shown that $\alpha_c \propto \sqrt{f}$ and $\alpha_d \propto f$, however, other properties including ϵ_{re}, Z, the power confinement factors, the dielectric constants of the film and substrate, and the loss tangents are, in general, frequency dependent.

According to the data presented in Fig. 4.4, there are two distinct frequency regions that can be used to describe the microwave properties. In the range 10 MHz - 15 GHz, the microwave index and impedance are frequency dependent, while at higher frequencies between 15 and 50 GHz, the index and impedance are frequency independent. Since we are also ultimately interested in the high frequency behavior, we consider a fitting of Eqn. 4.4 only in the high frequency region above 15 GHz. The total microwave loss calculated from Eqn. 4.2 for devices on films with thicknesses of 230, 350, and 500 nm is plotted as solid curves in Fig. 4.7. Also plotted is the fitted total loss according to Eqn. 4.4, where the fitting is done in the 15-50 GHz range. The fitting coefficients are plotted versus film thickness for the three gap spacings in Fig. 4.8. The conductor loss coefficient generally increases with film thickness and is larger for narrower gap spacings, while no clear trend is observed for the dielectric loss coefficient with respect to film thickness or electrode gap spacing. The conductor loss coefficient is quantitatively about an order of magnitude larger than the dielectric loss coefficient.

The values of the loss coefficients alone do not determine which mechanism dominates. A fair comparison of the two loss mechanisms is obtained by calculating the ratio of total conductor microwave loss ($\alpha_c\sqrt{f}$) to the total dielectric microwave loss ($\alpha_d f$). This ratio is plotted versus frequency for different film thicknesses and gap spacings in Fig. 4.9. Horizontal dashed lines are drawn where the ratio is equal to 1. Above this dashed line, the microwave attenuation losses are dominated by the conductor losses, and below the

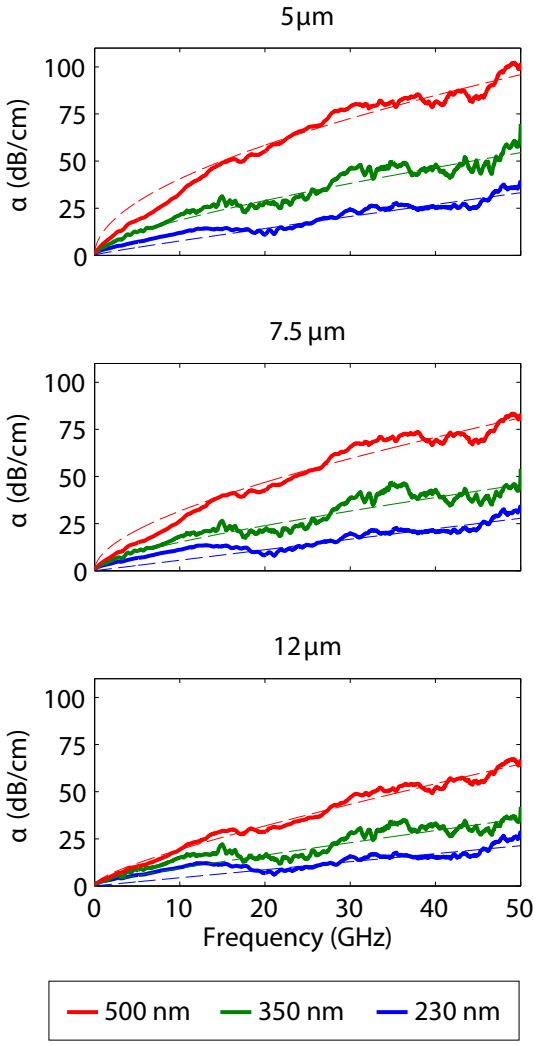

Figure 4.7. Calculated total microwave attenuation, in dB/cm, for different electrode gap spacings and film thicknesses (solid curves). Fitting of the data to Eqn. 4.4 in the 15-50 GHz region is given by the dashed curves. The films and devices are indicated in Tables C.1-C.3 in Appendix C.

line the losses are dominated by the dielectric losses. Some general trends observed are the following:

(1) The losses are dominated more by the conductor loss at low frequencies and by the the dielectric loss at high frequencies.

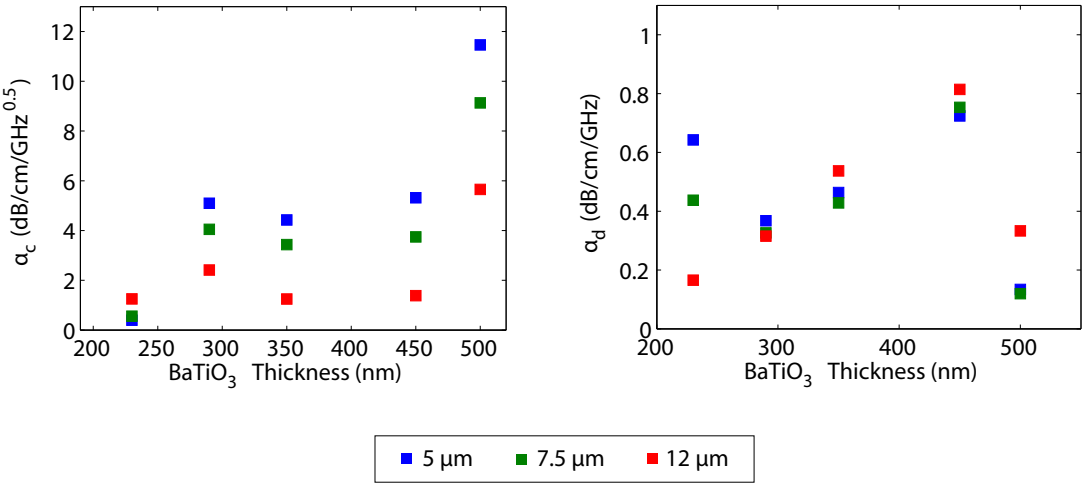

Figure 4.8. Conductor and dielectric loss coefficients obtained from fitting Eqn.4.4 to the measured microwave losses versus frequency. The coefficients are plotted versus $BaTiO_3$ thickness for different electrode gap spacings. The films and devices are indicated in Tables C.1-C.3 in Appendix C.

(2) A larger fraction of the losses are due to conductor loss in narrower gap spacing devices.

(3) The losses are dominated more by the conductor loss for devices on thicker films.

For devices on the film with 230 nm thickness, the losses are clearly dominated by the dielectric losses across the entire frequency range for all three electrode gap spacings. For devices on the 500 nm thick film, the losses are dominated across the entire frequency range by the conductor loss component for gap spacings of 5 and 7.5 µm. For the 12 µm gap spacing device on the 500 nm thick film, the losses are dominated by conductor loss up to approximately 22 GHz, beyond which the losses are dielectric dominated. For the intermediate film thickness, the losses are dominated by conductor loss for the 5 and 7.5 µm gap spacings and by the dielectric loss for the largest gap spacing across the entire frequency range.

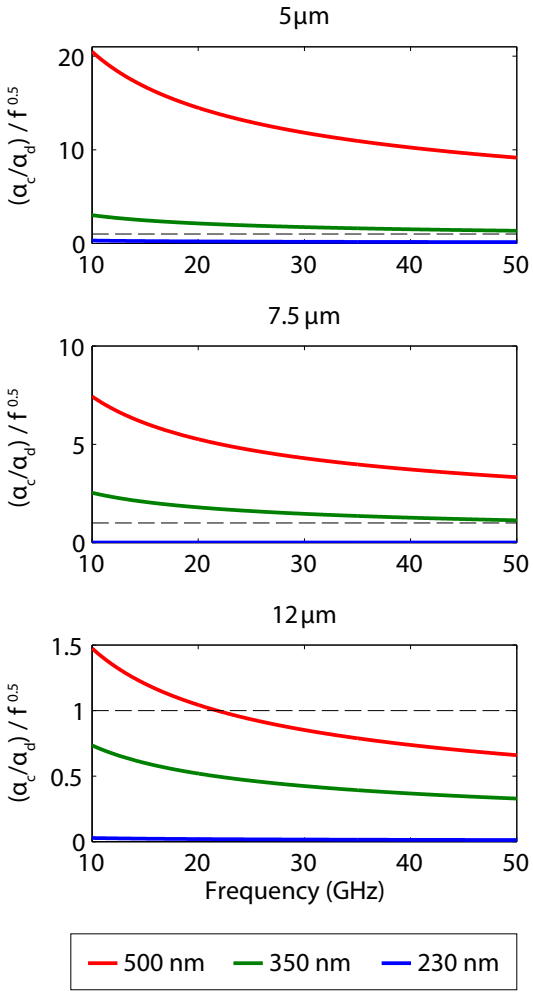

Figure 4.9. Ratio of the total conductor to dielectric microwave loss versus frequency for different film thicknesses and electrode gap spacings. The films and devices are indicated in Tables C.1-C.3 in Appendix C.

To maximize the electro-optic 3 dB bandwidth of a traveling wave modulator using these coplanar stripline electrodes, the microwave attenuation losses must be minimized. The trends observed from Fig. 4.9 provide insight as to how to minimize the losses depending on the gap spacing and film thickness. As noted above, the conductor loss dominates the total attenuation loss for devices on thicker $BaTiO_3$ films. According to

Eqn. 4.5, the conductor loss is a function of the electrode geometry, including the gap spacing, width, and thickness. The microwave losses could therefore be minimized for devices on thick (500 nm) $BaTiO_3$ films by optimizing the electrode geometry.

For devices on thinner films, the total microwave loss is lower and the dielectric loss is the dominant mechanism. According to Eqn. 4.6, the dielectric loss scales directly with the film permittivity and confinement of microwave power in the film and inversely with the microwave index. In both polycrystalline and single crystalline ferroelectric perovskites, the net spontaneous polarization and switching polarization is reduced in the presence of oxygen vacancy defects due to the pinning of domain wall motion[36,158]. While the switching polarization and film permittivity could be reduced by post-processing of epitaxial films via annealing in a reducing environment[158,8], this cannot be done without negatively affecting the electro-optic coefficients of the film. The non-zero electro-optic tensor elements for ferroelectric perovskites with *P4mm* symmetry, such as $BaTiO_3$ are[37]

$$\begin{aligned} r_{13} &= 2g_{12}P_s\epsilon_0(\epsilon_3 - 1) \\ r_{33} &= 2g_{11}P_s\epsilon_0(\epsilon_3 - 1) \\ r_{51} &= g_{44}P_s\epsilon_0(\epsilon_1 - 1) \end{aligned}$$

where g_{ik} are the quadratic electro-optic tensor elements, P_s is the spontaneous polarization, ϵ_0 is the permittivity of free space, and ϵ_k is the permittivity along the k^{th} principal direction. Since the electro-optic coefficient tensor elements are proportional to the permittivity tensor elements, a reduction in the film permittivity would reduce the effective electro-optic coefficient and thereby adversely affect device properties such as the modulation voltage.

At the same time, the dielectric loss contribution in thinner film devices could be reduced by reducing the confinement of microwave power within the film by, for example, increasing the electrode gap spacing or by introducing a buffer dielectric layer between the electrodes and $BaTiO_3$ film. Both of these methods, however, reduce the electro-optic overlap within the $BaTiO_3$ film and also lead to larger modulation voltages.

4.5. Summary and Conclusions

The microwave properties of $BaTiO_3$ films and coplanar stripline devices on these films were investigated through S-parameter measurements in the frequency range 10 MHz-50 GHz. The measurments were done on films with thickness between 230 and 500 nm, and the coplanar stripline devices had electrode gap spacings of 5, 7.5, and 12 µm. The following important observations were made:

(1) The microwave index is larger than the optical ridge waveguide mode index for all combinations of thickness and gap spacing

(2) The microwave characteristic impedance is smaller than 50 Ω for all devices.

(3) The microwave index and characteristic impedance are flat in the 15-50 GHz range. The index decreases rapidly between 10 MHz and 15 GHz while the impedance increases within the same range.

In addition to these observations, the following trends were observed with respect to electrode gap spacing and $BaTiO_3$ thickness:

(1) The microwave index decreases with increasing gap spacing and decreasing film thickness.

(2) The characteristic impedance decreases with decreasing gap spacing and increasing film thickness.

(3) The total microwave attenuation loss increases with decreasing gap spacing and increasing film thickness.

(4) The conductor loss dominates the total microwave attenuation loss for devices with narrower gap spacing on thicker $BaTiO_3$ films.

The electro-optic 3 dB bandwidth is a function of all the microwave properties discussed in this chapter. In particular, the electro-optic bandwidth is reduced due to mismatch between the microwave and optical mode indices, mismatch between the source and device impedances, and attenuation losses. The results discussed here show that all of these losses are larger for devices with narrower electrode gap spacing on thicker $BaTiO_3$ films. However, as discussed in Chapter 6, thicker film devices have larger electro-optic coefficients and larger electro-optic overlap factors, resulting in lower device modulation voltages. Thicker $BaTiO_3$ films on the order of 500 nm are also preferable for photonic crystal waveguide devices since thicker films provide a larger overlap between the photonic crystal structure and electro-optic medium. As such, it would be preferable to minimize the microwave losses of thick film devices. To do so, the following approaches could be taken:

(1) Optimize the electrode geometry with respect to gap spacing, width, and thickness to reduce the conductor loss coefficient.

(2) Reduce the microwave index and increase the characteristic impedance by depositing a low dielectric constant buffer layer between the electrodes and $BaTiO_3$ film.

(3) Reduce the total length of the device to minimize the length dependent losses, which include index mismatch and attenuation losses.

Approach 1 would require optimization of the function $\phi(g, w, t)$ in Eqn. 4.5 to minimize the conductor loss. It is noted that in using approach 1, the electrode geometry must fall within the specified ranges of validity found in reference such that the thickness is several times the microwave skin depth[50]. Thicknesses larger than 1 µm would require use of a thicker image reversal photoresist for lift-off and electroplating with a higher metal deposition rate. The second approach has been previously demonstrated for a 5 mm long $BaTiO_3$ modulator[140]; its application to shorter modulators, however, is limited since the half-wave voltage is necessarily higher in a shorter modulator. The third approach is the simplest, but it also results in an increase in the half-wave voltage. The second and third approaches could be applied to photonic crystal modulators, where the increase in the half-wave voltage caused by either the buffer layer or shorter electrodes is offset by the reduction in voltage due to electro-optic coefficient enhancement. The third approach in conjunction with photonic crystal waveguides is investigated theoretically in Chapter 7.

CHAPTER 5

$BaTiO_3$ Photonic Crystal Waveguides

5.1. Introduction

The interaction of near-infrared light with nanostructured waveguides using $BaTiO_3$ thin films was investigated through theoretical modeling and experiment. Photonic crystal waveguides with two different structures were investigated: hexagonal lattice, and line defect waveguides. The photonic crystal structures were designed using plane wave expansion (PWE) method to calculate the band structure and finite-difference time-domain (FDTD) modeling to simulate the passive wavelength-dependent transmission. The photonic crystal structures were patterned directly onto $Si_3N_4/BaTiO_3$ ridge waveguides using focused ion beam lithography. The transmission of the waveguides was measured using a continuous wave laser with tunable operation between 1500 and 1580 nm. The insertion loss, optical group index, and properties of the photonic crystal stop band were obtained from the measured transmission of hexagonal lattice photonic crystal waveguides. The measured properties and fabricated hole geometry observed in cross-section provided feedback to modeling to improve agreement with experiment. Excellent agreement in the wavelength-dependent transmission was obtained by accounting for the cross-sectional geometry of the milled holes. A stop band edge extinction of 23.5 dB was measured across a 25 nm span — a record for all nanostructured ferroelectric materials, demonstrating the potential of these waveguides for integrated optical filters. An average total insertion loss of 10 dB

and insertion loss per unit length of 0.289 dB/μm were measured outside the stop-band due to out-of-plane scattering in the photonic crystal region.

After demonstrating agreement between the simulated and measured properties of hexagonal lattice photonic crystal waveguides, the same simulation and fabrication techniques were used to design dispersion engineered line defect photonic crystal waveguides. Compared with the hexagonal lattice photonic crystal waveguides, line defect waveguides offer the advantage of tunable group index dispersion, which is of interest for applications requiring wavelength-independent operation such as dense wavelength division multiplexing. Waveguides having a moderate group index of approximately 16 over a wide (48 nm) optical bandwidth are demonstrated. This is the first known demonstration of dispersion engineered waveguides on a ferroelectric optoelectronic platform.

An understanding of the linear optical properties of the photonic crystal waveguides is an essential step toward investigating the effect of the photonic crystal structures on enhancing the Pockels effect. The experimental results obtained here are used to explain the measured Pockels coefficient enhancement discussed in the subsequent chapter through a model proposed in Section 5.7. The proposed model explains the electro-optic coefficient enhancement in $\chi^{(2)}$ photonic crystal waveguide modulators and is generalized for the case where the modulator consists of both ridge waveguide and photonic crystal waveguide segments within the total electro-optic interaction length. This model is based on a more general model proposed by Soljačić et al for the enhancement of nonlinear optical properties in photonic crystal waveguides[131,132]. According to the model of Soljačić et al, nonlinear optical properties such as the electro-optic coefficient are expected to be enhanced by a factor of $(n_{g,P}/n_{g,R})$, where $n_{g,P}$ is the optical group index of the photonic

crystal waveguide and $n_{g,R}$ is the optical group index of the ridge waveguide onto which the photonic crystal is patterned[65]. Using the model proposed in Section 5.7, $\chi^{(2)}$ photonic crystal modulators with a total photonic crystal length of 100 µm and group index of 25 are predicted to operate at half the voltage of an otherwise identical conventional modulator with a fourfold reduction in power. This model is used to further predict the ultimate performance of photonic crystal modulators in Chapter 7 in conjunction with the experimental microwave properties presented in Chapter 4.

5.2. Band Structure Calculations

Band structure calculations of the hexagonal lattice and line defect waveguides were done using the MIT Photonic Bands (MPB) *ab initio* simulation package on a UNIX computing platform (Linux Ubuntu). The three-dimensional geometry of the fabricated structures was approximated using a two-dimensional model. To represent the three-dimensional structure in two dimensions, the background medium was chosen to have an index equal to that of the waveguide mode calculated using a cross-sectional FDTD mode solver[96] (see Section 7.4). To simplify the analysis while providing useful information for the fabrication of devices, the only variable investigated for both the hexagonal lattice and line defect simulations is the ratio of hole radius (r) to lattice parameter (a).

For the line defect waveguides, the first row of holes was shifted inward by an amount equal to $0.124a$ to create a low dispersion region in $\omega(k)$. This parameter, as well as the shift of the second and third row of holes, could be further optimized to obtain a certain group index over a desired optical bandwidth[84,108]; a fixed first row hole shift was used here, however, in order to demonstrate proof-of-concept. Band structure simulations for

both hexagonal lattice and line defect geometries were done for r/a consistent with the hole geometry obtained from cross-sectional imaging of the fabricated photonic crystal structures.

The program MPB and its complementary FDTD solver, MEEP, are written such that they take advantage of the scale invariance of Maxwell's equations. This means that the simulation results for a given structure with a fixed geometry may be applied to other scaled representations of the same geometries by properly scaling the structure dimensions and wavelength. The units of the program are scaled to represent the scale invariance. The band structures are hence plotted as ω versus k where ω is in units of $2\pi c/a$ and k is in units of $2\pi/a$.

The unit cell, Brillouin zone, and high symmetry k-points are defined for the hexagonal lattice PC in Fig. 5.1. The band structure of the hexagonal PC was computed by exciting a dipole source within the unit cell to excite the eigenmodes, from which the allowed bands are calculated. The band structure of a hexagonal lattice PC with r/a ratio of 0.22 is shown in Fig. 5.1 (b). This ratio represents that obtained from the cross-section of fabricated structures for the majority of the fabricated hexagonal lattice PC waveguides. Light lines are drawn for air cladding and the MgO substrate (index of 1.7). For combinations of ω and k lieing between the air and substrate light lines, light will be guided in both the waveguide and the substrate[101]. This region is a lossy region since the light is not strictly confined to the waveguide. Two light red horizontal bands are drawn representing the omnidirectional TE bandgaps obtained for all k-vectors. The bottom of the upper band represents the band edge used for the hexagonal lattice waveguides in this work. For a lattice parameter of 770 nm, the corresponding wavelength of the band edge is 1546 nm. Compared with

the lower TE bandgap, the upper one also contains a complete TM bandgap, which is desirable for polarization-insensitive devices; however, the upper bandgap is within the lossy region. Lower losses could be obtained experimentally by choosing a smaller lattice parameter to access the bottom band gap at telecommunication wavelengths. While only the transmission of TE polarized light was investigated for the fabricated structures in this work, the same measurements could be performed using TM polarization. The hexagonal lattice PC were fabricated onto ridge waveguides such that light propagates in the $\Gamma - M$ direction. This was done in order to use the same techniques employed for silicon photonic crystal waveguides to engineer the dispersion of slow light[84]. In these waveguides light is confined horizontally — or equivalently prevented from propagating in the $\Gamma - K$ direction — by index guiding via the ridge waveguide structure. The relevant portion of the band structure is hence that between Γ and M. An enlarged diagram of the band structure between these two high symmetry points is given in Fig. 5.1 (c). For these wavevectors, the expected bandgap is between frequencies of 0.498 and 0.546 (a/c), where a is the lattice parameter and c is the speed of light in free space.

The band structure for TE polarized light was similarly calculated for the W1 line defect waveguides. For this type of PC, the supercell shown in the inset in Fig. 5.2 (a) was used in order to include the defect structure. Since the unit cell is elongated in the direction perpendicular to the line defect, the Brillouin zone is made artificially smaller and a larger number of bands need to be calculated in order to show the full picture of the band structure. A total of 20 bands were calculated for the W1 structure versus 6 for the hexagonal structure. The resulting band structures for k_x between 0.25 and 0.5 ($2\pi/a$) are shown in Fig. 5.2 (a) - (c) for r/a ratios of 0.22, 0.24, and 0.28. In these plots, the

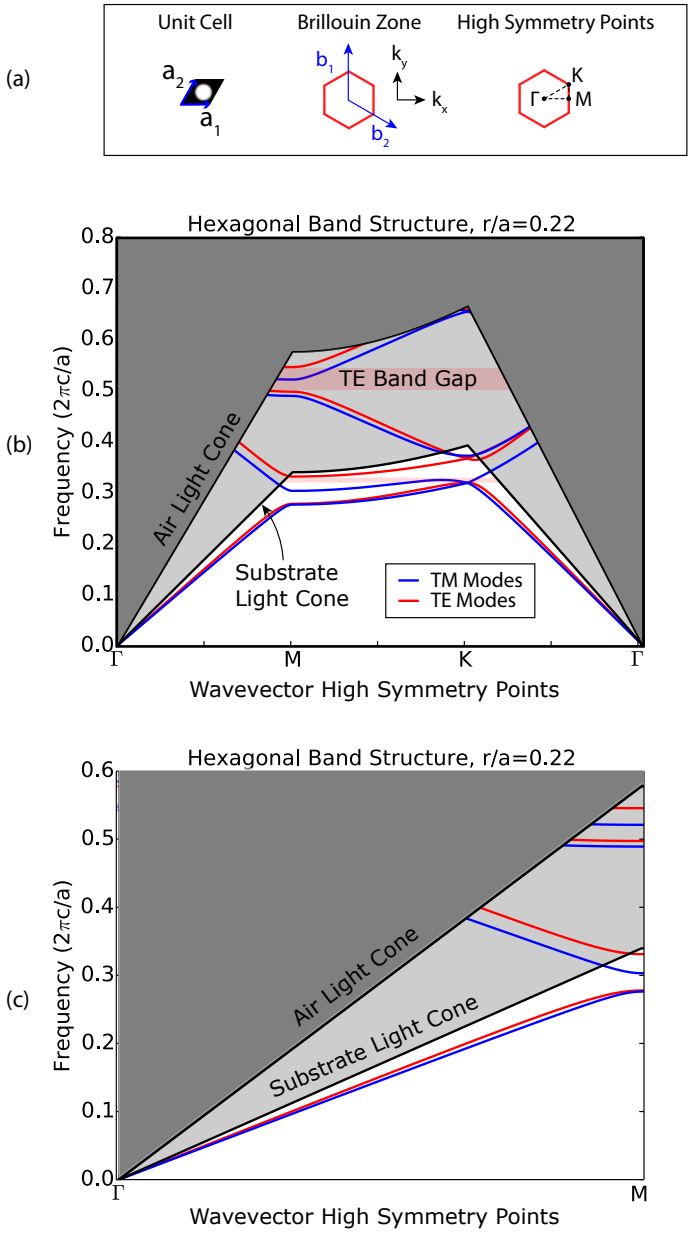

Figure 5.1. (a) Definition of the unit cell, Brillouin zone, and high symmetry points for the haxagonal 2D lattice. (b) Calculated band structure for the hexagonal lattice photonic crystal. (c) Magnified view of the band structure between the Γ and M points.

light cones are again shown corresponding to both the air and substrate. The gray region between the substrate and air light cones is a lossy region in which modes are guided in both the waveguide core and substrate but do not couple to the air region above[101]. The region bounded by the projected bands from the hexagonal lattice are shaded red. The defect mode band is colored blue, and the gap region is the unshaded region between the upper and lower red bands. For all r/a ratios, the defect mode is within the lossy region. This does not prevent guiding in the line defect mode, but limits the practical length of devices that can be used for measurements since in longer devices, light will couple from the waveguide to the cladding. For increasing r/a ratio, the gap becomes larger and the defect band is pulled further down from the high frequency band edge. For ratios of 0.22 and 0.24, the defect line in the lossy region is degenerate with the upper band edge in the non-lossy region over a small range of frequencies; this degeneracy is lifted for larger ratios.

For the application of modulators, the most important property obtained from the band structure is the group index, defined as $c(d\omega/dk)^{-1}$, where $c$is the speed of light in free space. It is calculated in the units used by MEEP as $(d\omega/dk)^{-1}$. The group index is plotted versus wavelength for line defect waveguides with a fixed lattice constant of $a = 530$ nm and r/a ratio between 0.18 and 0.28 in Fig. 5.2 (d). The group index is plotted for k_x between the lightcone and M. For a fixed lattice constant, the optical bandwidth of the defect mode decreases with increasing r/a, corresponding to a flattening of the defect band in the $\omega(k)$ diagram. This coincides with an increase in the group index. For the smallest r/a of 0.18, there is a spike in the group index near the long wavelength edge near 1745 nm. This spike is flattened into a plateau for larger r/a. The plateau region, over which the group index attains a moderately large and nearly constant value over a finite

optical bandwidth, is desirable for use in PC modulators to provide flexible operation over a finite bandwidth and to minimize signal distortion[19,167]. The curves shown in Fig. 5.2 (d) show the expected variation in group index with hole depth, which affects the hole radius as discussed in Section 5.4.2. The resonances of the group index for r/a of 0.18 and 0.20 arise from the enhanced interaction of the defect mode with the photonic crystal structure, in particular the shifted first row of holes, at certain frequencies[45].

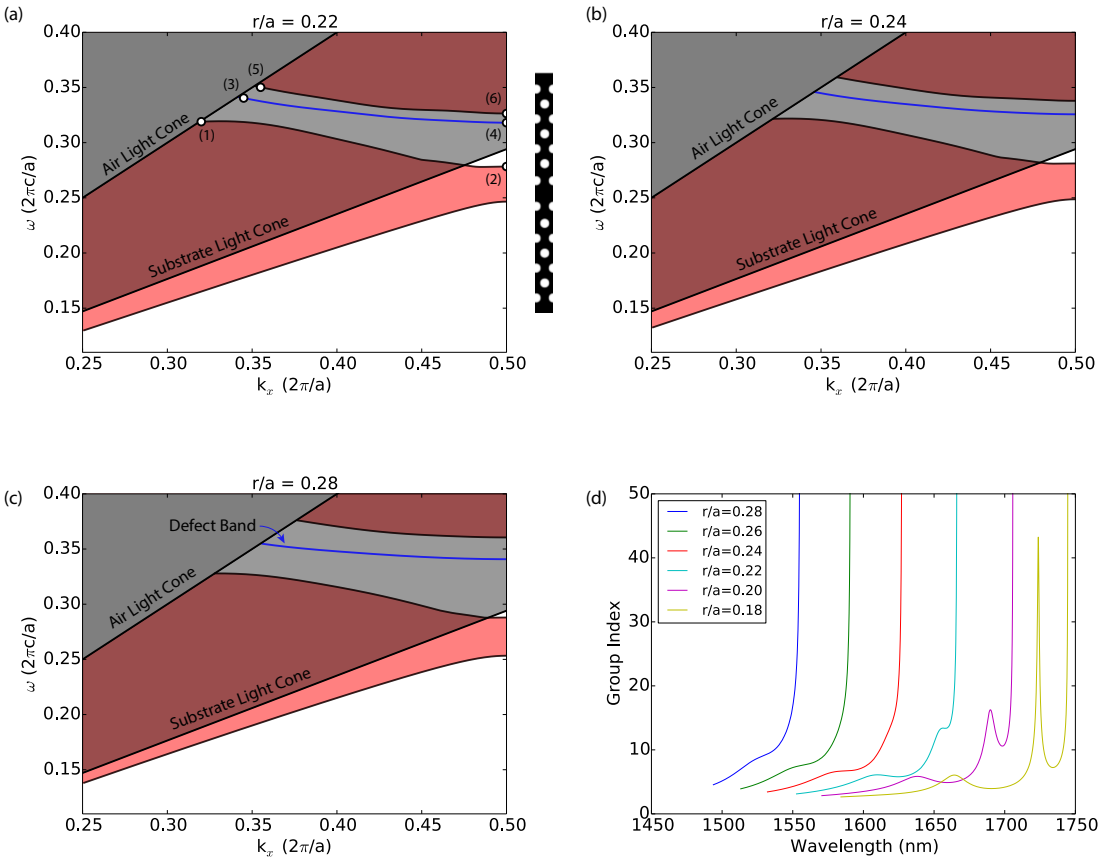

Figure 5.2. Calculated band structures of W1 line defect photonic crystal waveguides with r/a ratios of 0.22 (a), 0.24 (b) , and 0.28 (c) for propagation in the k_x direction. (d) Calculated group index for r/a between 0.18 and 0.28.

The calculated eigenmodes for various points in the band structure in Fig. 5.2 (a) are plotted in Fig. 5.3. The numbers next to each field profile correspond to the number in Fig. 5.2 (a). The H_z component of the field is plotted for TE excitation. The H_z field components are plotted at allowed k vectors corresponding to the first allowed frequency adjacent to the light cone and those at the Brillouin zone edge where the group index is the largest. The most important feature of these plots is that the optical field is not localized to the line defect region, which is due to guiding within the lossy region. While this would be an issue for cases where field confinement is required for nonlinear optical enhancement, this is not the case for enhancement of the Pockels effect where the enhancement depends only on the slowdown factor $S = (n_{g,P}/n_{g,R})$, where $n_{g,P}$ is the group index of the photonic crystal and $n_{g,R}$ is the group index of the ridge waveguide. While the optical field is not confined horizontally within the line defect, it is confined horizontally by the ridge waveguide structure. The delocalized fields shown in Fig. 5.3 are hence not an issue for electro-optic coefficient enhancement but indicate that the mode is not optimally confined. The confinement could be improved by either using the $BaTiO_3$ films as a suspended membrane with air cladding both above and below or by further optimizing the structure to shift the defect mode and band gap away from the substrate light line. This cannot be done by only changing the lattice constant since the plotted band diagrams are independent of the choice of lattice parameter; the value for the lattice parameter only sets the operating wavelength. It is especially important to note that, while the defect line mode is lossy, any measured enhancement of the electro-optic coefficient of devices using these waveguides necessarily comes from light that is slowed down by the photonic crystal and guided within the $BaTiO_3$ film since the MgO substrate has cubic symmetry

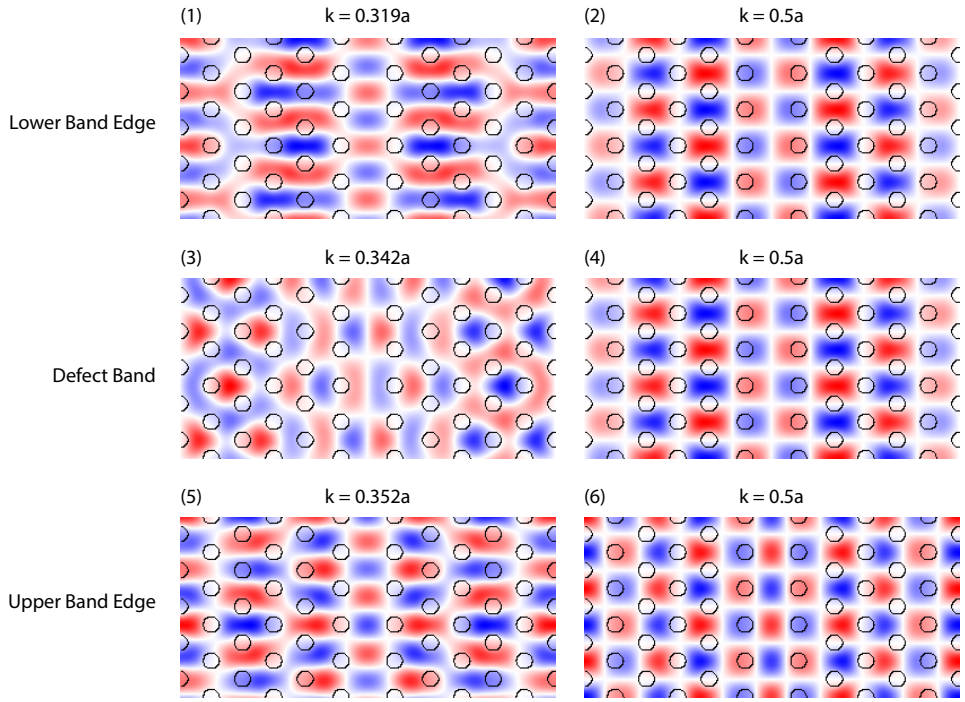

Figure 5.3. Calculated mode profiles corresponding to the points in the band structure in Fig. 5.2 (c).

and hence does not contribute to electro-optic modulation. Similarly, the Si_3N_4 ridge is amorphous and also lacks $\chi^{(2)}$ properties.

5.3. Finite-Difference Time-Domain Modeling

The transmission properties of the photonic crystal waveguides were calculated using the finite-difference time-domain method. The modeling was done using the software MIT MEEP[67] on a UNIX computing platform (Linux Ubuntu). Modeling in two-dimensions was found to provide good agreement between the simulated and measured transmission. To represent the three-dimensional structure in two dimensions, the background medium was chosen to have an index equal to that of the waveguide mode calculated using a cross-sectional FDTD mode solver (see Section 7.4).

The simulation geometries for the hexagonal lattice and photonic crystal waveguides are shown in Fig. 5.4. The geometry used for the hexagonal lattice simulations is identical to that patterned onto the ridge waveguides. For the line defect waveguides, the tapered regions were omitted since these do not contribute significantly to the slow light properties. Perfectly matched layer boundary conditions were used on all boundaries of the simulation region in order to eliminate the effect of spurious reflections on the transmission.

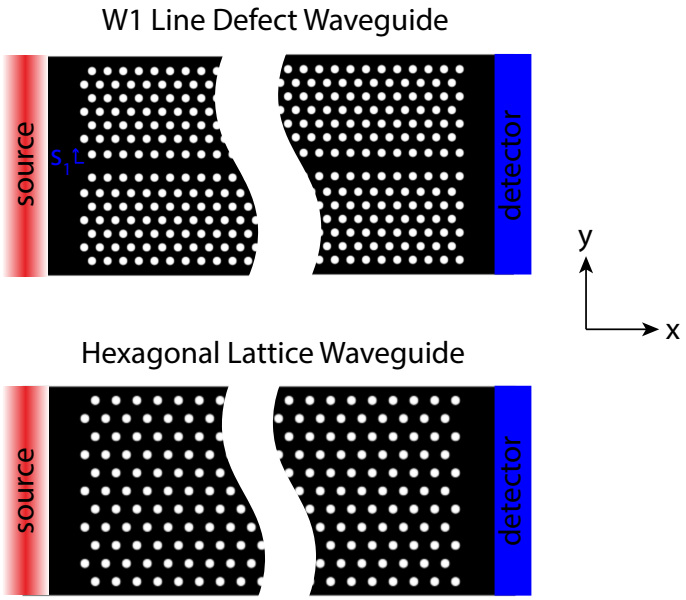

Figure 5.4. Simulation geometry for the line defect and hexagonal lattice photonic crystal waveguides.

The transmission through the structures in the x direction was calculated using a Gaussian pulse source. The source was excited at the position shown in Fig. 5.4 with Poynting vector in the x direction. The frequency (wavelength) dependent transmission was calculated by exciting the structure with a pulse source with an appropriate center frequency and span. A Gaussian pulse with pulse center frequency of 0.4 c/a and pulse

width of 0.3 c/a was used for simulations of both structures. The frequency-dependent transmission was calculated from the Fourier transform of the light transmitted through the structure after the field had decayed by a factor greater than 10^3 at the center of the simulation region. A uniform grid spacing of 20 pixels/a was used for the simulations of both structures. The time step was on the order of 0.01 a/c for both structures with a total required number of time steps on the order of 10^3. The simulation parameters for both structures are given in Tables 5.1 and 5.2.

Table 5.1. Parameters used for the hexagonal lattice FDTD simulations using MEEP.

Parameter	Value	Unit
Time Step	0.007	a/c
Simulation Time	207	a/c
Number of Time Steps	28×10^3	-
Pulse Center Frequency	0.5	c/a
Pulse Width	0.4	c/a
Grid Spacing	20	pixels/a

Table 5.2. Parameters used for the line defect FDTD simulations using MEEP.

Parameter	Value	Unit
Time Step	0.01	a/c
Simulation Time	500	a/c
Number of Time Steps	20×10^3	-
Pulse Center Frequency	0.4	c/a
Pulse Width	0.4	c/a
Grid Spacing	20	pixels/a

The simulated transmission spectra of the hexagonal lattice PC waveguides are summarized in the plots in Fig. 5.5. The transmission spectra are plotted for varying r/a ratio with a fixed lattice constant of a= 777 nm (Fig. 5.5 (a) and (b)) and for varying lattice

parameter for fixed r/a ratio (Fig. 5.5 (c) and (d)). As discussed in Section 5.4.2, the effective hole radius increases with hole depth due to the non-vertical sidewall angle of the holes fabricated with ion beam lithography. The varying r/a ratio hence represents the expected variation in the transmission for structures milled with different hole depths but with the same nominal hole radius. For a given hole depth, the position of the stop-band edge can be tuned by varying the lattice parameter. The simulations with varying lattice parameter with constant r/a ratio are hence applicable to the case where the hole depth, related to the total ion beam dose, is kept constant and the lattice parameter is tuned.

The wideband simulated transmission spectra for hexagonal PC waveguides with varying r/a ratio is given in Fig. 5.5 (a). Both the short and long wavelength band edges of the photonic band gap are blue shifted for increasing r/a. This follows from the simple relation $\lambda_0 \nu / n = c_0$, where λ_0 is the free space wavelength, ν is the frequency, n is the refractive index, and c_0 is the speed of light in vacuum. For increasing r/a, the effective refractive index of the guided modes decreases, hence the transmission spectra is blue-shifted. As shown in the magnified image of the long wavelength band edge in Fig. 5.5 (b), a change in r/a from 0.2 to 0.23 results in a approximately a 40 nm blue-shift of the transmission spectra. The range of r/a for the fabricated hexagonal lattice PC waveguides for a given lattice constant is between 0.210 and 0.224. The variation in the measured band edge was therefore expected to be within 40 nm.

The variation in the transmission with lattice parameter is shown in Fig. 5.5 (c) and (d). The wideband transmission plotted in Fig. 5.5 (c) shows a red-shifting of the transmission spectra with increasing lattice constant. This result is due to the scale invariance of Maxwell's equations. The magnified image of the long wavelength band edge in Fig. 5.5

(c) shows that the band edge is tunable by approximately 50 nm for an increase in lattice constant from 755 to 800 nm. In this study, the lattice parameter of fabricated structures was tuned between 740 and 777 nm, hence the measured band edge was expected to be between 1500 and 1600 nm.

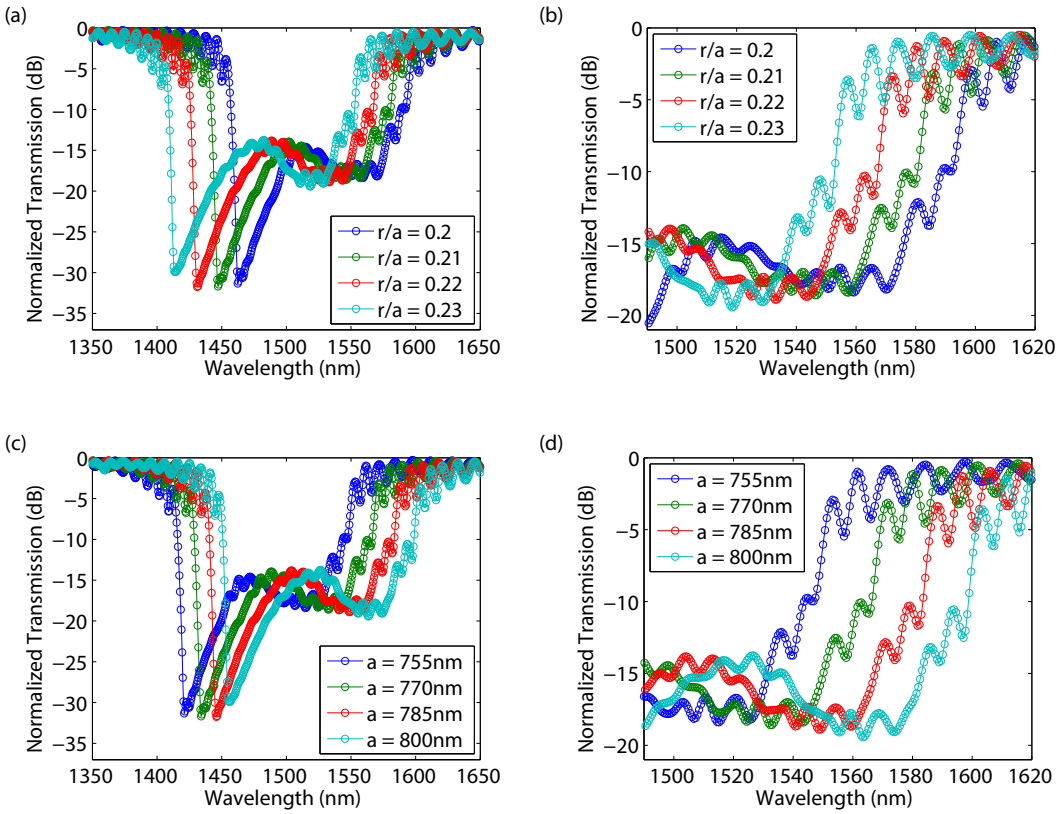

Figure 5.5. (a) Simulated transmission of hexagonal lattice photonic crystal waveguides for varying r/a ratio with fixed lattice constant of 777 nm. (b) Magnified view of (a) showing the long wavelength band edge. (c) Simulated transmission of hexagonal lattice photonic crystal waveguides for varying lattice parameter with fixed r/a of 0.2. (d) Magnified view of (c) showing the long wavelength band edge.

The simulated transmission spectra of the W1 line defect PC waveguides are summarized in Fig. 5.6. For the W1 waveguides, the effect of varying r/a ratio for two different lattice

parameters was considered. The wideband simulated transmission for a lattice constant of 530 nm is shown in Fig. 5.6 (a). The lattice constant of 530 nm positions the defect band calculated in Fig. 5.2 at a wavelength of 1550 nm. As observed in the case for the hexagonal lattice PC waveguides, the transmission spectra blue-shifts with an increase in r/a. As shown in Fig. 5.6 (b), the transmission for $a = 530$ nm is nearly constant in the wavelength range 1500-1600 nm with a roll-off in the transmission toward the long wavelength range. A lattice parameter of 730 nm positions a long-wavelength band edge within the optical C band (Fig. 5.6 (c)). The expected variation in the measured transmission is shown for $a = 730$ nm in Fig. 5.6 (d), which shows an approximately 40 nm shift with r/a between 0.18 and 0.22. Line defect waveguides with lattice parameters of 530 and 730 nm were both fabricated and characterized, as discussed below.

5.4. Fabricated Photonic Crystal Geometry

5.4.1. Hexagonal Lattice and Line Defect Structures

The photonic crystals were milled into the $BaTiO_3$ thin films using focused ion beam lithography. Details on the fabrication technique are given in Section 3.4.2. Representative SEM images of the fabricated hexagonal lattice photonic crystal waveguides are given in Fig. 5.7. As shown in the images, the photonic crystals were directly milled onto $Si_3N_4/BaTiO_3/MgO$ ridge waveguides. The ridge waveguides had widths of 2, 3, 4, 5, and 7 µm. The photonic crystals were milled onto both stand-alone ridge waveguides (Fig. 5.7 (a) and (d)) and modulators consisting of ridge waveguides between coplanar stripline electrodes (Fig. 5.7 (b) and (c)). All photonic crystals with measured transmission (see Section 5.5) had lengths of 44 unit cells; however, to demonstrate the ability to fabricate

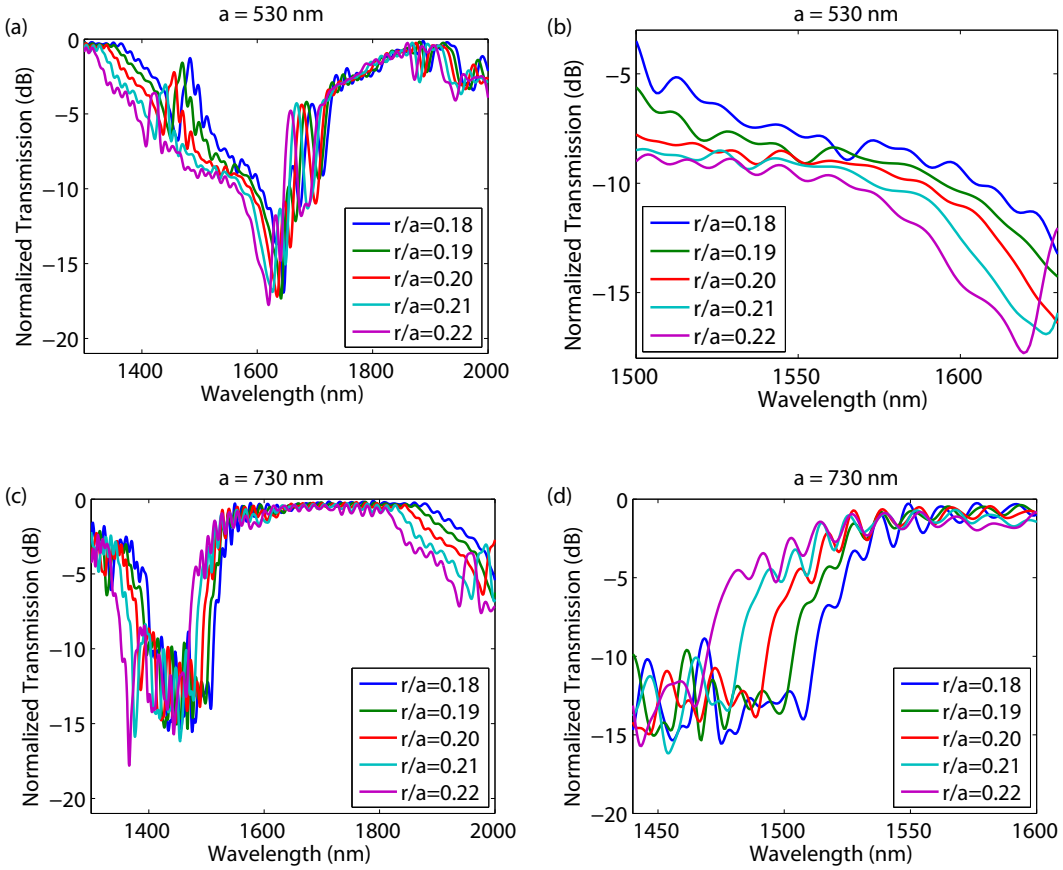

Figure 5.6. (a) Simulated transmission of W1 photonic crystal waveguides for varying r/a ratio with fixed lattice constant of 530 nm. (b) Magnified view of (a) showing the short wavelength band edge. (c) Simulated transmission of W1 photonic crystal waveguides for varying r/a ratio with a fixed lattice constant of 730 nm. (d) Magnified view of (c) showing the long wavelength band edge in the optical C band.

longer structures, photonic crystals as long as 308 µm were fabricated. A 308 µm long photonic crystal is shown in Fig. 5.7 (d) along with magnified images of top and bottom of the waveguide in Fig. 5.7 (e) and (f). The calculated angular misalignment is 0.002°. The hexagonal lattice photonic crystals were fabricated on films with thicknesses between

260 and 500 nm. A summary of all of the hexagonal lattice photonic crystals fabricated is given in Tables 5.8-5.12.

Representative SEM images of the line defect waveguides are shown in Fig. 5.8. The line defect waveguides were fabricated on $BaTiO_3$ films with 500 nm thickness. Line defect waveguides were fabricated both on independent waveguides (Fig. 5.8 (d)) and ridge waveguide modulators (Fig. 5.8 (a)). Compared with the hexagonal lattice waveguides, the line defect waveguides confine light horizontally within the line defect (Fig.5.8 (c)) via photonic band gap guiding; as such, it was necessary to couple light from the wider ridge waveguide mode into the narrow line defect region. The ridge waveguide region has a width on the order of microns while the line defect region has a width on the order of 500 nm. The coupling from the ridge waveguide mode to the line defect mode was achieved by incorporating tapered transition regions (Fig. 5.8 (d)). The tapered transition region between the ridge and photonic crystal modes consists of 40 unit cells with the holes displaced outward by $0.25a$ per row.

5.4.2. Geometry of Fabricated Structures

A common issue with focused ion beam lithography is that the fabricated structures have a tapered sidewall due to redeposition of sputtered material[151,22]. The three dimensional geometry of the fabricated photonic crystal structures was investigated by milling a trench into the structures and viewing the cross-section of the milled holes. Details on the cross-sectional milling are given in Section 3.4.2. The two parameters of interest from the cross-section are the hole depth and sidewall angle. Both of these parameters determine the effective hole radius, defined as the equivalent radius in a two-dimensional representation,

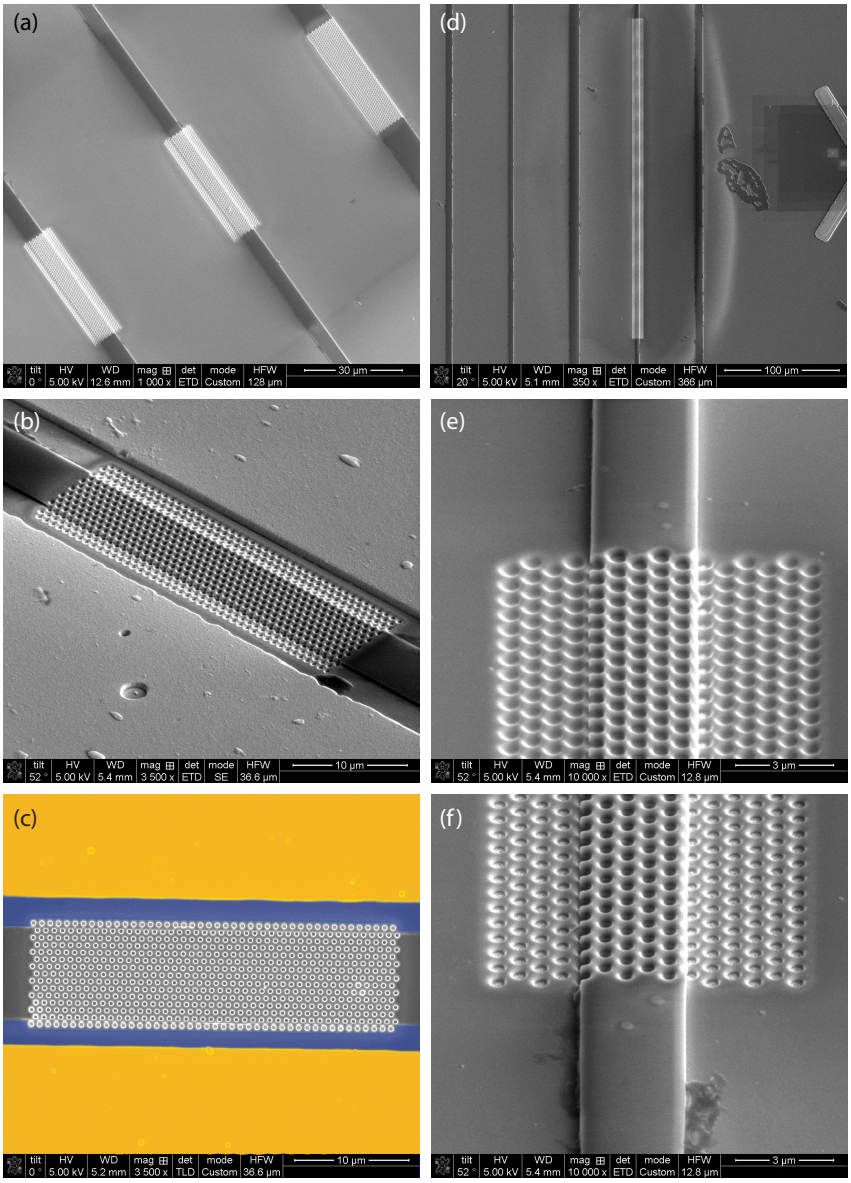

Figure 5.7. SEM images of hexagonal lattice photonic crystal waveguides. (a) Top angled view of three adjacent waveguides. (b) Top angled view of a hexagonal lattice photonic crystal waveguide modulator. (c) Top view of a modulator with the $BaTiO_3$ film colored blue and the electrodes colored gold. (d) Top angled SEM image of a 308 µm long photonic crystal. Magnified views of the the top and bottom of the waveguide are shown in (e) and (f), respectively, showing excellent alignment across a length of 308 µm.

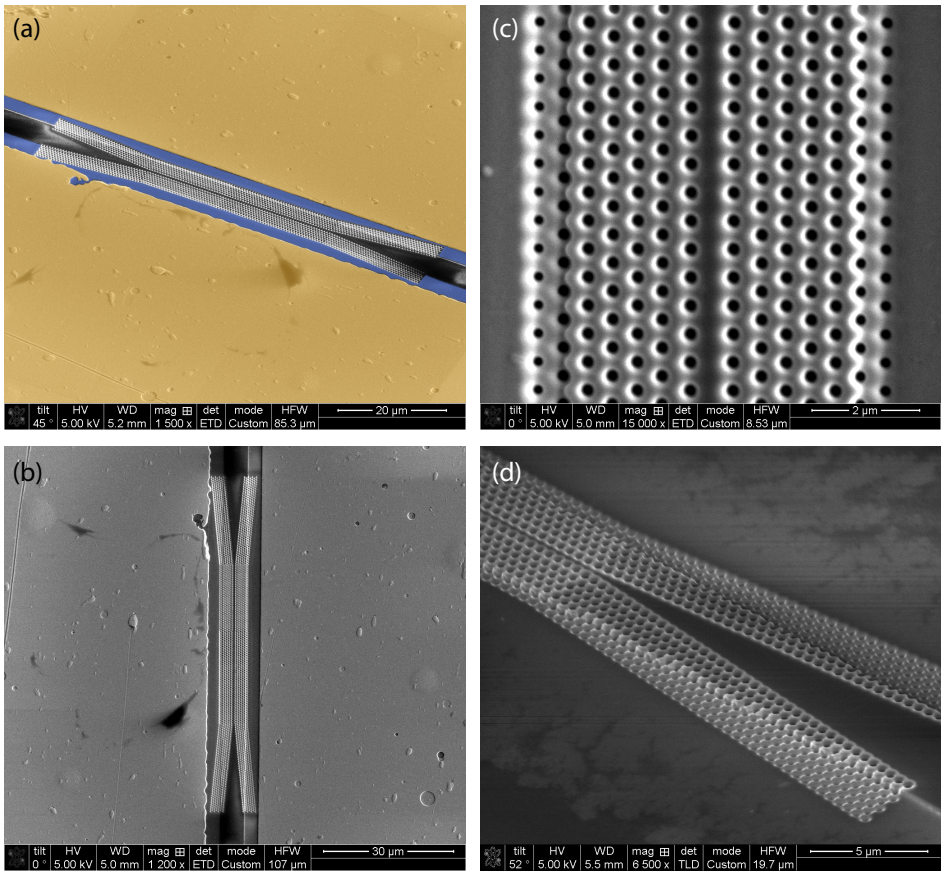

Figure 5.8. SEM images of the line defect waveguides. (a) Top angled view of a line defect modulator with the $BaTiO_3$ film colored blue and the electrodes colored gold. (b) Top view of the modulator. (c) Magnified view of the straight region of the line defect waveguide. (d) Top angled view of the tapered region.

which affects the transmission properties. As such, an experimental investigation of the milled hole geometry was necessary for improving the agreement between the experimental and simulated transmission properties.

The photonic crystal structures were milled using two different conductive coatings: a chromium layer with sacrificial polymethlmethacrylate (PMMA) lift-off underlayer, and a PEDOT:PSS coating. The advantages and disadvantages of each coating are further

discussed in Section 3.4.2 and the steps for applying both coatings are given in Section A.7. The choice of coating affects both the required total ion beam dose or sputtering time and the fabricated hole geometry. Representative cross-sectional images of identical holes milled with both coatings are given in Fig. 5.9. Details on creating and imaging the cross-sections are given in Section A.8.3. As shown in Fig. 5.9, the holes milled with the Cr/PMMA coating have a flatter region between holes, even when the hole depth is deeper. This is presumably due to the chromium acting as a better sacrificial layer to protect the underlying material. Since the patterning is rastered, the region between holes is subject to the tail of the Gaussian ion beam profile. According to the cross-sectional images, it appears that the chromium layer is less susceptible to erosion by the ion beam tail than is the conductive polymer coating.

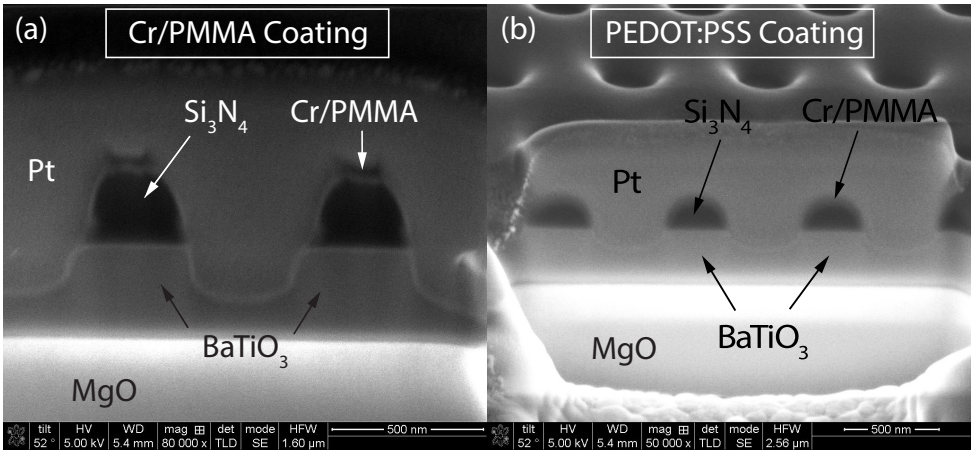

Figure 5.9. Cross-sectional image of the photonic crystal structure fabricated with (a) PEDOT:PSS conductive coating and (b) Cr/PMMA conductive coating.

A schematic of the cross-sectional geometry representing the imaged cross-sections of Fig. 5.9 is given in Fig. 5.10. In this schematic, several geometrical parameters are defined, including the sidewall angle α, the bottom and top hole diameters d_1 and d_2, respectively,

the hole depth h, and the film thickness t. The cross-sectional images show that the holes have a conical shape with a nearly flat bottom. Below a certain dose threshold, the holes do not fully penetrate the $BaTiO_3$ film. In order to compare the simulated to measured transmission, an effective two-dimensional hole radius is needed. This is obtained by considering the hole in the $BaTiO_3$ film as a conical cylinder of air with minimum diameter d_1, hole depth h, and sidewall angle α. Using this geometry, the average or effective hole radius of the conical cylinder is

$$d_{cyl,eff} = d_1 + \frac{h}{2}\tan\alpha \tag{5.1}$$

The effect of the finite hole depth is not considered in the calculation for effective hole diameter since the holes have a flat bottom and the un-structured region below the holes does not contribute to the band-like transmission properties that are imparted by the photonic crystal. Instead, it is expected that shallower holes would result in a lower extinction of light across the photonic crystal band edge. This is experimentally verified in Section 5.5 below. According to Eqn.5.1, the hole diameter for a representative two dimensional structure can be calculated from knowledge of the hole depth, bottom hole diameter, and sidewall angle.

The hole depth was measured as a function of total applied ion beam dose for samples coated with both conductive coatings. A simple model to describe the hole depth versus ion beam dose D is briefly derived here. The total linear hole depth versus applied dose is

$$h_{total} = r_1 D_1 + r_2 D_2 \tag{5.2}$$

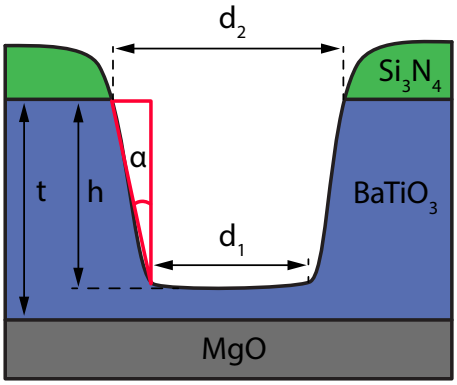

Figure 5.10. Schematic of the cross-sectional hole geometry.

where r_1 is the rate at which the coating and Si_3N_4 are etched, D_1 is the ion beam dose used to mill through the coating and Si_3N_4 layer, and r_2 and D_2 are the corresponding milling rates and ion beam dose for the $BaTiO_3$ film. For a total ion beam dose D, the hole depth is

$$h_{total} = D(r_1 f_1 + r_2 f_2) \tag{5.3}$$

where $f_1 \equiv D_1/D$ and $f_2 \equiv D_2/D$ are the fractions of the total ion beam dose used to mill through the coating/Si_3N_4 and $BaTiO_3$ layers, respectively. The variables f_1 and f_2 are defined as follows:

$$f_1 = \begin{cases} 1 & \text{for } D \le D_1 \\ \frac{D_1}{D} & \text{for } D > D_1 \end{cases} \quad \text{and} \quad f_2 = \begin{cases} 0 & \text{for } D \le D_1 \\ \frac{D-D_1}{D} & \text{for } D_1 < D \le D_1 + D_2 \\ \frac{D_2}{D} & \text{for } D > D_1 + D_2 \end{cases}$$

For an ion beam dose less than that required to mill through the conductive coating and Si_3N_4 — i.e., for a dose less than D_1 — only this layer is exposed to and sputtered by the

ion beam; for doses between D_1 and $D_1 + D_2$, the conductive coating, Si_3N and $BaTiO_3$ layers are milled, with the fraction of total dose used to mill the $BaTiO_3$ film increasing with total dose. For doses larger than $D_1 + D_2$, the underlying substrate is also partially milled; at this point, the fraction of the total dose required to mill through the $BaTiO_3$ layer starts to decrease. These dependences of f_1 and f_2 on the total dose D are shown graphically in Fig. 5.11 (a). The data is plotted for arbitrary values of milling rates $r_1 = 10 \times 10^3\,\mu m^3/s$ and $r_2 = 5 \times 10^3\,\mu m^3/s$ and for a total Si_3N_4/coating thickness of 200 nm and $BaTiO_3$ thickness of 500 nm. The total amounts of Si_3N_4 and $BaTiO_3$ milled through versus total dose are calculated as $h_1 = r_1 f_1 D$ and $h_2 = r_2 f_2 D$, respectively, and are plotted in 5.11 (b) for the same parameters used in (a). As shown in Fig. 5.11 (b), the depth into each layer is linear with applied dose. Using this model, it is therefore possible to fit a line to the measured hole depth into the $BaTiO_3$ film for different total ion beam doses, from which the sputtering rate of $BaTiO_3$ and a calibration curve for hole depth versus applied dose can be calculated. The total required ion beam dose to mill through the conductive coating and Si_3N_4 layers (D_1) is obtained from the x-intercept, from which the milling rate r_1 is determined through Eqns. 5.2 and 5.3. The milling rate of $BaTiO_3$ is obtained from the slope of the line.

Cross-sectional images of hole arrays milled with PEDOT:PSS and Cr/PMMA conductive coatings are given in Fig. 5.12 and 5.13, respectively. The procedure for milling the cross-sections is illustrated in Fig. 5.12. In this figure, panel (a) shows three arrays of holes milled with 4, 6, and $8\,mC/cm^2$ doses. The distortion in the SEM image is due to sample charging and increases toward the right, in the direction of increasing ion beam dose. Panel (b) shows a close-up image of the pattern milled with $8\,mC/cm^2$ dose. Some

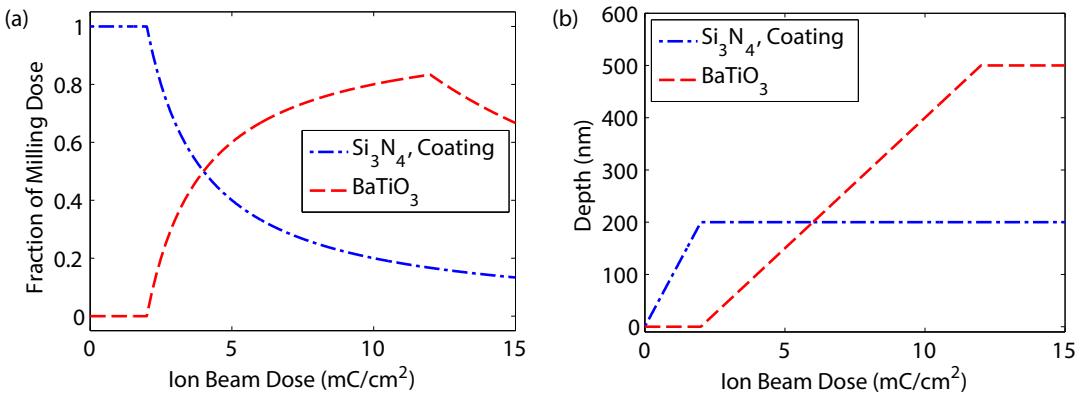

Figure 5.11. (a) Fraction of the total applied ion beam dose used to mill through the Si_3N_4 and $BaTiO_3$ layers versus total ion beam dose. (b) Depth milled into the Si_3N_4 and $BaTiO_3$ layers versus total ion beam dose. The calculations are done for 200 nm thick Si_3N_4 and 500 nm thick $BaTiO_3$.

astigmatism in the pattern is noted; however, this is not expected to significantly affect the sputtering rate and hole depth. Before milling the cross-section, the pattern is covered *in situ* with platinum (panel (c)). The cross-sections of the three patterns are shown in panels (d) through (f) with measurements taken with the microscope software. The depths of the holes into the $BaTiO_3$ film obtained from the cross-sectional images are plotted versus ion beam dose in Fig. 5.14 as red squares, and the linear fit to the data is plotted as the red dashed line. The measured hole depth into the $BaTiO_3$ film from the cross-sectional images in Fig. 5.13 is also plotted in Fig. 5.14 as blue circles, with the corresponding linear fit plotted as a blue dash-dot line. As shown in Fig. 5.14, the data is well fit to a line with R^2 values of 0.95 and 0.96 for the Cr/PMMA and PEDOT:PSS data, respectively. The calibration curves are the following:

$$\text{PEDOT:PSS: } h_{\text{BTO}} = 52D - 59 \quad [\text{nm}] \tag{5.4}$$

$$\text{Cr/PMMA: } h_{\text{BTO}} = 54D - 250 \quad [\text{nm}] \tag{5.5}$$

where D is the dose in mC/cm^2. The milling rates obtained from the linear fits are given in Table 5.3 in units of µm^3/µC. The milling rate through the PEDOT:PSS/Si_3N_4 layers is nearly twice as fast as that through the Cr/PMMA/Si_3N_4 layers. The mean volumetric milling rate through the $BaTiO_3$ film is 5.3×10^3 µm^3/µC.

Table 5.3. Empirically determined ion beam milling rates.

Layer	Milling Rate (µm^3/µC)
Cr (30 nm) / PMMA (50 nm) / Si_3N_4 (200 nm)	5.9×10^3
PEDOT:PSS (10 nm) / Si_3N_4 (110 nm)	11×10^3
$BaTiO_3$ (Cr/PMMA coating)	5.4×10^3
$BaTiO_3$ (PEDOT:PSS coating)	5.2×10^3

The cross-sectional images shown in Fig. 5.13 were additionally used to analyze the hole sidewall angle and to calculate the effective hole diameter versus ion beam dose. The measured bottom hole diameter, top hole diameter, hole depth, and sidewall angle are given for each of the three ion beam doses in Table 5.4. Two important observations are noted: 1) the bottom hole diameter is equal to the nominal hole diameter set by the GDSII file used to mill the pattern, and 2) the sidewall angle is nearly constant with depth, with an average value of 12°. In previous work, it was noted that the bottom hole diameter was smaller than the nominal value[81]; it is not difficult, however, to incorrectly underestimate the bottom hole diameter since its maximum value is measured only when the cross-sectional plane intersects the conical cylinder of the hole exactly at its center. Using the measured geometrical parameters and Eqn. 5.1, the effective hole diameter is calculated and given in the last column of Table 5.4. Since the diameter at the bottom of the hole is the smallest and equal to the nominal diameter, the effective diameter is always larger than the nominal value. Using the two observations noted above and Eqn.

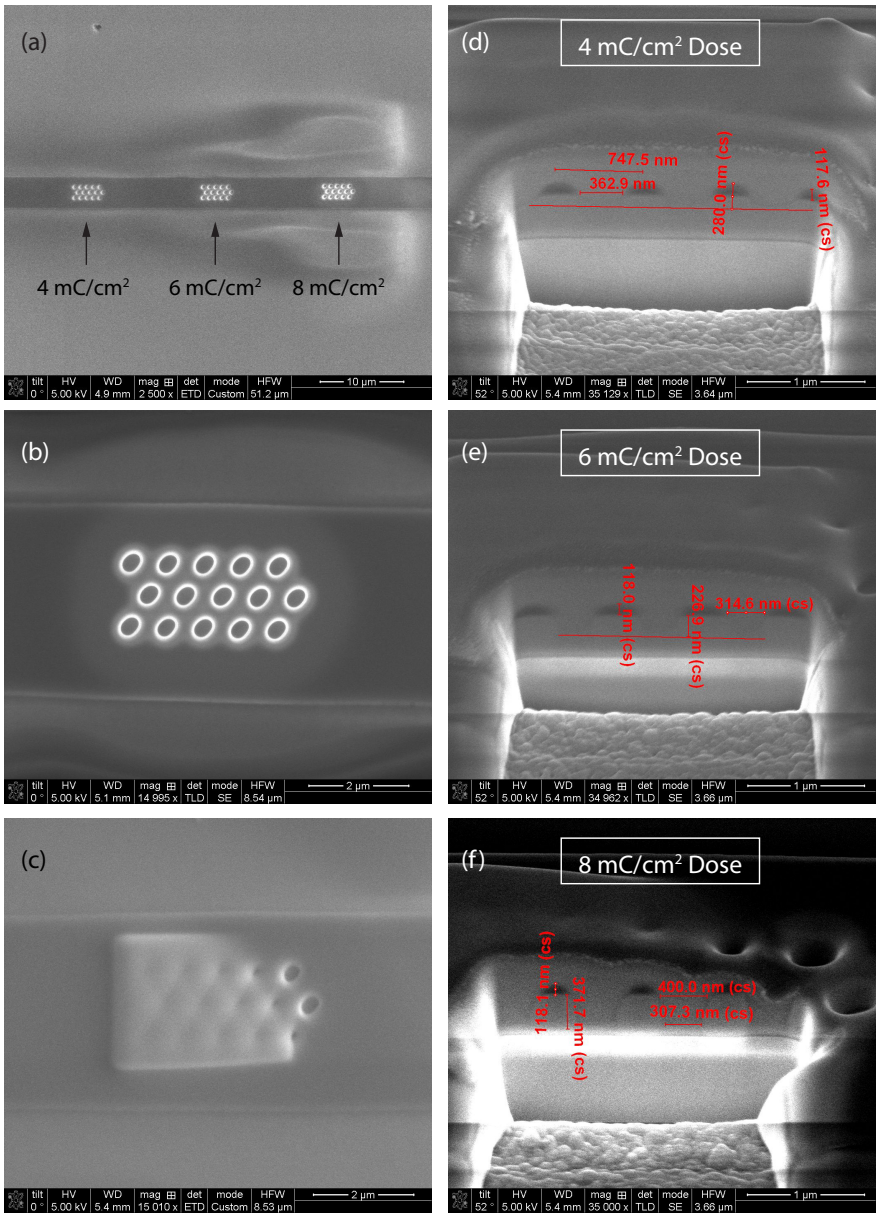

Figure 5.12. Analysis of the cross-sectional geometry of holes milled onto $Si_3N_4/BaTiO_3$ waveguides using PEDOT:PSS as the conductive coating. (a) SEM top view image of three arrays of holes milled with 4, 6, and 8 mC/cm^2 dose. (b) Magnified view of the pattern milled with 8 mC/cm^2 dose. (c) The 8 mC/cm^2 dose pattern covered with 300 nm of Pt deposited *in-situ*. (d)-(f) Cross-sectional images of the 4, 6, and 8 mC/cm^2 dose patterns.

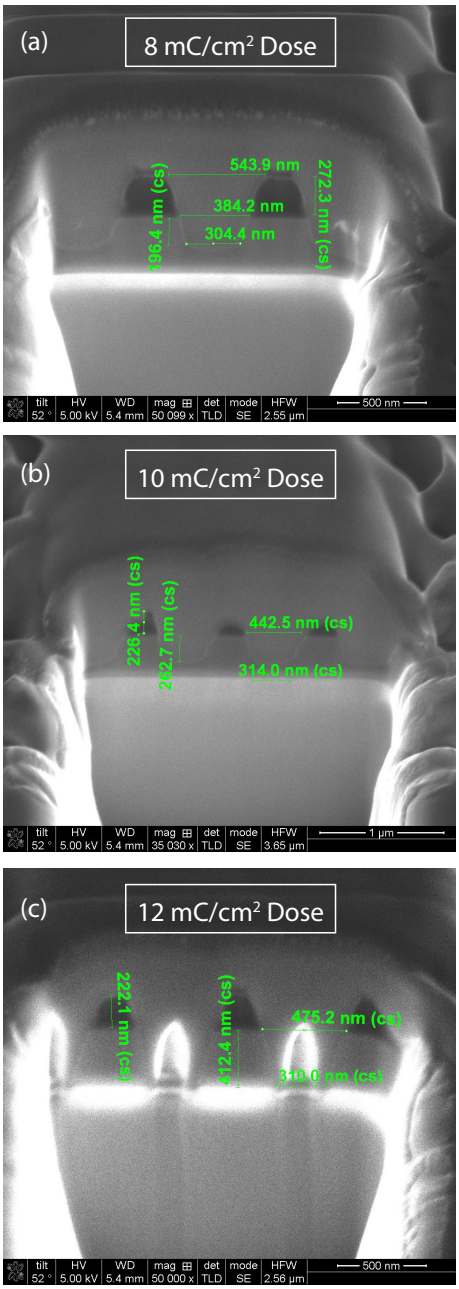

Figure 5.13. Cross-sectional SEM images of patterns made with a Cr/PMMA conductive coating with total ion beam doses of 8 mC/cm^2 (a), 10 mC/cm^2 (b), and 12 mC/cm^2 (c).

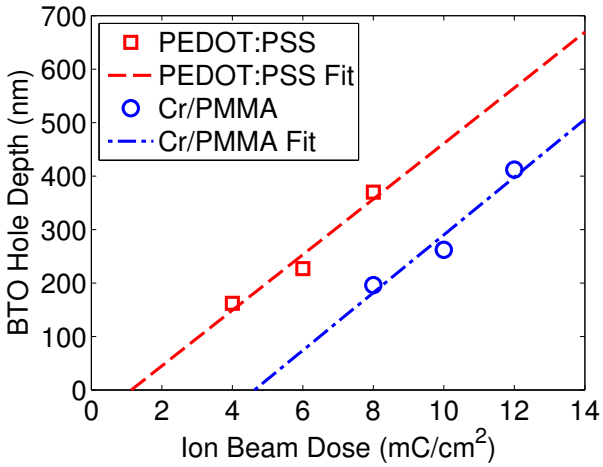

Figure 5.14. Calibration curves for determining the depth of the milled holes into the $BaTiO_3$ film versus applied total ion beam dose.

5.1 it is possible to calculate the effective hole diameter as a function of ion beam dose for different film thicknesses. The effective diameter is plotted versus ion beam dose in Fig. 5.15. The diameter in this figure is used to interpret the transmission results discussed in Section 5.5 with respect to the simulated transmission discussed in Section 5.3

Table 5.4. Summary of the observed cross-sectional hole geometry for holes milled through $Si_3N_4/BaTiO_3/MgO$ waveguides with 200 nm Si_3N_4 thickness and nominal hole diameter of 310 nm. The geometrical variables are defined in Fig. 5.10.

Dose (mC/cm^2)	d_1 (nm)	d_2 (nm)	h (nm)	α (°)	d_{eff} (nm)
8	309	384	196	11	328
10	314	443	262	14	346
12	310	475	412	11	351

5.5. Waveguide Transmission in the Optical C and L Bands

The transmission of the fabricated photonic crystal waveguides was measured using a continuous wave laser source (HP 8164A) with tunable wavelength between 1500 and 1580

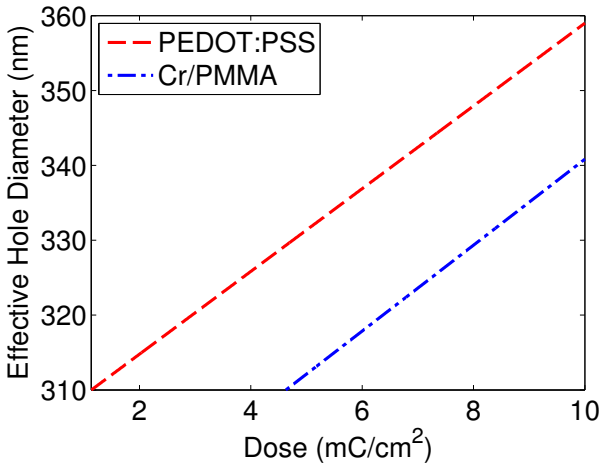

Figure 5.15. Effective hole diameter versus total applied ion beam dose for the two different conductive coatings.

nm. The measurement procedure is discussed in Section 3.6.2. A general overview of the analysis procedure and the description and organization of results is first discussed here. The measured transmission properties of the hexagonal lattice and line defect waveguides are then subsequently discussed separately.

For both the hexagonal lattice and line defect photonic crystal waveguides, the quantities of interest are the optical insertion loss, extinction across the stop-band (Extinction), center wavelength of the band edge (λ_c), width of the band edge (λ_w), and band edge sharpness (Extinction/λ_w). These quantities are defined graphically for an example measured transmission spectrum in Fig. 5.16. The insertion loss is the total optical loss due to waveguide coupling and on-chip scattering. The insertion loss defined in Fig. 5.16 includes both of these factors. The additional on-chip scattering loss due to the photonic crystal was obtained by measuring the insertion loss before and after photonic crystal patterning. The measured insertion loss of the un-patterned ridge waveguides is discussed in Section 5.5.1.

The extinction is defined here as the amount by which light is extinguished across the band edge. The band edge is defined by the three circles shown in Fig. 5.16, which indicate the extremes and center wavelength of the band edge. The high transmission

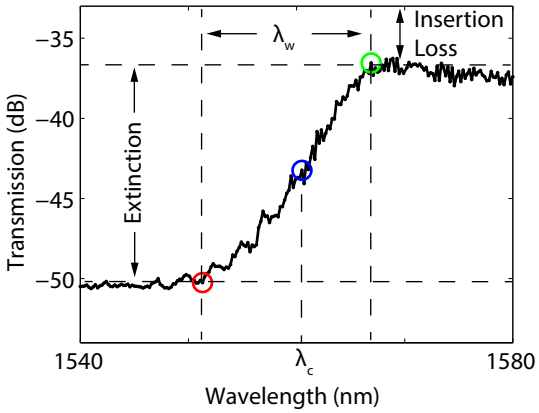

Figure 5.16. Diagram illustrating the transmission properties of the photonic crystal waveguides.

point of the band edge is indicated by a green circle, the low transmission point by a red circle, and the center wavelength by a blue circle. These points were determined by the following approach: first, the minimum and maximum transmission values were obtained, from which an average value was calculated. The wavelength corresponding to the average transmission value was ascribed as the center wavelength of the band edge. After determining the center wavelength, the minimum and maximum wavelengths of the band edge were determined as those at which the transmission increased or decreased by 45% from the value at the center wavelength. The band edge width, determined as the wavelength range between the minimum and maximum transmission values, therefore corresponds to an extinction that is 90% of the maximum attainable extinction. This method was chosen since it gives an accurate representation of both the extinction and

width of the stop band edge. If 100% of the extinction was used as the criteria for determining the band edge width, then the width would be unnecessarily large in some cases where a small peak occurs either inside or outside the stop band; 90% extinction was chosen as a compromise to accurately represent both the total extinction and band edge width. This method was used to analyze the stop band properties of all photonic crystal waveguides investigated.

The geometry and transmission properties of all photonic crystal waveguides are given below in tabular form. The data presented in these tables are obtained from the measured transmission spectra. The abbreviations used in the tables are defined in the List of Abbreviations and Symbols. The data in each table is organized such that it is specific to one wafer.

The data in each table is arranged in the following manner. The identity of the waveguide is given at the left side of the table. The waveguides on a given wafer are identified by "group" (G) and "waveguide" (WG) numbers. The naming convention for waveguides is explained by the wafer map in Fig.5.17. On each wafer, there are modulators and independent waveguides. As shown in Fig. 5.17, groups of modulators are given a number while groups of independent waveguides are given a number appended with "T." The "T" refers to "test"; photonic crystal patterns were tested on these waveguides before repeating them on waveguides in the modulator groups. The groups and waveguides are numbered from left to right in the direction of increasing gap spacing between electrodes. The two facets of the wafer are identified as shown in Fig. 5.17. The facets are identified such that, when the wafer is mounted for optical testing, the experimenter looking at the wafer couples light into Facet A and out of Facet B. Coupling of light into a waveguide is

sensitive to cracks at the facet edge, and insertion losses are more sensitive to the condition at the waveguide input than the output; hence, if a crack was present on Facet A, then light was instead coupled into the waveguide at Facet B.

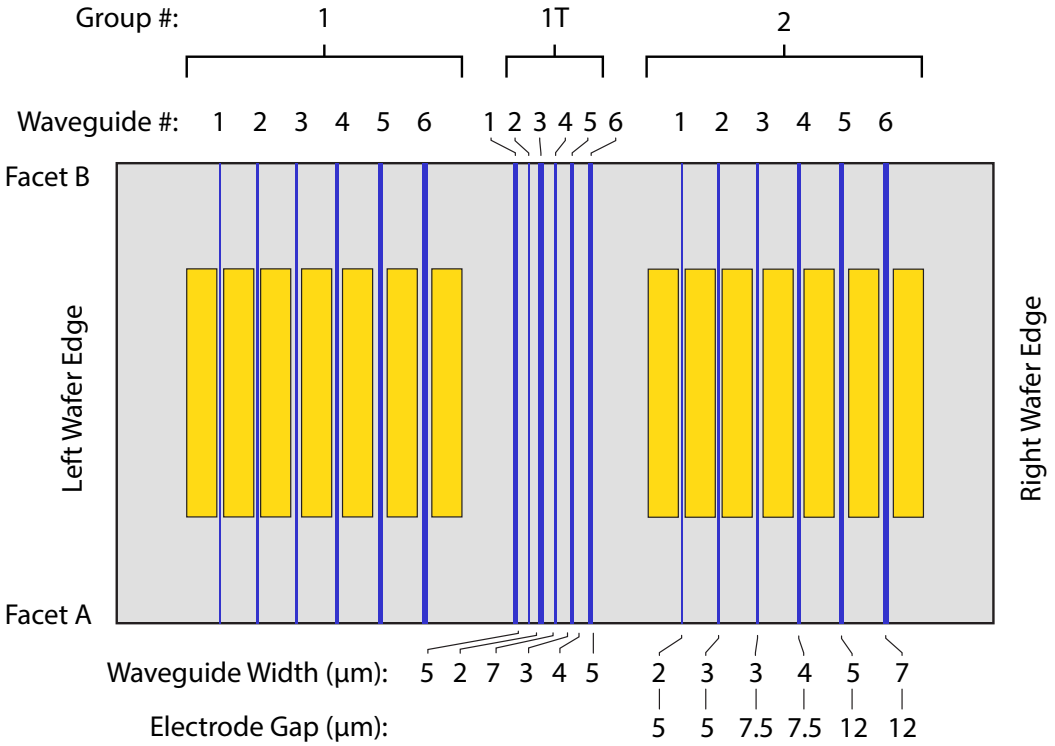

Figure 5.17. Schematic showing the arrangement of modulators and waveguides on a wafer fabricated using the 1 mm mask set.

Next to the waveguide identification in each table are the geometrical parameters defining the photonic crystal waveguide. These parameters include the lattice parameter (a), hole radius (r), number of unit cells (U.C.) in the direction of light propagation, length of the PC (L_P), ion beam dose, and depth of the holes into the $BaTiO_3$ film (h_{BTO}). The hole depth is estimated using the calibration curves for hole depth versus ion beam dose given in Section 5.4.2. All photonic crystals reported in Tables 5.8-5.16 were fabricated

using PEDOT:PSS as the conductive coating; hence, the calibration curve in Eqn. 5.4 was used for determining the hole depth.

Adjacent to the geometrical parameters in the tables are the measured optical properties. These include the insertion loss, extinction across the stop band edge, center wavelength of the band edge, and width of the band edge. For each waveguide, the measured insertion loss before and after patterning the photonic crystal waveguide is reported. The insertion loss before patterning was measured at a wavelength of 1563 nm using the setup described in 3.6.1. The insertion loss of the photonic crystal waveguides was determined as the average insertion loss outside the stop-band from the measured wavelength-dependent transmission. The additional insertion loss due to the photonic crystal waveguide was calculated as the difference of these two values (in dB). Adjacent to the insertion losses in the tables are the remaining measured optical properties grouped under the heading "Stop-band Properties."

5.5.1. Ridge Waveguides

The insertion loss of ridge waveguides was measured using the experimental technique discussed in Section 3.6.1. The insertion loss of several waveguides on 6 different wafers was measured, from which statistical results were obtained. The measured data is presented in the form of histograms in Fig. 5.18 for number of waveguides versus total insertion loss for each wafer.

The lower limit of insertion loss is limited by the theoretical maximum coupling efficiency. The maximum coupling efficiency was calculated using the approach of Albert et al[7], which assumes that the mode profile can be described by two overlapping ovals

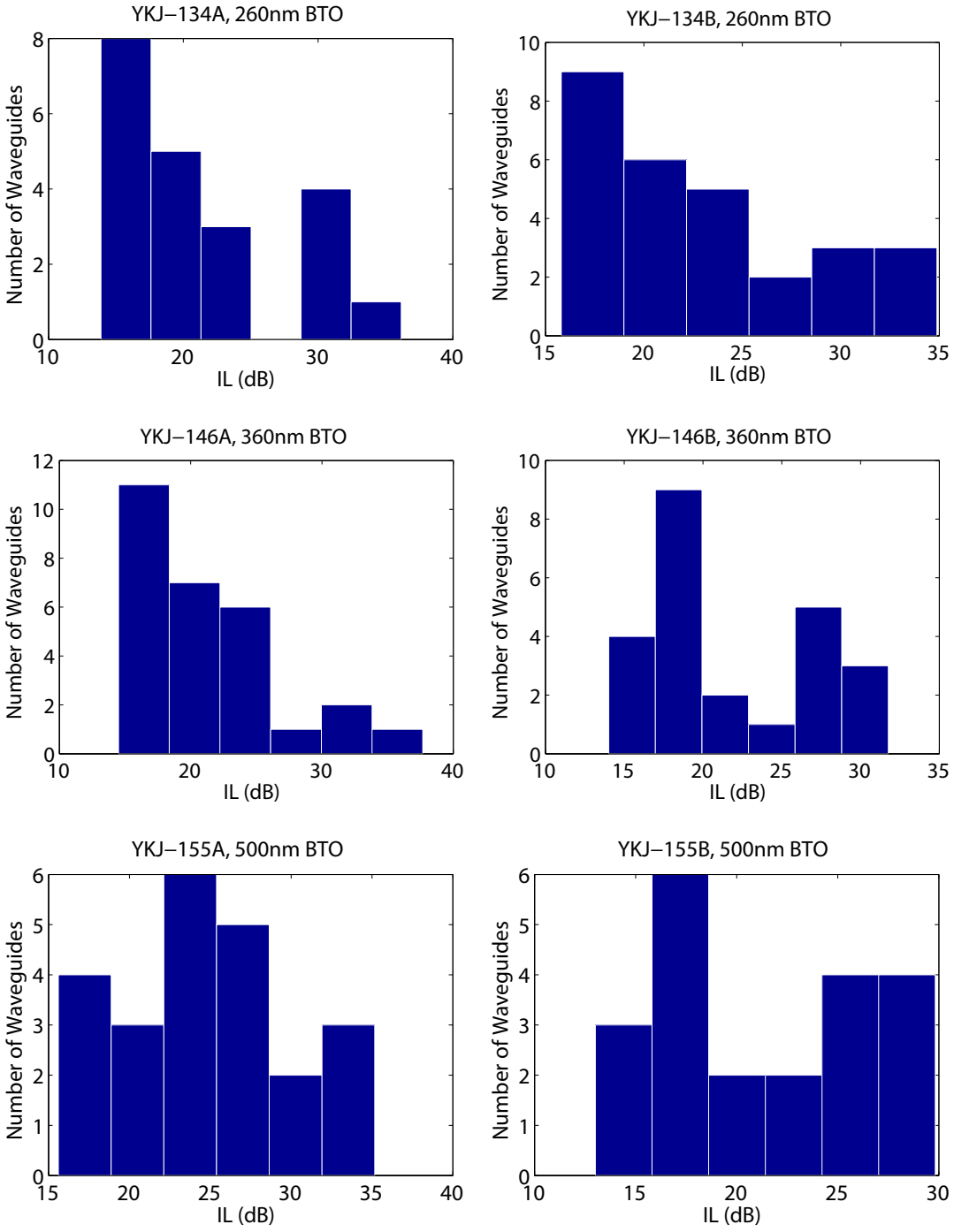

Figure 5.18. Histograms of insertion loss measured on 6 different wafers with $BaTiO_3$ thicknesses of 260, 360, and 500 nm.

and that the fiber mode is circular, as shown in Fig. 5.19. The mode overlap factor is calculated as[7]

$$I = \frac{4\left[\left(\frac{4}{w_f^2}+\frac{1}{w_u^2}\right)^{-1/2}+\left(\frac{4}{w_f^2}+\frac{1}{w_d^2}\right)^{-1/2}\right]^2}{\left(\frac{1}{w_f^2}+\frac{1}{w_{\|^2}}\right)w_f^2 w_{\|} w_{\perp}} \tag{5.6}$$

where the geometrical parameters w_f, w_u, w_d, $w_{\|}$, and $w_{\perp}$ are defined in Fig. 5.19. The mode profile calculated in Section 7.4 for a 300 nm thick film with 3 µm wide ridge waveguide has the approximate parameters given in Table 5.5. Using Eqn. 5.6 and the parameters in Table 5.5, the insertion loss is estimated to be 7 dB per facet, or 14 dB for input and output coupling with the tapered fiber. The minimum insertion loss for each wafer is given in Table 5.6. The minimum insertion loss values for each wafer are in good agreement with the estimation.

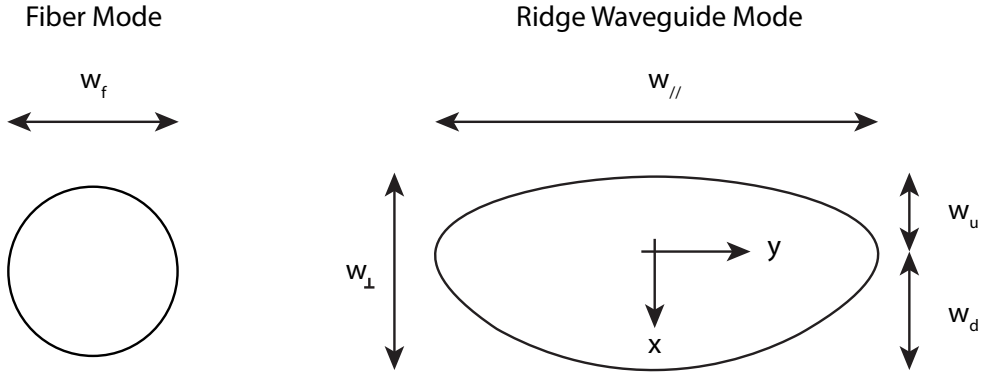

Figure 5.19. Schematic of the simplified fiber and ridge waveguide mode profiles used to calculate the coupling efficiency.

Table 5.5. Dimensions used to calculate the coupling efficiency between a tapered fiber and a ridge waveguide.

Parameter	Dimension
w_u	0.25 µm
w_d	0.25 µm
$w_\perp$	0.5 µm
$w_\parallel$	9 µm
w_f	1.7 µm

Other statistics given in Table 5.6 include the mean, maximum, and mean insertion loss (abbreviated IL) and the percent of waveguides with insertion loss less than 25 dB. The most notable feature is that these statistics do not strongly depend on the $BaTiO_3$ film thickness. The mean insertion loss is between 21 and 25 dB, and the maximum insertion loss is between 30 and 36 dB for all wafers. The median insertion loss is between 18 and 23 dB and is either equal to or less than the mean insertion loss for each wafer. These trends are more clearly visible in the histogram for all waveguides, shown in Fig. 5.20, which shows a peak that is closer to the minimum than maximum measured insertion loss.

Table 5.6. Measured ridge waveguide insertion loss statistics for several wafers.

		Insertion Loss (dB)				
Sample	$BaTiO_3$ (nm)	Min	Max	Mean	Median	% of WG with IL < 25 dB
YKJ-134A	260	14	36	21	18	66.7
YKJ-134B	260	16	35	23	22	66.7
YKJ-146A	360	15	38	21	21	66.7
YKJ-146B	360	14	32	22	19	53.3
YKJ-155A	500	16	35	25	23	54.2
YKJ-155B	500	13	30	21	21	58.3

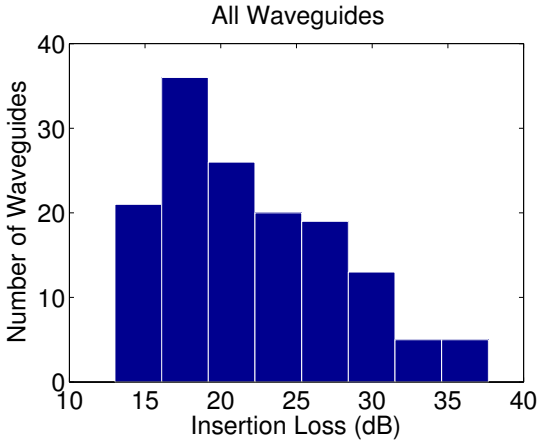

Figure 5.20. Histogram of insertion loss for measurements of waveguides on 6 different wafers.

5.5.2. Hexagonal Lattice PC Waveguides

The properties of the hexagonal lattice PC waveguides are given in Tables 5.7-5.12 organized by wafer. Hexagonal lattice PC waveguides were fabricated on wafers YKJ-155A, YKJ-155B, and YKJ-134B having $BaTiO_3$ film thicknesses of 500, 500, and 260 nm, respectively. The geometrical parameters of the PC waveguides are given in Tables 5.7, 5.9, and 5.11, and the measured transmission properties are summarized in Tables 5.8, 5.10, and 5.11. The thicknesses of these wafers represent the two extremes of thickness for practical devices; below 260 nm the TM optical mode is weakly guided, and above 500 nm the microwave losses limit the electro-optic response. Hexagonal lattice PC waveguides were fabricated with varying lattice parameter, r/a ratio, number of unit cells, and total ion beam dose to experimentally investigate the dependence of the transmission properties — insertion loss, extinction, band edge location, and band edge width — on these geometrical

Table 5.7. Summary of the geometrical properties of fabricated hexagonal lattice photonic crystals on sample YKJ-155A having 500 nm thick $BaTiO_3$. All waveguides in the set had the same number of unit cells (U.C.), total length L_p, lattice parameter a, hole radius r with values of 45, 35 µm, 777 nm, and 157.5 nm, respectively.

Device ID					
G	WG	Dose (mC/cm^2)	h_{BTO} (nm)	Effective r (nm)	Effective r/a
2	1	6	250	171	0.220
2	3	6	250	171	0.220
2	5	6	250	171	0.220
2	6	7	310	174	0.224
2T	1	4	150	165	0.213
2T	3	6.5	280	172	0.222
2T	4	6	250	171	0.220
2T	5	5	200	168	0.216
2T	6	6	250	171	0.220
3	3	3	100	163	0.210
3	5	4	150	165	0.213

parameters. The discussion below focuses first on the waveguides on each wafer, then on the transmission properties in aggregate.

Hexagonal lattice PC waveguides fabricated on YKJ-155A were patterned as a function of ion beam dose with all other geometrical parameters fixed. The geometry of these waveguides is summarized in Table 5.7. Total dose factors between 3 and 7 mC/cm^2 were used, representing an estimated hole depth between 100 and 310 nm into the 500 nm thick $BaTiO_3$ film. The holes penetrate between 20% and 62% of the total film thickness. An r/a ratio of 0.2 and lattice parameter of 777 nm were chosen for all patterns, representing a scale factor of 1.05 applied to the nominal geometry $a = 740$ nm and $r = 155$ nm used previously by our group[83]. This scaling factor was applied to move the stop-band edge to

a wavelength of 1550 nm. The PC waveguides on wafer YKJ-155A all had a length of 45 unit cells. This length was chosen based on the simulations discussed in Section 5.3. A length of 45 unit cells was chosen to represent a compromise between good stop band edge sharpness and insertion loss due to scattering both from fabrication imperfections and into the substrate due to the overlap of the substrate light cone discussed in Section 5.2.

The measured transmission spectra for hexagonal PC waveguides on wafer YKJ-155A are shown in Fig. 5.21. The transmission spectra are plotted separately for each waveguide and are labeled with the waveguide ID such that their measured properties can be located in Table 5.8. All transmission spectra shown in Fig. 5.21 have a clear band edge with center wavelength between 1500 and 1580 nm. It is especially noteworthy that the band edge is clearly visible when plotted on a semi-log plot with the transmission in units of decibels (dB). A clear band edge is observed even though the band edge is within the lossy region of the band structure according to Fig. 5.1. This demonstrates that the light is interacting with the photonic crystal structure. According to the extinction values reported in Table 5.8, the extinction does not strongly depend on hole depth. Extinction values between 7.1 and 14.4 dB were measured for structures with holes penetrating between 100 and 250 nm of the $BaTiO_3$ film. It is observed that the insertion loss increases with hole depth and the band edge width decreases with hole depth. Consequently, the band edge sharpness also increases with hole depth. These trends are further discussed below in aggregate with the data from waveguides on sample YKJ-155B.

Waveguides on sample YKJ-155B were used to determine the dependence of PC length and lattice parameter on the transmission properties. The geometry of the fabricated structures on this wafer are summarized in Table 5.9. Photonic crystals fabricated on

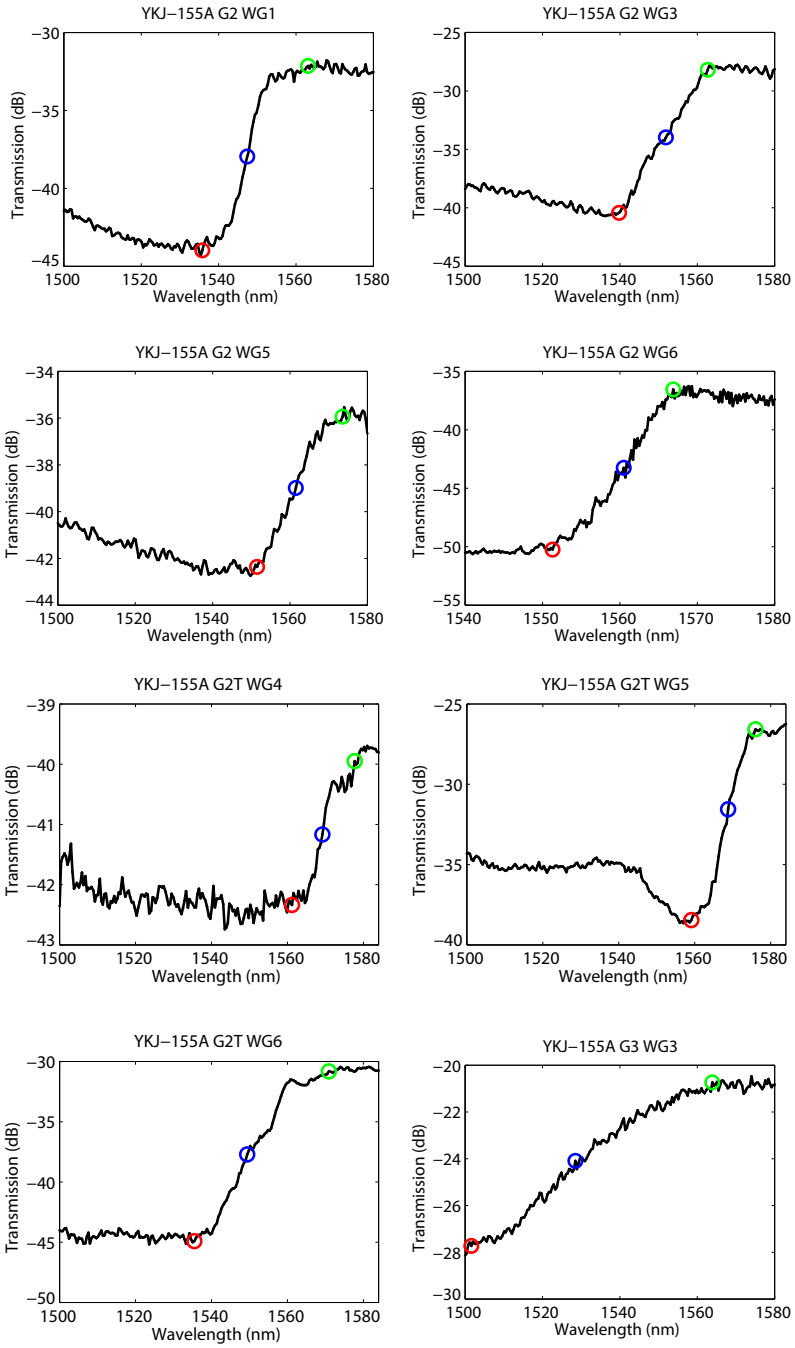

Figure 5.21. Measured transmission of hexagonal lattice photonic crystal waveguides on wafer YKJ-155A (500 nm $BaTiO_3$).

Table 5.8. Summary of the measured transmission properties of hexagonal lattice PC waveguides fabricated on sample YKJ-155A.

Device ID		Insertion Loss			Stop-Band Properties			
G	WG	Ridge (dB)	PC (dB)	Added (dB)	Extinction (dB)	λ_c (nm)	λ_w (nm)	Extinction/λ_w (dB/nm)
2	1	23	32	10	12	1547	27	0.4
2	3	30	28	-	12	1552	23	0.5
2	5	24	36	12	6	1562	22	0.3
2	6	16	37	21	14	1561	16	0.9
2T	1	21			No clear waveguide mode			
2T	3	23			No clear waveguide mode			
2T	4	22	40	18	2	1569	17	0.1
2T	5	21	27	5	12	1569	17	0.7
2T	6	22	31	9	14	1549	35	0.4
3	3	23	21	-	7	1529	62	0.1
3	5	16			No clear band edge			

this wafer all had the same ion beam dose (6 mC/cm^2) and the same nominal hole radius of 155 nm. For the length-dependent study, photonic crystals with 50, 100, 200, and 400 µm lengths were fabricated. Longer PC waveguides were fabricated in order to 1) demonstrate the ability to fabricate longer arrays with focused ion beam lithography and 2) measure the length-dependent transmission properties to elucidate mechanisms of scattering loss. As shown in Fig. 5.7 and discussed in Section 5.4.1, hexagonal lattice PC structures as long as 308 µm were fabricated with an angular alignment tolerance of 0.002°. A summary of the fabricated devices on sample YKJ-155B is given in Table 5.10. With the 1 mm wide writefield of the instrument used, PC waveguides as long as 1 mm can be potentially fabricated, although the resolution may suffer. PC waveguides of different lengths are of interest for studying the underlying physical loss mechanisms, which include out-of-plane scattering, in-plane scattering, backward scattering, inter-mode

scattering, and polarization-mixing scattering[61,72] in addition to the scattering to substrate modes. For the waveguides fabricated here, the extent of polarization-mixing scattering is of great interest since the waveguides lack symmetry in the out-of-plane direction and hence support only quasi-TE and quasi-TM modes. As discussed in Section 5.2, scattering to substrate modes is expected for both types of photonic crystal structures. This loss mechanism would be expected to be present in this work due to the fabricated waveguide structure but is nonexistent for typical silicon[115] and GaAs[32] PC slab waveguides which are fabricated on suspended films. While the longer PC waveguides were fabricated, no distinguishable optical mode was detected using a laser with 4 mW of nominal power, presumably due to the larger insertion losses; hence no analysis of the loss mechanisms are presented in this work, although the devices have been fabricated for measurements and analysis in the future with a higher powered tunable source. For the lattice parameter dependent study, lattice parameters of 740, 750, and 760 nm were used. Photonic crystals with a lattice parameter of 740 nm have the same geometry as that used previously by Li[79]. The lattice parameter was increased in order to determine the optimum value such that the center wavelength of the band edge coincided with 1560 nm. This was done both as a practical necessity for subsequent measurements with a fixed wavelength CW 1560 nm diode laser and so that the devices could be operated in the center of the optical C band for telecommunication applications. Of the devices on YKJ-155B, three had a measurable transmission spectrum as indicated in Table 5.10. The transmission spectra of these waveguides are shown in Fig. 5.22 along with the corresponding simulated transmission. Simulation predicts that, as the lattice parameter increases, the band edge should red-shift; this trend, however, is not clearly reflected in the measured spectra. A possible reason

Table 5.9. Summary of the geometrical properties of fabricated hexagonal lattice photonic crystals on sample YKJ-155B having 500 nm thick $BaTiO_3$. The ion beam dose, hole depth, hole radius, and effective hole radius were the same for all devices and had values of 6 mC/cm^2, 250 nm, 155 nm, and 168 nm, respectively.

Device ID		PC Geometry			
G	WG	U.C.	L_P (µm)	a (nm)	Effective r/a
2	6	400	308	760	0.221
2T	1	45	33.3	740	0.227
2T	5	45	33.8	750	0.224
2T	6	45	34.2	760	0.221
3T	1	200	154	770	0.219
3T	4	100	77	770	0.219
3T	5	50	38.5	770	0.219
3T	6	400	308	770	0.219

Table 5.10. Summary of the measured transmission properties of hexagonal lattice PC waveguides fabricated on sample YKJ-155B.

Device ID		Insertion Loss			Stop-Band Properties			
G	WG	Ridge (dB)	PC (dB)	Added (dB)	Extinction (dB)	λ_c (nm)	λ_w (nm)	Extinction/λ_w (dB/nm)
2	6	18			No optical mode observed			
2T	1	17	24	7	24	1525	25	0.9
2T	5	13			Waveguide damaged (chipped, facet B)			
2T	6	14	36	22	20	1535	9.9	2.2
3T	1	27			No optical mode observed			
3T	4	18			No optical mode observed			
3T	5	22	30	8	16	1528	18.7	0.9
3T	6	18			No optical mode observed			

for this is that two of the photonic crystals, those fabricated on G2T WG6 and G3T WG5, were fabricated on waveguides that support multiple modes at the measurement wavelengths. Another possible reason could be differing amounts of astigmatism in the ion beam used to fabricate the waveguides.

Regardless of the lattice parameter, there are several other noteworthy features in the transmission spectra for the waveguides on sample YKJ-155B. All three of the waveguides have an extinction greater than 16 dB, with a maximum extinction of 24 dB. The band edge of sample G2T WG6 has a width of 9.9 nm and an extinction of 20 dB. For this waveguide, the band edge sharpness is 2 dB/nm. Recently, an extinction of approximately 20 dB has been reported for a hexagonal lattice PC waveguide fabricated on the $LiNbO_3$ on insulator platform, a record extinction for all PC waveguides fabricated using either bulk or thin film ferroelectrics[23]. The band edge of the waveguide, however, spans more than 50 nm, giving a band edge sharpness of 0.4 dB/nm, a factor of 5 less than the best waveguide reported here. Moreover, all hexagonal lattice PC waveguides fabricated on wafer YKJ-155B have a band edge sharpness greater than or equal to 0.9 dB/nm, more than double that reported by Cai et al[23], and five waveguides on wafer YKJ-155A have a band edge sharpness greater than or equal to 0.4 dB/nm. The transmission properties of the PC waveguides demonstrated here on $BaTiO_3$ thin films therefore have the sharpest optical stop-band edges reported to date for ferroelectric materials.

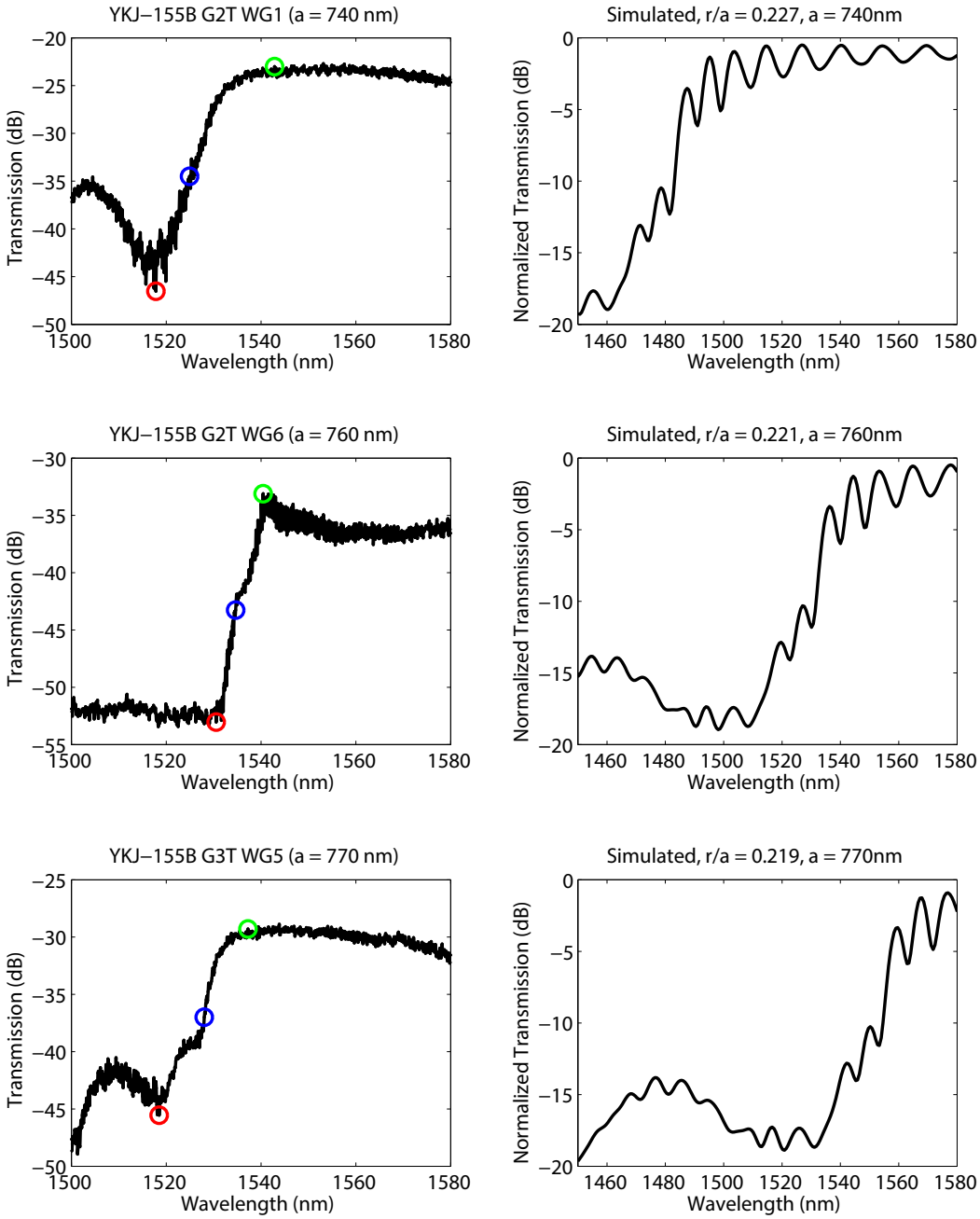

Figure 5.22. Measured transmission of hexagonal lattice photonic crystal waveguides on wafer YKJ-155B (500 nm $BaTiO_3$) with the corresponding simulated transmission spectra shown at right.

The last set of hexagonal lattice PC waveguides were fabricated on wafer YKJ-134B with 260 nm $BaTiO_3$ thickness. The PC waveguides on this wafer all have the same lattice constant, r/a ratio, and length; the only variable is the total ion beam dose or, equivalently, hole depth. Since the film thickness of this wafer is only 260 nm, an ion beam dose of $6\,mC/cm^2$ is enough to nearly penetrate the entire film thickness. PC waveguides were fabricated on this wafer for two purposes: 1) the microwave losses scale with the film thickness, hence PC modulators fabricated on this wafer have potentially the highest electro-optic bandwidth, and 2) the electro-optic coefficient is smaller in thinner films, hence the half-wave voltage of modulators on this wafer could be potentially reduced from their measured value of approximately 20 V to a reasonable value under 5 V. Additionally, the effect of the film thickness on the transmission properties of the PC has not been previously investigated.

The geometrical parameters of PC structures fabricated on wafer YKJ-134B are given in Table 5.11, and the measured transmission properties are summarized in Table 5.12. As shown in Table 5.12, an optical mode was observed only in waveguides with a total ion beam dose less than $4\,mC/cm^2$. For these waveguides, the holes penetrate no more than 58% of the total film thickness. The measured transmission spectra for these waveguides are shown in Fig. 5.23. Compared with the transmission spectra measured on samples YKJ-155A and YKJ-155B (Fig. 5.21 and 5.22, respectively), there is not a well-defined band edge. This is reflected in the calculated band edge sharpness, which is 0.088 dB/nm for both waveguides on this wafer, which is more than a factor of 10 smaller than that for any of the waveguides on wafer YKJ-155B. The lack of a well-defined band edge for any of the waveguides on wafer YKJ-134B is not entirely unexpected given the operating

Table 5.11. Summary of the geometrical properties of fabricated hexagonal lattice photonic crystals on sample YKJ-134B having 260 nm thick $BaTiO_3$. All waveguides had the same number of unit cells, total length L_P, lattice parameter a, hole radius r, and effective hole radius with values of 45, 35 µm, 777 nm, and 157.5 nm, respectively.

Device ID					
G	WG	Dose (mC/cm^2)	h_{BTO} (nm)	Effective r (nm)	Effective r/a
2	4	5	200	168	0.216
2	5	6	250	171	0.220
2T	3	5	200	168	0.216
2T	5	6	250	171	0.220
3	5	3	100	163	0.210
3	6	4	150	165	0.213
3T	1	3	100	163	0.210
3T	2	4	150	165	0.213

Table 5.12. Summary of the measured transmission properties of hexagonal lattice PC waveguides fabricated on sample YKJ-134B.

Device ID		Insertion Loss			Stop-Band Properties			
G	WG	Ridge (dB)	PC (dB)	Added (dB)	Extinction (dB)	λ_c (nm)	λ_w (nm)	Extinction/λ_w (dB/nm)
2	4	23			No distinguishable optical mode			
2	5	22			No distinguishable optical mode			
2T	3	17			No distinguishable optical mode			
2T	5	18			No distinguishable optical mode			
3	5	21	21	0	5	1545	57	0.088
3	6	18	23	5	No clear band edge			
3T	1	18	17	-	No clear band edge			
3T	2	18	22	5	3.1	1530	35	0.088

wavelength and film thickness. The ideal thickness for a photonic crystal slab is half of the PC periodicity[67]; below this thickness, the modes are weakly bound and are delocalized, hence transmission has little dependence on the photonic crystal structure. Since a lattice constant of 750-770 nm is required for operation in the optical C band (1535-1565 nm), a film thickness of approximately 380 nm is needed. As demonstrated here, a film thickness as large as 500 nm is sufficient for obtaining sharp band edges with large extinction.

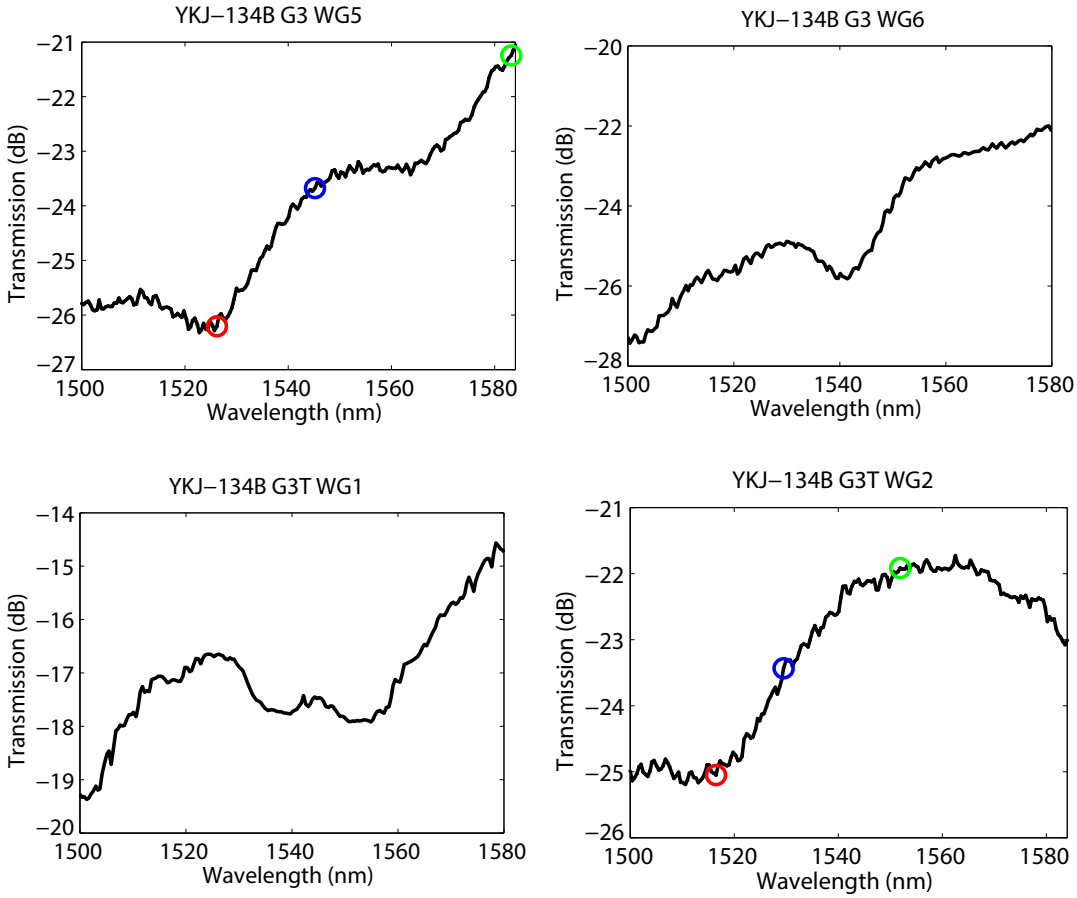

Figure 5.23. Measured transmission of hexagonal lattice photonic crystal waveguides on wafer YKJ-155B (500 nm $BaTiO_3$).

The transmission properties for the hexagonal lattice PC waveguides on wafers YKJ-155A and YKJ-155B are summarized in aggregate in Fig. 5.24. In this figure, the insertion loss and band edge width are plotted versus depth into the $BaTiO_3$ film, and the center wavelength is plotted versus lattice parameter of the photonic crystal. As observed on each wafer separately, the insertion loss increases with film thickness, and the band edge width decreases with film thickness. Both of these trends are attributed to increasing overlap between the propagating optical mode and the photonic crystal structure with increasing depth of the holes into the $BaTiO_3$ film. In Fig. 5.24 (c), the center wavelength of the band edge is observed to red-shift with increasing lattice parameter, as expected from simulation. The red-shifting with increasing lattice parameter is in good agreement with that predicted by the two dimensional FDTD simulations (Fig. 5.5 (d)), validating both the effective medium approach and the method of incorporating device fabrication feedback into the simulations.

Sharp band edges have previously been sought for use in electro-optic modulators, where the center wavelength of the band edge or defect mode within the band gap is shifted by electro-optic modulation of the high refractive index material of the PC[91 81 129 100 121]. While it is appealing to apply the electro-optic effect for tunable ferroelectric optical filters and modulators, there are two major issues with this approach: 1) it is nearly impossible to induce a sufficiently large optical modulation using any ferroelectric ceramic with a reasonable voltage (< 5V), and 2) this approach requires operation at either the PC band edge or at a defect mode within the photonic band gap, which are both inherently high loss regions. In the work of Lin et al[91] and Siraji et al[129], the electro-optic tunability of the band edge was simulated using a refractive index shift between 0.01 and 0.09. These

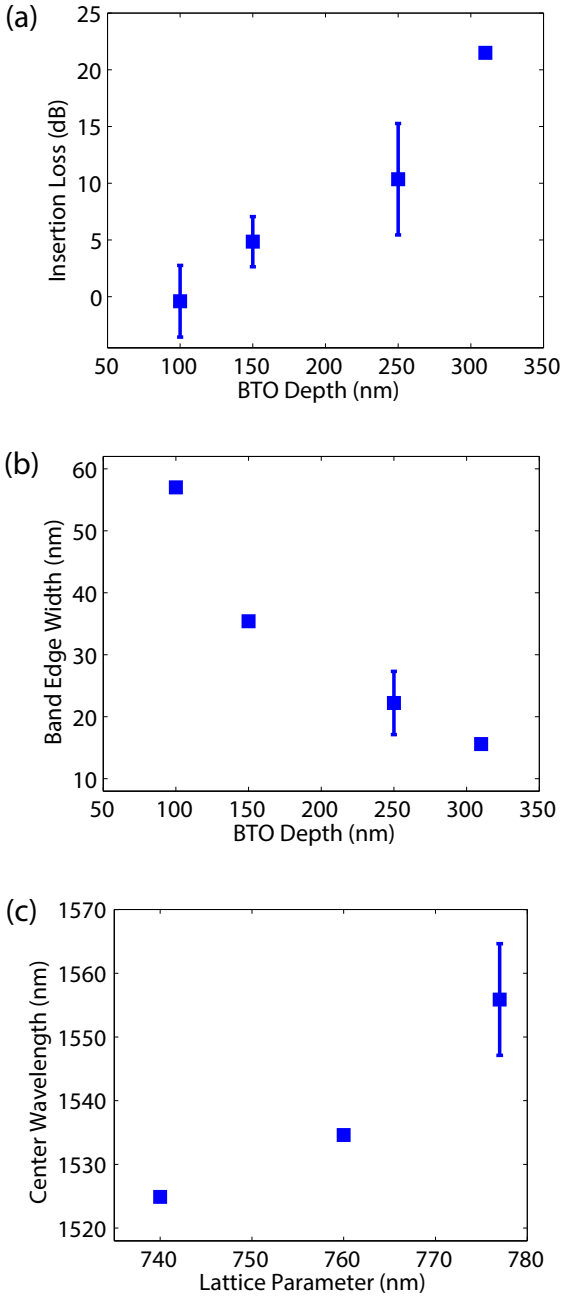

Figure 5.24. Aggregate optica transmission properties of hexagonal lattice photonic crystal waveguides on wafers YKJ-155A and YKJ-155B.

values are much larger than what can be realistically achieved for both thin film $BaTiO_3$ and thin film or bulk $LiNbO_3$. The refractive index shift is given by

$$\Delta n = \frac{1}{2} n^3 r_{eff} E$$

where r_{eff} is the effective in-device electro-optic coefficient and E is the applied electric field. In this work, effective in-device electro-optic coefficients as high as 300 pm/V were measured at a frequency of 1 MHz and optical wavelength of 1560 nm. The largest electro-optic coefficient measured of a $BaTiO_3$ thin film modulator is 360 pm/V[141]. At microwave frequencies, the electro-optic coefficient decreases due to a reduction in the dielectric constant and a clamping of frequency-dependent contributions to the electro-optic coefficient, such as ionic and dipolar effects[1]. For a mode index of 2.13, effective electro-optic coefficient of 300 pm/V, and applied field of 10×10^6 V/m, the expected refractive index shift is 0.0014, an order of magnitude smaller than that used to simulate the band edge shift in references[91 81 129]. With this refractive index shift, the band edge shifts negligibly, as shown in Fig. 5.25.

A large measured band edge shift has been reported for a PC waveguide fabricated on $LiNbO_3$[121]. Although the authors state that the effect is not due to photorefraction, however, both the measurement technique used by the authors and the material properties of the $LiNbO_3$ waveguide suggest that photorefraction could be a significant factor. The authors used a broadband light source with unspecified range and power to measure the transmission. The illumination of doped $LiNbO_3$ at visible wavelengths is known to cause significant photorefraction[53]. The photorefractive effect has been studied in both

[1]The measurement of the frequency dependent electro-optic coefficient is discussed in greater detail in the subsequent chapter

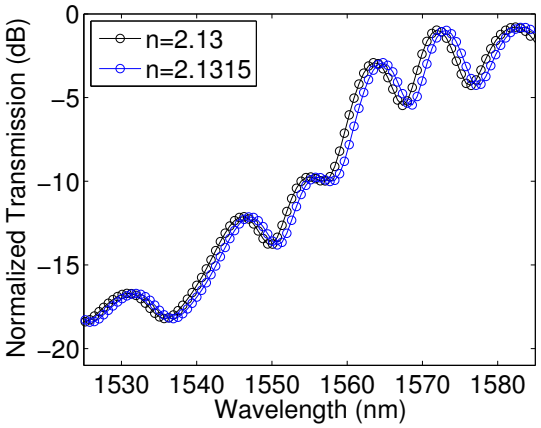

Figure 5.25. Simulated shift of the photonic crystal band edge due to a refractive index change by 0.0015.

Ti-diffused and annealed proton exchanged (APE) $LiNbO_3$ waveguides, showing an increase in the photorefractive effect with increasing optical power[47,48]. Since photorefraction is a carrier induced effect, it has a wavelength dependence that is determined by the impurity level within the electronic band gap of the material. The effects of photorefraction on the supposed electro-optically induced band edge shift could be excluded by using a tunable CW laser instead of the pulsed laser setup used by Roussey et al[121]. The band edge shift reported by Roussey et al is therefore not rigorously shown to be due exclusively to the electro-optic effect. Furthermore, the analytical model that the authors used to analyze the shift is in disagreement with the model proposed by Soljačić et al, as discussed in Section 5.7. The model used by Roussey et al follows that of Dumeige et al[39] for the enhancement of $\chi^{(2)}$ properties in photonic crystal waveguides, which relates the enhancement to an increase in the local density of optical states (LDOS). For true $\chi^{(2)}$ nonlinear optical effects such as second harmonic generation, the efficiency of the process is proportional to the optical power or, equivalently, LDOS; the electro-optic effect, however does not depend on

the optical input power. The explanation is as follows: nonlinear optical processes are those for which incident light induces a nonlinear response, which in turn modifies the incident light in a nonlinear way. Electro-optic effects (Pockels and Kerr) are described as nonlinear optical processes in the limit that the frequency of the stimulating field goes to zero, i.e., is much less than that of the optical field[127]. Since the stimulating field is responsible for inducing the nonlinear response of the material through the constitutive relations of Maxwell's equations and is, in the case of electro-optic effects, not an optical field, the LDOS therefore has no effect on the enhancement of electro-optic material properties.

Compared with previous work in our research group, the measured extinction here for hexagonal lattice PC waveguides is an order of magnitude larger[79 88]. This is attributed primarily to improvements in the measurement technique and also to improvements in the film quality and device fabrication. It is important to note that, in this work, all transmission measurements were done using tapered lensed fibers to couple light into and out of the waveguide. In previous work, light was coupled into and out of the waveguide using objective lenses with an iris between the output facet and output objective lens. In an objective lens system, the iris is required to block light scattered in the substrate, which is not insignificant compared to that guided in the waveguide mode[79]. With an iris, it is not difficult to either collect more light from the substrate or to cut out light from the waveguide mode, resulting in lower signal to noise ratio in the measurement. The tapered fiber setup has the additional advantage of simplicity of alignment; when set up properly, the fiber is approximately in the same plane as the top of the wafer and positioned within several microns from the waveguide facet. This is fairly easy to observe

using an overhead camera. In addition to the all-fiber setup used here, the measurements were done with a smaller sub-nanometer wavelength resolution (typically 0.1 nm) and with complete synchronization between the laser wavelength control and data acquisition, obtained by controlling both with the same LabVIEW program.

In addition to the improvements in measurement technique, improvements in the film quality and device fabrication also contribute to the higher measured extinction. Both the film quality and the quality of device fabrication affect the insertion loss of the waveguides and the measurable extinction depth. In particular, sample YKJ-155A has a rocking curve width of 0.47° and surface roughness <1.3 nm rms. For comparison, the narrowest previously reported rocking curve width of $BaTiO_3$ films is 0.28°, and the lowest rms roughness is 0.23 nm rms[150]. The values measured on the YKJ-155A film indicate that it has a low mosaicity corresponding to near layer-by-layer deposition. The low surface roughness and low mosaicity contribute to low propagation losses, which enable accurate measurement of the stop-band properties, especially the extinction depth whose maximum value is dependent on scattering losses outside the stop-band. Significant improvements were also made in the polishing of the waveguide facets. Li obtained a wafer yield of 20% by cleaving along [110], while all wafers in this work polished along the same direction were successful. As discussed in Section 5.5.1, the mean insertion loss due to waveguide coupling into and out of the ridge waveguides for all wafers is 22 dB, representing a mean total insertion loss of 8 dB due to the roughness of the facets. Insertion loss values were not previously reported by Li[79] and Lin[88]; however, the insertion losses reported here are close to the theoretical minimum, and the polishing step used here (described in detail in Section A.6 of Appendix A) is predicted to produce a flatter surface than cleaving.

5.5.3. Line Defect PC Waveguides

The properties of the line defect waveguides are given in Tables 5.14 and 5.16. Line defect PC waveguides were fabricated on wafers YKJ-155A and YKJ-155B. Similar to the case for the hexagonal lattice PC, the data is organized by wafer. The geometrical parameters of the PC W1 waveguides are given in Tables 5.13 and 5.15, and the measured transmission properties are summarized in Tables 5.14 and 5.16. The W1 PC waveguides were fabricated only on the 500 nm thick films due to the stronger observed interaction between the incident light and PC structures for the hexagonal lattice PC using these films.

The transmission properties of W1 waveguides were studied as a function of ion beam dose, or total hole depth, using wafer YKJ-155A. All PC structures fabricated on this wafer had a lattice parameter of 530 nm with a nominal hole radius of 96 nm. The lattice parameter of 530 nm was chosen in order to position the low dispersion, moderate group index region in the optical C band in accordance with the simulations discussed in Section 5.3. A nominal hole radius of 96 nm was chosen in order to target an effective r/a of 0.2 using the model for the dependence of hole radius on hole depth discussed in Section 5.4.2. Of the four waveguides fabricated on wafer YKJ-155A, those patterned with lower ion beam dose had a distinguishable optical mode. The measured transmission spectra for these two waveguides are shown in Fig. 5.26. The measured transmission of YKJ-155A G3T WG2 is in fair agreement with the simulated transmission of Fig. 5.6, showing a decrease in transmission between 1520 and 1560 nm, while that of YKJ-155A G3T WG2 does not show this trend. Since devices with deeper holes had no measurable transmission, it is likely the case that device YKJ-155A G3T WG3 had deeper holes than

that of the nominally identical device YKJ-155A G3T WG2. This is further supported by the approximately 10 dB higher insertion loss measured for the former. For the waveguide labeled YKJ-155A G3T WG3, strong interference fringes were measured, from which the group index was calculated as discussed in Section 5.6.

Based on the results obtained for waveguides on wafer YKJ-155A, waveguides were fabricated on wafer YKJ-155B with a constant ion beam dose of $4\,\mathrm{mC/cm^2}$. Three waveguides were fabricated with a lattice constant of 530 nm, and the fourth waveguide was fabricated with a lattice constant of 730 nm. All four of these waveguides had a measurable transmission. Two of the waveguides fabricated with $a = 530$ nm (G2 WG1 and G2 WG5) show a roll-off in the transmission with increasing wavelength, in agreement with the simulated transmission in Fig. 5.6. The measured spectrum for waveguide G2 WG2 shows a dip in the transmission that is slightly blue-shifted compared to the simulation. The variation in transmission is possibly due to fabrication imperfections associated with ion beam focus and astigmatism. The waveguide with lattice parameter $a = 730$ nm shows a long-wavelength band edge near 1500 nm, in good agreement with the simulated transmission in Fig. 5.6. Compared with the hexagonal lattice PC waveguides, the W1 waveguides have a wider band edge and lower extinction, as expected from simulation. The average band edge sharpness for the waveguides with $a = 530$ nm is 0.16 dB/nm, much smaller than the band edge sharpness of the hexagonal lattice PC waveguides fabricated on wafer YKJ-155B, all of which had a sharpness of 0.9 dB/nm or greater.

Table 5.13. Summary of the geometrical properties of line defect photonic crystal waveguides on sample YKJ-155A having 500 nm thick $BaTiO_3$. All waveguides had the same number of unit cells, total photonic crystal length L_P, lattice parameter a, and nominal hole radius r with values of 70, 37 µm, 530 nm, and 96 nm, respectively.

Device ID		PC Geometry							
G	WG	U.C.	L_P (µm)	Dose (mC/cm^2)	h_{BTO} (nm)	a (nm)	r (nm)	Effective r (nm)	Effective r/a
3T	2	70	37	3	100	530	96	101	0.191
3T	3	70	37	4	150	530	96	104	0.196
3T	4	70	37	6	250	530	96	109	0.206
3T	5	70	37	6	250	530	96	109	0.206

Table 5.14. Summary of the measured optical transmission properties of line defect photonic crystal waveguides on sample YKJ-155A having 500 nm thick $BaTiO_3$.

Device ID		Insertion Loss			Stop-Band Properties			
G	WG	Ridge (dB)	PC (dB)	Added (dB)	Extinction (dB)	λ_c (nm)	λ_w (nm)	Extinction/λ_w (dB/nm)
3T	2	26	29	3	2.2	1539	35	0.063
3T	3	18	39	21	-	-	-	
3T	4	28	No distinguishable optical mode					
3T	5	16	No distinguishable optical mode					

Table 5.15. Summary of the geometrical properties of line defect photonic crystal waveguides on sample YKJ-155B having 500 nm thick $BaTiO_3$. All waveguides had the same number of unit cells, ion beam dose, and hole depth with values of 70, 4 mC/cm^2, and 150 nm, respectively.

Device ID		PC Geometry				
G	WG	L_P (µm)	a (nm)	r (nm)	Effective r (nm)	Effective r/a
2	1	37	530	96	104	0.196
2	2	37	530	96	104	0.196
2	4	51	730	132	140	0.192
2	5	37	530	96	104	0.196

Table 5.16. Summary of the measured optical transmission properties of line defect photonic crystal waveguides on sample YKJ-155B having 500 nm thick $BaTiO_3$.

Device ID		Insertion Loss			Stop-Band Properties			
G	WG	Ridge (dB)	PC (dB)	Added (dB)	Extinction (dB)	λ_c (nm)	λ_w (nm)	Extinction/λ_w (dB/nm)
2	1	27	39	12	12	1547	38	0.316
2	2	24	36	12	5	1528	29.8	0.168
2	4	20	30	10	3.5	1502	5	0.7
2	5	15	42	27	6.6	1553	39	0.169

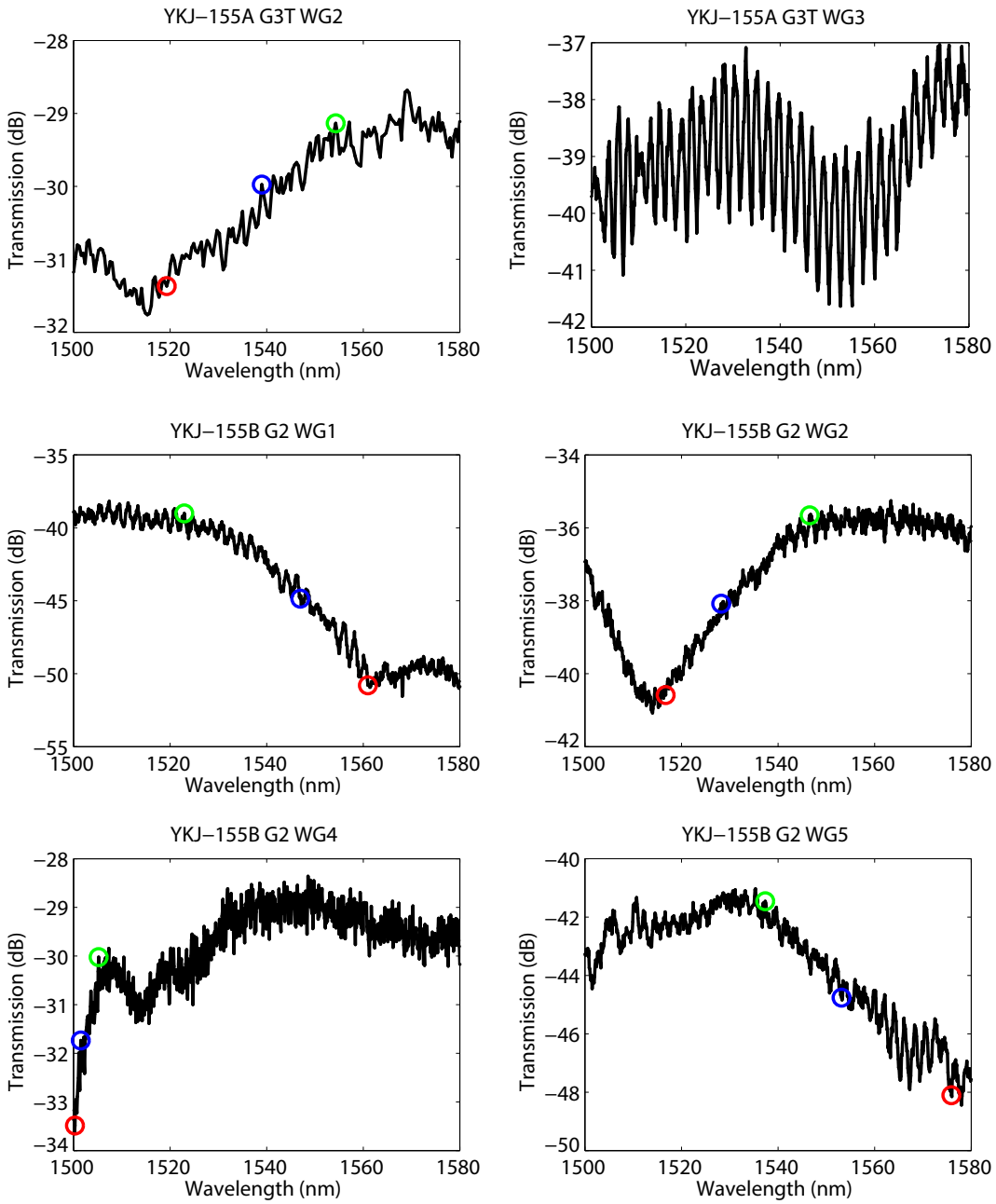

Figure 5.26. Measured transmission of line defect (W1) photonic crystal waveguides. The waveguide geometry for each is given in Tables 5.14 and 5.16.

5.6. Optical Group Index

The optical group index of the line defect waveguides was determined from the Fabry-Pérot fringes in the measured transmission spectra. For a fringe spacing of $\Delta\lambda$, the optical group index is

$$n_g = \frac{\lambda_c^2}{2l_c\Delta\lambda} \tag{5.7}$$

where λ_c is the center wavelength between fringes and l_c is the cavity length[115]. As shown in Fig. 5.26, several of the line defect waveguides have clear oscillations in their spectra. The oscillations are visible across the entire wavelength range with a period of approximately 2 nm. The oscillations were resolved in the transmission measurements by using a wavelength resolution of 0.1 nm. Fringes with the same period were not reproduced in transmission measurements of either the unpatterned ridge waveguide or in the absence of any waveguide (fiber to fiber transmission), suggesting that the fringes are due to the photonic crystal acting as an optical cavity. The fringes were observed with the same periodicity in multiple waveguides with the same photonic crystal geometry. While fringes with the same periodicity were not observed in the ridge waveguide, finer oscillations with sub-nm periodicity were observed (Fig. 5.27 (b)). To accurately measure these fringes, a wavelength resolution of 0.02 nm was used. For both the W1 and ridge waveguides, the fringe spacing is nearly constant across the entire wavelength region.

The group index was calculated by first calculating the fast Fourier transform (FFT) to view the spectrum in reciprocal space. As shown in Fig. 5.27 (c) and (d), there is a peak in the spectrum for the W1 waveguide at 0.43 nm^{-1} and a peak in the ridge waveguide spectrum at 4.6 nm^{-1}. The corresponding oscillation periods are 2.35 nm and 0.22 nm for

the W1 and ridge waveguides, respectively. It is noted that the fringe spacings differ by an order of magnitude. For measurements done in the same wavelength range, the fringe spacing is determined by the cavity length and group index. Both wafers (YKJ-155A and YKJ-155B) have a total waveguide length of approximately 2.4 mm. If the observed fringes for the W1 waveguide are due to Fabry Pérot reflections from the facets, then the group index calculated from Eqn. 5.7 would be less than 1, which is not impossible but highly unexpected. Using a cavity length of 37 µm corresponding to the straight segment of the PC, the group index is 8.8.

The group index dispersion was investigated by applying Eqn. 5.7 over a sliding wavelength range to consider multiple fringes in a single calculation. This approach was applied to waveguide G2 WG1 on wafer YKJ-155B. The measured transmission of this waveguide and its calculated group index are shown in Fig. 5.28. The drop in the transmission is in agreement with the simulation shown in Fig. 5.6 (b) apart from a slight blue-shift, likely due to a slightly lower mode index of the fabricated waveguide versus that used in the simulation. The calculated group index is nearly flat over the measurement range of 1500-1560 nm, with a slight increase in group index as the band edge is approached. It is noted that the W1 waveguides whose transmission is shown in Fig. 5.27 (a) and 5.28 have the same PC geometry and are fabricated on wafers with the same $BaTiO_3$ thickness. The group index of the former (YKJ-155A G3T WG3), however, is approximately half the value of that measured for the latter (YKJ-155B G2 WG1). This is attributed to the multiple ridge waveguide modes that are supported by the wider ridge waveguide of YKJ-155A G3T WG3.

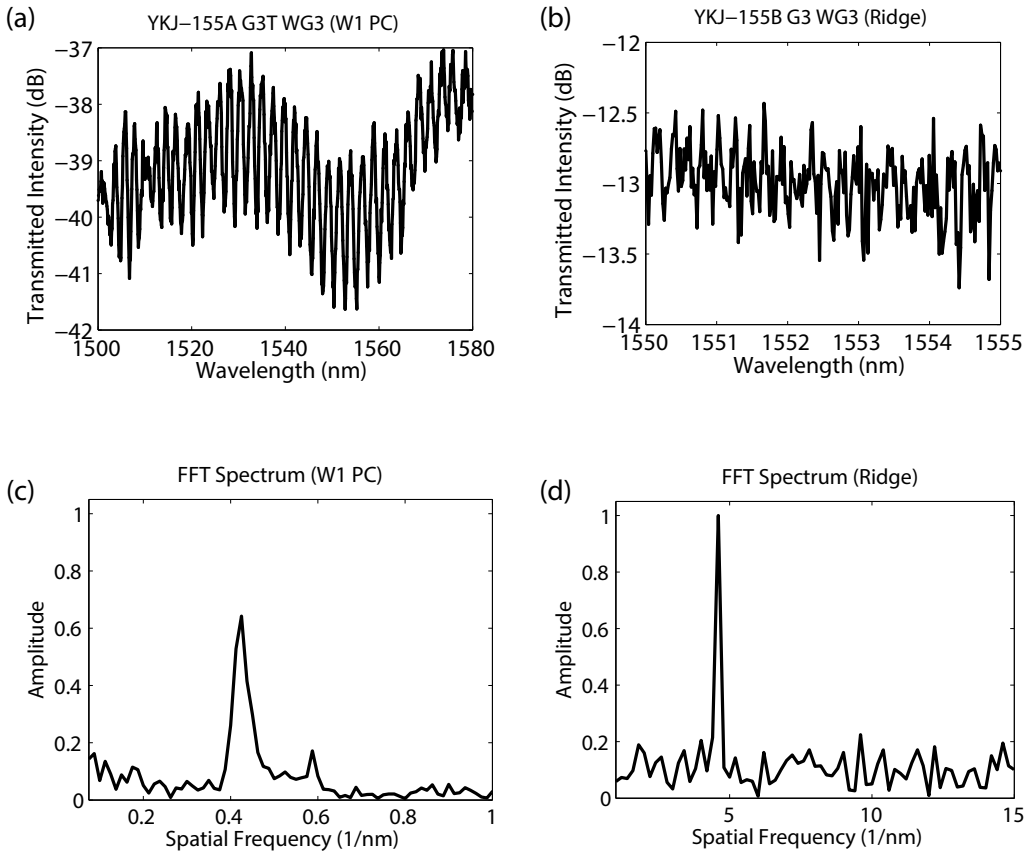

Figure 5.27. Measured transmission spectra of line defect (a) and ridge (b) waveguides. Calculated fast Fourier transform of the transmission spectrum of the W1 (c) and ridge (d) waveguides.

In both cases for the W1 waveguides, the measured group index is slightly higher than that predicted by simulation (Fig. 5.2). This discrepancy is tentatively attributed to the oversimplification of the two dimensional simulations. The actual waveguide consists of holes that do not fully penetrate the $BaTiO_3$ film and hence guides a hybrid ridge/PC mode. Furthermore, as shown in the calculated band structures of Fig. 5.2, it is likely that the PC waveguide is multi-mode. The ridge waveguide mode is also multi-mode for wider

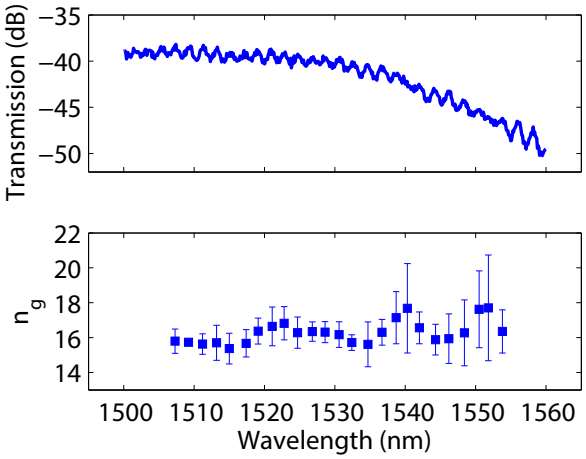

Figure 5.28. Measured transmission of waveguide G2 WG1 on wafer YKJ-155B and its wavelength dependent group index calculated from the fringe spacing.

ridge waveguides. Multi-mode effects have not yet been investigated for these waveguides but would be a worthwhile factor to consider in future work.

The most significant observation about the measured transmission of the W1 waveguides is the optical bandwidth over which the fringes are present. In resonant optical devices, the normalized delay bandwidth product (DBP), defined as

$$DBP = n_g \frac{\Delta\omega}{\omega} = n_g \frac{\Delta\lambda}{\lambda}$$

is a figure of merit for assessing the buffering capacity of slow light waveguides[9]. The buffering capacity describes the amount by which optical pulses are slowed. Slowing down of optical pulses is an important functionality for storing and adjusting the timing of optical pulses to be processed all-optically. For the waveguide YKJ-155B G2 WG1, an average group index of 16 is measured across a 50 nm bandwidth centered at 1530 nm, which gives a DBP of 0.52. The maximum previously reported DBP for a photonic

crystal waveguide is 0.37[76]. The especially wide optical bandwidth with flat group index reported here is unexpected given the simulated group index and the values for DBP reported in the literature. As such, it would be of interest to measure the group index using an alternative method to confirm the results. One such alternative method is via low coherence reflectometry, as proposed by Combrié et al[33].

5.7. Proposed Model for $\chi^{(2)}$ Enhancement in Photonic Crystal Waveguides

The phase delay in a waveguide with high group index is, in the most general sense, given by[132]

$$\delta\phi = \frac{2\pi L}{\lambda}\Gamma\frac{\delta n}{n}n_g \tag{5.8}$$

where $\delta\phi$ is the total phase delay, L is the interaction length, λ is the optical wavelength, n is the optical index, δn is the modulation of the refractive index, and Γ is the fraction of optical power confined in the region in which δn is being applied. For the case of an electro-optic material, the refractive index change is given by

$$\delta n = \frac{1}{2}n^3 r_{eff}\frac{V}{g}m(f) \tag{5.9}$$

where r_{eff} is the effective electro-optic coefficient representing the overall contribution from the electro-optic tensor elements, and V is the applied voltage across a gap spacing g. The effects of index mismatch between the co-propagating microwave and optical fields, impedance mismatch of the electrodes to that of the driving microwave signal, and attenuation losses of the microwave signal are accounted for by the factor $m(f)$, which is the electro-optic magnitude response of the device. It is unitless and has a value ≤ 1. The

measurement and modeling of $m(f)$ are described in Section 3.7.2. Substituting 5.9 into 5.8 gives the general relation for phase shift in a $\chi^{(2)}$ waveguide due to the electro-optic effect:

$$\delta\phi = \frac{\pi L}{\lambda}\Gamma n^2 n_g r_{eff}\frac{V}{g}m(f)$$

Here, we consider the reduction in voltage-length product and enhancement of the electro-optic coefficient in $\chi^{(2)}$ nonlinear waveguides. The approach is generalized for a photonic crystal modulator having a total interaction length L within which a photonic crystal of length L_P is placed. The length of the interaction region without the photonic crystal is $L_R = L - L_P$. The total phase delay in the ridge waveguide region without the photonic crystal is

$$\delta\phi_R = \frac{\pi L_R}{\lambda}\Gamma n^2 n_{g,R} r_{eff}\frac{V}{g}m(f)$$

It is noted that, for the case of a ridge waveguide where the operating wavelength is sufficiently far from the cutoff wavelength as is the case for the ridge waveguide devices reported in this work, the group index is nearly equal to the waveguide mode index n. The two indices, however, are kept separated in Eqn. for mathematical simplifications to follow.

The phase delay in the photonic crystal segment is given similarly by

$$\delta\phi_P = \frac{\pi L_R}{\lambda}\Gamma n^2 n_{g,P} r_{eff}\frac{V}{g}m(f)$$

The total phase delay $\delta\phi_T$ in the composite ridge and photonic crystal waveguide is then

$$\delta\phi_T = \delta\phi_R + \delta\phi_P = \frac{\pi}{\lambda}\Gamma n^2 r_{eff}\frac{V}{g}m(f)\left(n_{g,R}L_R + n_{g,P}L_P\right) \tag{5.10}$$

Using the result given in Eqn. 5.10 , the half-wave voltage of the composite waveguide modulator is obtained by setting $\delta\phi_T = \pi$ and solving for the voltage, which gives

$$V_\pi = \frac{\lambda g}{n^2 r_{eff} \Gamma L m(f)} \left[(1-x)n_{g,R} + x n_{g,P}\right]^{-1}$$

Solving for the voltage length product $V_\pi \cdot L$ gives

$$V_\pi \cdot L = \frac{\lambda g}{n^2 n_{g,R} r_{eff} \Gamma m(f)} \left[(1-x) + x(n_{g,P}/n_{g,R})\right]^{-1} \tag{5.11}$$

The generalized equation for the voltage-length product of a composite ridge/photonic crystal modulator should give the expected result for a ridge waveguide modulator when the photonic crystal segment is absent ($L_P = 0$). A simplification of Eqn. 5.11 indeed gives this result:

$$V_\pi \cdot L = \frac{\lambda g}{n^2 n_{g,R} r_{eff} \Gamma m(f)} \tag{5.12}$$

Comparing Eqn. 5.11 and 5.12, the effective electro-optic coefficient is enhanced in the composite waveguide modulator by the factor

$$f_{eo} = \left[(1-x) + x(n_{g,P}/n_{g,R})\right] \tag{5.13}$$

This is the same factor by which the voltage-length product is reduced. The enhancement factor is plotted versus the fractional filling factor x for different group indices between 5 and 25 in Fig. 5.29. Group indices in this range represent values which can be obtained experimentally. As discussed in Chapter 7, these values are also optimal for

enhancing device performance with respect to both voltage-length product and electro-optic bandwidth; higher values of group index result in larger index mismatch losses, which provide diminishing returns on electro-optic bandwidth. The plot shows that, even for a moderate group index in the photonic crystal region, a significant enhancement factor can be obtained. To put these calculations into perspective with what is currently technologically feasible, the same data is also plotted versus actual photonic crystal length for a modulator with total interaction length of 1 mm in Fig. 5.29 (b). As previously discussed in Section 5.5, the optical insertion losses in the photonic crystal waveguides currently limit the feasible total photonic crystal length to approximately 100 µm. With this length, an enhancement factor of more than 2 is predicted for a group index of 25, which would reduce the modulator voltage and power by factors of more than 2 and 4, respectively. Alternatively, the modulator size could be reduced, resulting in lower length-dependent microwave losses and a larger electro-optic bandwidth. Detailed calculations showing the range of possible combinations of voltage length product and electro-optic bandwidth in photonic crystal modulators are discussed in Chapter 7.

5.8. Summary and Conclusions

In this chapter, the modeling, fabrication, and characterization of hexagonal lattice PC waveguides and W1 line defect waveguide with hexagonal symmetry were discussed. As reflected in this chapter, the modeling, fabrication, and characterization are highly interdependent. The synergistic approach adopted here resulted in the realization of hexagonal lattice PC waveguides with record high band edge sharpness for any ferroelectric material and W1 line defect waveguides with a moderate group index of 16 over a wide

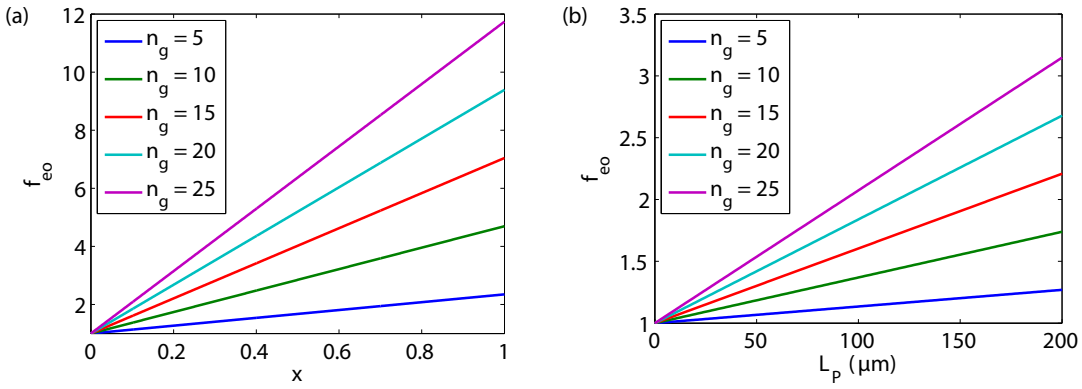

Figure 5.29. (a) Theoretical enhancement factor versus photonic crystal fractional filling factor x for photonic crystal group indices between 5 and 25. (b) Enhancement factor versus photonic crystal length for a total interaction length of 1 mm.

optical bandwidth of 50 nm with 1530 nm center wavelength. The major results presented in this chapter are summarized as follows:

(1) An effective medium approach in combination with two dimensional simulation geometry was found to provide good agreement in the simulated and measured transmission of hexagonal lattice and W1 line defect waveguides.

(2) The conical hole profile from ion beam milling was characterized and used to provide feedback to modeling. Knowledge of the depth dependence of the hole geometry was found to be instrumental in obtaining agreement between the simulated and measured transmission of both types of waveguides.

(3) Hexagonal lattice photonic crystal waveguides were characterized having a record high band edge sharpness of 2.0 dB/nm for all ferroelectric photonic crystal waveguides.

(4) Line defect W1 waveguides were demonstrated with measured transmission in agreement with the simulated transmission and an average group index of 16

across a 50 nm optical bandwidth. This demonstrates the applicability of these devices for wideband wavelength-division multiplexing schemes.

(5) A model is proposed for the enhancement of the electro-optic coefficient in $\chi^{(2)}$ photonic crystal waveguides in which the enhancement is due to the slowdown factor, $n_{g,P}/n_{g,R}$, where $n_{g,P}$ is the photonic crystal group index and $n_{g,R}$ is the ridge waveguide group index. An enhancement factor greater than 3 is predicted for a photonic crystal waveguide with 200 µm length and group index of 25.

The properties of photonic crystal waveguides elucidated in this work using $BaTiO_3$ as the waveguiding medium are of interest from both technological and scientific perspectives. Photonic crystal waveguide devices have been demonstrated or proposed using various optoelectronic platforms for directional couplers[35,95] and delay lines for all-optical signal processing[109] and microwave photonics[124]. These devices could potentially benefit from the enhanced functionality obtained when using a $\chi^{(2)}$ ferroelectric material as the optical guiding medium. As shown in the following chapter, both the hexagonal lattice PC waveguides and W1 line defect waveguides demonstrated here are additionally suitable for use in electro-optic modulators, where an enhancement of the electro-optic coefficients and reduction in modulation voltage are obtained by application of the theory presented in Section 5.7.

CHAPTER 6

Electro-Optical Properties of $BaTiO_3$ Thin Films

6.1. Introduction

The electro-optic properties of $BaTiO_3$ thin films and $BaTiO_3$ phase modulators were investigated at optical wavelengths in the range 1500-1580 nm and for modulating fields between 100 Hz and 40 GHz. At low frequencies, the half-wave voltage and effective in-device electro-optic (EO) coefficient were measured using a time-domain approach in which the device was over-driven outside its linear response regime in a polarizer-sample-compensator-analyzer (PSCA) setup as described in Section 3.7.1. At frequencies between 10 GHz and 50 GHz, an optical spectral analysis technique was used to probe EO material and device properties of $BaTiO_3$ modulators for the first time. At frequencies between 10 MHz and 30 GHz, a vector network analyzer was used to measure the frequency-dependent EO response.

The device properties of interest obtained from the EO measurements are the half-wave voltage, voltage-length product, and 3 dB EO bandwidth. The half-wave voltage — defined as the voltage required for a π phase shift — is an important device property that determines both the power consumption and modulation depth. The voltage-length product — defined as the product of the half-wave voltage and the electro-optical interaction length — is a figure of merit that describes the strength of the electro-optical interaction and is sometimes (imprecisely) used to describe the device "efficiency." The voltage-length

product can be quantified for any phase modulator regardless of the physical modulation mechanism; it is hence an important figure of merit for comparing different optoelectronic materials. Record low voltage-length products for $BaTiO_3$ films of $0.39\,V \cdot cm$ ($0.45\,V \cdot cm$) were measured at a modulation frequency of 100 Hz (1 MHz), which is nearly an order of magnitude smaller than the state-of-the-art for silicon modulators[117].

The 3 dB EO bandwidth, defined as the modulation frequency range over which the EO intensity response is within 3 dB of the value measured at low frequency, is an important metric for all intensity modulators regardless of the modulation mechanism. The 3 dB EO bandwidth was found to be larger for devices with wider electrode gap spacings on thinner $BaTiO_3$ films. Good agreement was found between the measured EO response and that predicted by the model of Rahman and Haxha[58], which includes the frequency-dependent microwave losses discussed in Chapter 4. Using the measured microwave properties and the model of Rahman and Haxha as a guide, a record large 28 GHz 3 dB EO bandwidth for $BaTiO_3$ conventional ridge waveguide modulators is demonstrated here (Fig. 6.8, top right plot).

The EO material properties obtained from the measurements discussed here are the in-device effective EO coefficient and its dependence on both applied ac and dc electric fields. The in-device effective EO coefficient is a scalar property that is dependent on the direction of the applied field, ferroelectric domain microstructure, and optical propagation direction as determined by the device architecture. For films processed with the same growth and annealing steps, the saturated effective EO coefficient at low frequencies (1 MHz) was found to increase with film thickness — from 147 pm/V for a 260 nm thick film to 306 pm/V for a 500 nm thick film — in agreement with the trend predicted by a

simple semi-empirical microstructural model for polydomain ferroelectric films presented in Chapter 7. The bias field at which the effective EO coefficient saturates was found to decrease with film thickness. This is tentatively attributed to a relaxation in strain energy and hence reduction in activation energy for domain wall motion and domain switching with increasing film thickness.

While appropriate for characterization at lower modulation frequencies, time-domain approaches are inadequate for studying EO material properties at high frequencies. This is especially important as researchers continue to investigate material properties at modulation frequencies above the operating limit of most current time-resolved detectors. To circumvent this issue, the optical spectral analysis technique was demonstrated here to study the EO material properties of $BaTiO_3$ films above 10 GHz for the first time. Using the method described in Section 3.7.3 along with the measured microwave properties of Chapter 4 and the model of Rahman and Haxha, the effect of microwave losses were isolated from the measurements, allowing for a first measurement of the effective EO coefficient in this frequency range for $BaTiO_3$ films. The effective EO coefficient decreased with modulation frequency over the range of 10-30 GHz, following the same trend measured previously for the dielectric constant[57]. In addition to the frequency response, the high sensitivity of the OSA technique made it especially suitable for investigating the wavelength-dependent EO properties of photonic crystal waveguide modulators, allowing for an experimental confirmation of the theory for EO coefficient enhancement presented in Section 5.7. A monotonic increase in the effective EO coefficient was measured approaching the photonic crystal band edge, indicating an increase in optical group index in agreement with theory. In the dispersion-engineered line defect (W1) modulators, a device enhancement factor of

1.4 was measured across a 50 nm wide optical bandwidth centered at 1524 nm. Within the photonic crystal region, an enhancement factor of 12 and effective EO coefficient of 900 pm/V are measured. This is the first demonstration of slow-light enhancement of the EO coefficient in a $\chi^{(2)}$ waveguide at microwave modulation frequencies. In addition to studying $\chi^{(2)}$ (Pockels effect) materials, the OSA technique demonstrated here is suitable for measuring the EO properties of any type of phase modulator material. It is expected that this technique will be especially useful for probing the high-frequency characteristics of silicon, graphene, and transition metal dichalchogenide materials.

6.2. Time Domain Measurements

Electro-optic properties of $BaTiO_3$ phase modulators were investigated at low frequency (1 MHz) using a polarizer-sample-compensator-analyzer (PSCA) experimental technique. The PSCA setup and the modeled large signal electro-optic response is discussed in detail in Section 3.7.1. Using this technique, the half-wave voltage and effective in-device EO coefficient were measured as a function of applied dc bias field for devices on $BaTiO_3$ films with thicknesses of 260, 360, and 500 nm. The PSCA measurement technique was also used to measure the modulation depth of $BaTiO_3$ modulators at low frequency.

An example EO waveform measured using the PSCA setup is shown in Fig. 6.1. The measured waveform shows a clear electro-optic response that is in remarkable agreement with that predicted by the model derived in Section 3.7.1. The measurement shown in Fig. 6.1 was obtained for a 1 mm long modulator on sample YKJ-155B with 5 µm electrode gap spacing. A 100 Hz, 8 V_{pp} applied signal with 3 V dc bias was applied to the device.

The measured voltage-length product of 0.39 V·cm is a record low value for all $BaTiO_3$ modulators in the literature.

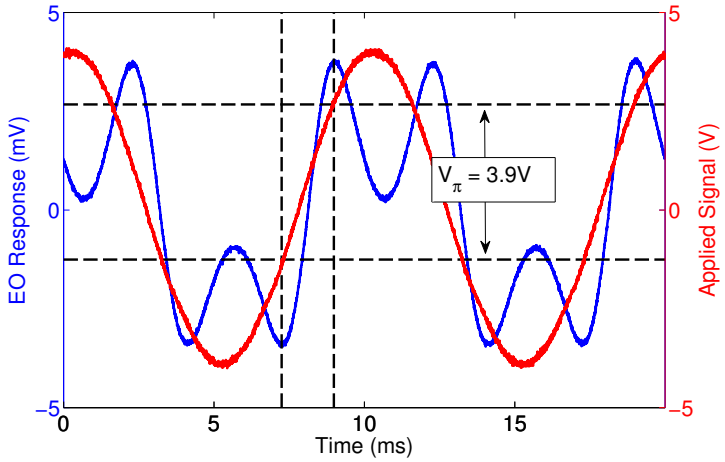

Figure 6.1. Example of a measured electro-optic waveform showing the procedure for directly measuring the half-wave voltage by comparing the input and output signals.

The agreement between the measured EO response and that predicted by the model derived in Section 3.7.1 is further demonstrated in Fig. 6.2. The measured response shown at the left side of the figure is for device G3 WG1 with a 5 µm wide electrode gap spacing and 1 mm long electrodes on sample YKJ-155A. The measurements were obtained while applying a constant dc bias voltage of 5 V, for which a 7.54 V half-wave voltage was measured. The over-driven electro-optic response using a PSCA setup was measured for peak-to-peak voltages of 12, 15, 18, and 20 V_{pp} at a modulation frequency of 1 MHz. For the configuration used in the PSCA measurements, the modeled response given by Eqn. 3.6 and for $V_\pi = 7.54$ V is plotted at the right for the same applied peak-to-peak voltages. Apart from a slight deformation in the measured waveforms that is due to the RC response time of the measurement system, excellent agreement is obtained between the

measured and modeled response, demonstrating the efficacy of the measurement technique for determining the low-frequency half-wave voltage.

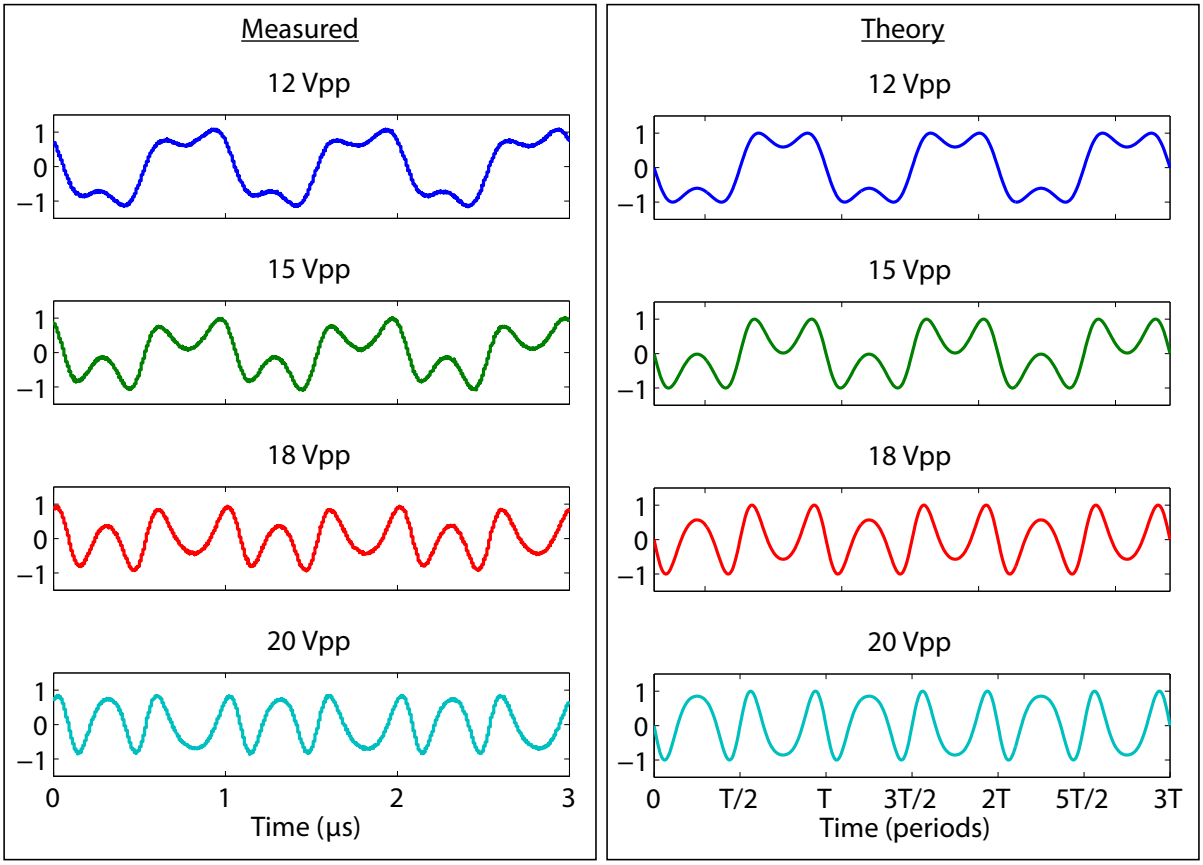

Figure 6.2. Comparison of the modeled and measured electro-optic response versus applied peak-to-peak voltage. The measurements were done on device YKJ-155A G3 WG1 with a 5 V applied dc bias.

The modulation depth of the same device was measured at low frequency as a function of applied peak-to-peak voltage. The modulation depth or extinction ratio (ER) in dB is defined as

$$ER = 10 \log_{10} \left(\frac{T_{max}}{T_{min}} \right)$$

where the maximum and minimum measured transmission values (T_{max} and T_{min}, respectively) are defined in Fig. 6.3 (a). The measured extinction ratio is nearly linear with applied voltage up to V_π, at which the extinction ratio saturates as expected from the PSCA model. A maximum extinction ratio of 9.8 dB is measured in the PSCA configuration.

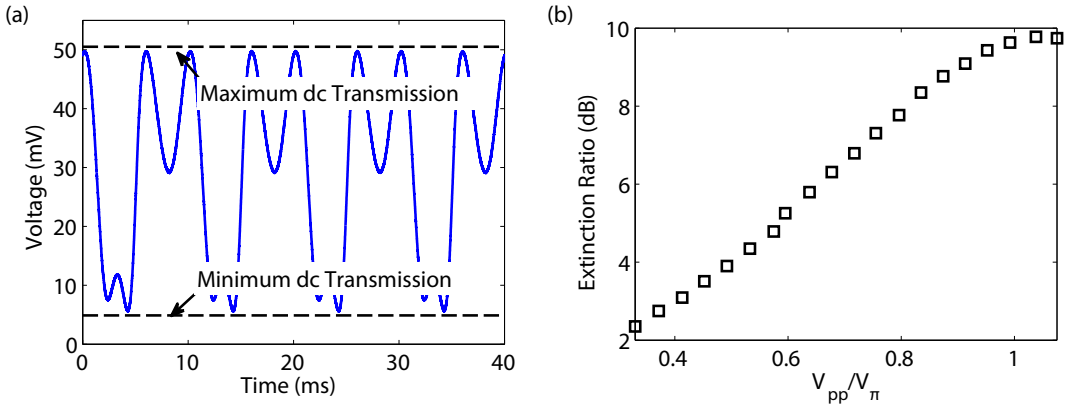

Figure 6.3. (a) Example of an over-driven electro-optic response waveform measured through a PSCA setup with the maximum and minimum transmission values defined. (b) Extinction ratio versus applied voltage obtained from the measured electro-optic response waveforms. Sample: YKJ-146A G4 WG2.

The half-wave voltage measurements were used to measure the bias dependent electro-optic response of $BaTiO_3$ films with different thicknesses at a modulation frequency of 1 MHz. The dependence of the EO properties on the film thickness is of interest for a number of reasons. As discussed in Chapter 4, the microwave losses — which include index mismatch with the co-propagating optical wave, attenuation losses, and reflection losses — all increase with film thickness, hence thinner $BaTiO_3$ films are predicted to have higher electro-optic bandwidths. It is thus of interest to determine if the electro-optic properties also have a thickness dependence. The film thickness is expected to impact the dielectric and electro-optic properties primarily through the epitaxial strain, which affects

the ferroelectric domain structure. In addition to studying the EO properties versus film thickness, the effect of annealing cooling rate was also studied by performing fast and slow cooling steps on two pieces of the same wafer (YKJ-155A and YKJ-155B).

An example of the measured ac-coupled bias-dependent EO response is shown in Fig. 6.4 for device G3 WG1 on wafer YKJ-155A. The measured EO response is shown for applied bias voltages of 4, 6, 8, and 10 V (8, 12, 16, and 20 kV/cm bias field, respectively) and an applied ac field with 12 V_{pp} swing and 1 MHz modulation frequency. The double frequency component of the measured EO response increases with applied bias and appears to remain unchanged beyond 8 V applied bias. According to the modeled response discussed in Section 3.7.1, the increasing nonlinearity of the response with increasing bias voltage indicates that the half-wave voltage decreases and the effective EO coefficient effectively increases with applied bias voltage for moderate dc bias fields, in agreement with previously observed trends for $BaTiO_3$ thin films[141,143,144]. This is due to an increase in the poling efficiency of ferroelectric domains with a larger applied bias field. For all films investigated in this study, the electrodes were oriented along <110> such that the applied electric field is along $<1\bar{1}0>$. For this orientation, all four ferroelectric domain variants with polar axis in the plane of the film and along [100] experience a poling field of $E/\sqrt{2}$ perpendicular to the polar axis and are hence subject to 180° switching[103]. A saturation in the measured electro-optic coefficient results when the poling field is sufficiently large to have switched all in-plane domain variants such that the dipole moments are aligned with the applied field.

The bias dependent half-wave voltage and effective in-device EO coefficient are plotted for devices on wafers of different $BaTiO_3$ thickness in Fig. 6.5. The half-wave voltage was

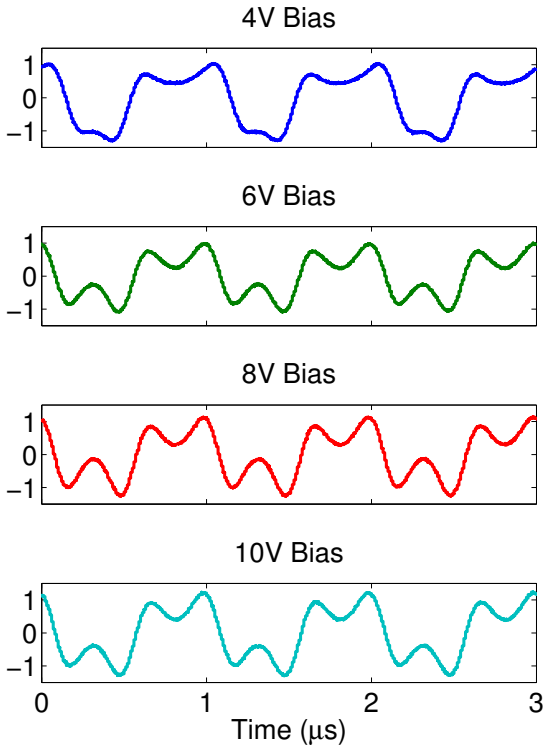

Figure 6.4. Measured ac-coupled EO response through the PSCA setup as a function of applied dc bias voltage. The measurements were done on device G3 WG1 on wafer YKJ-155A.

obtained directly from the over-driven electro-optic response, as described in Section 3.7.1, and the effective EO coefficient was calculated using Eqn. 3.8 and the mode indices and overlap factors calculated in Section 7.4. For each device, the EO coefficient is observed to increase with applied bias field. A clear saturation of the EO coefficient is observed for the devices on the 500 nm thick films, while the saturation is less clear for the other two films with thicknesses of 260 and 360 nm. This is attributed to the larger field required to fully pole the in-plane ferroelectric domains of thinner films and the limitations of the measurement setup, namely the 20 Vpp maximum voltage swing of the SRS DS335 function generator. The bias field at which the electro-optic coefficient saturates was

estimated from the plots in Fig. 6.5 as the field at which the electro-optic coefficient stops monotonically increasing for the 260 and 360 nm thick films and as the field at which the EO coefficient achieves 90% of its maximum value for the 500 nm thick film. The saturation bias field and the corresponding EO coefficient at this field are plotted versus film thickness in Fig. 6.6. The saturation bias field is observed to decrease with increasing film thickness, and the saturated EO coefficient is observed to increase with film thickness. The bias field dependence on film thickness is in agreement with the observed dependence of the coercive field on film thickness for epitaxial $BaTiO_3$ films on (100) MgO[66]. The decreasing coercive field was explained by Jeong et al to be due to a relaxation of in-plane strain imposed by the epitaxy with increasing film thickness[66]. The increase in effective EO coefficient with increasing film thickness follows the same trend for the predicted increase in the in-plane dielectric constant with increasing film thickness explained by a semi-empirical model in Section 7.2. As explained in Section 7.2, the EO coefficient tensor elements for $BaTiO_3$ are proportional to the dielectric tensor elements. For example, the largest tensor element r_{51} is given by

$$r_{51} = g_{44} P_s \epsilon_0 (\epsilon_1 - 1)$$

where g_{44} is a quadratic electro-optic tensor element, P_s is the spontaneous polarization, and ϵ_1 is the principal dielectric tensor element along one of the in-plane principal directions. The trend elucidated by the measurements are hence in agreement with the trend predicted by a semi-empirical model, although additional measurements of the spontaneous polarization and Kerr coefficients would be needed to confirm agreement with the above relationship.

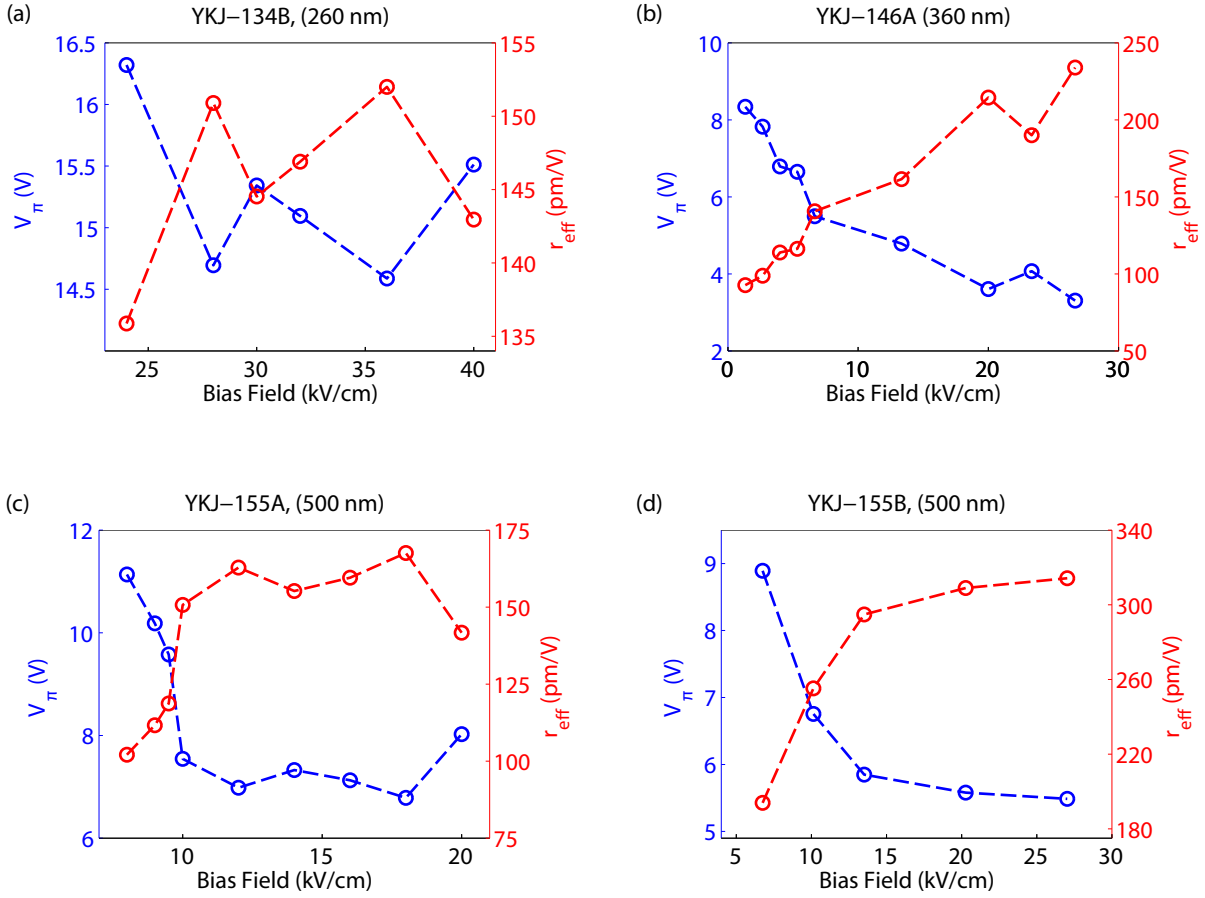

Figure 6.5. Electro-optic coefficient measured on samples YKJ-134B G4 WG2 (a), YKJ-146A G4 WG1 (b), YKJ-155A G3 WG1 (c), and YKJ-155B G2 WG4 (d) versus bias field. All measurements are made with a 1 MHz modulation frequency.

The measurements done on each wafer are summarized in Tables 6.1-6.4. The measurements of maximum r_{eff} and the corresponding bias field and voltage-length product are reported for each electrode gap spacing. As reflected in the measurements, of the 12 to 18 devices on each wafer, it was in many cases not possible to directly measure the half-wave voltage. Several factors contribute to the difficulty in directly measuring the half-wave voltage using the PSCA approach. These include the short modulator

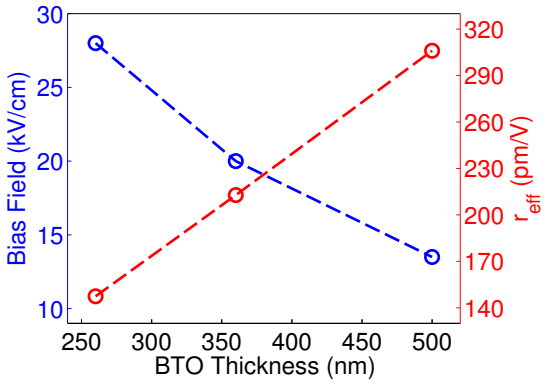

Figure 6.6. Measured saturation bias field and electro-optic coefficient versus film thickness. . The measurements are obtained from samples YKJ-134B G4 WG2, YKJ-146A G4 WG1, and YKJ-155B G2 WG4.

length (1 mm), limited bias voltage (50 V), limited peak-to-peak voltage (20 V_{pp}), and low signal-to-noise ratio due to large optical insertion losses. While these factors did preclude the direct measurement of V_π on several devices, especially earlier ones fabricated with electrodes oriented along <100> and before applying the post-waveguide annealing step, the range imposed by these measurement constraints represent reasonable operating bounds for practical devices. Regardless of these limitations, the half-wave voltage was measurable using the PSCA technique for at least one device on each of the four wafers with post-waveguide annealing. Furthermore, the half-wave voltage was measurable for each electrode gap spacing on wafers YKJ-146A and YKJ-155B.

All the wafers except for YKJ-155A were annealed using a slow cooling step after waveguide fabrication using the annealing parameters in Table A.4. Wafer YKJ-155A was also annealed after waveguide fabrication, but the annealing was done using a fast cooling step with the parameters given in Table A.5. Wafers YKJ-155A and YKJ-155B were cleaved from the same film and hence were subject to the same film growth conditions and post-growth annealing step in oxygen. According to the data presented in Fig. 6.5 and

Tables 6.3 and 6.4, the sample subject to the slow cooling step has a significantly larger saturated EO coefficient. The coercive field, however, appears to be approximately the same. This suggests that the difference in the EO properties of these two films is of a point defect origin rather than due to the strain-induced ferroelectric microstructure. To test this hypothesis, a study of the film chemistry through x-ray photoelectron spectroscopy is recommended similar to that done previously for $BaTiO_3$ films grown by by molecular beam epitaxy[156].

Several trends are observed for the data presented in Tables 6.1-6.4. For all wafers, the minimum half-wave voltage and minimum $V_\pi \cdot L$ for each device increases with the electrode gap spacing, as predicted by the proportional relation between these variables and the gap spacing. There is some inconsistency in the EO coefficient for different gap spacing devices on the same wafer. These inconsistencies are believed to be due to the limitations of the measurement technique. One particular issue with the PSCA approach is the large EO intensity modulation that was observed during measurements in the absence of the analyzer. For a pure phase modulator, no intensity modulation should be observed in the absence of the analyzer. The intensity modulation was determined to be of electro-optic origin and not electrical cross-talk since it changed with applied bias field and disappeared when either the laser was turned off or when the microwave probes were lifted from the electrodes. The intensity modulation was observed on different devices to be either in-phase and out-of-phase with the signal obtained through the PSCA setup, indicating that it could affect the measured half-wave voltage both positively and negatively. There was no general trend observed with the intensity modulation; it was particularly dominant for some devices and absent on others. The intensity modulation

effect is believed to be due to one or both of the facets acting as linear polarizers, an effect that is possibly induced by facet polishing and is hence not systematic. Regardless of the intensity modulation effect, the trends observed with respect to the bias field and film thickness are reasonable.

Table 6.1. Measured electro-optic properties of devices on wafer YKJ-134B (260 nm BTO).

G	WG	Gap Spacing (µm)	V_π (V)	Bias Voltage (V)	Bias Field (kV/cm)	r_{eff} (pm/V)	$V_\pi \cdot L$ (V·cm)
4	2	5	14.6	18	36	152	1.46
3	3	7.5	>20	-	-	<166	>2.0
3	5	12	>20	-	-	<266	>2.0

Table 6.2. Measured electro-optic properties of devices on wafer YKJ-146A (360 nm BTO). The electrode length is 2.9 mm.

G	WG	Gap Spacing (µm)	V_π (V)	Bias Voltage (V)	Bias Field (kV/cm)	r_{eff} (pm/V)	$V_\pi \cdot L$ (V·cm)
4	1	7.5	3.3	20	26.7	233	0.96
4	2	9	8.1	24	26.7	115	2.35
4	3	10.5	9.6	25	23.8	113	2.78

6.3. Frequency Domain Electro-Optic Response

The small-signal frequency-dependent EO response was measured using the vector network analyzer calibrated detection scheme discussed in Section 3.7.2. The measurements were done on wafers with $BaTiO_3$ thicknesses of 260, 360, and 500 nm and for devices with electrode gap spacings of 5, 7.5, and 12 µm on each wafer. The measured response was additionally compared with that predicted by the model of Rahman and Haxha using

Table 6.3. Measured electro-optic properties of devices on wafer YKJ-155A (500 nm BTO).

G	WG	Gap Spacing (µm)	V_π (V)	Bias Voltage (V)	Bias Field (kV/cm)	r_{eff} (pm/V)	$V_\pi \cdot L$ (V·cm)
3	1	5	6.8	9	18	172	0.68
3	3	7.5	>20	-	-	<	>2.0
3	5	12	>20	-	-	<	>2.0

Table 6.4. Measured electro-optic properties of devices on wafer YKJ-155B (500 nm BTO).

G	WG	Gap Spacing (µm)	V_π (V)	Bias Voltage (V)	Bias Field (kV/cm)	r_{eff} (pm/V)	$V_\pi \cdot L$ (V·cm)
2	2	5	4.46	3	6	260	0.45
2	4	7.5	5.49	20	27	314	0.55
2	5	12	11.9	10	8.3	229	1.2
2	6	12	13.2	15	12.5	206	1.3

measured frequency-dependent measurements of the microwave properties to determine the validity of this model for predicting the ultimate electro-optic device performance.

The small signal response is plotted for each film thickness according to electrode gap spacing in Fig. 6.7. The measured EO response decreases monotonically with frequency with ripples in the response due to measurement error. The largest source of random error in the measurements is the movement of the fibers, and the largest source of systematic error is the frequency response of the amplifier and bias tee, which is not removed during calibration prior to measurements but is removed mathematically post-measurement. A horizontal line at -3 dB is drawn in each plot to facilitate visualization of the 3 dB EO bandwidth. The 3 dB EO bandwidth was observed to increase with decreasing film thickness and with increasing electrode gap spacing. The smaller than expected difference in the electro-optic response between devices on the 260 nm thick film versus those on

the 360 nm thick film is due to the addition of a 150 nm SiO_2 buffer layer on the 360 nm thick film, which was added to decrease the microwave losses.

The measured small signal EO frequency response was compared to that predicted by the model of Rahman and Haxha[58] discussed in Section 3.7.2. The response was modeled using the measured frequency-dependent microwave properties (effective index, characteristic impedance, and total microwave loss) presented in Chapter 4. The modeled and measured responses are shown for each device in Fig. 6.8. For all devices, there is a local minimum in the modeled response at approximately 15 GHz, which is where there is the largest discrepancy in most cases with the measured response. In all cases, the modeled 3 dB EO bandwidth is equal to or less than that which is obtained from the measured response. The discrepancy is quantified in Table 6.5, which shows the measured and modeled EO bandwidth for each device. The measured EO 3 dB bandwidth was obtained as the frequency at which the EO response falls below -3 dB without having first fallen below -5.5 dB. As shown in Table 6.5 and Fig. 6.8, the modeled and measured EO bandwidths show the same general trends of increasing bandwidth with larger gap spacing and smaller film thickness; the modeled response, however is a more conservative estimate.

The major difference between the modeled and measured response is that the measured response includes the effect of the frequency-dependent EO coefficient while the modeled response does not. By using the measured frequency-dependent microwave index, impedance, and attenuation losses in the model, the effects of the frequency-dependent dielectric constant are included in the modeled response. The frequency dependence of these terms may implicitly affect the modeled EO response; however, the absence of the electro-optic coefficient from the model mathematically indicates that the intrinsic EO

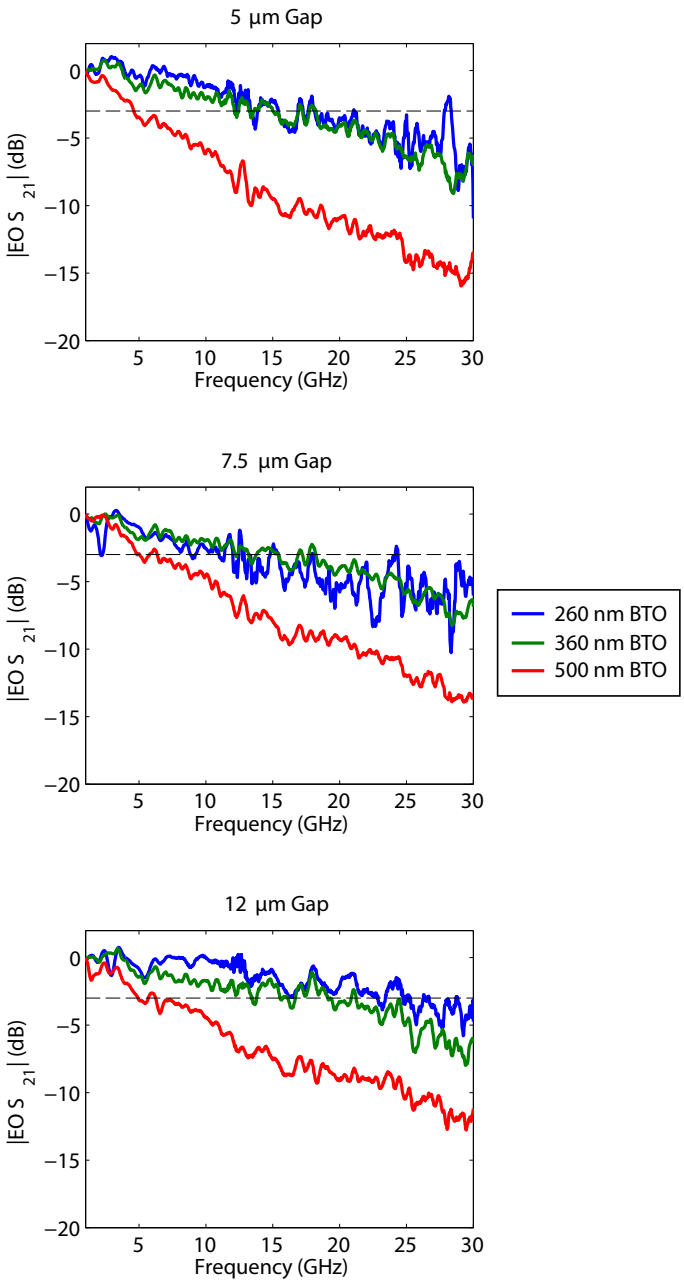

Figure 6.7. Measured electro-optic frequency response of ridge waveguide modulators on wafers with $BaTiO_3$ film thicknesses of 260, 360, and 500 nm. The devices have 1 mm long electrodes. The data is plotted according to electrode gap spacing.

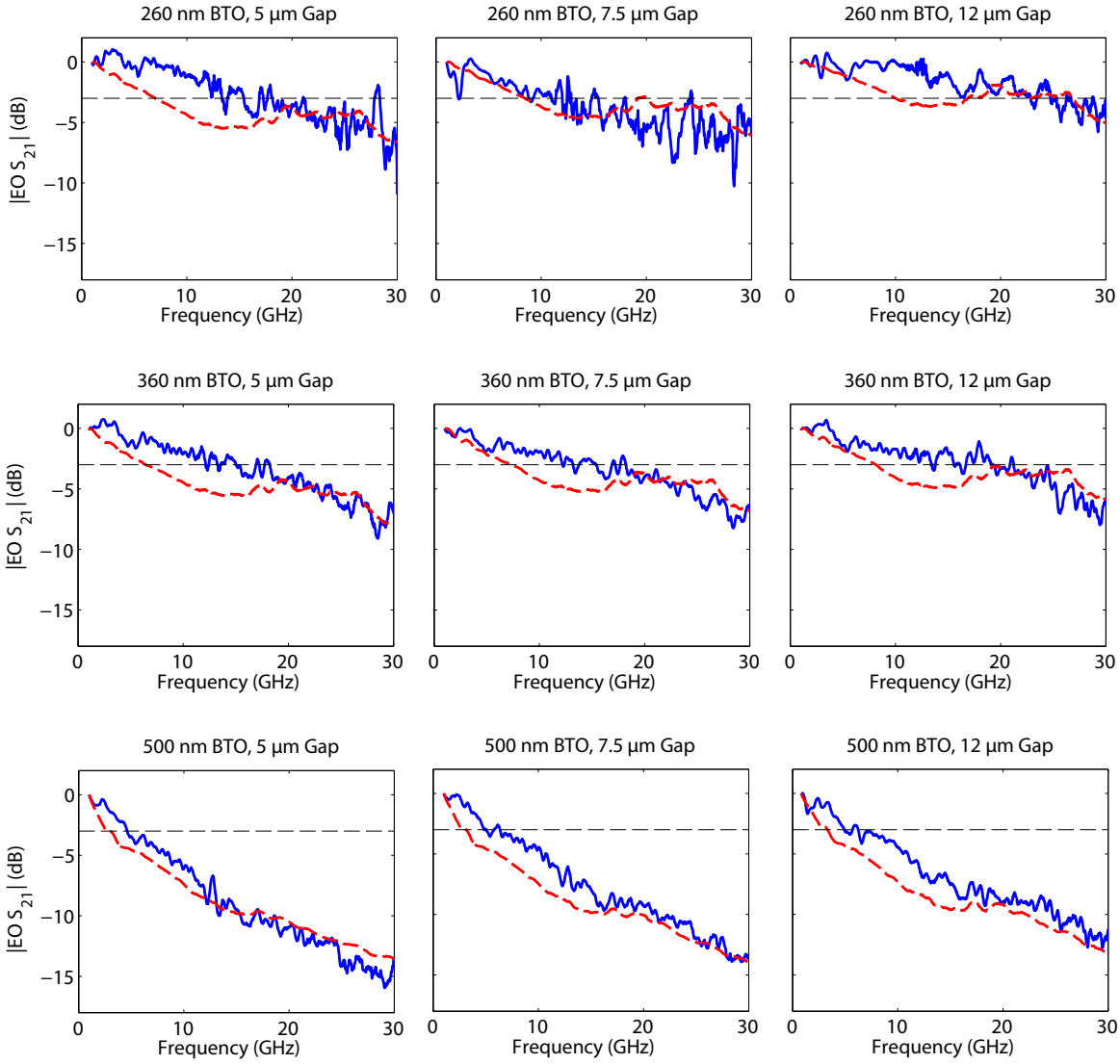

Figure 6.8. Comparison of the measured and modeled electro-optic frequency response for modulators with gap spacings of 5, 7.5, and 12 µm on wafers with $BaTiO_3$ thicknesses of 260, 360, and 500 nm. The measured responses are given by the blue solid curves, and the modeled responses are given by the red dashed curves.

material response is frequency independent. The model of Rahman and Haxha may be ammended by multiplying the response given by Eqn. 3.9 by a frequency-dependent

Table 6.5. Comparison of the modeled and measured 3 dB electro-optic bandwidths.

Sample	Thickness (nm)	G	WG	Gap Spacing (µm)	3 dB EO Bandwidth (GHz) Modeled	Measured
		2	1	5	7.0	21
YKJ-134B	260	2	3	7.5	20	15
		2	6	12	27	28
		2	1	5	6.4	18
YKJ-146B	360	3	4	7.5	7.3	18
		3	6	12	8.1	21
		2	2	5	2.6	4.6
YKJ-155B	500	3	4	7.5	3.1	6.3
		3	6	12	3.3	6.2

magnitude response term for the effective EO coefficient of the form $m_{eo} = r_{eff}(f)/r_{eff}(0)$, where $r_{eff}(f)$ is the frequency-dependent effective EO coefficient and $r_{eff}(0)$ is the EO coefficient at a low frequency reference point, i.e. at 1 MHz. The modified EO magnitude response would then be of the form

$$m(f) = m_{mw}(f)m_{eo}(f)$$

where $m_{mw}(f)$ is the modeled response given by Haxha et al[58]. In order to apply this model, the measured electro-optic coefficient between 10 MHz and 10 GHz would need to first be measured. This could be achieved by adapting the optical spectral analysis technique described in Sections 3.7.3 for measurements below 10 GHz by using an optical spectrum analyzer with a narrower resolution bandwidth.

Since the modeled EO response plotted in Fig. 6.8 includes only microwave-dependent losses and excludes an explicit frequency-dependence of the EO coefficient, the modeled response can be used to remove the effects of the microwave field on any analysis of the EO

coefficient at microwave frequencies. This is done for determination for the EO coefficient in the 10-40 GHz range using the optical spectral analysis technique in Section 6.4.

6.4. Optical Spectral Analysis

The optical spectral analysis technique discussed in Section 3.7.3 was used to measure the effective in-device EO coefficient in $BaTiO_3$ modulators for modulation frequencies between 10 and 30 GHz and for optical wavelengths in the range of 1500 to 1580 nm. Measurements were done on conventional ridge waveguide, hexagonal lattice photonic crystal, and line defect (W1) photonic crystal waveguide modulators. The measured raw EO sideband response versus frequency is first discussed. Using these measurements and the microwave measurements discussed in Chapter 4 along with the EO response model of Rahman and Haxha[58], the frequency- and wavelength-dependent EO coefficients of all three types of modulators are calculated. Finally, the modulation voltage-dependent response is discussed, from which the high frequency phase delay is obtained.

6.4.1. Frequency Dependent Electro-Optic Sideband Response

The measured raw phase modulated sideband response as a function of frequency for conventional modulators for two different wafers is given in Fig. 6.9. The measurements were taken with a -3 dBm modulation input power to the microwave amplifier and 10 V dc bias. A diode laser with 1561.7 nm operating wavelength and nominal output power of 20 mW was used. The sideband response is plotted as intensity versus sideband displacement frequency from the center peak, Δf. The frequency displacement was calculated as

$$\Delta f = \frac{c}{\lambda^2}\Delta\lambda$$

where c is the speed of light in free space, λ is the optical center wavelength of the laser, and $\Delta\lambda$ is the displacement in wavelength from the center peak. According to the theoretical response discussed in Section 3.7.3, the sideband peak is displaced by an amount equal to the modulation frequency. Excellent agreement is obtained between the applied modulation frequency and the position of the sideband peaks with respect to the center laser peak, which indicates that the measured peaks are due to EO phase modulation and are not side peaks of the laser. At low modulation frequencies, e.g. 10 GHz, sidepeaks up to order 3 are measured for a noise floor of -85 dBm obtained when the OSA is set to its highest sensitivity level. As expected, the higher order peaks of the 10 GHz modulation measurement line up exactly with the 20 and 30 GHz first order peaks. the peak shape is a convolution of the filtering lineshape of the optical spectrum analyzer with the lineshape of the laser. The lineshape therefore does not contain information pertaining to the physics of the EO effect in the $BaTiO_3$ film, such as inhomogeneous line broadening due to a distribution of relaxation times. In order to probe these effects, an OSA with a narrower bandwidth would be needed.

The sideband peak intensities decrease with increasing modulation frequency due primarily to microwave losses associated with the electrodes. The dependence of the EO frequency response on the microwave losses was measured independently through both EO frequency response measurements with a calibrated vector network analyzer setup and EO response modeling using microwave properties obtained from S-parameter measurements (see Section 6.3). The frequency-dependent sideband response is equivalent to that measured using a vector network analyzer. This is demonstrated by comparing the frequency dependent responses measured using the VNA and OSA approaches (Fig.

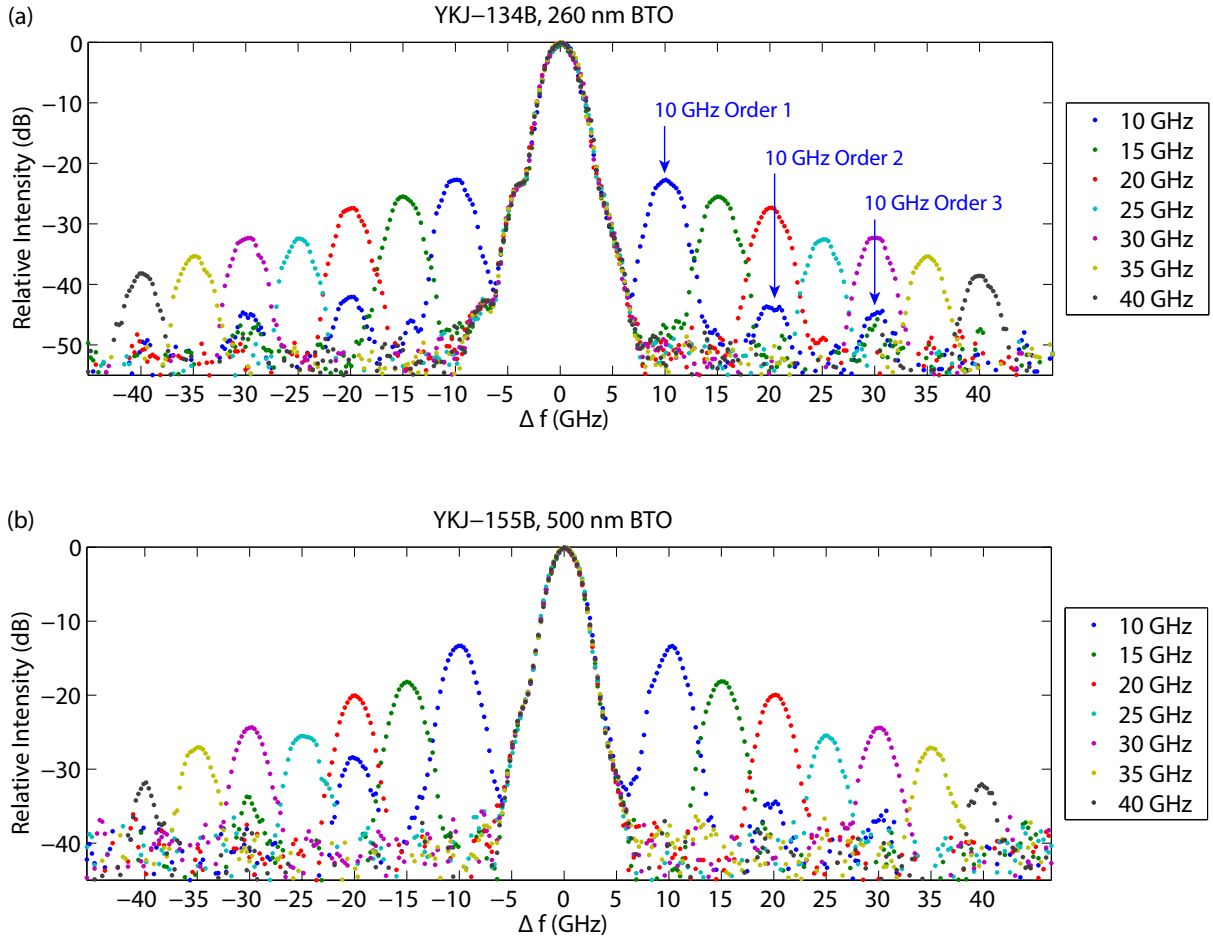

Figure 6.9. Example optical sideband spectra of identical devices on wafers with (a) 260 and (b) 500 nm $BaTiO_3$ thickness. The measurements were done with -3 dBm input power and with a 10 V dc bias field applied. Both devices have an electrode gap spacing of 5 µm.

6.10, where the response measured at 10 GHz (the minimum frequency for the OSA measurements) is taken as the reference. As shown in Fig. 6.10, excellent agreement is obtained between the two measurement techniques. This demonstrates that the OSA technique may be used to measure the EO response out to frequencies beyond that which

can be practically measured with a VNA. Barring limitations from the microwave losses, EO response measurements up to and beyond 1 THz are possible with this technique[75].

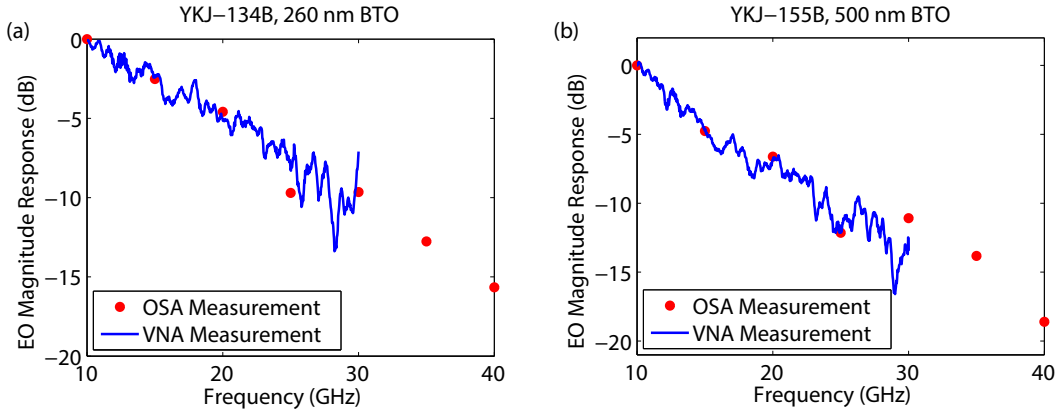

Figure 6.10. Comparison of the electro-optic magnitude frequency response measured using the optical spectral analysis and vector network analyzer methods for devices on (a) 260 nm and (b) 500 nm thick $BaTiO_3$ films.

6.4.2. Frequency-Dependent Electro-Optic Coefficient

Using the measured EO sideband response such as that shown in Fig. 6.9, the modeled EO response such as that shown in Fig. 6.10, and the approach outlined in Section 3.7.3, the frequency-dependent electro-optic coefficient was calculated at modulation frequencies above 10 GHz. The calculated frequency-dependent electro-optic coefficient for modulators with identical electrode structure on films with thicknesses of 260 and 500 nm are shown in Fig. 6.11. The same dc bias and ac input power were used for both sets of measurements. The electro-optic coefficient generally decreases with frequency in the 10-30 GHz range with the sharpest decrease between 10 and 15 GHz. The observed trend of decreasing EO coefficient with frequency follows that of the measured dielectric constant of $BaTiO_3$ thin films on MgO[57] and has a similar frequency dependence to that of the measured

microwave index (see Section 4.3). This is not unexpected given the direct relationship between the effective electro-optic coefficient and the in-plane permittivity, the latter of which decreases with modulation frequency according to Hamano et al[57].

For both devices shown in Fig. 6.11, the measured effective EO coefficient at 10 GHz is approximately half the value measured at 1 MHz for the same electrical bias condition, which suggests that the effective EO coefficient also decreases significantly between 1 MHz and 10 GHz. According to Teranishi et al[147], the decrease in dielectric constant of polycrystalline $BaTiO_3$ between 100 kHz and 10 GHz is dominated by dipolar effects which result from oscillations of domain walls between pinning sites. The transient time-domain electro-optic response of epitaxial $BaTiO_3$ films was previously described by a Kohlrausch-Williams-Watts (KWW) stretched exponential function in time, indicating a distribution of relaxation times due to a non-uniform domain size distribution[98 80]. The decrease in the effective EO coefficient for modulation frequencies between 1 MHz and 10 GHz would hence be expected to be modeled as a Debeye dielectric response with the relaxation time constant τ given by

$$\tau = \frac{\beta\langle\tau\rangle}{\Gamma(1/\beta)}$$

where β is a stretching exponent that has a value between 0 and 1 and Γ is the Euler gamma function[12]. The frequency-dependent EO coefficient of the 260 nm thick film appears to level-off above 30 GHz, and the EO coefficient of the 500 nm thick film levels off between 20 and 25 GHz. Both films show an undulation in the frequency dependent EO coefficient at 25 GHz, which is not attributed to measurement error. This is possibly due to a resonance in the electro-optic coefficient frequency response due to dipolar interactions

in $BaTiO_3$. Additional measurements with finer resolution would need to be taken in the vicinity of the resonance to further investigate its origin.

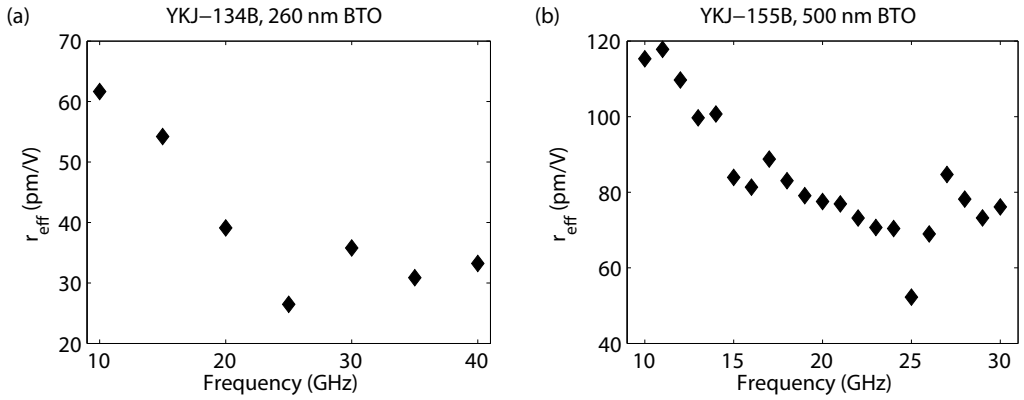

Figure 6.11. Frequency-dependent electro-optic coefficient measured on waveguides with identical device geometry apart from the $BaTiO_3$ film thickness.

The OSA technique was also used to study the electro-optic coefficient enhancement in dispersion-engineered W1 modulators. The frequency-dependent electro-optic coefficient for two similar W1 modulators on the same wafer having a lattice constant of 530 nm is shown in Fig. 6.12 (a). The two modulators are identical apart from the ridge waveguide width, which is 2 µm for one device (G2 WG1) and 3 µm for the other (G2 WG2). Several measurements were taken for each modulator, from which a 90% confidence interval in the measurement was calculated. The frequency-dependent electro-optic coefficient is nearly identical for the two devices, indicating the robustness of the measurement technique.

The electro-optic coefficient enhancement in the W1 waveguide was measured by comparing the frequency dependent electro-optic coefficient obtained for a conventional and W1 modulator on the same wafer that are otherwise identical apart from the photonic crystal. The frequency dependent EO coefficient of the two devices is shown in Fig. 6.12

(b). A clear enhancement of the effective EO coefficient is observed across the entire frequency range with a calculated enhancement factor between 1.3 and 1.5 (Fig. 6.12 (c)). The enhancement is well beyond the measurement uncertainty, given by the error bars, which indicate a 90% confidence interval and includes measurements done on different days with different input and output coupling conditions. At least four measurements are used to calculate the uncertainty at each frequency. The measured enhancement was compared to the theoretical enhancement described in Section 5.7, where the theoretical enhancement factor is (Eqn. 5.13)

$$f_{eo} = (1 - x) + x(n_{g,P}/n_{g,R})$$

where x is the fraction of the device interaction length containing the photonic crystal, $n_{g,P}$ is the group index of the photonic crystal waveguide, and $n_{g,R}$ is the group index of the ridge waveguide. For an average measured PC group index of 16.3 (the measurement is discussed in Fig. 5.28), ridge waveguide group index of 2.13, and $x = 0.037$ corresponding to a 37 µm long photonic crystal in a 1 mm long interaction length, the expected enhancement factor is 1.25. The measured enhancement of 1.4 is slightly larger than this value, which is tentatively attributed to uncertainty in the group index measurement and the effect of the tapered region of the photonic crystal waveguide on the slow light properties. The enhancement of the electro-optic coefficient in only the PC region is $f_{eo,loc} = n_{g,P}/{n_{g,R}}^{65}$, which according to Eqn. 5.13 gives

$$f_{eo,local} = \frac{n_{g,P}}{n_{g,R}} = \frac{f_{eo} - (1 - x)}{x}$$

Using the measured average enhancement factor of 1.4 and $x = 0.037$, the local enhancement factor is 12. For an intrinsic electro-optic coefficient of 76 pm/V at 30 GHz, the corresponding locally enhanced electro-optic coefficient in the PC region is 900 pm/V. This is quite a remarkable enhancement. This is the first demonstration of slow light enhancement of the electro-optic coefficient in a ferroelectric $\chi^{(2)}$ waveguide at microwave frequencies.

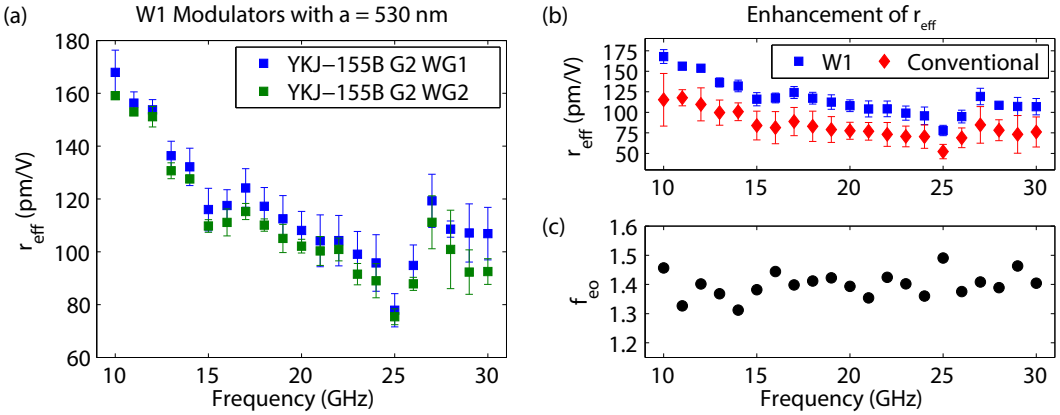

Figure 6.12. (a) Frequency-dependent electro-optic coefficient measured in two identical W1 waveguides at an optical wavelength of 1530 nm. (b) Electro-optic coefficient versus frequency of W1 (YKJ-155B G2 WG1) and conventional modulator (YKJ-155B G3 WG1). (c) Empirical enhancement factor versus frequency calculated from the data in (b).

6.4.3. Wavelength-Dependent Electro-Optic Coefficient

The wavelength-dependent electro-optic coefficient was measured for both hexagonal lattice and line defect photonic crystal modulators to demonstrate the dispersive properties of these devices. According to the theory proposed for the enhancement of the electro-optic coefficient in high group index waveguides (Section 5.7), the electro-optic coefficient is a function of optical group index, which may be a function of wavelength, e.g., have dispersion.

As discussed in Chapter 5, the group index is defined as $n_g \equiv c(d\omega/dk)^{-1}$, where c is the speed of light in free space. The group index of light approaches infinity near photonic band edges, where $d\omega/dk$ approaches zero. The property is especially pronounced in hexagonal lattice photonic crystal waveguides, which, unlike the line defect waveguides discussed in Chapter 5, are not engineered to have a flat dispersion region. Hexagonal lattice photonic crystal waveguide modulators are hence an excellent model system for demonstrating the dispersion of the electro-optic coefficient induced by wavelength-dependent slow light effects. Line defect waveguide modulators, which were designed to have a moderate group index with low dispersion, are expected to show a wideband enhancement of the EO coefficient when compared to conventional ridge waveguide modulators.

The wavelength-dependent EO coefficient for two hexagonal lattice photonic crystal modulators is shown in Fig. 6.13. The measured EO coefficient is plotted along with the measured waveguide transmission. Both the EO coefficient measurements and transmission were measured under the same electrical bias conditions. The measurements were done at a modulation frequency of 10 GHz with a 10 V bias to pole ferroelectric domains. The electro-optic coefficient monotonically increases across the band edge from the high to low transmission regions, in agreement with the expected increase in group index across the band edge in the same direction. The group index is known from theory[9] and experiment[115] to increase toward the band edge, i.e., it increases as the transmission decreases. This imposes a trade-off between increased insertion loss and increased electro-optic coefficient for the hexagonal lattice photonic crystal devices. Maximum enhancement factors of 1.8 and 2.4 are measured for the two devices. This is the first demonstration of an engineered dispersion in the electro-optic coefficient of a $\chi^{(2)}$ ferroelectric material. It is especially

noteworthy that this is demonstrated at a technologically relevant modulation frequency of 10 GHz.

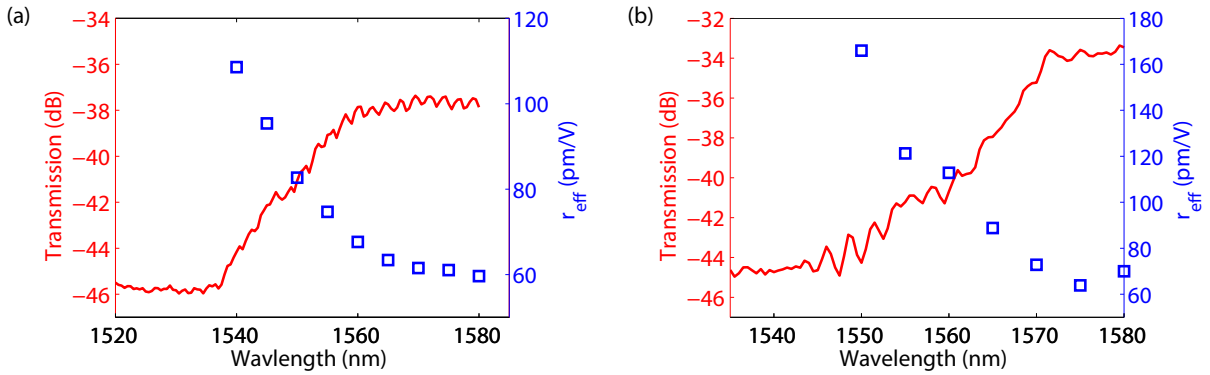

Figure 6.13. Measured transmission and electro-optic coefficient versus wavelength for hexagonal lattice photonic crystal modulators with (a) 7.5 and (b) 12 µm gap spacing. The measurements were done using a 10 GHz modulation frequency and 10 V bias voltage. Samples: (a) YKJ-155A G2 WG3, (b) YKJ-155A G2 WG5.

The wavelength-dependent electro-optic properties of a W1 waveguide are summarized in Fig. 6.14. The measured transmission and calculated group index (Fig. 6.14 (a) and (b), respectively) are reproduced from Fig. 5.28 to show along with the measured effective EO coefficient and its enhancement. The electro-optic coefficient of the W1 modulator has a value of 123 pm/V at 1530 nm and decreases to a value of 111 pm/V at 1560 nm. The reduction in the electro-optic coefficient across the band edge is attributed to coupling of optical power from the line defect mode to the ridge waveguide mode at wavelengths closer to the forbidden region. It is expected that, for a waveguide with only a line defect mode, the electro-optic coefficient would increase toward the band edge due to the increase in group index. Regardless of this effect, wideband slow light enhancement of the effective EO coefficient by a factor of 1.3 is measured in a 48 nm window centered about 1524 nm

(Fig. 6.14). This demonstrates the potential use of $\chi^{(2)}$ photonic crystal modulators with wideband enhancement for wavelength division multiplexing schemes.

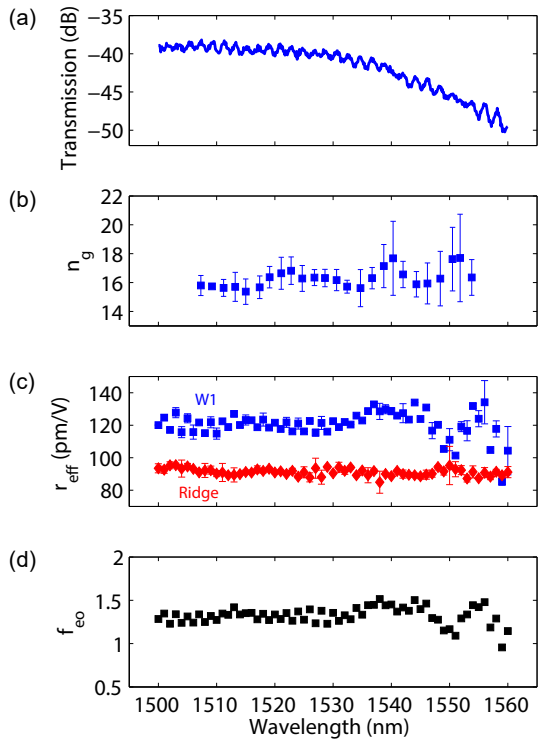

Figure 6.14. Wideband optical and electro-optic properties of a W1 photonic crystal waveguide modulator. (a) Measured transmission versus optical wavelength. (b) Group index calculated from the fringes measured in the transmission. (c) Measured wavelength-dependent EO coefficient. (d) Wavelength-dependent enhancement factor calculated from (c). Sample: YKJ-155B G2 WG1.

6.4.4. Voltage-Dependent Electro-Optic Sideband Response

The electro-optically phase-modulated sideband response was additionally characterized as a function of applied voltage with all other parameters fixed. The voltage-dependent spectra at a modulation voltage of 10 GHz and optical carrier wavelength of 1530 nm are

shown for the W1 modulator in Fig. 6.15. The sideband peak intensity increases with applied voltage, which is due to an increase in electro-optic phase delay. The phase delay, z, given by (Eqn. 3.13)

$$z \equiv \frac{\omega_0 n_x^3 r_{eff}}{2c} \Gamma A_{mw} m(f) L$$

was calculated by taking the ratio of the measured central peak to first order sideband peak intensities and solving numerically for the argument of the squared Bessel function $J_n^2(z)$ that describes the n^{th} order peak intensity (see Section 3.7.3 for a mathematical description)[128]. The phase delay calculated using this approach is plotted in Fig. 6.15 (b) for both a W1 modulator and otherwise identical conventional ridge modulator. An enhancement is observed in agreement with that calculated for the electro-optic coefficient across the entire voltage range. Both modulators show a nonlinear dependence of the phase delay on applied voltage. This difference is attributed to the large off-diagonal electro-optic tensor elements $r_{51} = r_{42}$ of the single crystal $BaTiO_3$ film, which adds a quadratic dependence to the voltage-dependent phase delay[6]. The measured phase delay is lower than expected given the electro-optic coefficients calculated in Fig. 6.12. This is due to the significant attenuation of the microwave field at a modulation frequency of 10 GHz. This can be reduced by either further shortening the electrodes or impedance matching to minimize the microwave losses.

For comparison, the voltage-dependent sideband response and phase delay were also characterized for a conventional modulator (YKJ-155B G3 WG3) at modulation frequencies of 10 and 25 GHz. The measured amplitude-dependent response for a phase modulator with a 7.5 µm electrode gap spacing on wafer YKJ-155B with 500 nm $BaTiO_3$ thickness is shown in Fig. 6.16 (a). The phase delay versus applied voltage was calculated from

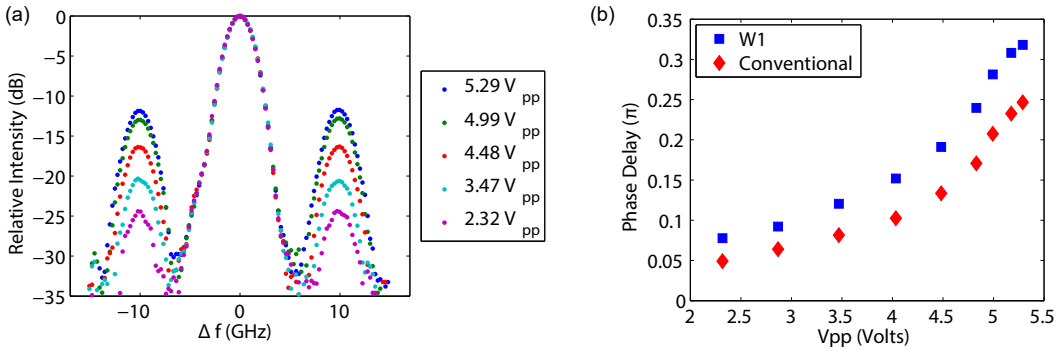

Figure 6.15. Phase modulator amplitude response. (a) Measured electro-optic sideband response as a function of applied voltage. (b) Phase delay versus voltage calculated from the data in (a). Sample: YKJ-155B G2 WG2.

the measured voltage-dependent spectra for modulation frequencies of 10 and 25 GHz. The phase delay plotted in Fig. 6.16 (b) shows a linear response at low voltages, with a super-linear response as the voltage increases, as was observed for the case of the modulators with 5 µm gap spacing whose response is plotted in Fig. 6.15. The measured phase delay is smaller across the entire voltage range for the 25 GHz modulation field due to the larger microwave losses at this frequency.

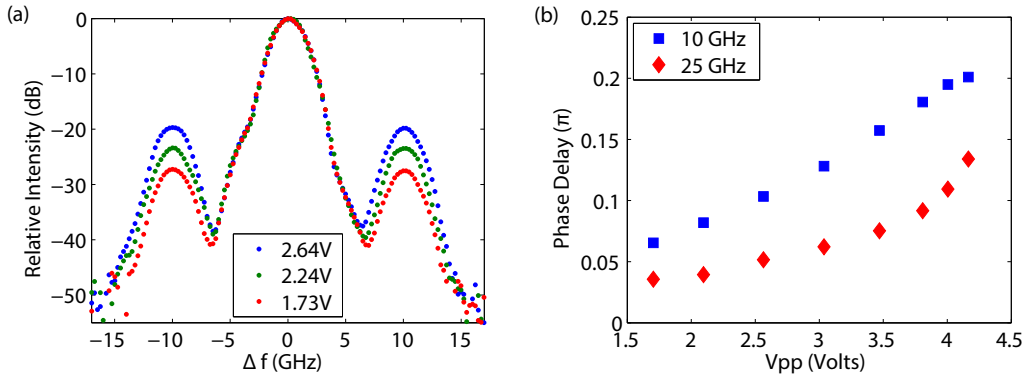

Figure 6.16. Phase modulator amplitude response at different modulation frequencies. (a) Voltage dependent spectra for 10 GHz modulation frequency. (b) Phase delay calculated from the voltage dependent spectra at frequencies of 10 and 25 GHz. Sample: YKJ-155B G3 WG3.

6.5. Summary and Conclusions

The electro-optical properties of epitaxial $BaTiO_3$ films were measured for modulation frequencies in the range of 100 Hz to 50 GHz and over optical wavelengths between 1500 and 1580 nm using time-domain, frequency-domain, and optical spectral analysis techniques. The major results obtained for this work are the following:

(1) Record low voltage-length products for $BaTiO_3$ films of $0.39\,\mathrm{V}\cdot\mathrm{cm}$ ($0.45\,\mathrm{V}\cdot\mathrm{cm}$) were measured at a modulation frequency of 100 Hz (1 MHz) in the smallest (1 mm long) traveling-wave $BaTiO_3$ modulator to date at a wavelength of 1560 nm.

(2) A record large 3 dB EO bandwidth for all $BaTiO_3$ modulators (28 GHz) was measured. The measurement was demonstrated for a modulator with the lowest measured microwave losses and the largest predicted 3 dB EO bandwidth at a wavelength of 1560 nm.

(3) The effective in-device EO coefficient was observed to increase with film thickness. At 1 MHz, an effective EO coefficient of 306 pm/V (147 pm/V) was measured for a 500 nm (260 nm) thick film. At 10 GHz, the electro-optic coefficient decreases to approximately 40% of its value at 1 MHz to 115 pm/V and 61 pm/V for the 500 and 260 nm thick films, respectively.

(4) A monotonic increase in the effective EO coefficient was measured approaching the photonic crystal band edge near 1550 nm of a hexagonal lattice photonic crystal modulator, in agreement with that predicted by the model for the EO coefficient enhancement described in Section 5.7.

(5) An enhancement factor of 1.4 was measured in a W1 line defect modulator with a corresponding local enhancement factor of 12 and local EO coefficient of 900 pm/V

in the photonic crystal region, the first demonstration of slow light enhancement of the EO coefficient in a $\chi^{(2)}$ waveguide at microwave frequencies.

As a convenient reference for the reader, the electro-optic properties are summarized along with the microwave properties specific to a single device in Table C.4 of Appendix C. These properties include the half-wave voltage, bias field, effective in-device electro-optic coefficient, and electro-optic bandwidth, microwave index, characteristic impedance, and total microwave loss at 50 GHz.

The optical spectral analysis approach demonstrated here for determining the EO properties above 10 GHz is expected to be an important measurement technique for measuring the phase modulation properties of other materials, including silicon, graphene, and transition metal dichalchogenides. The sensitivity of this approach also makes it an exceptional technique for demonstrating light-matter interaction enhancement for phenomena at microwave to terahertz modulation frequencies and could hence be applied to the study of plasmonic devices as well. In addition to the photonic crystal structures measured here with hexagonal lattice symmetry, photonic crystal electro-optic waveguides with honeycomb[10] and coupled cavity[107] structures are recommended for future work for. The former could potentially be used for employing Klein tunneling as an electro-optic modulation mechanism, and the latter could be used to achieve wide band slow light without a photonic band gap. The demonstration of EO coefficient enhancement here with this technique validates the approach for enhancing the EO properties and reducing the modulation voltage required for $BaTiO_3$ modulators. A reduction of the modulation voltage also allows for a reduction of the electrode length, which in turn reduces the total microwave losses and allows for a simultaneous increase in electro-optic bandwidth. The

ultimate performance predicted for $BaTiO_3$ photonic crystal modulators designed based on this approach is discussed in the subsequent chapter.

CHAPTER 7

Modeling of $BaTiO_3$ Conventional and Photonic Crystal Waveguide Modulators

7.1. Introduction

The predicted device properties of conventional and PC modulators were investigated through numerical and analytical modeling with input of electro-optic properties and microwave properties from device measurements. The two overall device properties of interest are the voltage-length product ($V_\pi \cdot L$) and electro-optic 3 dB bandwidth (f_{3dB}). These device properties are functions of the following fundamental optical, microwave, and electro-optic properties: optical mode index, microwave mode index, electro-optic overlap factor, dielectric and conductor loss coefficients, microwave impedance, and electro-optic coefficient. These properties are in turn dependent on geometrical factors including the ridge waveguide width, $BaTiO_3$ film thickness, and electrode gap spacing and on material properties including the thickness-dependent effective electro-optic coefficient and dielectric constant of the $BaTiO_3$ film. Predicted values for the voltage-length product and electro-optic bandwidth were calculated by choosing reasonable values for the geometrical factors and material properties of the dielectric layers, calculating the geometry-dependent optical and microwave mode properties, and then feeding these values into analytical and numerical models for the voltage-length product and electro-optic bandwidth.

The high optical group index of PC modulators affects both the voltage-length product and the electro-optic bandwidth. Qualitatively, the slowing down of light due to a high optical group index enhances light-matter interactions, resulting in an effective increase in the electro-optic coefficient or, equivalently, a reduction in the modulation voltage[9]. This effect on the voltage-length product is quantified by the analytical model for the reduction in modulation voltage in $\chi^{(2)}$ PC modulators discussed in Section 5.7. The enhancement of the effective electro-optic coefficient enables a reduction in total interaction length while maintaining reasonable values for the voltage-length product. By reducing the total interaction or, equivalently, electrode length, the length-dependent total microwave losses are reduced, resulting in an increase in electro-optic bandwidth. The overall result for PC modulators is a smaller device footprint with smaller modulation voltages and larger electro-optic bandwidths compared to conventional ridge waveguide modulators. The results of the calculations presented here show that slow light waveguides enable operation in a regime that cannot be achieved with conventional ridge waveguide modulators. Devices with volt level operating voltage and electro-optic 3 dB bandwidths as high as 48 GHz are predicted for films with the measured electro-optic and microwave properties discussed in previous chapters. The calculations here represent a conservative estimate of the ultimate performance of $BaTiO_3$ conventional and photonic crystal modulators. Further advances can be made by improvements to the film quality to increase the effective electro-optic coefficient to its predicted bulk crystal value.

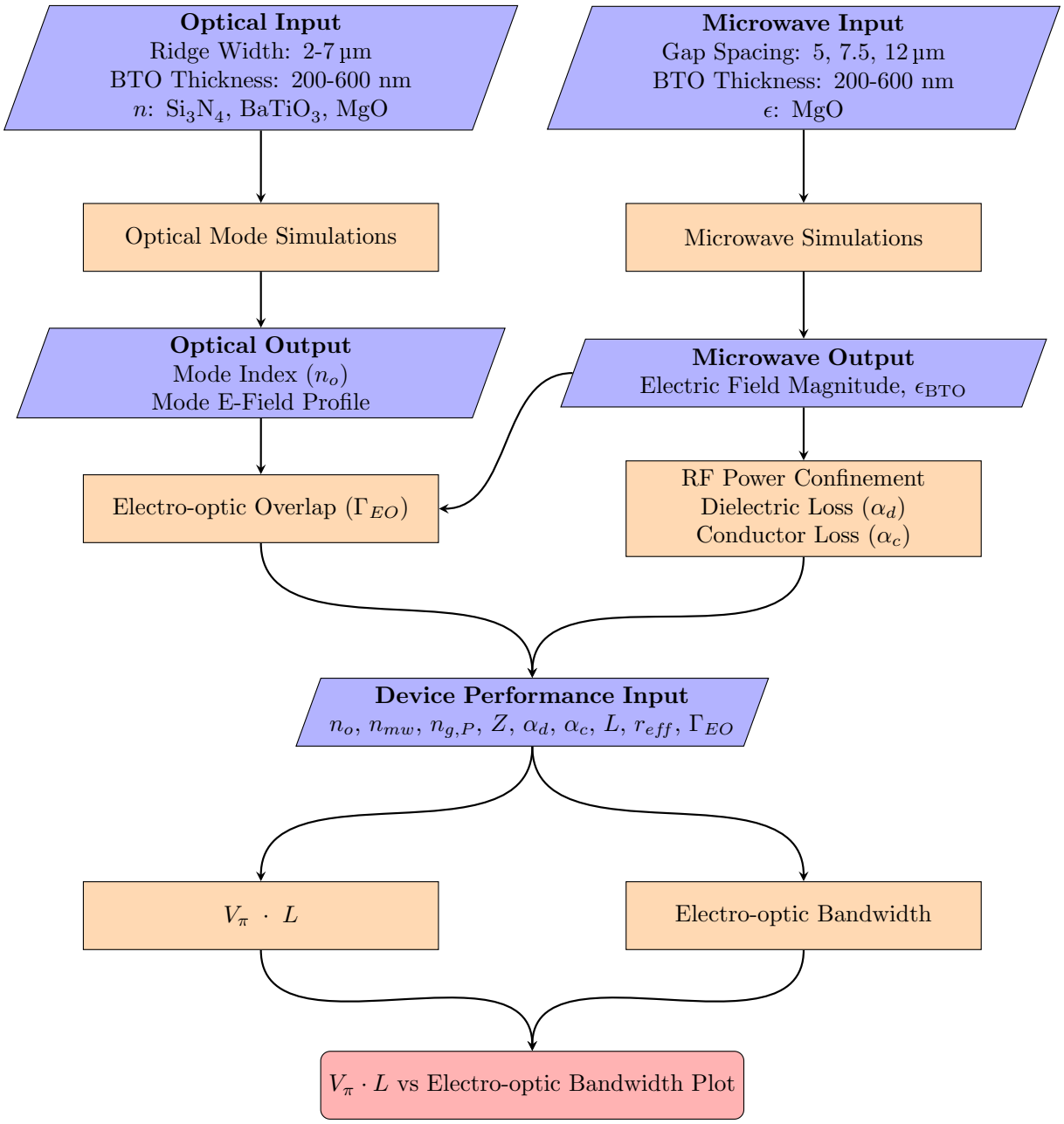

Figure 7.1. Flow chart showing the sequence of calculations for obtaining the voltage length product versus electro-optic bandwidth figures.

7.2. Simulation Flow and Choice of Material and Geometry Parameters

A flow chart detailing the sequence of calculations for obtaining the voltage-length product and electro-optic bandwidth is given in Fig. 7.1. The sequence of calculations starts with separate calculations for obtaining optical and microwave properties, indicated by the two separate branches in the top half of the diagram. At the top of the flow chart are the input parameters, which include geometrical parameters and material properties. The dimensions chosen for the optical waveguide and microwave electrodes are largely determined by the confinement of light in a purely photonic mode. In this work, device operation at a wavelength of 1550 nm is considered. For a purely photonic mode, the minimum geometric confinement is on the order of $\lambda_0/(2n)$, where λ_0 is the free space wavelength and n is the optical mode index. As shown in Section 7.4 below, the mode confinement is also a function of the film thickness. Electrode gap spacings of 5, 7.5, and 12 µm were considered since these are the smallest technologically feasible dimensions that do not pose a significant optical loss via gold absorption. These dimensions also serve as a compromise between decreasing the half-wave voltage and increasing the electro-optic bandwidth which is elucidated by the full set of these calculations and discussed in Section 7.6. $BaTiO_3$ film thicknesses of 200-600 nm were chosen since this represents a reasonable range of optical thickness for mode confinement and reasonable film growth time.

The required input material parameters are for the optical indices and microwave dielectric constants of the various insulating layers in the multilayer device structure. The values chosen are given in Table 7.1. The optical refractive indices given in Table 7.1 are for a wavelength of 1550 nm. In bulk single crystalline tetragonal $BaTiO_3$, light experiences a refractive index of $n_o = 2.42$ and $n_e = 2.36$ when polarized along the c and

Table 7.1. Dielectric constant and refractive index values used for the calculations of the voltage-length product and electro-optic bandwidth.

Material	Dielectric Constant	Refractive Index
Air	1	1
$BaTiO_3$	thickness dependent	2.31
MgO	9.8	1.73
Si_3N_4	-	2.01

a axes, respectively, at a wavelength of 632.8 nm. The orientation of domains in thin film $BaTiO_3$ influence the refractive indices such that light polarized in the plane of the film (TE) experiences an effective refractive index[149]

$$n_{TE} = (c)n_o + \frac{1}{2}(a)n_e + \frac{1}{2}(a)n_o$$

where (c) is the fraction of c domains, (a) is the fraction of a domains, n_e is the extraordinary refractive index, and n_o is the ordinary refractive index. For light polarized perpendicular to the plane of the film (TM), the effective refractive index is

$$n_{TM} = (c)n_e + (a)n_o$$

The refractive indices of $BaTiO_3$ films grown epitaxially on MgO were reported by Towner et al[149] to be $n_e = 2.37$ and $n_o = 2.39$ at 632.8 nm. For a film with 33% of the domains oriented along the $c-$axis, $n_{TE} - n_{TM} = 0.0001$. The difference in the expected polarization dependent refractive index is sufficiently small such that it has a negligible impact on the results presented here for the mode electric field profile calculations. For simplicity, an isotropic refractive index of 2.31 was used for the $BaTiO_3$ film. This value represents a typical value measured at 1550 nm using optical reflectometry.

The dielectric constants are given for operation at 50 GHz. The dielectric constant of MgO at 50 GHz is well known[57 70]; the dielectric constant of the $BaTiO_3$ thin films, however, is dependent on the domain structure and film thickness and is not yet well characterized according to the film microstructure. The effective dielectric constant of polydomain $BaTiO_3$ grown by MOCVD on (100) MgO at GHz frequencies was previously reported by Hamano et al as an isotropic value for frequencies in the range 0.05 to 40.05 GHz[57]. The isotropic dielectric constant was determined as a function of frequency by comparing measured and simulated S_{11} data. The constants were measured on a single film with 650 nm $BaTiO_3$ thickness. The frequency response of the real part of the dielectric constant was well-fitted to a Curie Von Schweidler relationship given by

$$\epsilon'(\omega) = \epsilon'(0) - A'\omega^m$$

where $\epsilon'(0) = 2715$ is the low frequency value, ω is the angular frequency, and A' and m are fitting parameters with values of 1.10 and 0.29, respectively. Direct application of this empirical result to the study here is limited by the following: the $BaTiO_3$ dielectric tensor should be anisotropic, and the degree of anisotropy should be dependent on the film thickness. Additionally, while not stated by Hamano et al, their model is applicable in only a certain frequency range. It is known that polydomain $BaTiO_3$ has a resonance in its dielectric constant due to the ionic polarization contribution in the frequency range of 10-100 GHz[147]; care should thus be taken when extrapolating the model beyond the highest frequency measurement at 40.05 GHz.

The simple model proposed by Towner et al for describing the dielectric properties of polydomain $BaTiO_3$ films at optical frequencies can be extended to describe the

dielectric properties at lower frequencies. The dielectric tensor elements of bulk single crystalline $BaTiO_3$ were previously measured by Zgonik et al under clamped conditions as $\epsilon_{xx} = \epsilon_{yy} = 2200$ and $\epsilon_{zz} = 56$[175]. Applying the model of Towner et al, the tensor elements of the film are described as

$$\epsilon_{xx,f} = (c)\epsilon_{xx} + \frac{1}{2}(a)\epsilon_{zz} + \frac{1}{2}(a)\epsilon_{xx} \tag{7.1}$$

$$\epsilon_{zz,f} = (c)\epsilon_{zz} + (a)\epsilon_{xx} \tag{7.2}$$

Towner et al observed a linear fit for the measured areal fraction of (c) domains versus film thickness following the equation

$$(c) = 6.0288 \times 10^{-4} t - 0.0117 \tag{7.3}$$

with $(a) = 1 - (c)$ and t is the film thickness in nanometers. Towner et al did not discuss the fitting error, and the negative intercept limits the applicable range of film thicknesses; the fit, however, can be reasonably used for the film thicknesses (200-600 nm) in this simulation study. Using Eqns. 7.1-7.3 along with the tensor elements of bulk single crystalline $BaTiO_3$, an estimate of the dc dielectric tensor elements as a function of distance from the epitaxial interface is plotted in Fig. 7.2 (a). Since the dependence of the domain fraction in the out-of plane direction includes the effect of a strain gradient induced by the epitaxy, the effect of the strain gradient is thus included in the calculation for the tensor elements. Due to the linear relation between the areal fraction of (c) domains and film thickness, the macroscopic dielectric constant is a spatially varying function in the out-of-plane direction. As expected, the out-of-plane tensor element is largest closer

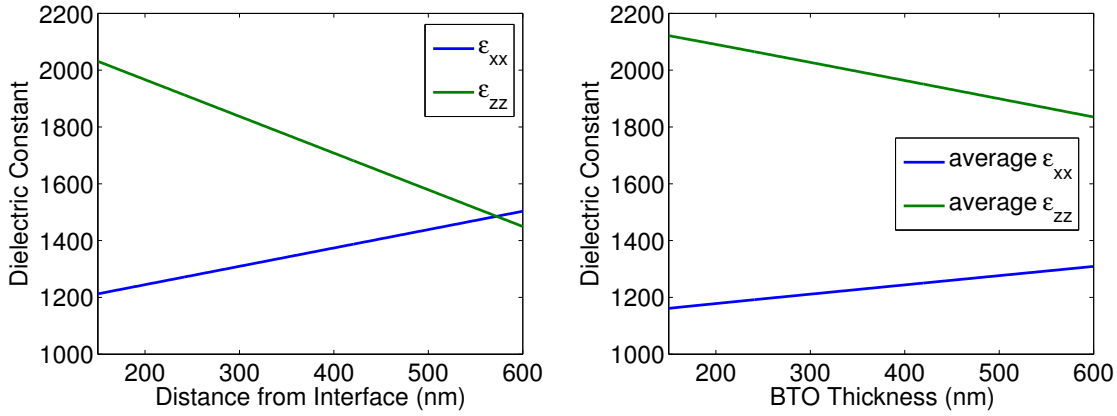

Figure 7.2. Calculated dielectric constant tensor elements in polydomain $BaTiO_3$ epitaxially grown on (100) MgO versus distance from the epitaxial interface (a). Average value of the tensor elements as a function of film thickness (b). The plotted values are for dc conditions.

to the epitaxial interface where the tensile strain imposed by the substrate causes most of the domains to have their polarization lie in the plane of the film. The out-of-plane tensor element decreases toward the film surface where a larger fraction of (*c*) domains are present. The opposite trend is observed for the in-plane tensor element. The average value of the dielectric tensor elements in the film versus film thickness are shown in Fig. 7.2 (b). The overall effect of the polydomain microstructure on the averaged dielectric tensor elements is a smaller difference between the tensor elements when compared to that of the bulk crystal. The films, however, still have significant anisotropy.

The calculated tensor elements plotted in Fig. 7.2 represent an upper bound of the expected values for the films in the frequency range of interest, 1-100 GHz. As noted previously, the frequency response of the real part of the dielectric constant of polydomain $BaTiO_3$ films has been observed to follow a Curie Von Schweidler relationship, with a

significant reduction in the value of ϵ' in the range of 1-40 GHz. As such, the value of the tensor elements given in Fig. 7.2 should be smaller at higher frequencies.

Using the input geometrical and material parameters discussed, separate calculations were performed for obtaining optical and microwave mode properties. The optical mode index and optical electric field for TE and TM modes were obtained using a finite difference time domain (FDTD) mode solver[42]. The microwave parameters, namely the effective index (n_{mw}), impedance (Z), and electric field magnitude, are obtained from finite element simulations using the software Maxwell ANSYS. The software is relevant for the frequencies studied here as quasi-static analysis has been shown to be an accurate modeling technique up to 100 GHz[46]. The microwave field magnitude is then used to calculate the RF power confinement in the thin film and substrate, which is subsequently used to calculate the total microwave losses. The microwave and optical field magnitudes next serve as the input for calculating the electro-optic overlap factor.

At this point, all simulated parameters required as input variables for calculating the voltage-length product and electro-optic bandwidth are known. These are supplemented with experimental values for the electro-optic coefficient (r_{eff}) measured on films of different thicknesses. For these calculations, the high-frequency electro-optic coefficient estimated as 40% of the value measured at 1 MHz was used. This was done in accordance with the comparison made in Chapter 6 between the measured r_{eff} at 1 MHz and frequencies between 15 and 30 GHz. As noted in Chapter 6, r_{eff} is flat above 10 GHz out to 40 GHz; it is assumed that there is no significant reduction in r_{eff} between 40 GHz the highest modeling frequency of 200 GHz. This assumption is made assuming that the electronic contribution to r_{eff} is the dominant mechanism at frequencies above 10 GHz, as discussed

in Chapter 6. The voltage-length product is calculated for conventional and photonic crystal modulators using the general model developed in Section 5.7. The electro-optic bandwidth is calculated using the model by Haxha et al[58] discussed in Section 3.7.2. All calculations of $V_\pi \cdot L$ versus electro-optic bandwidth are then plotted according to the various input parameters such as electrode gap spacing, $BaTiO_3$ film thickness, and electro-optic interaction length. From these aggregate plots, a linear relation is observed between voltage-length product and electro-optic bandwidth when plotted on a log-log scale. This relation can be used as a general design rule when designing thin film $BaTiO_3$ modulators. This simulation approach may be extended for other material platforms including silicon on insulator and lithium niobate for designing next generation high-speed and low-voltage modulators.

7.3. Microwave Properties

Calculations of the conductor and dielectric loss coefficients were done using analytical methods with input of numerical results from Maxwell ANSYS calculations. The cross-sectional geometry of the coplanar stripline electrode devices simulated is shown in Fig. 7.3. Electrode gap spacings (g) of 5, 7.5, and 12 µm were used. The box shown in the figure represents the boundary of the simulation region, extending 44 microns from the top of the $BaTiO_3$ surface and 60 microns from the side of the structure. The boundary defines the simulation area or solution region; all sources outside the boundary have no effect on the simulation. The boundary is not an artificial ground; the simulated electric field is neither tangential nor normal to the boundary.

The microwave simulations were done at a 50 GHz excitation with a total voltage of 10 V applied across the electrodes. The software implements an iterative solution process with at least 10 passes and a solution error less than 0.05%. Data output from the simulations include the vectorial electric field magnitude and total structure capacitance. The structure capacitance was calculated with and without the dielectric layers to determine the effective microwave index and match it via iteration to the measured values, as discussed in Section 7.3.1. The vectorial electric field magnitude was exported and used to calculate the power confinement (Section 7.3.3) and electro-optic overlap factor (Section 7.5).

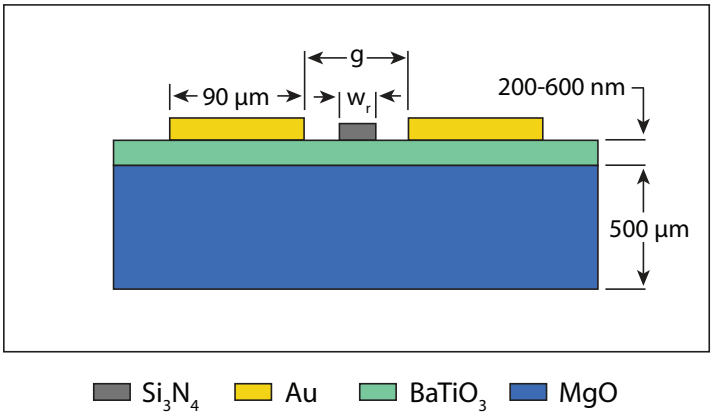

Figure 7.3. Simulation geometry for the microwave simulations.

7.3.1. Dielectric Constant of $BaTiO_3$ at 50 GHz

An estimate of the film thickness dependent dielectric constant at 50 GHz was obtained by matching the measured microwave mode index discussed in Chapter 4 Section 4.3 with that obtained by modeling. The approach was simplified by the fact that the mode index is a much stronger function of the in-plane than out-of-plane dielectric constant due to most of the field lines being parallel to the in-plane direction; the modeling was hence done

by assuming an isotropic value for the dielectric constant. In order to keep the number of calculations to a minimum while producing useful results, all calculations were done at a frequency of 50 GHz.

The simulated microwave effective index was calculated as

$$n = \sqrt{C/C_0}$$

where C (C_0) is the capacitance in the presence (absence) of the dielectric layers. The calculations were done iteratively with varying $BaTiO_3$ dielectric constant to match the simulated index with the measured index. The measured microwave index and characteristic impedance are reproduced in Fig. 7.4 (a) and (b); values of the index and impedance used in subsequent calculations were obtained by linear interpolation between the measurements in these plots. The thickness-dependent dielectric constant of $BaTiO_3$ obtained from the iterative refractive index calculations is plotted in Fig. 7.4 (c). The effective permittivity of the film increases with film thickness, following the trend predicted for the in-plane dielectric constant, ϵ_{xx}. A significant variation over the thickness range of 150 to 450 nm is calculated with a slightly decreasing value of the dielectric constant for larger thicknesses. In addition to the expected thickness dependence of ϵ_{xx} that is due to the variation in domain orientation, the thickness dependence of the dielectric constant is likely also due to a relaxation to the bulk tetragonal structure with increasing film thickness. The calculated dielectric constant plotted in Fig. 7.4 (c) was used for further calculations of the dielectric and conductor loss coefficients.

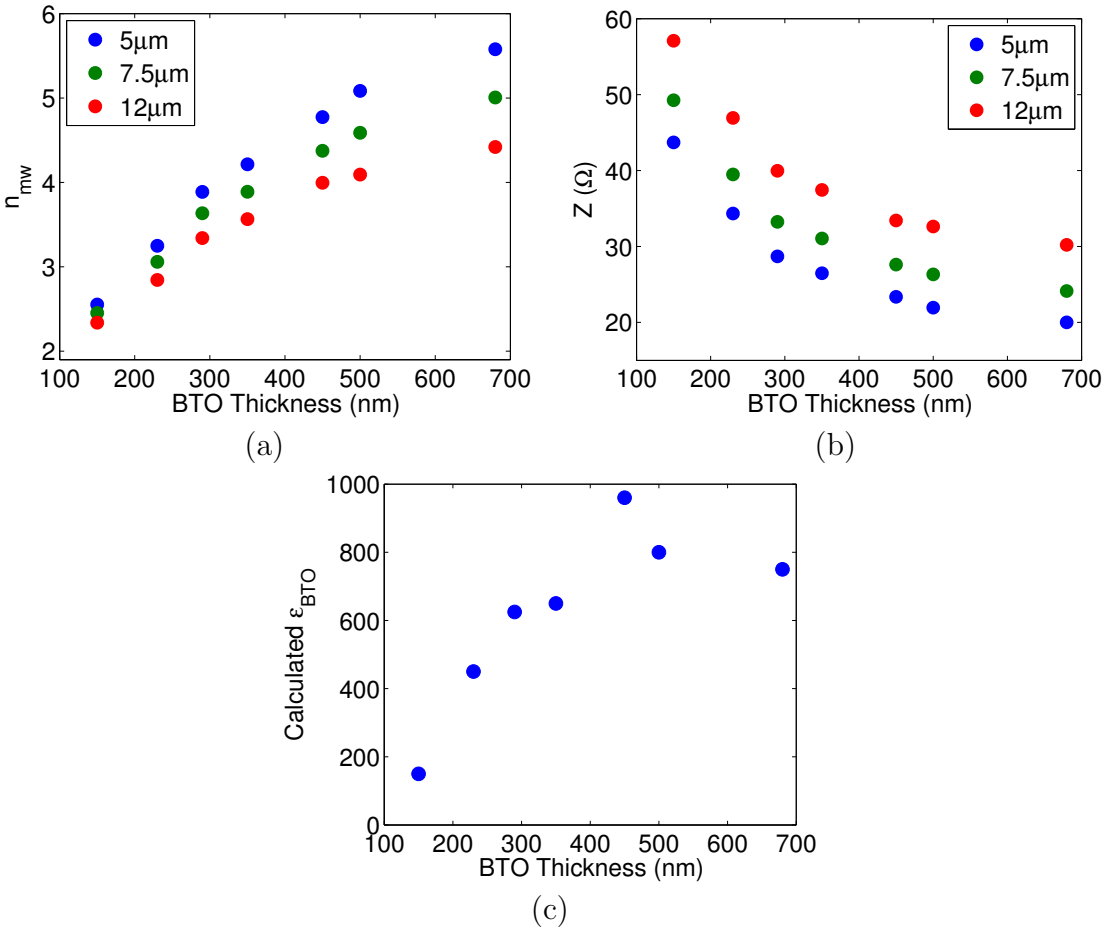

Figure 7.4. (a) Measured microwave effective index versus $BaTiO_3$ thickness for different electrode gap spacings. (b) Calculated impedance versus $BaTiO_3$ thickness versus $BaTiO_3$ thickness for different electrode gap spacings. (c) Calculated in-plane $BaTiO_3$ dielectric constant versus thickness from the measured microwave index.

7.3.2. Conductor Loss Coefficient

The conductor losses were calculated using the numerical method of Yamashita et al[172].

As discussed in Section 2.2.2, the conductor loss determined by the method of Yamashita

et al is given by the analytical expression

$$\alpha_c = \alpha_{c,0} n_{eff} = 8.686 \frac{\pi}{\lambda_0} n_{mw} \left(\frac{C^a - C^a_\delta}{C^a_\delta} \right) \tag{7.4}$$

where λ_0 is the free space microwave wavelength, n_{mw} is the effective microwave index, C^a is the capacitance of the transmission line in vacuum, and C^a_δ is the capacitance of the line when the walls of the conductor are receded by half of the skin depth, δ. The skin depth is given by

$$\delta = \frac{1}{\sqrt{f \mu \sigma \pi}}$$

where f is the microwave frequency, μ is the permeability of the conductor, and σ is the conductivity of the conductor. At a frequency of 50 GHz, the skin depth is 352 nm. Linearly interpolated values of the measured effective microwave index were used in the calculations. The conductor losses scale directly with the effective dielectric constant (ϵ_{re}). Since n_{eff} is larger for devices with thicker $BaTiO_3$ and smaller gap spacings, larger conductor losses should be expected for these devices. This is indeed the case, as shown in Fig. 7.5, which shows an increase in conductor loss with increasing $BaTiO_3$ thickness and decreasing gap spacing.

7.3.3. Microwave Power Confinement

The electric field magnitude was calculated for $BaTiO_3$ thicknesses of 200, 300, 400, 500, and 600 nm and for gap spacings of 5, 7.5, and 12 µm using the finite element approach with Maxwell ANSYS. The simulations were done for a 50 GHz excitation and a differential voltage of +5 and −5 V applied to the left and right electrodes. The dielectric constant

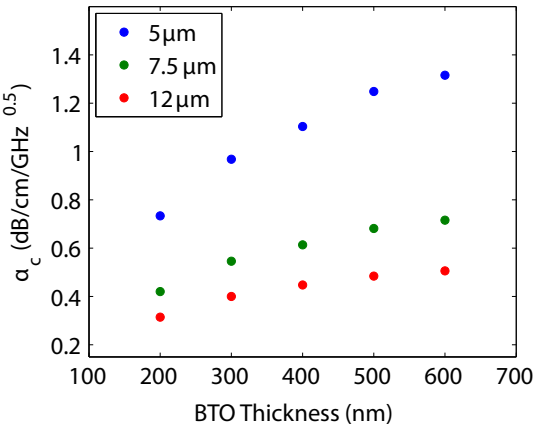

Figure 7.5. Conductor loss coefficient versus $BaTiO_3$ thickness for different electrode gap spacings calculated using Eqn 7.4.

for the each dielectric material used in the simulations is given in Table 7.1. An example plot of the simulated field magnitude is given in Fig. 7.6.

The confinement of microwave power Γ in the lossy dielectric layers ($BaTiO_3$ and MgO) was calculated from the simulated microwave fields as

$$\Gamma_a = \frac{\iint_a |E_m|^2 dx\, dy}{\iint_A |E_m|^2 dx\, dy}$$

where a represents the area of interest, for example the film, A represents the entire cross sectional area of the device, and $|E_m|$ is the magnitude of the electric field. The confinement in the $BaTiO_3$ film (MgO substrate) increases (decreases) with film thickness. This is expected since, in thicker film devices, the film occupies more of the device cross-section. While only a small amount of microwave field is confined in the $BaTiO_3$ film, the energy density is high due to the high dielectric constant. Larger power confinement factors were calculated for devices with thicker $BaTiO_3$ films and narrower gap spacings, in agreement with the microwave index calculations.

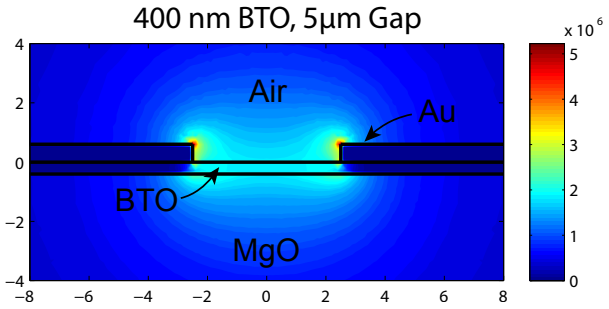

Figure 7.6. Example of the simulated microwave electric field profile for a device with 400 nm thick $BaTiO_3$ film and 5 µm gap spacing. The units are V/m.

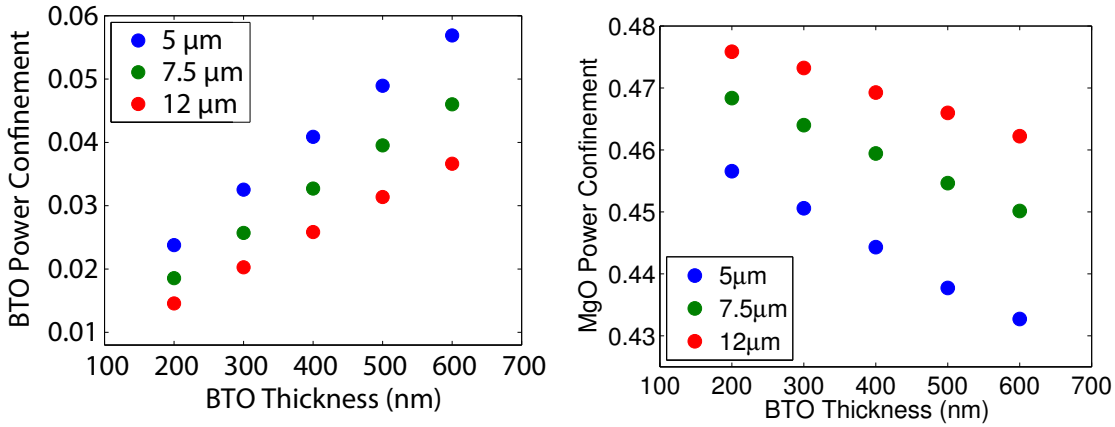

(c) (d)

Figure 7.7. Microwave power confinement factors versus $BaTiO_3$ thickness for different electrode gap spacings.

7.3.4. Dielectric Loss Coefficient

The dielectric loss coefficients α_d were calculated from the power confinement factors considering the two-layer structure as[113]

$$\alpha_d = \frac{\pi f}{n_{\mu w} c} \left(\Gamma_f \epsilon_f \tan\delta_f + \Gamma_s \epsilon_s \tan\delta_s\right) \tag{7.5}$$

where f is the microwave frequency, c is the speed of electromagnetic propagation in free space, ϵ is the dielectric constant, and $\tan\delta$ is the dielectric loss tangent. The subscript f (s) indicates properties for the film (substrate). For the $BaTiO_3$ film and MgO substrates, loss tangents of 0.05 and 3×10^{-4} were used, respectively[57]. The effective dielectric constant of $BaTiO_3$ calculated from the measured microwave index (Fig. 7.4 (c)) at 50 GHz and the dielectric constant for MgO at microwave frequencies above 10 GHz were used in the calculations. The dielectric losses (Fig. 7.8) increase with $BaTiO_3$ thickness and with decreasing gap spacing, following the same trend as the microwave power confinement in the $BaTiO_3$ film.

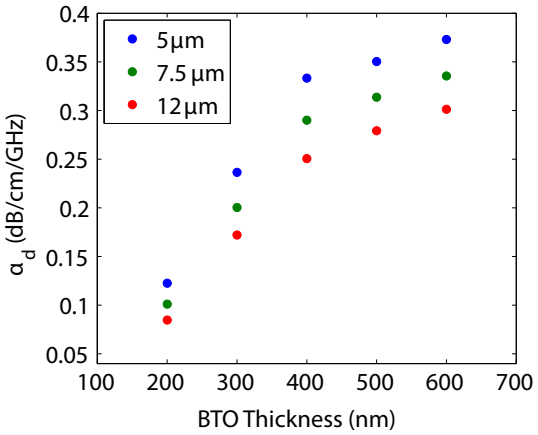

Figure 7.8. Dielectric losses versus $BaTiO_3$ thickness for different gap spacings calculated using Eqn. 7.5.

7.4. Optical Mode Properties

The fundamental TE and TM optical modes were calculated for all combinations of film thickness and ridge width. $BaTiO_3$ film thicknesses of 200, 300, 400, 500, and 600 nm and Si_3N_4 ridge widths of 2, 3, 4, 5, 6, and 7 µm were considered. For each of

the 30 geometrical combinations, several iterations of the mode solver were required to obtain the fundamental mode for TE and TM polarizations. The iteration producing a mode with a maximum intensity at the waveguide center and a single node was chosen as that representing the fundamental mode. Plots of the simulated optical intensity in the waveguide cross-section for TE and TM modes for increasing film thickness are given in Fig. 7.9. For $BaTiO_3$ thickness below 300 nm, the TM mode is cut off, precluding the use of these films for single arm phase modulators which require propagation of both TE and TM modes; these films, however, may be used to guide TE polarized light in a Mach Zehnder configuration. They may also be used as a polarization-dependent filter. For BTO thicknesses between 300 and 600 nm, both TE and TM modes are confined within the BTO film. The optical mode index for TE and TM modes is plotted in Fig. 7.10 (a) and (b). The TE index is larger for all thicknesses, and the birefringence between the TE and TM modes decreases from 0.13 for 200 nm thick $BaTiO_3$ to 0.057 for 600 nm thick $BaTiO_3$.

7.5. Electro-optic Overlap

The electro-optic overlap factor was calculated as[141]

$$\Gamma_{eo} = \frac{g}{V} \frac{\iint_{BTO} E_m |E_o|^2 dxdy}{\iint_{BTO} |E_o|^2 dxdy}$$

where V is the applied ac voltage amplitude, E_m is the microwave field magnitude, E_o is the optical electric field, and x and y are the rectangular coordinates of the device cross-section. The simulated fields from the microwave and optical mode calculations were used to calculate the overlap factor. A plot of the electro-optic overlap factor versus $BaTiO_3$

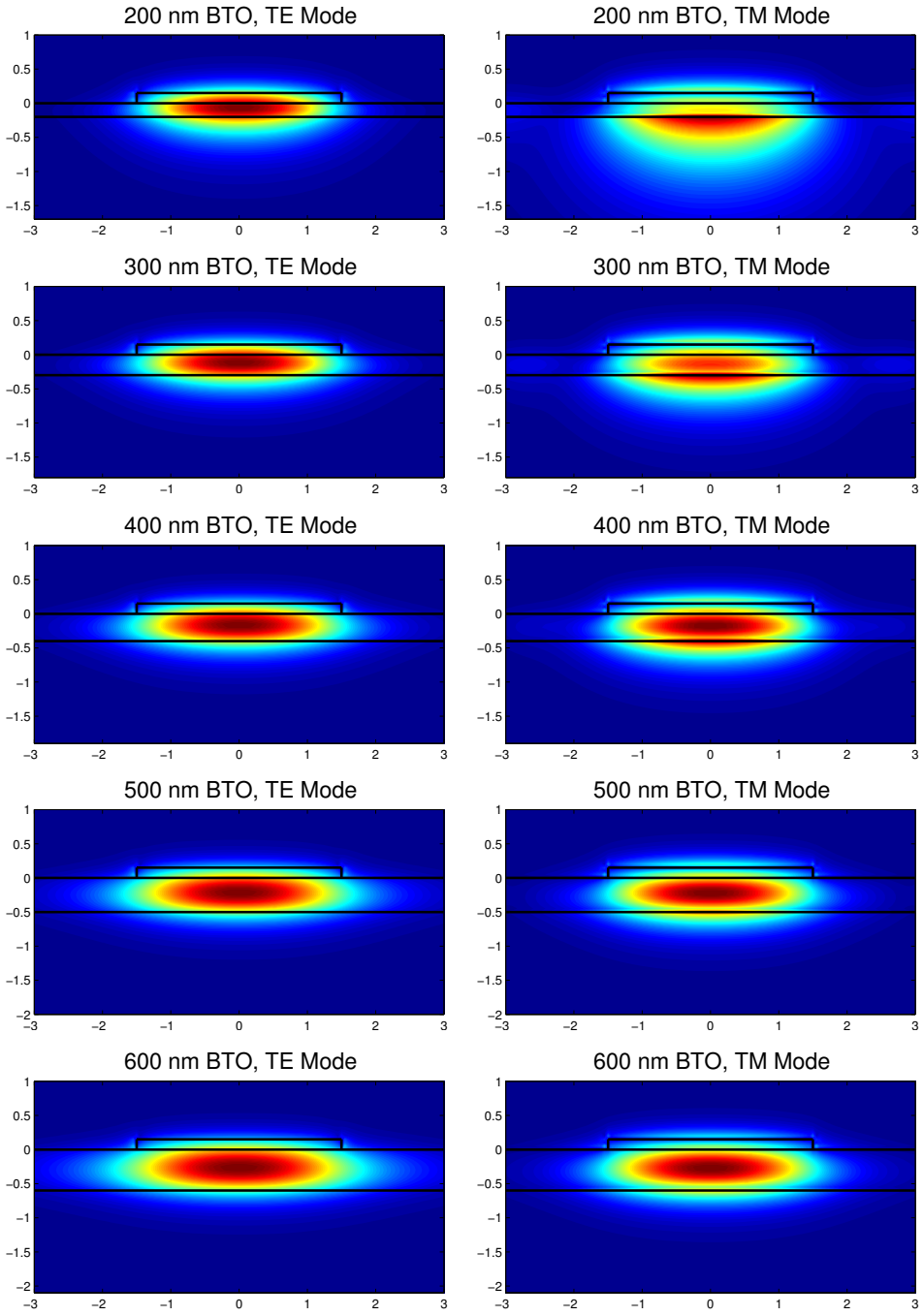

Figure 7.9. Simulated optical TE and TM mode profiles for BTO thickness of 200, 300, 400, and 600 nm. The ridge width is 3 µm.

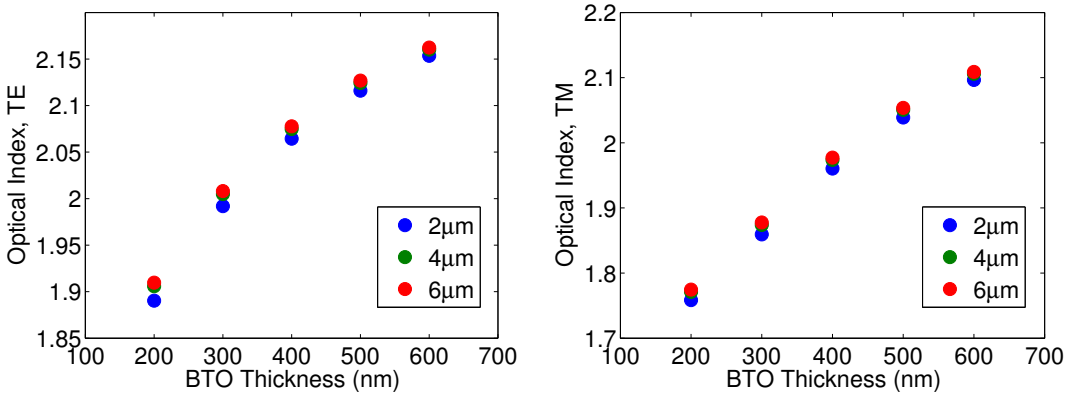

Figure 7.10. Optical index for the fundamental TE (a) and TM (b) optical modes versus $BaTiO_3$ thickness for different ridge widths.

thickness for different gap spacings is given in Fig. 7.11. There is a weak dependence of

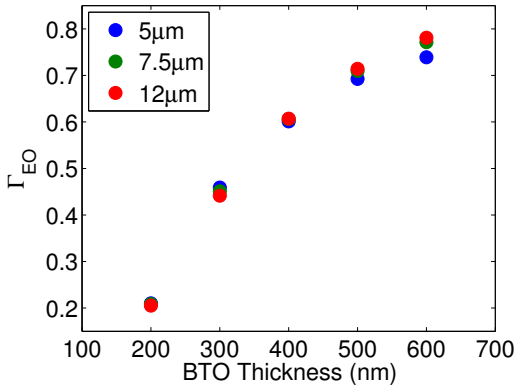

Figure 7.11. Calculated electro-optic overlap factor for different gap spacings versus $BaTiO_3$ thickness.

the overlap on the electrode gap spacing; however, there is a strong dependence on the film thickness. The overlap factor increases from approximately 0.2 for 200 nm thick $BaTiO_3$ to greater than 0.7 for 600 nm thick films. The increase in overlap factor follows the same trend as that for the power confinement in the $BaTiO_3$ layer. With more microwave power

confined in the layer that is guiding the optical mode, a larger overlap factor is expected which is indeed the case.

7.6. Voltage-Length Product and Electro-Optic Bandwidth Predictions

Plots of the predicted voltage-length product versus electro-optic bandwidth were obtained using the optical and microwave properties calculated as detailed in Sections 7.3 and 7.4 and the equations for voltage-length product and electro-optic bandwidth as discussed in Chapter 6. These equations are reproduced here for reference. The general equation for the voltage-length product is

$$V_\pi \cdot L = \frac{\lambda_0 g}{n^2 r_{eff} \Gamma_{eo}} \left[(1-x)n_{g,R} + x n_{g,P}\right]^{-1}$$

where λ_0 is the free space optical wavelength, g is the electrode gap spacing, n is the optical mode index, $n_{g,R}$ is the waveguide group index, Γ_{eo} is the electro-optic overlap factor, r_{eff} is the effective electro-optic coefficient, $n_{g,P}$ is the photonic crystal waveguide group index, and x is a dimensionless factor defined as L_P/L_T where L_P is the photonic crystal length and L_T is the total interaction length. The electro-optic bandwidth was calculated using the relation proposed by Rahman and Haxha[58] described in Section 3.7.2, which is a function of the microwave and optical mode indices, conductor and dielectric loss coefficients, and characteristic impedance. The measured microwave index and characteristic impedance and the calculated optical index, conductor loss coefficient, and dielectric loss coefficients discussed in the preceding sections of this chapter were used in the calculations.

7.6.1. Conventional Ridge Waveguide Modulators

The predicted performance for conventional modulators is shown in Fig. 7.12 on a log-log plot. The calculations were done for total interaction (electrode) lengths of 1, 1.5 and 2 mm. Devices with the same interaction length are grouped by colored region. Also shown on the plot is a gray box corresponding to the goal region for device performance: < 0.2 V·cm and > 25 GHz bandwidth. For simplicity, the results are shown only for modulators with a 2 µm Si_3N_4 ridge width. The points for other ridge widths are omitted since the device performance is nearly independent of the ridge width with all other geometrical parameters fixed. On the log-log scale, there appears to be linear relation between $V_\pi \cdot L$ and electro-optic bandwidth for where the only variable is either the gap spacing or film thickness which can be expressed in the form

$$\log(V_\pi \cdot L) = a \log(b \cdot f_{3dB}) \tag{7.6}$$

where a and b are constants and f_{3dB} is the electro-optic bandwidth. Fitting parameters for Eqn. 7.6 for 1 mm long conventional modulators with respect to electrode gap spacing and $BaTiO_3$ thickness are given in Tables 7.2. The data in Fig. 7.12 quantifies several trends that are expected given the results presented in Sections 7.4 and 7.3. For example, it is known that narrower electrode gap spacings should reduce the voltage-length product since $V_\pi \cdot L$ is proportional to the gap spacing; smaller gap spacings, however, are also responsible for larger microwave mode indices and larger confinement of microwave power in the $BaTiO_3$ film, both of which contribute to higher microwave losses. There is therefore a trade-off observed between voltage length product and electro-optic bandwidth where the

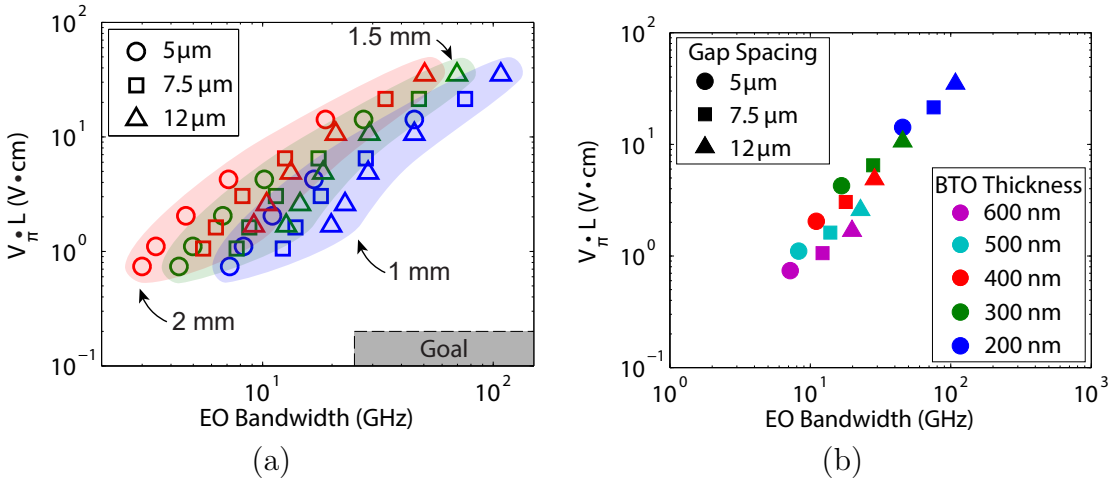

Figure 7.12. (a) Calculated voltage-length product versus calculated electro-optic bandwidth for all geometrical combinations for conventional modulators with 2 µm Si_3N_4 ridge width. (b) Calculations for a total interaction length of 1 mm, plotted according to gap spacing and $BaTiO_3$ thickness.

variable is the gap spacing. This is observed in Fig. 7.12 (b) where the data corresponding to devices with 1 mm long electrodes are plotted according to both gap spacing and film thickness. For a given device length and film thickness, $V_\pi \cdot L$ decreases with smaller gap spacing but the electro-optic bandwidth increases with larger gap spacing. A similar trade-off is observed with respect to the film thickness. Lower voltage-length products are predicted for devices on thicker films due to both higher electro-optical overlap and higher effective electro-optic coefficients, but higher bandwidths are predicted for devices on thinner films. As a result of this trade-off of voltage-length product and electro-optic bandwidth, there are no conventional traveling-wave devices that are expected to operate in the goal region for the parameter set investigated.

Table 7.2. Fitting parameters to Eqn. 7.6 for 1 mm long conventional traveling-wave modulators with a given electrode gap spacing.

Gap Spacing (µm)	a	b
5	1.56	0.131
7.5	1.59	0.0560
12	1.74	0.0455

Table 7.3. Fitting parameters to Eqn. 7.6 for 1 mm long conventional traveling-wave modulators with a given $BaTiO_3$ film thickness.

$BaTiO_3$ Thickness (nm)	a	b
200	1.03	0.116
300	0.908	0.109
400	0.904	0.0733
500	0.832	0.0455
600	0.823	0.0308

7.6.2. Photonic Crystal Modulators

The analysis of voltage-length product versus electro-optic bandwidth was repeated for photonic crystal modulators with optical group indices between 5 and 10 and total device lengths of 250, 500 and 750 µm. These lengths are longer than the fabricated devices with measured transmission properties (see Chapter 6) but are not unreasonably long. For example, photonic crystal waveguides with lengths on the order of millimeters have previously been reported[62]. The total device length here applies to both the photonic crystal length and the electrode (interaction) length. A similar analysis could be applied for composite modulators consisting of both photonic crystal and ridge waveguide segments. The results are plotted according to gap spacing and photonic crystal length in Fig. 7.13 (a) and (b), respectively. The major result obtained from these plots is that photonic crystal modulators can be designed to operate within the goal region shaded gray. This is

in contrast to the case for conventional modulators in which no devices were predicted to operate in the goal region. A comparison of all the results for conventional modulators and all photonic crystal modulators is shown in Fig. 7.13 (c). Compared with the conventional modulators, the operation region of the photonic crystal modulators is shifted down and to the right, i.e. toward lower voltage-length products and higher electro-optic bandwidths. In addition to reducing the voltage length product, it is important to know the operating voltage of the photonic crystal modulators. Plots of half-wave voltage versus electro-optic bandwidth are given in Fig. 7.14 for conventional and photonic crystal modulators. While no conventional modulators are predicted to have < 10 V_{pp} operation with > 25 GHz bandwidth, a subset of photonic crystal modulators with 250 µm length meet and exceed these requirements. It is important to note that the full V_π is not necessary for practical device operation; a lower voltage is required to obtain the modulation depths for data center applications. A V_π of 10 V is lower than most silicon modulators proposed for data center applications[135]. Overall, these results support the hypothesis that a modest increase in waveguide group index can be exploited to lower the device size and operating voltage while increasing the electro-optic bandwidth.

The results presented here are simulations that predict the device performance of future photonic crystal modulators having modest group indices and reasonable lengths. While an increase in the waveguide group index is shown to improve the device properties, group indices that are too large (> 20) start to show negative effects on the electro-optic bandwidth due to large velocity mismatch between the microwave and optical modes. It is possible that a trade-off in group index and photonic crystal length could be used to further optimize the device performance in composite modulators consisting of both

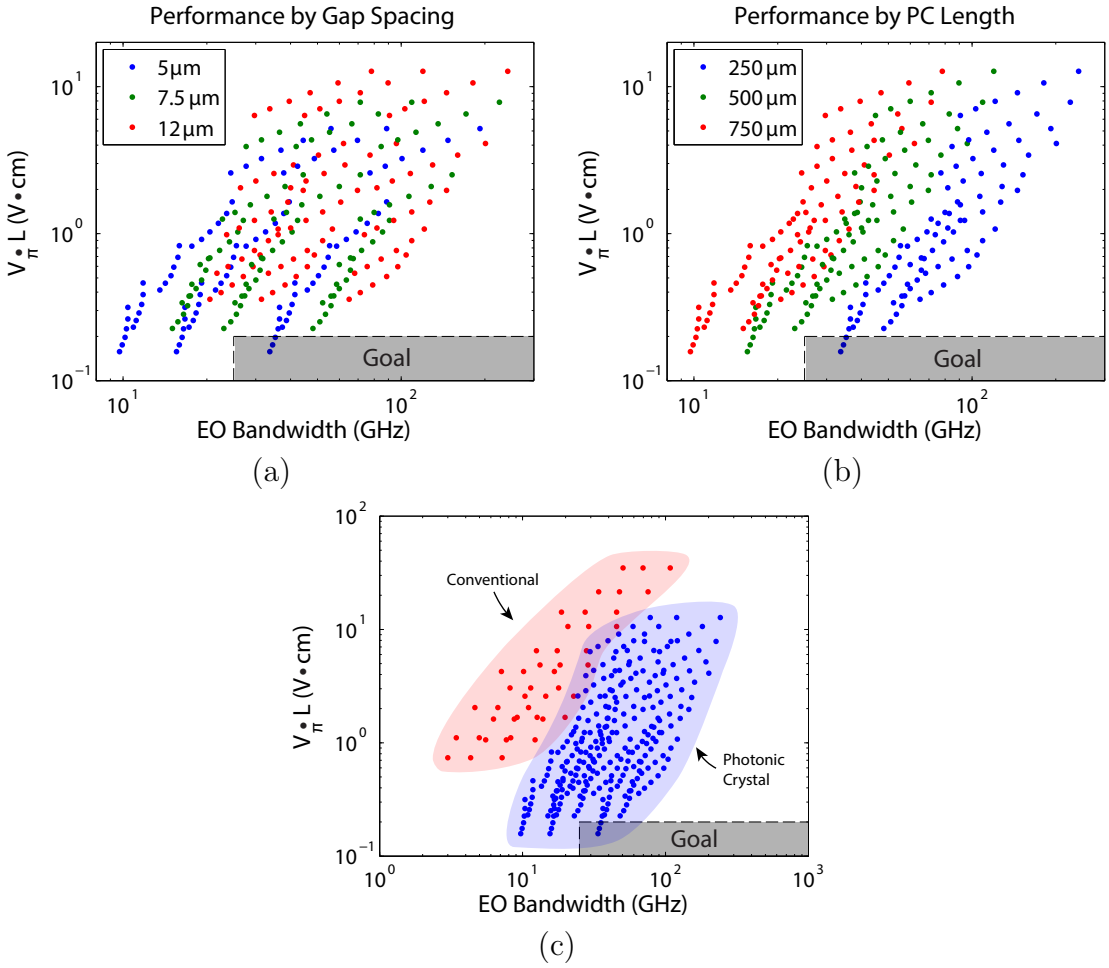

Figure 7.13. Predicted performance of photonic crystal modulators arranged by gap spacing (a) and photonic crystal length (b). Performance of all conventional and photonic crystal modulators (c).

photonic crystal and ridge waveguide segments. For example, a smaller photonic crystal segment ($< 250\,\mu$m with higher group index (> 20) may be embedded within a device with a longer interaction length to yield a lower-voltage and higher bandwidth device. Such an optimization should realistically be done in conjunction with feedback from device fabrication. A major obstacle to demonstrating the modulators simulated here with longer photonic crystal lengths lies in the optical propagation losses. As discussed in

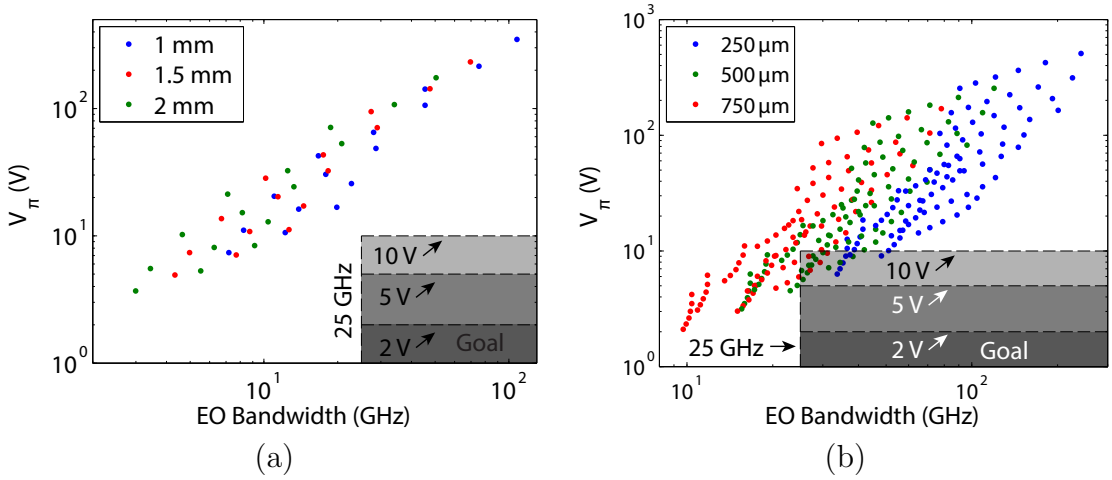

Figure 7.14. Predicted performance of (a) conventional and (b) photonic crystal electro-optic modulators plotted as half-wave voltage versus electro-optic bandwidth.

Chapter 6, the photonic crystal waveguides patterned in this study have a typical insertion losses of 10 dB or, per length, 0.3 dB/µm within the photonic crystal region. For a total device length of 250 µm, the expected loss is approximately 70 dB. In order to realistically test the devices simulated here, the losses should be reduced by an order of magnitude to 0.03 dB/µm or smaller, which will require further improvements in the fabrication. The dependence of the insertion losses on focused ion beam fabrication imperfections have previously been investigted for $LiNbO_3$ photonic crystal devices, in which it was determined that the conical profile results in out-of-plane losses[22]. Such losses due to out-of-plane scattering could be presumably reduced by improving the milled hole shape by using e-beam lithography and reactive ion etching to produce more vertical sidewalls. For alternative etching techniques to work, the etching chemistry would need to be optimized. Successful fabrication of nanophotonic structures on $LiNbO_3$ has been demonstrated using

reactive ion etching with SF_6 [59,118]. This could be used as a starting point for investigating the viable etching chemistries for $BaTiO_3$ thin films.

7.7. Summary and Conclusions

The voltage-length product and electro-optic bandwidth of conventional and photonic crystal traveling-wave modulators on the $BaTiO_3$/MgO platform were evaluated through numerical and analytical modeling. The calculations were done over a parameter space of reasonable device dimensions for determining device geometries with low voltage-length products and high electro-optic bandwidths. From the aggregate data, a logarithmic relation was found between the voltage-length product and electro-optic bandwidth of the form $\log(V_\pi \cdot L) = a \log(b \cdot f_{3dB})$ when either the electrode gap spacing or $BaTiO_3$ film thickness is the variable. The fitting coefficients a and b were obtained from the simulation results for enabling rapid design of modulators meeting specified requirements for voltage and bandwidth. For the parameter space investigated, no conventional modulators were predicted to have both $< 0.2\,\mathrm{V \cdot cm}$ voltage-length product and $< 25\,\mathrm{GHz}$ electro-optic bandwidth. By extending the analysis for photonic crystal modulators with sub-millimeter length, it was shown that photonic crystal devices with moderately enhanced group index could achieve both lower voltage-length product and higher electro-optic bandwidth. As an example, a 250 µm long photonic crystal device with 9.1 V half-wave voltage and 48 GHz electro-optic bandwidth is predicted. It is important to note that the calculations presented here for both conventional and PC modulators represent a starting point from which device performance can be further improved. At high frequencies, the electro-optic coefficient tensor elements r_{51} and r_{42} of bulk $BaTiO_3$ crystals are $r_{51} = r_{42} = 800$ pm/V, with a

maximum effective coeffcient of approximately 620 pm/V predicted for mixed domain films[24], significantly larger than the maximum r_{eff} used in this study. There is hence potential for further reductions in V_π and further increases in electro-optic bandwidth beyond what is reported here for $BaTiO_3$ modulators. In order to demonstrate the PC devices reported here, the device insertion loss will need to be improved from the current 0.3 dB/µm to 0.03 dB/µm. Improvement in the insertion loss are expected to result from an improvement in device fabrication by investigating alternative etching techniques with greater vertical etching selectivity, such as reactive ion etching. Demonstrating photonic crystal devices with the properties predicted here would be a significant advancement toward compact, high-bandwidth, and low-voltage modulators.

CHAPTER 8

Summary and Conclusions

The microwave, electro-optic, and optical properties of $BaTiO_3$ films were measured to demonstrate the applicability of this material for use in high speed electro-optic devices for telecommunication and data network applications. The microwave properties of epitaxial $BaTiO_3$ thin film coplanar stripline devices and the optical and electro-optic properties of $BaTiO_3$ conventional and photonic crystal waveguide modulators were experimentally studied for wavelengths in the optical C band and for technologically relevant modulation frequencies up to 50 GHz. The microwave properties were determined between 10 MHz and 50 GHz via measurement of the microwave scattering parameters. These measurements were used to model the electro-optic response, which was found to be in good agreement with high frequency electro-optic response measurements obtained using a calibrated vector network analyzer setup. The effective electro-optic coefficients of $BaTiO_3$ thin films were measured for the first time at modulation frequencies between 10 and 40 GHz using an optical spectral analysis technique. Photonic crystal waveguides with hexagonal lattice and line defect structures were designed and fabricated. The passive optical transmission properties of the photonic crystal waveguides were measured for wavelengths between 1500 and 1580 nm, which span the optical C band (1530-1565 nm), the relevant wavelength window used for telecommunications. The optical spectral analysis technique was used to demonstrate a wideband enhancement of the electro-optic coefficient in $BaTiO_3$ line defect photonic crystal waveguide modulators and a dispersion in the enhancement across

the stop-band of photonic crystal modulators with hexagonal lattice symmetry, in good agreement with the trends predicted by a theory for the enhancement proposed here. Finally, the results of the microwave measurements were applied in conjunction with the theory for electro-optic coefficient enhancement to predict the ultimate performance of $BaTiO_3$ photonic crystal waveguide modulators. Modulators with less than 2 V_{pp} operation and greater than 60 GHz electro-optic bandwidth are predicted for sub-millimeter long devices. The work presented here is a major advancement in meeting the requirements for modulators in next generation telecommunication and data network applications.

The specific results of this work are enumerated at the end of each chapter. The most important results are summarized here:

(1) The microwave properties of 1 mm long $BaTiO_3$ coplanar stripline devices were measured in the frequency range of 10 MHz to 50 GHz. The microwave losses of $BaTiO_3$ modulators, which include index mismatch with the co-propagating optical wave, impedance mismatch to a 50 Ω system, and attenuation losses, were all found to decrease with wider electrode gap spacings and thinner $BaTiO_3$ films.

(2) Excellent agreement was obtained between the experimental transmission and theoretical modeling of $BaTiO_3$ photonic crystal waveguides using an effective medium FDTD approach and feedback to modeling provided by cross-sectional imaging of structures fabricated with focused ion beam lithography. The feedback provided to modeling enabled the demonstration of hexagonal lattice photonic crystal waveguides with a record high band edge sharpness of 2.0 dB/nm for all ferroelectric photonic crystal waveguides to date.

(3) Line defect dispersion-engineered $BaTiO_3$ photonic crystal waveguides were modeled and characterized for the first time. An average group index of 16 was measured across a 50 nm optical bandwidth, enabling operation of these devices for wide optical bandwidths employed for wavelength-division multiplexing of data streams.

(4) A model was proposed for the enhancement of the electro-optic coefficient in $\chi^{(2)}$ photonic crystal waveguides in which the enhancement is proportional to the slowdown factor of the photonic crystal. This model was used to quantify an electro-optic coefficient enhancement of 1.4 in a 1 mm long $BaTiO_3$ modulator containing a 37 µm long W1 photonic crystal segment. An enhancement factor of 12 and effective electro-optic coefficient of 900 pm/V was obtained in the photonic crystal region, a record high value for all $BaTiO_3$ devices.

(5) A monotonic increase in the effective electro-optic coefficient was measured approaching the photonic band edge of a hexagonal lattice $BaTiO_3$ photonic crystal waveguide modulator. This is in agreement with the model for the electro-optic coefficient enhancement, which states that the electro-optic coefficient enhancement increases proportional to the optical group index, and the known fact that the group index increases toward infinity as a band edge is approached.

(6) A record large 3 dB electro-optic bandwidth of 28 GHz was measured for all $BaTiO_3$ conventional modulators. This record was obtained through insight from microwave property measurements, which indicate that the largest electro-optic bandwidths of coplanar stripline devices on $BaTiO_3$ are obtained for those with wider gap spacings on thin $BaTiO_3$ films.

(7) Record low voltage-length products of $BaTiO_3$ films of $0.39\,V \cdot cm$ ($0.45\,V \cdot cm$) were measured at a modulation frequency of 100 Hz (1 MHz) in the smallest traveling-wave $BaTiO_3$ modulator to date. This value was obtained for a modulator with the narrowest electrode gap spacing on the thickest $BaTiO_3$ film characterized here having the largest electro-optic overlap factor.

(8) The measured microwave properties and the proposed model for the electro-optic coefficient enhancement in $\chi^{(2)}$ photonic crystal modulators was used to predict the ultimate performance of $BaTiO_3$ photonic crystal modulators. The implementation of moderate group index waveguides is shown through modeling to reduce the voltage-length product, which allows for a reduction in modulator length. A reduction in the modulator length reduces the total microwave losses, thereby increasing the predicted electro-optic bandwidth. $BaTiO_3$ photonic crystal modulators with greater than 40 GHz 3 dB electro-optic bandwidth and less than 0.2 V·cm voltage-length product are predicted in sub-millimeter lengths.

Bibliography

[1] Interconnect. Technical report, International Technology Roadmap for Semiconductors, 2013.

[2] S Abel, M Sousa, C Rossel, D Caimi, MD Rossell, R Erni, J Fompeyrine, and C Marchiori. Controlling tetragonality and crystalline orientation in $BaTiO_3$ nanolayers grown on si. *Nanotechnology*, 24(28):285701, 2013.

[3] Stefan Abel, Thilo Stöferle, Chiara Marchiori, Daniele Caimi, Lukas Czornomaz, Christophe Rossel, Marta Rossell, Rolf Erni, Marilyne Sousa, Heinz Siegwart, et al. Electro-optical active barium titanate thin films in silicon photonics devices. In *Integrated Photonics Research, Silicon and Nanophotonics*, pages IW4A–5. Optical Society of America, 2013.

[4] Stefan Abel, Thilo Stöferle, Chiara Marchiori, Christophe Rossel, Marta D Rossell, Rolf Erni, Daniele Caimi, Marilyne Sousa, Alexei Chelnokov, Bert J Offrein, et al. A strong electro-optically active lead-free ferroelectric integrated on silicon. *Nature Communications*, 4:1671, 2013.

[5] G.P. Agrawal. *Fiber-optic Communication Systems*. Wiley-Interscience, 2001.

[6] Michel Aillerie, N Theofanous, and MD Fontana. Measurement of the electro-optic coefficients: description and comparison of the experimental techniques. *Applied Physics B*, 70(3):317–334, 2000.

[7] Jacques Albert and Gar Lam Yip. Insertion loss reduction between single-mode fibers and diffused channel waveguides. In *OE/Fiber LASE'88*, pages 173–179. International Society for Optics and Photonics, 1988.

[8] JR Anderson, GW Brady, WJ Merz, and JP Remeika. Effects of ambient atmosphere on the stability of barium titanate. *Journal of Applied Physics*, 26(11):1387–1388, 1955.

[9] Toshihiko Baba. Slow light in photonic crystals. *Nature Photonics*, 2(8):465–473, 2008.

[10] Omri Bahat-Treidel, Or Peleg, Mark Grobman, Nadav Shapira, Mordechai Segev, and T Pereg-Barnea. Klein tunneling in deformed honeycomb lattices. *Physical Review Letters*, 104(6):063901, 2010.

[11] Michael J Banach, Max D Alexander, Stephen Caracci, and Richard A Vaia. Enhancement of electro-optic coefficient of doped films through optimization of chromophore environment. *Chemistry of Materials*, 11(9):2554–2561, 1999.

[12] Alessandro Belardini, Lorenzo Dominici, MC Larciprete, F Michelotti, Alain Rousseau, and Amédée Ratsimihety. Enhanced stability of the second order optical properties of high-T_g fluorinated electro-optic copolymer. *Applied Physics Letters*, 89(23):231110, 2006.

[13] John A Belot, Deborah A Neumayer, Charles J Reedy, Daniel B Studebaker, Bruce J Hinds, Charlotte L Stern, and Tobin J Marks. Volatility by design. synthesis and characterization of polyether adducts of bis (1, 1, 1, 5, 5, 5-hexafluoro-2, 4-pentanedionato) barium and their implementation as metal-organic chemical vapor deposition precursors. *Chemistry of Materials*, 9(7):1638–1648, 1997.

[14] A. F. Benner, M. Ignatowski, J.A. Kash, D.M. Kuchta, and M.B. Ritter. Exploitation of optical interconnects in future server architectures. *IBM Journal of Research and Development*, 49:755–775, 2005.

[15] Nenad Bozinovic, Yang Yue, Yongxiong Ren, Moshe Tur, Poul Kristensen, Hao Huang, Alan E Willner, and Siddharth Ramachandran. Terabit-scale orbital angular momentum mode division multiplexing in fibers. *Science*, 340(6140):1545–1548, 2013.

[16] Charles A Brackett. Dense wavelength division multiplexing networks: Principles and applications. *Selected Areas in Communications, IEEE Journal on*, 8(6):948–964, 1990.

[17] A Brimont, DJ Thomson, FY Gardes, JM Fedeli, GT Reed, J Martí, and P Sanchis. High-contrast 40 Gb/s operation of a 500 μm long silicon carrier-depletion slow wave modulator. *Optics Letters*, 37(17):3504–3506, 2012.

[18] A Brimont, DJ Thomson, P Sanchis, J Herrera, FY Gardes, JM Fedeli, GT Reed, and J Martí. High speed silicon electro-optical modulators enhanced via slow light propagation. *Optics Express*, 19(21):20876–20885, 2011.

[19] Jan-Michael Brosi, Christian Koos, Lucio Claudio Andreani, Michael Waldow, Juerg Leuthold, and Wolfgang Freude. High-speed low-voltage electro-optic modulator with a polymer-infiltrated silicon photonic crystal waveguide. *Optics Express*, 16(6):4177–4191, 2008.

[20] Michael D. Brunsman. Verification of on-wafer (SOLT) calibration. Technical report, Agilent, 2003.

[21] DL Bullock, Chun-Ching Shih, and RS Margulies. Photonic band structure investigation of two-dimensional Bragg reflector mirrors for semiconductor laser mode control. *JOSA B*, 10(2):399–403, 1993.

[22] GW Burr, S Diziain, and M-P Bernal. The impact of finite-depth cylindrical and conical holes in lithium niobate photonic crystals. *Optics Express*, 16(9):6302–6316, 2008.

[23] Lutong Cai, Huangpu Han, Shaomei Zhang, Hui Hu, and Keming Wang. Photonic crystal slab fabricated on the platform of lithium niobate-on-insulator. *Optics Letters*, 39(7):2094–2096, 2014.

[24] Pau Castera, Ana M Gutierrez, Domenico Tulli, Sébastien Cueff, Regis Orobtchouk, Pedro Rojo Romeo, Guillaume Saint-Girons, and Pablo Sanchis. Electro-optical modulation based on pockels effect in $BaTiO_3$ with a multi-domain structure. *IEEE Photonics Technology Letters*, 28(9):990–993, 2016.

[25] Pau Castera, Domenico Tulli, Ana M Gutierrez, and Pablo Sanchis. Influence of $BaTiO_3$ ferroelectric orientation for electro-optic modulation on silicon. *Optics Express*, 23(12):15332–15342, 2015.

[26] Papichaya Chaisakul, Delphine Marris-Morini, Mohamed-Said Rouifed, Jacopo Frigerio, Daniel Chrastina, Jean-René Coudevylle, Xavier Le Roux, Samson Edmond, Giovanni Isella, and Laurent Vivien. Recent progress in GeSi electro-absorption modulators. *Science and Technology of Advanced Materials*, 15(1):014601, 2013.

[27] Papichaya Chaisakul, Delphine Marris-Morini, Mohamed-Saïd Rouifed, Giovanni Isella, Daniel Chrastina, Jacopo Frigerio, Xavier Le Roux, Samson Edmond, Jean-René Coudevylle, and Laurent Vivien. 23 GHz Ge/SiGe multiple quantum well electro-absorption modulator. *Optics Express*, 20(3):3219–3224, 2012.

[28] Erli Chen and Stephen Y Chou. Characteristics of coplanar transmission lines on multilayer substrates: Modeling and experiments. *IEEE Transactions on Microwave*

Theory and Techniques, 45(6):939–945, 1997.

[29] Feng Chen. Photonic guiding structures in lithium niobate crystals produced by energetic ion beams. *Journal of Applied Physics*, 106(8):081101, 2009.

[30] Xiaonan Chen, Yun-Sheng Chen, Yang Zhao, Wei Jiang, and Ray T Chen. Capacitor-embedded 0.54 pJ/bit silicon-slot photonic crystal waveguide modulator. *Optics Letters*, 34(5):602–604, 2009.

[31] P Colman, C Husko, S Combrié, I Sagnes, CW Wong, and A De Rossi. Temporal solitons and pulse compression in photonic crystal waveguides. *Nature Photonics*, 4(12):862–868, 2010.

[32] S Combrié, Evelin Weidner, Alfredo DeRossi, Shailendra Bansropun, Simone Cassette, Anne Talneau, and Henri Benisty. Detailed analysis by Fabry-Perot method of slab photonic crystal line-defect waveguides and cavities in aluminium-free material system. *Optics Express*, 14(16):7353–7361, 2006.

[33] Sylvain Combrié, Evelin Weidner, Alfredo De Rossi, Simone Cassette, Philippe Hamel, Yves Jaouën, Renaud Gabet, Anne Talneau, et al. Investigation of group delay, loss, and disorder in a photonic crystal waveguide by low-coherence reflectometry. *Applied Physics Letters*, 90(23):231104, 2007.

[34] Bill Corcoran, Christelle Monat, Christian Grillet, David J Moss, Benjamin J Eggleton, TP White, Liam O'Faolain, and Thomas F Krauss. Green light emission in silicon through slow-light enhanced third-harmonic generation in photonic-crystal waveguides. *Nature Photonics*, 3(4):206–210, 2009.

[35] F Cuesta-Soto, A Martinez, J Garcia, F Ramos, P Sanchis, J Blasco, and J Marti. All-optical switching structure based on a photonic crystal directional coupler. *Optics Express*, 12(1):161–167, 2004.

[36] Dragan Damjanovic. Ferroelectric, dielectric and piezoelectric properties of ferroelectric thin films and ceramics. *Reports on Progress in Physics*, 61(9):1267, 1998.

[37] M DiDomenico Jr. and SH Wemple. Oxygen-octahedra ferroelectrics. I. Theory of electro-optical and nonlinear optical effects. *Journal of Applied Physics*, 40(2):720–734, 1969.

[38] Po Dong, Shirong Liao, Hong Liang, Wei Qian, Xin Wang, Roshanak Shafiiha, Dazeng Feng, Guoliang Li, Xuezhe Zheng, Ashok V Krishnamoorthy, et al. High-speed and compact silicon modulator based on a racetrack resonator with a 1 V drive voltage. *Optics Letters*, 35(19):3246–3248, 2010.

[39] Y Dumeige, P Vidakovic, S Sauvage, I Sagnes, JA Levenson, C Sibilia, M Centini, G D'Aguanno, and M Scalora. Enhancement of second-harmonic generation in a one-dimensional semiconductor photonic band gap. *Applied Physics Letters*, 78(20):3021–3023, 2001.

[40] Elizabeth H Edwards, Leon Lever, Edward T Fei, Theodore I Kamins, Zoran Ikonic, James S Harris, Robert W Kelsall, and David AB Miller. Low-voltage broad-band electroabsorption from thin Ge/SiGe quantum wells epitaxially grown on silicon. *Optics Express*, 21(1):867–876, 2013.

[41] RJP Engelen, Yoshimasa Sugimoto, Yoshinori Watanabe, Jeroen P Korterik, Noaki Ikeda, Niek F van Hulst, Kiyoshi Asakawa, and Laurens Kuipers. The effect of higher-order dispersion on slow light propagation in photonic crystal waveguides. *Optics Express*, 14(4):1658–1672, 2006.

[42] Arman B Fallahkhair, Kai S Li, and Thomas E Murphy. Vector finite difference modesolver for anisotropic dielectric waveguides. *Journal of Lightwave Technology*, 26(11):1423–1431, 2008.

[43] Dazeng Feng, Shirong Liao, Hong Liang, Joan Fong, Bhavin Bijlani, Roshanak Shafiiha, B Jonathan Luff, Ying Luo, Jack Cunningham, Ashok V Krishnamoorthy, et al. High speed GeSi electro-absorption modulator at 1550 nm wavelength on SOI waveguide. *Optics Express*, 20(20):22224–22232, 2012.

[44] Victor Fouad Hanna. Finite boundary corrections to coplanar stripline analysis. *Electronics Letters*, 16(15):604–606, 1980.

[45] Lars H Frandsen, Andrei V Lavrinenko, Jacob Fage-Pedersen, and Peter I Borel. Photonic crystal waveguides with semi-slow light and tailored dispersion properties. *Optics Express*, 14(20):9444–9450, 2006.

[46] Michael Y Frankel, Robert H Voelker, and James N Hilfiker. Coplanar transmission lines on thin substrates for high-speed low-loss propagation. *Microwave Theory and Techniques, IEEE Transactions on*, 42(3):396–402, 1994.

[47] Takumi Fujiwara, Xiaofan Cao, Ramakant Srivastava, and Ramu V Ramaswamy. Photorefractive effect in annealed proton-exchanged $LiNbO_3$ waveguides. *Applied Physics Letters*, 61(7):743–745, 1992.

[48] Takumi Fujiwara, Ramakant Srivastava, Xiaofan Cao, and Ramu V Ramaswamy. Comparison of photorefractive index change in proton-exchanged and Ti-diffused $LiNbO_3$ waveguides. *Optics Letters*, 18(5):346–348, 1993.

[49] Sergey V. Gaponenko. *Introduction to Nanophotonics*, pages 199–239. Cambridge University Press, 2010.

[50] Ramesh Garg, Inder Bahl, and Maurizio Bozzi. *Microstrip lines and slotlines*. Artech house, 2013.

[51] S Gevorgian, H Berg, H Jacobsson, and T Lewin. Application notes-basic parameters of coplanar-strip waveguides on multilayer dielectric/semiconductor substrates, part 1: high permittivity superstrates. *Microwave Magazine, IEEE*, 4(2):60–70, 2003.

[52] Giovanni Ghione and C Naldi. Analytical formulas for coplanar lines in hybrid and monolithic MICs. *Electronics Letters*, 20(4):179–181, 1984.

[53] AM Glass, D Von der Linde, and TJ Negran. High-voltage bulk photovoltaic effect and the photorefractive process in $LiNbO_3$. *Applied Physics Letters*, 25(4):233–235, 1974.

[54] Lanlan Gu, Wei Jiang, Xiaonan Chen, Li Wang, and Ray T Chen. High speed silicon photonic crystal waveguide modulator for low voltage operation. *Applied Physics Letters*, 90(7):071105, 2007.

[55] C Haffner, W Heni, Y Fedoryshyn, J Niegemann, A Melikyan, DL Elder, B Baeuerle, Y Salamin, A Josten, U Koch, et al. All-plasmonic Mach–Zehnder modulator enabling optical high-speed communication at the microscale. *Nature Photonics*, 9(8):525–528, 2015.

[56] Yohei Hamachi, Shousaku Kubo, and Toshihiko Baba. Slow light with low dispersion and nonlinear enhancement in a lattice-shifted photonic crystal waveguide. *Optics Letters*, 34(7):1072–1074, 2009.

[57] T Hamano, DJ Towner, and BW Wessels. Relative dielectric constant of epitaxial $BaTiO_3$ thin films in the GHz frequency range. *Applied Physics Letters*, 83:5274, 2003.

[58] Shyqyri Haxha, BM Rahman, and Kenneth TV Grattan. Bandwidth estimation for ultra-high-speed lithium niobate modulators. *Applied Optics*, 42(15):2674–2682, 2003.

[59] H Hu, AP Milenin, RB Wehrspohn, H Hermann, and W Sohler. Plasma etching of proton-exchanged lithium niobate. *Journal of Vacuum Science & Technology A*, 24(4):1012–1015, 2006.

[60] Xuan Hu, Sébastien Cueff, Pedro Rojo Romeo, and Régis Orobtchouk. Modeling the anisotropic electro-optic interaction in hybrid silicon-ferroelectric optical modulator. *Optics Express*, 23(2):1699–1714, 2015.

[61] Stephen Hughes, L Ramunno, Jeff F Young, and JE Sipe. Extrinsic optical scattering loss in photonic crystal waveguides: role of fabrication disorder and photon group velocity. *Physical Review Letters*, 94(3):033903, 2005.

[62] Chad A Husko, Sylvain Combrié, Pierre Colman, Jiangjun Zheng, Alfredo De Rossi, and Chee Wei Wong. Soliton dynamics in the multiphoton plasma regime. *Scientific Reports*, 3, 2013.

[63] Shin-ichiro Inoue and Akira Otomo. Electro-optic polymer/silicon hybrid slow light modulator based on one-dimensional photonic crystal waveguides. *Applied Physics Letters*, 103(17):171101, 2013.

[64] Kenneth P. Jackson and Clint L. Schow. VCSEL-based transceivers for data communications. In Rainer Michalzik, editor, *VCSELs: fundamentals, technology and applications of vertical-cavity surface-emitting lasers*, page 446. Springer, 2013.

[65] Rune S Jacobsen, Karin N Andersen, Peter I Borel, Jacob Fage-Pedersen, Lars H Frandsen, Ole Hansen, Martin Kristensen, Andrei V Lavrinenko, Gaid Moulin, Haiyan Ou, et al. Strained silicon as a new electro-optic material. *Nature*, 441(7090):199–202, 2006.

[66] Young Kyu Jeong and Bruce W Wessels. Properties of epitaxial barium titanate thin films using a highly volatile Ba (hfa) 2triglyme precursor. *Journal of Vacuum Science & Technology B*, 33(5):051206, 2015.

[67] John D Joannopoulos, Steven G Johnson, Joshua N Winn, and Robert D Meade. *Photonic Crystals: Molding the Flow of Light*. Princeton University Press, 2011.

[68] Sajeev John. Strong localization of photons in certain disordered dielectric superlattices. *Physical Review Letters*, 58(23):2486, 1987.

[69] Steven G Johnson, Attila Mekis, Shanhui Fan, and John D Joannopoulos. Molding the flow of light. *Computing in Science & Engineering*, 3(6):38–47, 2001.

[70] V Kazmirenko, Y Poplavko, L Pereverzeva, Y Prokopenko, Beomjin Kim, Minki Jeong, and Sunggi Baik. Ferroelectric thin film microwave examination. *Ferroelectrics*, 286(1):353–356, 2003.

[71] Jeffrey B Knorr and Klaus-Dieter Kuchler. Analysis of coupled slots and coplanar strips on dielectric substrate. *Microwave Theory and Techniques, IEEE Transactions on*, 23(7):541–548, 1975.

[72] Eiichi Kuramochi, Masaya Notomi, S Hughes, Akihiko Shinya, T Watanabe, and L Ramunno. Disorder-induced scattering loss of line-defect waveguides in photonic crystal slabs. *Physical Review B*, 72(16):161318, 2005.

[73] H Kurt, K Üstün, and L Ayas. Study of different spectral regions and delay bandwidth relation in slow light photonic crystal waveguides. *Optics Express*, 18(26):26965–26977, 2010.

[74] F Lacour, N Courjal, M-P Bernal, A Sabac, C Bainier, and M Spajer. Nanostructuring lithium niobate substrates by focused ion beam milling. *Optical Materials*, 27(8):1421–1425, 2005.

[75] Mark Lee, Howard E Katz, Christoph Erben, Douglas M Gill, Padma Gopalan, Joerg D Heber, and David J McGee. Broadband modulation of light by using an electro-optic polymer. *Science*, 298(5597):1401–1403, 2002.

[76] Feng-Chun Leng, Wen-Yao Liang, Bin Liu, Tong-Biao Wang, and He-Zhou Wang. Wideband slow light and dispersion control in oblique lattice photonic crystal waveguides. *Optics Express*, 18(6):5707–5712, 2010.

[77] G Lenz, BJ Eggleton, C Kd Madsen, and RE Slusher. Optical delay lines based on optical filters. *Quantum Electronics, IEEE Journal of*, 37(4):525–532, 2001.

[78] J Lettieri, JH Haeni, and DG Schlom. Critical issues in the heteroepitaxial growth of alkaline-earth oxides on silicon. *Journal of Vacuum Science & Technology A*, 20(4):1332–1340, 2002.

[79] Jianheng Li. *Investigation of Electro-optic Properties of Barium Titanate Epitaxial Thin Films, Photonic Crystals and Modulators*. PhD thesis, Northwestern University, 2012.

[80] Jianheng Li, Pao Tai Lin, and BW Wessels. Polarization reversal and backswitching dynamics in epitaxial $BaTiO_3$ thin films. *Journal of Applied Physics*, 106(5):054113–054113, 2009.

[81] Jianheng Li, Zhifu Liu, Yongming Tu, Seng-Tiong Ho, Il Woong Jung, Leonidas E Ocola, and Bruce W Wessels. Photonic crystal waveguide electro-optic modulator with a wide bandwidth. *Journal of Lightwave Technology*, 31(10):1601–1607, 2013.

[82] Jianheng Li, Zhifu Liu, and Bruce W Wessels. Photonic crystal waveguide electro-optic modulator for GHz bandwidth applications. In *Frontiers in Optics*, page FThW4. Optical Society of America, 2011.

[83] Jianheng Li, Zhifu Liu, Bruce W Wessels, Yongming Tu, Seng-Tiong Ho, Alexandra Joshi-Imre, and Leonidas E Ocola. Hexagonal photonic crystal waveguide based on barium titanate thin films. In *SPIE OPTO*, pages 79340R–79340R. International Society for Optics and Photonics, 2011.

[84] Juntao Li, Thomas P White, Liam O'Faolain, Alvaro Gomez-Iglesias, and Thomas F Krauss. Systematic design of flat band slow light in photonic crystal waveguides. *Optics Express*, 16(9):6227–6232, 2008.

[85] Zhi-Yuan Li and Lan-Lan Lin. Photonic band structures solved by a plane-wave-based transfer-matrix method. *Physical Review E*, 67(4):046607, 2003.

[86] Jian Liang, Li-Yong Ren, Mao-Jin Yun, and Xing-Jun Wang. Wideband slow light with ultralow dispersion in a w1 photonic crystal waveguide. *Applied Optics*, 50(31):G98–G103, 2011.

[87] Che-Yun Lin, Xiaolong Wang, Swapnajit Chakravarty, Beom Suk Lee, Weicheng Lai, Jingdong Luo, Alex K.-Y. Jen, and Ray T. Chen. Electro-optic polymer infiltrated silicon photonic crystal slot waveguide modulator with 23 dB slow light enhancement. *Applied Physics Letters*, 97:093304, 2010.

[88] Pao Tai Lin. *Investigation of the Optical Properties of Ferroelectric Oxide Thin Film Photonic Crystals*. PhD thesis, Northwestern University, 2009.

[89] Pao Tai Lin, Alexandra Imre, Leonidas E Ocola, and BW Wessels. Thin film ferroelectric photonic crystals and their application to thermo-optic switches. *Optics Communications*, 282(16):3364–3367, 2009.

[90] Pao Tai Lin, Fei Yi, Seng-Tiong Ho, and Bruce W Wessels. Two-dimensional ferroelectric photonic crystal waveguides: simulation, fabrication, and optical characterization. *Journal of Lightwave Technology*, 27(19):4330–4337, 2009.

[91] PT Lin, Z Liu, and BW Wessels. Ferroelectric thin film photonic crystal waveguide and its electro-optic properties. *Journal of Optics A: Pure and Applied Optics*, 11(7):075005, 2009.

[92] Shawn-Yu Lin, Edmund Chow, Vince Hietala, Pierre R Villeneuve, and JD Joannopoulos. Experimental demonstration of guiding and bending of electromagnetic waves in a photonic crystal. *Science*, 282(5387):274–276, 1998.

[93] Yu-De Lin and Syh-Nan Tsai. Coplanar waveguide-fed uniplanar bow-tie antenna. *Antennas and Propagation, IEEE Transactions on*, 45(2):305–306, 1997.

[94] Jialei Liu, Guangming Xu, Fenggang Liu, Iwan Kityk, Xinhou Liu, and Zhen Zhen. Recent advances in polymer electro-optic modulators. *Rsc Advances*, 5(21):15784–15794, 2015.

[95] Tao Liu, Armis R Zakharian, Mahmoud Fallahi, Jerome V Moloney, and Masud Mansuripur. Design of a compact photonic-crystal-based polarizing beam splitter. *Photonics Technology Letters, IEEE*, 17(7):1435–1437, 2005.

[96] Zhifu Liu, Jianheng Li, Yongming Tu, Seng-Tiong Ho, and Bruce W Wessels. Ultrafast modulators based on nonlinear photonic crystal waveguides. In *SPIE OPTO*, pages 794905–794905. International Society for Optics and Photonics, 2011.

[97] Zhifu Liu, Pao-Tai Lin, Bruce W Wessels, Fei Yi, and Seng-Tiong Ho. Nonlinear photonic crystal waveguide structures based on barium titanate thin films and their optical properties. *Applied Physics Letters*, 90(20):201104, 2007.

[98] Zhifu Liu, AL Meier, and BW Wessels. Dynamic response of polydomain ferroelectric barium titanate epitaxial thin films and its field dependence. *Journal of Applied Physics*, 104(6):064115, 2008.

[99] H Lu, B Sadani, N Courjal, G Ulliac, N Smith, V Stenger, M Collet, FI Baida, and M-P Bernal. Enhanced electro-optical lithium niobate photonic crystal wire

waveguide on a smart-cut thin film. *Optics Express*, 20(3):2974–2981, 2012.

[100] Huihui Lu, Benattou Sadani, Gwenn Ulliac, Nadège Courjal, Clément Guyot, J-M Merolla, Manuel Collet, Fadi Issam Baida, and M-P Bernal. 6-micron interaction length electro-optic modulation based on lithium niobate photonic crystal cavity. *Optics Express*, 20(19):20884–20893, 2012.

[101] Jean-Michel Luortioz, Henri Benisty, Vincent Berger, Jean-Michel Gérard, Daniel Maystre, Alexei Tchelnokov, and Dominique Pagnoux. *Photonic Crystals: Towards Nanoscale Photonic Devices*. Springer, 2008.

[102] RA McKee, FJ Walker, and MF Chisholm. Crystalline oxides on silicon: the first five monolayers. *Physical Review Letters*, 81(14):3014, 1998.

[103] Anthony Meier. *Investigation of the Effect of Ferroelectric Domain Structure and Dynamics on the Electro-Optic Properties of Polydomain Epitaxial Barium Titanate Thin Films*. PhD thesis, Northwestern University, 2007.

[104] Attila Mekis, JC Chen, I Kurland, Shanhui Fan, Pierre R Villeneuve, and JD Joannopoulos. High transmission through sharp bends in photonic crystal waveguides. *Physical Review Letters*, 77(18):3787, 1996.

[105] A Melikyan, L Alloatti, A Muslija, D Hillerkuss, PC Schindler, J Li, R Palmer, D Korn, S Muehlbrandt, Dries Van Thourhout, et al. High-speed plasmonic phase modulators. *Nature Photonics*, 8(3):229–233, 2014.

[106] David Miller. Device requirements for optical interconnects to CMOS silicon chips. In *Photonics in Switching*, page PMB3. Optical Society of America, 2010.

[107] Momchil Minkov and Vincenzo Savona. Wide-band slow light in compact photonic crystal coupled-cavity waveguides. *Optica*, 2(7):631–634, 2015.

[108] Christelle Monat, Bill Corcoran, Majid Ebnali-Heidari, Christian Grillet, Benjamin J Eggleton, Thomas P White, Liam O'Faolain, and Thomas F Krauss. Slow light enhancement of nonlinear effects in silicon engineered photonic crystal waveguides. *Optics Express*, 17(4):2944–2953, 2009.

[109] Daisuke Mori and Toshihiko Baba. Dispersion-controlled optical group delay device by chirped photonic crystal waveguides. *Applied Physics Letters*, 85(7):1101–1103, 2004.

[110] Hong C Nguyen, Satoshi Hashimoto, Mizuki Shinkawa, and Toshihiko Baba. Compact and fast photonic crystal silicon optical modulators. *Optics Express*, 20(20):22465–22474, 2012.

[111] F Niu and Bruce W Wessels. Epitaxial growth and strain relaxation of $BaTiO_3$ thin films on $SrTiO_3$ buffered (001) Si by molecular beam epitaxy. *Journal of Vacuum Science & Technology B*, 25(3):1053–1057, 2007.

[112] Kazuto Noguchi, Osamu Mitomi, and Hiroshi Miyazawa. Millimeter-wave Ti:$LiNbO_3$ optical modulators. *Journal of Lightwave Technology*, 16(4):615, 1998.

[113] Keisuke Noguchi, H Miyazawa, and O Mitomi. Frequency-dependent propagation characteristics of coplanar waveguide electrode on 100GHz Ti: $LiNbO_3$ optical modulator. *Electronics Letters*, 34(7):661–663, 1998.

[114] RA Norwood, MG Kuzyk, and RA Keosian. Electro-optic tensor ratio determination of side-chain copolymers with electro-optic interferometry. *Journal of Applied Physics*, 75(4):1869–1874, 1994.

[115] Masaya Notomi, K Yamada, Akihiko Shinya, J Takahashi, C Takahashi, and I Yokohama. Extremely large group-velocity dispersion of line-defect waveguides in photonic crystal slabs. *Physical Review Letters*, 87(25):253902, 2001.

[116] Wolfram HP Pernice, Chi Xiong, Frederick J Walker, and Hong X Tang. Design of a silicon integrated electro-optic modulator using ferroelectric $BaTiO_3$ films. *Photonics Technology Letters, IEEE*, 26(13):1344–1347, 2014.

[117] Graham T Reed, G Mashanovich, FY Gardes, and DJ Thomson. Silicon optical modulators. *Nature Photonics*, 4(8):518–526, 2010.

[118] Z Ren, PJ Heard, Joseph Michael Marshall, Pam A Thomas, and S Yu. Etching characteristics of $LiNbO_3$ in reactive ion etching and inductively coupled plasma. *Journal of Applied Physics*, 103(3):034109, 2008.

[119] M Riaziat, S Bandy, and G Zdasiuk. Coplanar waveguides for MMICs. *Microwave Journal*, 30:125, 1987.

[120] Majid Riaziat, Irene Zubeck, Steve Bandy, and George Zdasiuk. Coplanar waveguides used in 2-18 GHz distributed amplifier. In *Microwave Symposium Digest, 1986 IEEE MTT-S International*, pages 337–338. IEEE, 1986.

[121] M Roussey, M-P Bernal, N Courjal, D Van Labeke, FI Baida, and R Salut. Electro-optic effect exaltation on lithium niobate photonic crystals due to slow photons. *Applied Physics Letters*, 89(24):241110, 2006.

[122] Matthieu Roussey, Fadi I Baida, and Maria-Pilar Bernal. Experimental and theoretical observations of the slow-light effect on a tunable photonic crystal. *JOSA B*, 24(6):1416–1422, 2007.

[123] B.E.A. Saleh and M.C. Teich. *Fundamentals of Photonics*. Wiley-Interscience, 2007.

[124] Juan Sancho, Jerome Bourderionnet, Juan Lloret, Sylvain Combrié, Ivana Gasulla, Stephane Xavier, Salvador Sales, Pierre Colman, Gaelle Lehoucq, Daniel Dolfi, et al. Integrable microwave filter based on a photonic crystal delay line. *Nature Communications*, 3:1075, 2012.

[125] Masatoshi Saruwatari. All-optical signal processing for terabit/second optical transmission. *Selected Topics in Quantum Electronics, IEEE Journal of*, 6(6):1363–1374, 2000.

[126] Claus Schöllhorn, Weiwei Zhao, Michael Morschbach, and Erich Kasper. Attenuation mechanisms of aluminum millimeter-wave coplanar waveguides on silicon. *Electron Devices, IEEE Transactions on*, 50(3):740–746, 2003.

[127] Yuen-Ron Shen. *Principles of nonlinear optics*. Wiley-Interscience, New York, NY, USA, 1984.

[128] Yongqiang Shi, Lianshan Yan, and Alan Eli Willner. High-speed electro-optic modulator characterization using optical spectrum analysis. *Lightwave Technology, Journal of*, 21(10):2358–2367, 2003.

[129] Ashfaqul Anwar Siraji and Md Shamsul Alam. A tunable photonic double heterostructure cavity on ferroelectric barium titanate. *Photonics Technology Letters, IEEE*, 25(17):1676–1679, 2013.

[130] David R Smith, SL McCall, PM Platzman, R Dalichaouch, N Kroll, and S Schultz. Photonic band structure and defects in one and two dimensions. *JOSA B*, 10(2):314–321, 1993.

[131] Marin Soljačić and John D Joannopoulos. Enhancement of nonlinear effects using photonic crystals. *Nature Materials*, 3(4):211–219, 2004.

[132] Marin Soljačić, Steven G Johnson, Shanhui Fan, Mihai Ibanescu, Erich Ippen, and JD Joannopoulos. Photonic-crystal slow-light enhancement of nonlinear phase sensitivity. *JOSA B*, 19(9):2052–2059, 2002.

[133] Richard A Soref and Brian R Bennett. Electro-optical effects in silicon. *Quantum Electronics, IEEE Journal of*, 23(1):123–129, 1987.

[134] R Spreiter, Ch Bosshard, F Pan, and P Günter. High-frequency response and acoustic phonon contribution of the linear electro-optic effect in DAST. *Optics Letters*, 22(8):564–566, 1997.

[135] Matthew Streshinsky, Ran Ding, Yang Liu, Ari Novack, Yisu Yang, Yangjin Ma, Xiaoguang Tu, Edward Koh Sing Chee, Andy Eu-Jin Lim, Patrick Guo-Qiang Lo, et al. Low power 50 Gb/s silicon traveling wave Mach-Zehnder modulator near 1300 nm. *Optics Express*, 21(25):30350–30357, 2013.

[136] Frederik Sulser, Gorazd Poberaj, Manuel Koechlin, and Peter Günter. Photonic crystal structures in ion-sliced lithium niobate thin films. *Optics Express*, 17(22):20291–20300, 2009.

[137] Zhipei Sun, Amos Martinez, and Feng Wang. Optical modulators with 2D layered materials. *Nature Photonics*, 10(4):227–238, 2016.

[138] Allen Taflove and Korada R Umashankar. The finite-difference time-domain method for numerical modeling of electromagnetic wave interactions. *Electromagnetics*, 10(1-2):105–126, 1990.

[139] P Tang, AL Meier, DJ Towner, T Hamano, and BW Wessels. $BaTiO_3$ waveguide modulators with 360 pm/v effective electro-optic coefficient at 1.55 μm. In *Optical Amplifiers and Their Applications/Integrated Photonics Research Topical Meetings (The Optical Society of America, Washington, DC, 2004), PD3-1*, 2004.

[140] P Tang, AL Meier, DJ Towner, and BW Wessels. High-speed travelling-wave $BaTiO_3$ thin-film electro-optic modulators. *Electronics Letters*, 41(23):1, 2005.

[141] Pingsheng Tang, AL Meier, DJ Towner, and BW Wessels. $BaTiO_3$ thin-film waveguide modulator with a low voltage-length product at near-infrared wavelengths of 0.98 and 1.55 μm. *Optics Letters*, 30(3):254–256, 2005.

[142] Pingsheng Tang, DJ Towner, T Hamano, AL Meier, and BW Wessels. Electro-optic modulation up to 40 GHz in a barium titanate thin film waveguide modulator. *Optics*

Express, 12(24):5962–5967, 2004.

[143] Pingsheng Tang, DJ Towner, AL Meier, and BW Wessels. Low-voltage, polarization-insensitive, electro-optic modulator based on a polydomain barium titanate thin film. *Applied Physics Letters*, 85, 2004.

[144] Pingsheng Tang, DJ Towner, Anthony L Meier, and BW Wessels. Low-loss electro-optic $BaTiO_3$ thin film waveguide modulator. *Photonics Technology Letters, IEEE*, 16(8):1837–1839, 2004.

[145] Yongbo Tang, Jonathan D Peters, and John E Bowers. Energy-efficient hybrid silicon electroabsorption modulator for 40-Gb/s 1-V uncooled operation. *Photonics Technology Letters, IEEE*, 24(19):1689–1692, 2012.

[146] Yongbo Tang, Jonathan D Peters, and John E Bowers. Over 67 GHz bandwidth hybrid silicon electroabsorption modulator with asymmetric segmented electrode for 1.3 μm transmission. *Optics Express*, 20(10):11529–11535, 2012.

[147] Takashi Teranishi, Takuya Hoshina, and Takaaki Tsurumi. Wide range dielectric spectroscopy on perovskite dielectrics. *Materials Science and Engineering: B*, 161(1):55–60, 2009.

[148] David J. Towner. *Investigation of ferroelectric domain structure and nonlinear optical properties in barium titanate epitaxial thin films*. PhD thesis, Northwestern University, 2004.

[149] DJ Towner, TJ Lansford, and BW Wessels. Three dimensional domain structure in epitaxial barium titanate thin films. *Journal of Electroceramics*, 13(1-3):89–93, 2004.

[150] DJ Towner, J Ni, TJ Marks, and BW Wessels. Effects of two-stage deposition on the structure and properties of heteroepitaxial $BaTiO_3$ thin films. *Journal of Crystal Growth*, 255(1):107–113, 2003.

[151] AA Tseng. Fabrication of nanoscale structures using ion beams. *Focused Ion Beam Systems: Basics and Applications*, pages 187–214, 2007.

[152] Rodney S Tucker, Gadi Eisenstein, and Steven K Korotky. Optical time-division multiplexing for very high bit-rate transmission. *Lightwave Technology, Journal of*, 6(11):1737–1749, 1988.

[153] Venu Vaithyanathan, J Lettieri, W Tian, A Sharan, A Vasudevarao, YL Li, A Kochhar, H Ma, J Levy, P Zschack, et al. c-axis oriented epitaxial $BaTiO_3$ films on (001) Si. *Journal of Applied Physics*, 100(2):024108, 2006.

[154] C Veyres and V Fouad Hanna. Extension of the application of conformal mapping techniques to coplanar lines with finite dimensions. *International Journal of Electronics Theoretical and Experimental*, 48(1):47–56, 1980.

[155] Yurii A Vlasov, Martin O'Boyle, Hendrik F Hamann, and Sharee J McNab. Active control of slow light on a chip with photonic crystal waveguides. *Nature*, 438(7064):65–69, 2005.

[156] JL Wang, J Leroy, G Niu, G Saint-Girons, B Gautier, B Vilquin, and N Barrett. Chemistry and structure of $BaTiO_3$ ultra-thin films grown by different O_2 plasma power. *Chemical Physics Letters*, 592:206 – 210, 2014.

[157] Zheng Wang and Shanhui Fan. Compact all-pass filters in photonic crystals as the building block for high-capacity optical delay lines. *Physical Review E*, 68(6):066616, 2003.

[158] William L Warren, Karel Vanheusden, Duane Dimos, Gordon E Pike, and Bruce A Tuttle. Oxygen vacancy motion in perovskite oxides. *Journal of the American Ceramic Society*, 79(2):536–538, 1996.

[159] Cheng P Wen. Coplanar waveguide: A surface strip transmission line suitable for nonreciprocal gyromagnetic device applications. *Microwave Theory and Techniques, IEEE Transactions on*, 17(12):1087–1090, 1969.

[160] Cheng P Wen. Coplanar-waveguide directional couplers. *Microwave Theory and Techniques, IEEE Transactions on*, 18(6):318–322, 1970.

[161] Bruce W Wessels. Ferroelectric epitaxial thin films for integrated optics. *Annual Review of Materials Research*, 37:659–679, 2007.

[162] Harold A Wheeler. Formulas for the skin effect. *Proceedings of the IRE*, 30(9):412–424, 1942.

[163] Peter J Winzer. Spatial multiplexing: The next frontier in network capacity scaling. In *Optical Communication (ECOC 2013), 39th European Conference and Exhibition on*, pages 1–4. IET, 2013.

[164] Ed L Wooten, Karl M Kissa, Alfredo Yi-Yan, Edmond J Murphy, Donald A Lafaw, Peter F Hallemeier, David Maack, Daniel V Attanasio, Daniel J Fritz, Gregory J McBrien, et al. A review of lithium niobate modulators for fiber-optic communications systems. *Selected Topics in Quantum Electronics, IEEE Journal of*, 6(1):69–82, 2000.

[165] Jan Hendrik Wülbern, Jan Hampe, Alexander Petrov, Manfred Eich, Jingdong Luo, Alex K-Y Jen, Andrea Di Falco, Thomas F Krauss, and Jürgen Bruns. Electro-optic modulation in slotted resonant photonic crystal heterostructures. *Applied Physics Letters*, 94(24):241107, 2009.

[166] Fengnian Xia, Thomas Mueller, Yu-ming Lin, Alberto Valdes-Garcia, and Phaedon Avouris. Ultrafast graphene photodetector. *Nature Nanotechnology*, 4(12):839–843, 2009.

[167] Fengnian Xia, Lidija Sekaric, and Yurii Vlasov. Ultracompact optical buffers on a silicon chip. *Nature Photonics*, 1(1):65–71, 2007.

[168] Chi Xiong, Wolfram HP Pernice, Joseph H Ngai, James W Reiner, Divine Kumah, Frederick J Walker, Charles H Ahn, and Hong X Tang. Active silicon integrated nanophotonics: ferroelectric $BaTiO_3$ devices. *Nano Letters*, 14(3):1419–1425, 2014.

[169] Qianfan Xu, Bradley Schmidt, Sameer Pradhan, and Michal Lipson. Micrometre-scale silicon electro-optic modulator. *Nature*, 435(7040):325–327, 2005.

[170] Eli Yablonovitch. Inhibited spontaneous emission in solid-state physics and electronics. *Physical Review Letters*, 58(20):2059, 1987.

[171] H Yamaguchi. Line dose dependence of silicon and gallium arsenide removal by a focused gallium ion beam. *Le Journal de Physique Colloques*, 48(C6):C6–165, 1987.

[172] Eikichi Yamashita, Ke Ren Li, and Yoichi Suzuki. Characterization method and simple design formulas of MCS lines proposed for MMIC's. *IEEE Transactions on Microwave Theory Techniques*, 35:1355–1362, 1987.

[173] Amnon Yariv and Pochi Yeh. *Optical Waves in Crystals*. Wiley-Interscience, 2003.

[174] Zhao Yong, Zhang Ya-Nan, Di Wu, and Qi Wang. Wideband slow light with large group index and low dispersion in slotted photonic crystal waveguide. *Journal of Lightwave Technology*, 30(17):2812–2817, 2012.

[175] Marko Zgonik, P Bernasconi, M Duelli, R Schlesser, P Günter, MH Garrett, D Rytz, Y Zhu, and X Wu. Dielectric, elastic, piezoelectric, electro-optic, and elasto-optic tensors of $BaTiO_3$ crystals. *Physical Review B*, 50(9):5941, 1994.

[176] Cheng Zhang, Larry R Dalton, Min-Cheol Oh, Hua Zhang, and William H Steier. Low V_π electro-optic modulators from CLD-1: Chromophore design and synthesis, material processing, and characterization. *Chemistry of Materials*, 13(9):3043–3050, 2001.

[177] Cheng Zhang, Chuanguang Wang, Larry R Dalton, Hua Zhang, and William H Steier. Progress toward device-quality second-order nonlinear optical materials. 4. a trilink high $\mu\beta$ NLO chromophore in thermoset polyurethane: A "guest-host" approach to larger electrooptic coefficients. *Macromolecules*, 34(2):253–261, 2001.

[178] Xingyu Zhang, Chi-Jui Chung, Amir Hosseini, Harish Subbaraman, Jingdong Luo, Alex Jen, Robert Neilson, Charles Lee, and Ray T Chen. High performance optical modulator based on electro-optic polymer filled silicon slot photonic crystal waveguide. 2015.

[179] Xingyu Zhang, Amir Hosseini, Swapnajit Chakravarty, Jingdong Luo, Alex K-Y Jen, and Ray T Chen. Wide optical spectrum range, subvolt, compact modulator based on an electro-optic polymer refilled silicon slot photonic crystal waveguide. *Optics Letters*, 38(22):4931–4934, 2013.

APPENDIX A

Processing Details

A.1. Si_3N_4 Deposition

Silicon nitride films were deposited onto $BaTiO_3$ films via plasma enhanced chemical vapor deposition using the NPE-4000 PECVD chamber in the MRC cleanroom. The steps for depositing the Si_3N_4 films are the following:

(1) Clean wafers ($BaTiO_3$/MgO sample and a small piece of a silicon wafer) with acetone and methanol. Blow dry with nitrogen. Inspect wafers under an optical microscope to ensure cleanliness.

(2) Turn on the nitrogen process gas for the NPE-4000 PECVD system.

(3) Vent the load lock. Load the $BaTiO_3$/MgO sample and silicon piece. Close the load lock door, and load the samples into the chamber. Pump down the PECVD main chamber until a base pressure on the order of 10^{-6} Torr is achieved.

(4) Heat the platen to 250 °C. After the temperature passes through 250 °C increase the platen to the deposition temperature, 300 °C.

(5) Load the recipe for Si_3N_4 deposition. The recipe was modified to stabilize the plasma and to achieve a growth rate of approximately 10 nm/min. The recipe parameters are provided in Table A.1 below.

(6) Open the ammonia tank in the cleanroom chase. Turn on the process gases (SiH_4 and NH_3) inside the cleanroom by opening the wall valves and gas cabinet controls.

(7) Run the deposition recipe for the required deposition time. The deposition time is calculated using the empirically determined deposition rate of 10 nm/min. Typical deposition times are 15-25 minutes. Ensure that the plasma is stable throughout the deposition.

(8) Turn off the ammonia tank main valve in the chase 12-15 minutes before the termination of the deposition process. This prevents excess use of ammonia, the residual gases of which need to be purged from the system after deposition.

(9) After the deposition has terminated, turn off the SiH_4 gas valves only. Leave the NH_4 wall valve and gas cabinet valve open. Turn off the heater.

(10) Run the NH_3 pumpdown recipe for 15-20 minutes, or until the flow rate of NH_3 is less than 0.2 sccm. Turn off the main valve to the NH_3 tank in the chase.

(11) Unload the samples after the platen has cooled below 100 °C. Use the silicon reference piece to measure the refractive index and thickness of the Si_3N_4 film. High quality Si_3N_4 has no particles as detected by an optical microscope and a refractive index between 1.98 and 2.01.

A.2. Waveguide Lithography

A positive photolithography step was used to define ridge waveguides with widths between 2 and 7 µm on the silicon nitride films. The detailed photolithography steps are as follows:

Table A.1. Process parameters for PECVD deposition of Si_3N_4 films.

Parameter	Value	Unit
SiH_4 Flow	100	sccm
NH_3 Flow	40	sccm
RF Power	40	W
Pressure	320	mTorr
Substrate Temperature	300	°C
Deposition Time	15-25	minutes

(1) Mount the sample onto the Headway spin coater in the MRC cleanroom. Ensure that there is a sufficient vacuum for holding the sample in place.

(2) Spin the sample using the following steps:

   (a) 500 rpm for 10 seconds

   (b) 4000 rpm for 45 seconds

(3) While the sample is spinning at 4000 rpm, do the following, in order:

   (a) Spray acetone onto the sample with a wash bottle for 2 seconds

   (b) While still spraying acetone, spray isopropyl alcohol. Stop spraying acetone and continue spraying isopropyl alcohol for another 1-2 seconds.

   (c) Immediately spray the sample dry with nitrogen. Continue drying with nitrogen until the spinning sequence stops.

(4) Use a dropper to apply one drop of hexamethyldisilazane (HMDS) adhesion promoter onto the wafer while it is at rest. Run the above spinning recipe again to completion to spread the HMDS.

(5) Clean a glass pipette by blowing with nitrogen. Use the pipette to extract a small amount of AZ5214E photoresist (MicroChemicals). Apply enough photoresist

to completely cover the wafer while it is at rest. Run the spinning recipe to completion.

(6) Since the samples are typically rectangular in shape, an edge bead of photoresist forms due to spin coating; it is thickest at the corners of the sample. Apply a small amount of acetone to a clean room TexWipe and remove the edge bead at the corners by sweeping outwards from the sample. Removing the edge bead at the corners is critical for proper exposure.

(7) Bake the sample on a hot plate for 50 seconds at 90 °C

(8) Use the MA6 mask aligner to align the lithographic mask to the wafer. A 75 µm separation gap is used for alignment. After aligning, expose the sample using "hard contact" mode for 1.5 seconds.

(9) Prepare a 1:3 AZ400K:DIW (deionized water) developer solution. Immerse the sample in the solution for approximately 45 seconds, or until it clear ridges appear without color variation between ridges.

(10) After removing the sample from the developer solution, immediately rinse gently with running water, then dry immediately with nitrogen. Inspect the sample under an optical microscope to determine if the features are under- or over-developed or wavy. If there are any issues with the patterns, remove the photoresist by immersing in acetone and gently wiping with a cotton swab and repeat all the above steps. Between one and five iterations may be necessary with more iterations typical for smaller samples.

(11) Post-expose bake the sample for 5 minutes at 105 °C.

A.3. Reactive Ion Etching

The positive photolithography step leaves behind strips of polymerized photoresist that serve as a pattern for the ridge waveguides. The strips serve as a sacrificial layer to protect the underlying Si_3N_4 while the surrounding Si_3N_4 is etched. Reactive ion etching is a vertical, anisotropic etching process that results in nearly vertical sidewalls for the ridges. A CF_4 and O_2 etching chemistry was used to etch the Si_3N_4 ridges. The steps for the reactive ion etching step are as follows:

(1) Turn on the required process gases, O_2 and N_2, in the clean room chase.

(2) Turn on the SAMCO 10NR-RIE and load samples to be etched. Run the etching recipe for Si_3N_4 (see Table A.2).

(3) Run the chamber cleaning recipe to clean the chamber.

(4) Remove the photoresist by cleaning with acetone and methanol.

Table A.2. Parameters used for etching Si_3N_4 ridge waveguides.

Parameter	Value	Unit
CF_4 Flow	30	sccm
O_2 Flow	5	sccm
RF Power	200	W
Pressure	2	Pa
Time	2-3	minutes

A.4. Rapid Thermal Processing

Two annealing steps were introduced into the CMOS processing to alter the crystallinity and stoichiometry of the films as discussed in Section 3.4.1. Both anneals were done using

the rapid thermal processor in the MRC cleanroom. The annealing parameters are given in Tables A.3-A.5.

Table A.3. Parameters for post-growth annealing of $BaTiO_3$ films.

Parameter	Value	Unit
Ramp rate, up	15	°C/s
Temperature	900	°C
Total Pressure, O_2	4	Torr
O_2 Flow	100	sccm
Time	45	minutes
Ramp rate, down		°C/s

Table A.4. Parameters for annealing after waveguide fabrication using a slow cooling step.

Parameter	Value	Unit
Ramp rate, up	15	°C/s
Temperature	350	°C
Total Pressure, O_2	4	Torr
O_2 Flow	100	sccm
Time	30	minutes
Ramp rate, down, 900 to 800 °C	1	°C/s
Ramp rate, down, 800 to 150 °C	0.3	°C/s

Table A.5. Parameters for annealing after waveguide fabrication using a fast cooling step.

Parameter	Value	Unit
Ramp rate, up	15	°C/s
Temperature	350	°C
Total Pressure, O_2	4	Torr
O_2 Flow	100	sccm
Time	30	minutes
Ramp rate, down	4.1	°C/s

A.5. Image Reversal Lithography, Metal Deposition, and Lift-off

Image reversal lithography was used to define patterns for electrodes. The processing steps are as follows:

(1) Follow steps 1-6 in Section A.2 for spin coating AZ5214E photoresist.

(2) Bake the wafer with photoresist at 90 celsius for 60 seconds.

(3) Use the MA6 mask aligner to align the electrode pattern with the previously fabricated waveguides. Use the same procedure as done in Section A.2 except increase the exposure time to 2 seconds.

(4) Remove the sample from the mask aligner and bake at 105 °C for 60 seconds. This step is critical for reversing the cross-linking of the resist upon exposure to UV light such that the regions not exposed are removed during the development stage.

(5) Apply a UV flood exposure for 60 seconds.

(6) Prepare a 1:3 AZ400K:DIW (deionized water) solution and develop the sample for approximately 25 seconds.

(7) Remove the sample from the developer solution, rinse immediately with running DIW, and gently dry with nitrogen.

After patterning the resist for electrodes, a gold film was deposited onto the sample using electron beam metal evaporation. The processing steps are the following:

(1) Mount samples onto glass slides and load into the evaporation chamber. Pump down the system to 5×10^{-6} Torr.

(2) Enter the deposition parameters for titanium into the system. Deposit a 10 nm titanium adhesion layer.

(3) After the titanium deposition has terminated, enter the deposition parameters for gold into the system. Note that due to a tooling factor of 1.00, the actual thickness of gold deposited is approximately twice the value entered for the terminal thickness.

(4) After completing the metal deposition, vent the chamber to atmospheric pressure and remove the samples. Sonicate in acetone for several minutes until the excess gold has lifted off. For thick gold films, gently remove the excess gold with a cotton swab while immersing the sample in acetone.

A.6. Facet Polishing

After patterning waveguides and electrodes, the facets of the sample containing the waveguide ports must be polished. Waveguide fabrication leaves on the sample a Si_3N_4 border approximately 300 µm wide that must be removed in order for the waveguide ports to be flush with the facet. For the case of <110> oriented waveguides, additional material must be removed as discussed in Section 3.4.1. The steps for polishing are the following:

(1) Follow steps 1-3, 5, and 7 of Section A.2 for applying a layer of photoresist to protect the surface of the sample during polishing.

(2) For samples with <110> oriented waveguides, use 600 grit silicon carbide paper to remove a significant portion of two of the wafer's corners to expose the waveguides to the coupling facet. Note that in the remainder of polishing, approximately 350 µm of additional material will be removed.

(3) Mount a 15 µm diamond lapping film onto the polishing wheel of the MultiPrep polishing machine in the NU*ANCE* EPIC Facility. Remove 200-300 µm of material from the facet edge.

(4) Replace the 15 µm lapping film with a 6 µm diamond lapping film. Continue polishing for approximately 2 minutes until 45-60 µm of material is removed.

(5) Repeat step 4 with a 3 µm diamond lapping film. Polish for approximately 10 minutes to remove 20 µm of material.

(6) Repeat step 4 with a 1 µm diamond lapping film. Polish for approximately 1 hour to remove 10 µm of material.

(7) Visually inspect the sample facets with an optical microscope to ensure that no large cracks are present on the waveguide ports. Remove the photoresist with acetone.

A.7. Conductive Coatings for Ion Beam Lithography

Two different conductive coatings were used for ion beam lithography milling of photonic crystal arrays: PEDOT:PSS, and Cr/PMMA. The application and deposition of these films are described below.

A.7.1. PEDOT:PSS Conductive Polymer Coating

A suspension of PEDOT:PSS (Heraus, Clevios) was applied uniformly to wafers by spin coating and post-baking using the steps as follows:

(1) In the CNM cleanroom, mount the sample onto a small piece of silicon (1.5 × 1.5 cm) using double-sided carbon tape. Mount the silicon piece with the sample onto the spin coater reserved for conductive polymer films.
(2) Draw a small amount of PEDOT:PSS suspension using a pipette. Apply enough of the suspension to completely cover the sample. The suspension has a large surface tension and will form a large bead on the sample.
(3) Spin the sample for 5 seconds at 500 rpm and 45 seconds at 3500 rpm.
(4) After the spinning sequence is complete, post-bake the sample at 75 °C for 60 seconds. The sample is now ready for mounting inside the FIB/SEM chamber.

A.7.2. Cr/PMMA Conductive Coating

A multilayer of Cr/PMMA was applied by first spin coating a 50 nm film of PMMA and then depositing a 30 nm film of Cr by e-beam deposition.

A.7.2.1. PMMA spin coating

(1) If A2 PMMA is not available, dilute 8 mL of A5 PMMA with 12 mL of anisole.
(2) Mount the sample onto the Headway spinner in the MRC cleanroom. Using a pipette, apply enough of the PMMA solution to completely cover the sample.
(3) Spin the sample for 5 seconds at 500 rpm followed by 45 seconds at 4000 rpm.
(4) Remove the sample from the spinner and post-bake at 180 °C for 90 seconds.

A.7.2.2. Cr Deposition

(1) Mount samples onto glass slides and load into the evaporation chamber. Pump down the system to 5×10^{-6} Torr.

(2) Enter the deposition parameters for chromium into the system. Deposit a 30 nm layer of Cr.

(3) After completing the metal deposition, vent the chamber to atmospheric pressure and remove the samples.

A.8. Focused Ion Beam Lithography

Patterning of photonic crystal arrays via ion beam lithography requires alignment of the writefield and properly loading a GDSII file. The steps for doing this are the following.

A.8.1. Writefield Alignment

(1) With the stage at 0° tilt, turn on the electron beam. Use the "xT Align" tool to align the wafer such that the ridge waveguides are oriented vertically on the screen.

(2) Use the procedure described by the tool manager to tilt the stage to the working condition at 52°.

(3) Turn on the ion beam and ensure that the liquid metal ion source is stable. Pause the electron beam. Set the current of the ion beam to that used for patterning (0.46 nA). Take an image with the ion beam at a magnification of 1000x. If the ion beam is relatively well aligned, the image should be nearly the same as the

electron beam image. Adjust the brightness and contrast of the ion beam while taking snapshots so that features on the wafer can be discerned.

(4) Navigate to a portion of the wafer away from the waveguides but along the same horizontal line on which the center of the photonic crystals will be positioned. A position near the alignment markers for CMOS lithography is suitable.

(5) Zoom in to the maximum magnification of the ion beam (1,280,000x), then un-pause the ion beam. Wait 20 seconds for a hole to be milled into the sample.

(6) Zoom out to 80,000x. Make fine adjustments to the focus and stigmation in the X and Y directions to bring the hole into focus and make it appear round. After making adjustments, pause the ion beam. The adjustments should be made within 20 seconds to avoid making the hole so wide such that it cannot be focused on.

(7) Zoom out to 1000x. Take a snapshot with the ion beam. Un-pause the electron beam. Beam shift the electron beam so that its focal point is concentric with that of the ion beam.

(8) Turn on the Raith Elphy Multibeam signal router and open the Multibeam patterning software. Navigate to "Positions." Create a new position ("start") and read the current coordinates of the ion beam. Save the position.

(9) Navigate horizontally to the top of the left-most visible electrode. Zoom in to a magnification of 1000x and take an image with the ion beam. Position the cross-hair such that it is on the top edge of the electrode.

(10) Click on the tab labeled "$XY \leftrightarrow UV$" and click on "Angular Alignment." Read the current position as "P1."

(11) Repeat step 9 on the right-most visible electrode. Repeat step 10 and read the current point as "P2." Accept the correction. This will provide a coarse angular alignment of the writefield.

(12) Navigate to the position "start" created in step 8 under the "Positions" tab. Re-focus the electron beam. Take an image with the ion beam.

(13) Click on the "Writefield Control" tab. Right click on the required writefield and click "set."

(14) Change the ion beam magnification so that it matches that set in step 13. Take a snapshot with the ion beam. Iteratively increase the brightness and take a snapshot until the brightness in the image is saturated.

(15) On the Raith computer, go to "File" then "New Image." In the window that pops up, click on "New Image."

(16) Navigate back to the "Writefield Control" tab on the Raith computer. Under "Writefield Alignment," click on "Manual" and right click on the appropriate alignment procedure. For example, for a 100 µm writefield, select the alignment procedure "Align WF 100 um 10 micron from center." Click on "Execute." Wait until a new image appears with three green boxes.

(17) While holding down the control key "Ctrl," click and drag the mouse to the center of the hole in the image (created in step 5). After releasing, wait for the next image to be generated. Repeat this procedure two more times.

(18) At the end of the third alignment step, a window will appear showing the changes to the magnification, position, and angular alignment of the ion beam. Accept all

changes. For writefields of 200 µm or larger, repeat steps 14-17 one or two more times to further improve the alignment.

A.8.2. Load and Mill Pattern

(1) Under the "Design" tab, open the GDSII file for patterning. The patterns can be loaded onto the Raith computer by first downloading onto the Support PC, then accessing it through the intranet connection.

(2) Click on "Edit." In the new window that opens, click on "Writefield Parameters." In the new window, create a new writefield with dimensions equal to the writefield set in step 13 of A.8.1. Set the new writefield as active. If done correctly, the pattern should now be centered within a dashed square with side length equal to the writefield size.

(3) Under the "Design" tab, click on "Patterning Options" and set the number of loops to 50.

(4) Go to "File," "New Position List". Under the "Design" tab, click and drag the top of the "tree" to the first row of the position list window.

(5) Right click on the new position and select "Parameters." Change both the U and V coordinates to 0.

(6) Click on "Calculator." Enter in the desired ion beam dose. Ensure that the ion beam current is 0.46 nA. Set the line spacing and area step size to 20 nm. Re-calculate the dwell time until no errors appear. Click "Ok" to accept the patterning parameters.

(7) Click on "Times" to calculate the expected patterning time. Typical patterning times are >10 minutes for patterns using a 100 µm writefield up to 1 hour for patterns using a 500 µm writefield.

(8) Under the "$XY \leftrightarrow UV$" tab, click on "Origin Correction." On the SEM computer, navitage the ion beam cross-hair to the center of a waveguide for patterning. Take an image with the ion beam to ensure that the cross-hair is centered. Set the correct magnification of the ion beam corresponding to that set by the writefield and take another image. On the Raith computer under "Origin Correction," reset the origin to the current position.

(9) Right click on the position in the position list and click "Pattern." The Elphy system will then control the ion beam column for writing the pattern.

A.8.3. Cross-Sectional Imaging

(1) Tilt the sample stage to 0° and navigate to the feature whose cross-section is to be imaged.

(2) Increase the stage height from 5.0 to 5.2 mm.

(3) Insert the platinum injection needle and enable the heater for *in situ* platinum deposition. The injection needle requires a few minutes to reach the setpoint temperature.

(4) While the injection needle is heating, increase the magnification such that a rectangular region to be coated with platinum covers about 60-80% of the SEM image. Pause the electron beam and increase the current to 1.6 pA. Take a single snapshot with the electron beam. The electron beam is paused and snapshots

are taken to avoid charging the sample. Charging the same will result in poor cross-sectional imaging.

(5) Under the "Patterning" tab, set the material to "Pt e-dep." Draw a rectangle on the SEM screen to define the patterning region. The region should be approximately 25 µm^2. Set the platinum deposition thickness to 300 nm.

(6) Start the platinum deposition using the electron beam. The deposition should take about 5 minutes depending on the area chosen.

(7) After patterning has finished, remove the injection needle. Tilt the sample stage to 52°.

(8) Take an image with the ion beam. Set the magnification such that the platinum coated feature covers 60-80% of the ion beam image.

(9) Under the "Patterning" tab, select "Regular Cross-Section" and draw a rectangle that is approximately 5 µm wide and 3 µm tall. The rectangle should be positioned near the bottom of the screen and should partially overlap the platinum region.

(10) Set the regular cross-section depth to a value between 800 nm and 1.5 µm. The cross-sectional trench should be deeper than the structure to be imaged.

(11) Start the regular cross-section patterning. It should take about 1 minute to complete. When it is finished, take an image with the ion beam.

(12) After milling the regular cross-section, select the "Cleaning Cross-Section" pattern. At the top edge of the regular cross-section trench, draw a rectange that is approximately the same width as or narrower than the width of the regular cross-section and approximately 100 nm tall.

(13) Start the cleaning cross-section patterning. The patterning should take no more than 30 seconds. The purpose of the cleaning cross-section step is to prepare the vertical facet of the regular cross-section for imaging with the electron beam.

(14) Set the electron beam dose to 0.98 pA. Un-pause the electron beam and image the cross-section using the immersion mode of the microscope. Measurements can be taken by first taking a snapshot with the electron beam, then using the tools under the "Annotation" tab. Ensure that the measurements account for the 52° tilt by selecting the "Cross-Section" under measurement adjustments.

APPENDIX B

Optical Alignment

The following procedure was used to align a lensed fiber to the input of a ridge waveguide. The single mode fiber was mounted via a fiber mount (Elliot Martock MDE 717) onto a to a 3-axis precision fiber flexure stage (Elliot Martock MDE750 fiber holder mounted onto an Elliot Martock MDE122 flexure stage). The objective lens was mounted onto an identical 3-axis precision stage (Elliot Martock MDE122). The positioning stages have 20 nm resolution and 2 mm range for all three axes. The sample was mounted onto a waveguide mount with rotational degrees of freedom along the x and z directions (Elliot Martock MDE747). The waveguide mount was mounted onto a precision stage (Elliot Martock MDE883) with two rotational and one translational degrees of freedom. The degrees of freedom for the system are summarized in Table B.1. The procedure detailed here fixes the degrees of freedom of the fiber, sample, and objective lens to optimize the coupling of optical power from the lensed fiber to the ridge waveguide. The procedure references the setup shown in Fig. B.1:

(1) The sample is focused on using an overhead camera (Watec 902H2, not shown in the schematic). The sample stage is adjusted until the entire wafer is in focus for translations in the x and z directions. This step fixes the θ_x and θ_z degrees of freedom of the sample stage.

(2) The sample stage is lowered slightly such that it is just out of focus. The fiber is then advanced toward the left edge of the wafer. The fiber is adjusted in the y direction until it is in focus with the overhead camera and is then advanced over the waveguide. The θ_y degree of freedom of the sample stage is adjusted until the fiber is aligned parallel to the waveguide. This is achieved when the fiber tip is imaged over the waveguide across its entire length for a fiber translation along the z direction. This step fixes the θ_y degree of freedom of the sample stage.

(3) The sample stage is lowered out of the beam path, and the fiber is advanced along z until it is focused onto the imaging plane using the objective lens. Adjustments are then made to the x and y position of the fiber and objective lens until the image shown in Fig. B.2 is obtained with a CCD camera with focal point at the imaging plane. This step fixes the x and y degrees of freedom of the fiber and objective lens.

(4) The fiber is pulled back along $-z$ until it is no longer over the wafer and is near the left (input) facet. The wafer is then raised in the y direction such that it is in the same imaging plane as the fiber tip. Small adjustments are made to the x, y, and z position of the fiber and the x and y positions of the sample stage until a waveguide mode such as that in Fig. 3.10 is imaged.

Table B.1. Description of the degrees of freedom of the optical components shown in Fig. B.1.

Component	Degrees of Freedom
Fiber	x, y, z
Sample	x, y, θ_x, θ_y, θ_z
Objective Lens	x, y, z

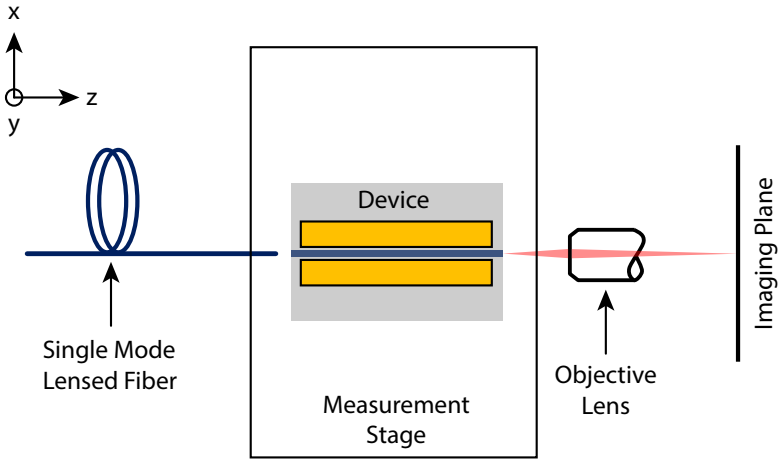

Figure B.1. Schematic showing alignment to a ridge waveguide. An overhead camera used to imagethe device and fiber in the xz plane is not shown.

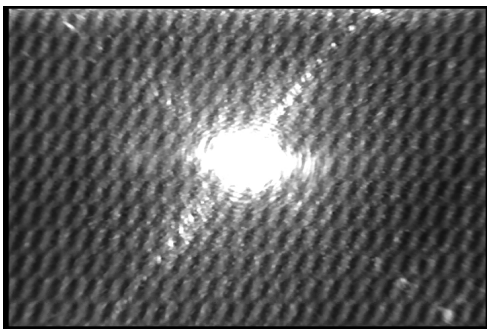

Figure B.2. Image obtained with the IR camera with focal point at the imaging plane in Fig. B.1 when the focal point of the fiber is coincident with that of the objective lens.

APPENDIX C

Microwave and Electro-Optic Data

Table C.1. Summary of the microwave property measurements for devices with 5 µm gap spacing on $BaTiO_3$ wafers with thicknesses between 150 and 680 nm.

Film				Bandwidth					
ID	Thickness (nm)	G	WG	3 dB S_{21} (GHz)	10 dB S_{11} (GHz)	n_{mw}	Z (Ω)	α_c (dB/cm/$\sqrt{\text{GHz}}$)	α_d (dB/cm/GHz)
YKJ-39	150	1	1	50	50	2.6	44	2.6	0.00
YKJ-125[1]	230	2	1	37	9.6	3.2	34	0.4	0.64
YKJ-82a	250	2	1	14	6.1	3.7	30	2.9	0.48
YKJ-134B	260	2	1	50	11	3.3	34	1.9	0.29
YKJ-134B	260	3	1	37	6.9	3.4	32	1.6	0.39
YKJ-85[2]	290	4	1	12	5.7	3.8	29	4.3	0.42
YKJ-85	290	3	1	11	5.1	3.9	29	5.1	0.37
PC-05[1,2]	250	3	1	9.2	3.8	4.2	26	4.4	0.46
YKJ-97	450	5	1	6.5	2.7	4.8	23	3.8	0.83
YKJ-97[2]	450	2	1	6.2	2.6	4.9	23	5.3	0.72
YKJ-155A	500	2	2	5.9	2.5	4.7	24	11.5	0.13
YKJ-155A	500	3	1	5.2	2.2	4.9	23	8.9	0.51
YKJ-155B[1,2]	500	2	2	4.0	2.1	5.1	22	12.2	0.19
YKJ-155B	500	3	2	4.2	2.1	5.1	22	11.8	0.19
YKJ-99B	680	3	1	4.4	1.7	5.6	20	10.3	0.33

[1]Data included in frequency-dependent plots in Chapter 4.
[2]Data included in thickness-dependent plots in Chapter 4.

Table C.2. Summary of the microwave property measurements for devices with 7.5 µm gap spacing on $BaTiO_3$ wafers with thicknesses between 150 and 680 nm.

Film				Bandwidth					
ID	Thickness (nm)	G	WG	3 dB S_{21} (GHz)	10 dB S_{11} (GHz)	n_{mw}	Z (Ω)	α_c (dB/cm/$\sqrt{\text{GHz}}$)	α_d (dB/cm/GHz)
YKJ-39	150	2	4	50	50	2.5	49	2.7	0.00
YKJ-125[1]	230	2	4	50	19	3.1	39	0.56	0.44
YKJ-82a	250	2	4	29	10	3.5	34	1.2	0.62
YKJ-134B	260	2	3	50	15	3.1	39	1.3	0.31
YKJ-134B	260	4	4	50	13	3.1	39	1.4	0.30
YKJ-85[2]	290	4	4	19	8.9	3.6	34	3.0	0.42
YKJ-85	290	3	3	15	8.0	3.6	33	4.0	0.33
PC-05[1]	250	3	3	13	5.9	3.9	31	3.4	0.43
YKJ-97	450	4	4	9.6	3.7	4.4	28	4.7	0.35
YKJ-97	450	2	4	10	3.8	4.4	27	3.7	0.75
YKJ-155A	500	2	3	8.4	3.6	4.3	28	9.1	0.12
YKJ-155A	500	3	3	7.7	3.1	4.4	27	9.0	0.14
YKJ-155B[1,2]	500	2	4	6.1	3.0	4.6	26	8.8	0.37
YKJ-155B	500	3	4	6.5	3.1	4.6	26	8.5	0.35
YKJ-99B	680	3	4	6.8	2.6	5.0	24	9.8	0.03

[1]Data included in frequency-dependent plots in Chapter 4.
[2]Data included in thickness-dependent plots in Chapter 4.

Table C.3. Summary of the microwave property measurements for devices with 12 µm gap spacing on $BaTiO_3$ wafers with thicknesses between 150 and 680 nm.

Film				Bandwidth					
ID	Thickness (nm)	G	WG	3 dB S_{21} (GHz)	10 dB S_{11} (GHz)	n_{mw}	Z (Ω)	α_c (dB/cm/$\sqrt{\text{GHz}}$)	α_d (dB/cm/GHz)
YKJ-39	150	2	6	50	50	2.3	57	2.1	0.00
YKJ-125[1]	230	2	6	50	50	2.8	47	1.3	0.17
YKJ-82a	250	2	6	47	18	3.3	41	0.58	0.53
YKJ-134B	260	2	6	50	50	2.9	47	1.4	0.16
YKJ-134B	260	4	6	50	50	2.9	46	0.8	0.28
YKJ-85[2]	290	4	6	47	17	3.3	40	2.0	0.36
YKJ-85	290	3	6	38	17	3.3	40	2.4	0.32
PC-05[1]	250	3	5	30	11	3.6	37	1.2	0.54
YKJ-97	450	4	6	27	6.5	4.0	33	2.4	0.38
YKJ-97	450	2	6	18	7.1	4.0	34	1.4	0.81
YKJ-155A	500	2	5	12	6.0	4.0	33	5.7	0.33
YKJ-155A	500	3	5	11	5.4	4.1	33	5.3	0.35
YKJ-155B[1,2]	500	2	6	10	5.6	4.1	33	3.6	0.78
YKJ-155B	500	3	6	11	5.7	4.1	33	3.8	0.71
YKJ-99B	680	2	6	11	4.7	4.4	30	5.0	0.41

[1]Data included in frequency-dependent plots in Chapter 4.
[2]Data included in thickness-dependent plots in Chapter 4.

Table C.4. Summary of the electro-optic and microwave properties for specific devices. The data is presented in order of increasing $BaTiO_3$ film thickness. Gap: electrode gap spacing, L: electrode length, V_π : half-wave voltage, Bias: applied dc bias voltage, Γ_{EO}: electro-optic overlap factor, r: effective electro-optic coefficient, $V_\pi \cdot L$: voltage-length product, n_{mw}: microwave index, Z: characteristic impedance, α: total microwave attenuation at 50 GHz, BW: bandwidth. The half-wave voltage and electro-optic coefficient are obtained for a modulation frequency of 1 MHz.

Sample	Thickness (nm)	Gap (µm	L (mm)	V_π (V)	Bias (V)	Γ_{EO}	r (pm/V)	$V_\pi \cdot L$ (V·cm)	n_{mw}	Z (Ω)	α (dB/cm)	EO 3 dB BW (GHz)
YKJ-134B	260	5	1	14.4	14	0.45	125	1.46	3.3	33	20	18
YKJ-134B	260	7.5	1	>20	N/A	0.45	N/A	>2	3.1	39	17	18
YKJ-134B	260	12	1	>20	N/A	0.45	N/A	>2	2.9	47	8.5	28
YKJ-146A	360	7.5	2.9	4.4	16	0.61	155	1.28	2.3	51	60	5.4
YKJ-146A	360	9	2.9	8.0	24	0.61	103	2.32	2.6	49	68	8.6
YKJ-146A	360	10.5	2.9	9.2	25	0.61	104	2.67	2.9	45	58	9.7
YKJ-146A	360	15	2.9	13.2	20	0.61	104	3.84	2.9	48	43	11
YKJ-146B	360	5	1	13.4	30	0.61	99	1.34	3.5	32	21	18
YKJ-146B	360	7.5	1	>20	N/A	0.61	N/A	>2	3.4	35	16	18
YKJ-146B	360	12	1	>20	N/A	0.61	N/A	>2	3.2	41	14	21
YKJ-155A	500	5	1	4.3	15	0.74	254	0.43	4.9	23	103.7	3.4
YKJ-155A	500	7.5	1	14.5	15	0.74	113	1.45	4.4	27	88	8.6
YKJ-155A	500	12	1	>20	N/A	0.74	N/A	>2	4.1	33	67	10
YKJ-155B	500	5	1	3.9	3	0.74	280	0.39	5.1	22	76	4
YKJ-155B	500	7.5	1	5.49	20	0.74	298	0.55	4.6	26	67	6.3
YKJ-155B	500	12	1	13.2	15	0.74	198	1.32	4.1	33	62	7.5